



**Defense Special Weapons Agency  
Alexandria, VA 22310-3398**



**DNA-TR-95-59-V3**

**Advanced Simulator Power Flow  
Technology/Advanced Radiation Simulation  
Volume 3—Computational Methods  
for POS and Vacuum Power Flow**

**Donald Parks, et al.  
Maxwell Technologies Inc.  
Federal Division  
8888 Balboa Avenue  
San Diego, CA 92123-1506**

**September 1998**

**Technical Report**

**CONTRACT No. DNA 001-93-C-0229**

**Approved for public release;  
distribution is unlimited.**

**19981028 035**

**DESTRUCTION NOTICE:**

Destroy this report when it is no longer needed.  
Do not return to sender.

PLEASE NOTIFY THE DEFENSE SPECIAL WEAPONS  
AGENCY, ATTN: CSTI, 6801 TELEGRAPH ROAD,  
ALEXANDRIA, VA 22310-3398, IF YOUR ADDRESS IS  
INCORRECT, IF YOU WISH IT DELETED FROM THE  
DISTRIBUTION LIST, OR IF THE ADDRESSEE IS NO  
LONGER EMPLOYED BY YOUR ORGANIZATION.



## DISTRIBUTION LIST UPDATE

This mailer is provided to enable DSWA to maintain current distribution lists for reports. (We would appreciate your providing the requested information.)

- ☐ Add the individual listed to your distribution list.
- ☐ Delete the cited organization/individual.
- ☐ Change of address.

### NOTE:

Please return the mailing label from the document so that any additions, changes, corrections or deletions can be made easily. For distribution cancellation or more information call DSWA/IMAS (703) 325-1036.

NAME: \_\_\_\_\_

ORGANIZATION: \_\_\_\_\_

#### OLD ADDRESS

#### CURRENT ADDRESS

\_\_\_\_\_  
\_\_\_\_\_  
\_\_\_\_\_

\_\_\_\_\_  
\_\_\_\_\_  
\_\_\_\_\_

TELEPHONE NUMBER: (    ) \_\_\_\_\_

#### DSWA PUBLICATION NUMBER/TITLE

#### CHANGES/DELETIONS/ADDITIONS, etc.)

(Attach Sheet if more Space is Required)

\_\_\_\_\_  
\_\_\_\_\_  
\_\_\_\_\_

\_\_\_\_\_  
\_\_\_\_\_  
\_\_\_\_\_

DSWA OR OTHER GOVERNMENT CONTRACT NUMBER: \_\_\_\_\_

CERTIFICATION OF NEED-TO-KNOW BY GOVERNMENT SPONSOR (if other than DSWA): \_\_\_\_\_

SPONSORING ORGANIZATION: \_\_\_\_\_

CONTRACTING OFFICER OR REPRESENTATIVE: \_\_\_\_\_

SIGNATURE: \_\_\_\_\_

CUT HERE AND RETURN



# REPORT DOCUMENTATION PAGE

Form Approved

OMB No. 0704-0188

Public reporting burden for this collection of information is estimated to average 1 hour per response including the time for reviewing instructions, searching existing data sources, gathering and maintaining the data needed, and completing and reviewing the collection of information. Send comments regarding this burden estimate or any other aspect of this collection of information, including suggestions for reducing this burden, to Washington Headquarters Services, Directorate for Information Operations and Reports, 1215 Jefferson Davis Highway, Suite 1204, Arlington, VA 22202-4302, and to the Office of Management and Budget, Paperwork Reduction Project (0704-0188), Washington, DC 20503.

1. AGENCY USE ONLY (Leave blank)		2. REPORT DATE 980901	3. REPORT TYPE AND DATES COVERED Technical 931001 - 961030	
4. TITLE AND SUBTITLE Advanced Simulator Power Flow Technology/Advanced Radiation Simulation Volume 3—Computational Methods for POS and Vacuum Power Flow			5. FUNDING NUMBERS C - DNA 001-93-C-0229 PE - 4662 PR - AB TA - AJ WU - DH00011	
6. AUTHOR(S) Donald Parks, Randy Ingermanson, Paul Steen, John Thompson, and Jack Watrous				
7. PERFORMING ORGANIZATION NAME(S) AND ADDRESS(ES) Maxwell Technologies Inc. Federal Division 8888 Balboa Avenue San Diego, CA 92123-1506			8. PERFORMING ORGANIZATION REPORT NUMBER MTFD300-28	
9. SPONSORING/MONITORING AGENCY NAME(S) AND ADDRESS(ES) Defense Special Weapons Agency 6801 Telegraph Road Alexandria, VA 22310-3398 EST/Ware			10. SPONSORING/MONITORING AGENCY REPORT NUMBER  DNA-TR-95-59-V3	
11. SUPPLEMENTARY NOTES This work was sponsored by the Defense Special Weapons Agency under RDT&E RMC Code B4662D GE 00011 3300A AB 25904D.				
12a. DISTRIBUTION/AVAILABILITY STATEMENT  Approved for public release; distribution is unlimited.			12b. DISTRIBUTION CODE	
13. ABSTRACT (Maximum 200 words)  This is the third of 3 volumes describing work for the Advanced Simulator Power Flow Technology/Advanced Radiation Simulation Program. This volume, for FY96, deals with analytical, computational and experimental studies of power flow in vacuum feed and switch regions of pulsed power, inductive energy store systems. Section 1 reports on the development and testing of algorithms for computing the electron magnetohydrodynamic Hall effect in MHD fluid codes. Section 2 contains numerical studies via Mach2 of coupled electron Hall and fluid flow effects in plasma opening switch experiments conducted in the parallel plate geometry of the Hawk generator. In Sections 3 and 4, respectively, Mach2 is applied to the analysis of freely expanding flashboard plasmas and of plasmas injected through the anode structure into the switch gap of ACE 4. Section 5 deals with experimental evidence indicating that switch voltage is limited by effects originating at the electrode surfaces and with physical models to quantify these effects. Sections 6 and 7 describe SPOCK, a user friendly code for rapid analysis of the pulsed power. Section 8 describes development of the triangular, unstructured grid, electromagnetic PIC code, TRIMAX, and its application to power flow studies in ACE 4.				
14. SUBJECT TERMS  Pulsed Power Aboveground Simulation  Inductive Energy Store Plasma Opening Switch			15. NUMBER OF PAGES 284	
			16. PRICE CODE	
17. SECURITY CLASSIFICATION OF REPORT UNCLASSIFIED	18. SECURITY CLASSIFICATION OF THIS PAGE UNCLASSIFIED	19. SECURITY CLASSIFICATION OF ABSTRACT UNCLASSIFIED	20. LIMITATION OF ABSTRACT  SAR	



**UNCLASSIFIED**

**SECURITY CLASSIFICATION OF THIS PAGE**

**CLASSIFIED BY:**

N/A since Unclassified.

**DECLASSIFY ON:**

N/A since Unclassified.

**CLASSIFICATION OF THIS PAGE**  
**UNCLASSIFIED**

## SUMMARY

This report, Volume 3, describes work performed in Fiscal Year 1996 (FY96 under contract DNA001-93-C-0229, the third year of a three-year program titled *Advanced Simulator Power Flow Technology for Advanced Radiation Simulation*. The first volume for FY94 was issued as DNA-TR-95-59.

The objective of the program is to model, design and validate means for achieving more efficient power transfer from the capacitor prime energy storage systems up to and including the dynamic radiation source of the simulator. This report deals primarily with analytical, computational and experimental studies related to this objective, focusing primarily on power flow in the plasma opening switch (POS) and in the vacuum feed region separating switch and load regions in pulsed power, inductive energy store systems and, to a lesser degree, on the performance of PRS loads interacting with a switch.

The MHD codes previously used at Maxwell for POS calculations did not accurately represent all of the physical mechanisms that would allow us to predict switch voltage and current transfer to a load. We have incorporated the electron magnetohydrodynamic Hall effect, which does allow voltage to develop as the plasma thins in the course of its evolution under pulsed power, into Mach2 and into the plane geometry version of DELTA. Whether this effect alone is sufficient to account for observed voltages in microsecond conduction time switches is not yet known. It is quite possible, but by no means certain, that locally unbalanced charges or other physical effects not accounted for in quasineutral theories dominate the opening phase of a POS. Algorithms to represent the Hall effect are the subject of Section 1. A scheme, named AlgoC, based on upwind differencing is shown by intensive testing on problems supporting analytical solutions to be the most successful of these.

The application of a version of Mach 2 containing AlgoC to the analysis of the Hawk parallel plate experiment is the subject of Section 2. The experiment was conceived to permit ready access of diagnostics, in particular HeNe interferometry, to measure the distribution of electron density throughout the plasma. The electron distribution is measured in situ both before and during the time that plasma conducts current from a Marx generator. The calculations were conceived not only to make direct comparisons with experiment, but also to determine the importance of the Hall effect under conditions of density comparable to those used in microsecond class switches.

Two pieces of evidence suggest that the Hall effect is important and that its inclusion in a simulation allows the simulation to agree better with experiment. The first is the polarity effect. Changing the polarity of current flow in the simulations leads to significant differences in how the electron number density distribution evolves throughout the conduction phase. The second is the comparison of the evolution of electron number density as obtained in an ideal MHD simulation, in a positive polarity Hall MHD simulation, with that observed experimentally. The growth of the evacuated region between the inner electrode and the main body of plasma, in particular, is modeled much more faithfully with the positive polarity Hall MHD calculation than with the ideal MHD calculation. Further pieces of compelling evidence would likely be obtained by an examination of the experiment in which current polarity was reversed, but at the time of these investigations, the data for that experiment had not yet been sufficiently processed to be useful for such purposes.

The Hawk parallel plate experiment was the only experiment that was analyzed with an MHD-Hall code. The analyses of experiments conducted on ACE 4 and its flashboard plasma sources, described in Sections 2, 3 and 4, were performed with the Hall effect turned off in Mach2.

The principle objective of the analysis in Section 3 was twofold, first to perform further validation tests of Mach2, and second, to learn the effect of anode structure on the distribution of plasma in the anode-cathode gap. Interferometry shows that the plasma distribution is affected by such details as the shape and spacing of the anode rods and vanes. The vanes result in electron number densities which are a half to a third those which result when circular rods are used, and result in a time-behavior more slowly paced than that seen with the circular rods. These features, captured in the Mach 2 simulations, are in large measure a consequence of the magnetic fields entrained in the plasma following its injection from the flashboards. A second feature revealed by both computations and experiment is the formation of plasma jets, a tendency much more strongly revealed for vanes than for rods. The comparison indicates that the simulation is producing electron densities which are in the same ballpark as those seen experimentally, and that there are similarities in overall timing. Differences could very well be an underestimation of plasma resistivity by the Spitzer model used in the calculation.

Detailed comparisons between Mach 2 simulations and ACE 4 switch experiments, Section 4, show promise in their ability to reveal significant details in the nature of the conduction phase. These details include the increased ionization that occurs during the conduction phase and the rapid thinning of the plasma as the conduction phase comes to an end. Within the initial uniform temperature and axial density family of computations, a temperature between 1.5 and

2.0 eV gave the best fit to experimental data. Uncertainties remain because initial temperatures are not uniform throughout the plasma, nor is the axial distribution of electron density. These calculations were performed without the Hall effect. It still remains to use the experimental data to validate the ability of Mach2 to calculate POS voltage waveforms. These calculations will require not only the Hall algorithm, but also an algorithm for properly treating the boundary at conducting surfaces. It is also likely that physical mechanisms not contained in Mach2, such as the effects associated with the generation of neutrals, will have to be incorporated into the code.

In Section 5 the hypothesis is set forth that neutral atoms evolving from surfaces or by other means are at the root of particular features observed in interferometric and spectroscopic probing of the switch plasma, and in the waveforms observed in electrical measurements. The experimental data supporting this hypothesis is presented. The essential elements of the hypothesis are that during the conduction phase neutrals atoms are left behind the primary conduction path of the switch, that these atoms become ionized during the opening phase, and if present in sufficient quantity present an alternate, low impedance path for current. A simple model to describe this ionizing cloud of neutrals is given and used in a circuit model to predict how it may affect the electrical characteristics of a plasma opening switch. These predictions were among the first applications of the new circuit code, SPOCK, the subject of Sections 6 and 7.

The computational engine of SPOCK is SPICE, an industry-standard circuit analysis tool developed at the University of California at Berkeley over the last two decades. It is encapsulated in MIRIAD, whose modern software architecture underlies the system survivability tool MOSAIC developed by Maxwell for DSWA. SPICE allows a user to build complex circuits from simple circuit components, such as resistors, capacitors, inductors, transmission lines, and switches, as well as from MOSFETS and many other components which are of little or no interest for pulsed power applications. It also allows the programmer to build new devices in the C programming language and integrate them into SPICE. MIRIAD provides a framework for linking one or more codes with a graphical user interface, including menus, forms and plotting capabilities. A unique feature of MIRIAD is its ability to connect the outputs and inputs of multiple codes into one seamless whole. The power and user convenience of the MIRIAD framework comes from a good graphical user interface, a facility to create multiple versions of a code on a variety of UNIX workstations, IBM PC clones running Windows 95 or Windows NT, and the integrability of other codes and models at some later date.

In order to make SPICE a practical tool for pulsed power applications several new devices were developed. These devices include but are not limited to plasma opening switches and load devices of the BRS and PRS types. The code has been tested and validated for a large number of applications. Section 7, which describes the new devices incorporated into SPOCK, contains an application to a DECADE DM1 module driving a BRS load.

Section 8 is exclusively devoted to a discussion of the TRIMAX PIC code. Previously developed for the study of vacuum power flow during our PBFA II electromagnetic modeling effort for Sandia National Laboratories (1984-1991), this code has been extended under the present DSWA work to support a full particle-in-cell capability. Based upon an unstructured triangular mesh created by the S3Mesh automatic (hybrid Delaunay/advancing front) grid generator, the code provides for economy of cells, highly realistic (2-D) geometry, and is fully vector/concurrent, providing for efficient utilization of modern computing platforms. Notable capabilities of the code now include space-charge-limited-emission from conformal and multiply connected surfaces (eliminating non-physical field enhancement of boundary stair- stepping inherent in traditional FDTD PIC codes), and the ability to treat ACE 4/DECADE high-aspect ratio, convoluted geometries without severe storage penalty, accuracy losses and overly prohibitive timestep restrictions. The code has a modern graphical user interface which supports extensive data visualization capabilities (including provision for animation) and runs in a UNIX workstation environment. In Sections 8.1 through 8.3 the theoretical basis underlying the code's mixed Galerkin finite element techniques is outlined. Our unique algorithm for evaluation of the discrete particle current inner product source term contributions arising in the variational methods is described in Section 8.4. A code capability summary is presented in Section 8.5. Parallel processing considerations are discussed in Section 8.6. Finally, Section 8.7 is devoted to code testing and applications, including PIC simulation of the recent ACE 4 plasma opening switch (POS)/dummy load experiments.

**CONVERSION FACTORS FOR U.S. CUSTOMARY TO METRIC (SI)  
UNITS OF MEASUREMENT**

To Convert From	To	Multiply By
angstrom	meters (m)	1.000 000 x E -10
atmosphere (normal)	kilo pascal (kPa)	1.013 25 x E +2
bar	kilo pascal (kPa)	1.000 000 x E +2
barn	meter <sup>2</sup> (m <sup>2</sup> )	1.000 000 x E -28
British thermal unit (thermochemical)	joule (J)	1.054 350 x E +3
cal (thermochemical)/cm <sup>2</sup>	mega joule/m <sup>2</sup> (MJ/m <sup>2</sup> )	4.184 000 x E -2
calorie (thermochemical)	joule (J)	4.184 000
calorie (thermochemical)/g	joule per kilogram (J/kg)*	4.184 000 x E +3
curies	gig becquerel (Gbcq) <sup>+</sup>	3.700 000 x E +1
degree Celsius	degree kelvin (K)	°K = °C + 273.15
degree (angle)	radian (rad)	1.745 329 x E -2
degree Fahrenheit	degree kelvin (K)	°K = (°F + 459.67)/1.8
electron volt	joule (J)	1.602 19 x E -19
erg	joule (J)	1.000 000 x E -7
erg/second	watt (W)	1.000 000 x E -7
foot	meter (m)	3.048 000 x E -1
foot-pound-force	joule (J)	1.355 818
gallon (U.S. liquid)	meter <sup>3</sup> (m <sup>3</sup> )	3.785 412 x E -3
inch	meter (m)	2.540 000 x E -2
jerk	joule (J)	1.000 000 x E +9
joule kilogram (J/kg) (radiation dose absorbed)	gray (Gy)*	1.000 000
kilotons	terajoules	4.183
kip (1000 lbf)	newton (N)	4.448 222 x E +3
kip/inch <sup>2</sup> (ksi)	kilo pascal (kPa)	6.894 757 x E +3
ktap	newton-second/m <sup>2</sup> (N-s/m <sup>2</sup> )	1.000 000 x E +2
micron	meter (m)	1.000 000 x E -6
mil	meter (m)	2.540 000 x E -5
mile (international)	meter (m)	1.609 344 x E +3
ounce	kilogram (kg)	2.834 952 x E -2
pound-force (lbf avoirdupois)	newton (N)	4.488 222
pound-force inch	newton-meter (N•m)	1.129 848 x E -1
pound-force/inch	newton/meter (N•m)	1.751 268 x E +2
pound-force/foot <sup>2</sup>	kilo pascal (kPa)	4.788 026 x E -2
pound-force/inch <sup>2</sup> (psi)	kilo pascal (kPa)	6.894 757
pound-mass (lbm avoirdupois)	kilogram (kg)	4.535 9024 x E -1
rad (radiation dose absorbed)§	gray (Gy)*	1.000 000 x E -2
roentgen§	coulomb/kilogram (C/kg)	2.579 760 x E -4
shake	second (s)	1.000 000 x E -8
slug	kilogram (kg)	1.459 390 x E -1
torr (mm Hg, O° C)	kilo pascal (kPa)	1.333 22 x E -1

\* The gray (Gy) is the accepted SI unit equivalent to the energy imparted by ionizing radiation to a mass and corresponds to one joule/kilogram.

+ The becquerel (Bq) is the SI unit of radioactivity; 1 Bq = 1 event/s.

## TABLE OF CONTENTS

Section	Page
SUMMARY .....	iii
CONVERSION TABLE .....	vii
FIGURES .....	xii
 1    EFFORTS LEADING TO AND A DESCRIPTION OF A NEW HALL EFFECT ALGORITHM FOR MACH2 .....	 1
1.1    INTRODUCTION .....	1
1.2    HISTORY OF THE HALL EFFECT IN MACH2 .....	2
1.3    FIRST ATTEMPT – IMPLICIT MULTIGRID ALGORITHM (IMA) .....	6
1.4    NEW ALGORITHM DEVELOPMENT .....	9
1.5    GROSSMANN TEST PROBLEMS .....	12
1.6    SUMMARY – THEORY VS MACH2 .....	19
 2    HAWK PARALLEL PLATE POS MODELING .....	 55
2.1    DESCRIPTION OF EXPERIMENTS .....	55
2.2    DESCRIPTION OF SIMULATION SETUP .....	57
2.3    DISCUSSION OF SIMULATION RESULTS AND COMPARISON TO EXPERIMENTS .....	 60
 3    FLASHBOARD PLASMA INTERACTION WITH ANODE VANES .....	 93
 4    OPENING SWITCH SIMULATIONS .....	 112
4.1    SIMULATION OF EXTENDED TRANSPARENT ANODE EXPERIMENT – SHOT 1037 .....	 112
4.2    SIMULATION OF MESH SHOT – SHOT 1727 .....	114
 5    THE ROLE OF NEUTRAL ATOMS IN PLASMA OPENING SWITCHES .....	 146
5.1    SALIENT EXPERIMENTAL RESULTS .....	146
5.2    POSSIBLE SOURCES OF NEUTRALS .....	148
5.3    IONIZATION AND HEATING OF THE GAS .....	152
5.3.1    Seeding of the Gas by Photoionization .....	152
5.3.2    Joule Heating and Collisional Ionization .....	153
5.4    IMPEDANCE OF THE SECONDARY PLASMA .....	155
5.5    EFFECT OF NEUTRALS ON SWITCH PERFORMANCE .....	157

## TABLE OF CONTENTS (Continued)

Section	Page
6 SPOCK: SPICE-BASED POWERFLOW OPTIMIZING CIRCUIT KIT .....	188
6.1 SPICE .....	188
6.2 MIRIAD .....	188
6.3 PHYSICS MODELS .....	189
6.4 WRITING A SPICE DEVICE .....	190
6.5 NEW SPICE DEVICES .....	191
6.5.1 POS Devices .....	191
6.5.2 Load Devices .....	192
6.5.3 Function Devices .....	193
6.5.4 Miscellaneous Devices .....	194
6.6 CONVENTIONAL SPICE DEVICES .....	196
6.7 SPOCK SIMULATION OF DM1 WITH ELECTRON-BEAM LOAD .....	196
6.8 CONCLUSIONS .....	196
7 POS DEVICES .....	201
7.1 POS CONDUCTION MODELS .....	201
7.1.1 1-D Snowplow (SP1) .....	201
7.1.2 1-D Hall Effect Device (EH1) .....	204
7.2 POS OPENING MODELS .....	205
7.2.1 R-dot Opening Model (ORD) .....	206
7.2.2 Z-flow Opening Model (OZF) .....	207
7.2.3 Erosion Z-flow Opening Model (OEZ) .....	208
7.2.4 Limited Erosion Z-flow Opening Model (OEL) .....	210
7.3 POS SHORTING MODELS .....	211
7.3.1 Simple Short-circuit Model (OSM) .....	212
7.3.2 Temperature-Dependent Shorting Model (OST) .....	213
7.4 LOAD DEVICES .....	215
7.4.1 1-D PRS (PRS) .....	215
7.4.2 Bremsstrahlung Diode (BRD) .....	217
7.4.3 Plasma-Filled Diode (PFD) .....	220



## TABLE OF CONTENTS (Continued)

Section	Page
7.5 FUNCTION DEVICES .....	222
7.5.1 O-D Analytic Function (FANØ) .....	222
7.5.2 O-D Function on Grid (FGRØ) .....	222
7.5.3 1-D Analytic Function (FAN1) .....	224
7.5.4 1-D Function on Grid (FRG1) .....	224
7.5.5 2-D Constant Function (FCN2) .....	224
7.5.6 2-D Product Function (FPR2) .....	224
7.5.7 Function History (HIST) .....	225
7.6 MISCELLANEOUS DEVICES .....	225
7.6.1 Convolute (CNV) .....	225
7.6.2 Explosively Driven Flux Compressor (EDFC) .....	227
7.6.3 Current Source (ISC) .....	228
7.6.4 Voltage Source (VSC) .....	228
7.6.5 Timed Switch (SWT) .....	228
7.6.6 Ammeter (IMR) .....	229
7.6.7 Inductance Estimator (LVI) .....	230
8 TRIMAX UNSTRUCTURED GRID ELECTROMAGNETIC PIC CODE EXTENSIONS .....	231
8.1 MOTIVATION .....	231
8.2 TRIMAX FINITE ELEMENT FIELD SOLVER .....	231
8.2.1 Variational Principles for Maxwell's Equations .....	232
8.2.2 Nédélec's Method (ELnHC) .....	233
8.2.3 ECHL and MECHL Methods .....	236
8.2.4 Energy Conservation .....	237
8.2.5 Timestepping .....	238
8.2.6 Mass Matrix Solution .....	240
8.2.7 Time Integration Methods .....	240
8.3 SOME FIELD ALGORITHM CONSIDERATIONS .....	241
8.3.1 Difficulties with the ECHL Method .....	241
8.3.2 Some Comments on Criticism of the Nédélec Method .....	241

## TABLE OF CONTENTS (Continued)

Section	Page
8.4    PARTICLE PUSH AND CURRENT ALGORITHMS .....	242
8.4.1    Weak Form of Continuity Equation .....	243
8.4.2    Weak Form Determination of Charge for Space-Charge Limited Surface Emission .....	244
8.4.3    Evaluation of Particle Current Basis Function Inner Products .....	244
8.5    TRIMAX PIC CODE CAPABILITIES .....	246
8.6    PARALLEL PROCESSING .....	247
8.7    APPLICATIONS .....	247
8.7.1    Space-Charge Limited Emission Tests .....	247
8.7.2    Gyro Orbit Test .....	248
8.7.3    MITL Test .....	249
8.7.4    TEM Lumped Inductive Boundary Condition Test (ELnHC) .....	249
8.7.5    Space-Charge Limited Emission from Complex Floating Conductors .....	249
8.7.6    Dielectric Test .....	250
8.7.7    TRIMAX Test Problem Result Summary .....	250
8.7.8    TRIMAX 2-D PIC Simulations of ACE 4 .....	251
9    REFERENCES .....	261

## FIGURES

Figure	Page
1-1 Standard Hall algorithm results on coaxial test problem at $t=0.25$ ns .....	20
1-2 The standard Hall algorithm develops a numerical instability which causes growth of the magnetic field to physically untenable levels .....	21
1-3 The IMA algorithm gives qualitatively correct penetration of the magnetic field at early times .....	22
1-4 The IMA algorithm leads to the development and propagation from cathode to anode of magnetic vortices .....	23
1-5 At this time the presumed numerical instability has grown to intolerable levels ....	26
1-6 The effect of adding a small amount of resistive diffusion to the calculation is to quench the numerical instability .....	27
1-7 The effect of adding a small amount of resistive diffusion to the calculation is to quench the numerical instability .....	28
1-8 For the variable density case (see text) field propagation with the IMA algorithm does not follow the theoretical expectation .....	29
1-9 Results for AlgoC propagation of a square pulse in a finite medium .....	31
1-10 Orthogonal grid used to compare with calculations on a non-orthogonal grid .....	33
1-11 Contours of $rB_\theta$ at $t=2.5$ ns for orthogonal grid calculation .....	34
1-12 Density contours on the orthogonal grid .....	35
1-13 Non-orthogonal grid used to compare with calculations on an orthogonal grid ....	36
1-14 Contours of $rB_\theta$ at 2.5 ns for non-orthogonal grid calculation .....	37
1-15 Density contours on non-orthogonal grid .....	38
1-16 Problem 1 electron number density profile .....	39
1-17 Mach2 results for $rB_\theta$ contours of Problem 1 at (a) 501 ns and (b) 851 ns .....	40
1-18 Problem 2 electron number density profile .....	42

## FIGURES (Continued)

Figure	Page
1-19 Mach2 results including Hall effect for electron number density contours in Problem 2 at 1.8 ns .....	43
1-20 Mach2 result including Hall effect for $rB_\theta$ contours in Problem 2 at 1.8 ns .....	44
1-21 Mach2 result without Hall effect for electron number density contours in Problem 2 at 1.8 ns .....	45
1-22 Mach2 result without Hall effect for $rB_\theta$ contours in Problem 2 at 1.8 ns .....	46
1-23 Problem 3 electron number density profile .....	47
1-24 The magnetoshock for Problem 3 at 16 ns .....	48
1-25 The magnetoshock for Problem 3 has reached the end of the computational domain at 32 ns .....	49
1-26 Mach2 results for $rB_\theta$ contours in Problem 4 at 1 ns .....	50
1-27 Mach2 results for $rB_\theta$ contours in Problem 4 at 2.5 ns .....	51
1-28 Problem 5 electron number density .....	52
1-29 Mach2 results for $rB_\theta$ contours in Problem 5 at 100 ns .....	53
1-30 Mach2 results for $rB_\theta$ contours in Problem 5 at 300 ns .....	54
2-1 Observed electron number density at time close to that of initiation of pulsed power .....	63
2-2 Mean degree of ionization versus temperature for a $CF_2$ plasma at an ion density of $2 \times 10^{15} \text{ cm}^{-3}$ .....	64
2-3 Measured electron density contour with guns only at 1 $\mu\text{s}$ before firing Marx .....	65
2-4 Simulated electron density contours ( $T=1 \text{ eV}$ ) with guns only at 1 $\mu\text{s}$ before firing Marx .....	66
2-5 Simulated electron density contours ( $T = 2 \text{ eV}$ ) with guns only at 1 $\mu\text{s}$ before firing Marx .....	67

## FIGURES (Continued)

Figure	Page
2-6 Measured electron density contours at 500 ns .....	68
2-7 Measured electron density contours at 550 ns .....	69
2-8 Measured electron density contours at 575 ns .....	70
2-9 Measured electron density contours at 600 ns .....	71
2-10 Measured electron density contours at 700 ns .....	72
2-11 Mach2 ideal MHD (no Hall effect) simulation .....	73
2-12 Mach2 Hall MHD simulation in positive polarity .....	80
2-13 Mach2 Hall MHD simulation in negative polarity .....	86
3-1 Simulation mesh for case of circular rods .....	99
3-2 Simulation mesh for case of rectangular vanes .....	100
3-3 Measured electron density for rodded case.....	101
3-4 Measured electron density distribution for vaned case.....	102
3-5 Measured electron densities for flashboard only, shot 1303 .....	103
3-6 Measured electron densities for flashboard only, shot 1317 .....	104
3-7 Electron number density contour plots from the circular rod simulation at times $t = 2501$ ns and $t = 3501$ ns .....	105
3-8 Plasma velocity vector from the lower left hand corner of simulation domain at a time between 2501 ns and 3501 ns .....	107
3-9 Magnetic field at 3001 ns .....	108
3-10 Blowup of left hand corner of Figure 3-9 .....	109
3-11 Simulated interferometric line-of-sight signals .....	110
3-12 Electron density contour for vaned anode at $t = 4 \mu\text{s}$ .....	111

## FIGURES (Continued)

Figure	Page
4-1 Interferrometric signals for pre-shot 1037, channels 3-8 .....	118
4-2 Responses from channels 3 and 4 for the flashboard only case as well as for the pulsed power case .....	119
4-3 Comparison of experimental and simulated line electron densities for channel 3 ..	120
4-4 Comparison of experimental and simulated line electron densities for channel 4 ..	121
4-5 Comparison of experimental and simulated line electron densities for channel 5 ..	122
4-6 Comparison of experimental and simulated line electron densities for channel 6 ..	123
4-7 Comparison of experimental and simulated line electron densities for channel 7 ..	124
4-8 Comparison of experimental and simulated line electron densities for channel 8 ..	125
4-9 These ion density plots help reveal the cause for the shapes of the density profiles (see text) .....	126
4-10 Experimental electron density for flashboard only case – no pulsed power .....	130
4-11 Comparison of measured and simulated electron densities for three simulation temperatures .....	131
4-12 Comparison of measured and simulated electron densities for three simulation temperatures .....	132
4-13 Comparison of measured and simulated electron densities for three simulation temperatures .....	133
4-14 Comparison of measured and simulated electron densities for three simulation temperatures .....	134
4-15 Comparison of measured and simulated electron densities for three simulation temperatures .....	135
4-16 Comparison of measured and simulated electron densities for three simulation temperatures .....	136

## FIGURES (Continued)

Figure	Page
4-17 Comparison of measured and simulated electron densities for three simulation temperatures .....	137
4-18 Comparison of measured and simulated electron densities for three simulation temperatures .....	138
4-19 Simulated electron density contours for a temperature of 1.5 eV at (a) 500 ns and (b) 600 ns .....	139
4-20 Simulated electron number density contours for a temperature of 2.5 eV at (a) 400 ns (b) 500 ns and (c) 600 ns .....	141
4-21 Line integrated electron densities for a flashboard only simulation .....	144
4-22 Simulated electron density contours at a time when different LOS-signals have converged (see text) .....	145
5-1 ACE 4 extended transport anode configuration .....	160
5-2 Typical density distribution in the POS .....	161
5-3 Densities, current and switch voltage for 3.0 $\mu$ s delay .....	162
5-4 Densities, currents and switch voltage for 2.5 $\mu$ s delay .....	163
5-5 ACE 4 Shot 1305 .....	164
5-6 Experimental configuration used with interferometry .....	165
5-7 Experimental configuration with conical extension used for interferometry .....	166
5-8 Switch voltage and electron densities observed in shots 1937 (no extension) and 1959 (2.5 cm extension) .....	167
5-9 Switch voltage and electron densities observed in shots 1937 (no extension) and 1959 (2.5 cm extension) .....	168
5-10 Switch voltage and electron densities observed in shots 1937 (no extension) and 1959 (2.5 cm extension) .....	169

## FIGURES (Continued)

Figure	Page
5-11 Switch voltage and electron densities observed in shots 1937 (no extension) and 1959 (2.5 cm extension) .....	170
5-12 Switch voltage and electron densities observed in shots 1937 (no extension) and 1959 (2.5 cm extension) .....	171
5-13 Switch voltage and electron densities observed in shots 1937 (no extension) and 1959 (2.5 cm extension) .....	172
5-14 Switch voltage and electron densities observed in shots 1937 (no extension) and 1959 (2.5 cm extension) .....	173
5-15 Density and current measurements on HAWK using guns .....	174
5-16 Ionizing neutrals form a magnetized parasitic plasma on the generator side of the primary snowplowed plasma .....	175
5-17 Experimental arrangement used for spectroscopic measurements on ACE 4 .....	176
5-18 Switch voltage relative H $\alpha$ and >5 keV intensities observed for Shot 1937 .....	177
5-19 Line profiles versus wavelength for Shot 1937.....	178
5-20 Reflection coefficients .....	179
5-21 Particle and energy sputtering coefficients by hydrocarbons with normally incident particles .....	180
5-22 Particle and energy sputtering coefficients of hydrocarbons with normally incident particles .....	181
5-23 Circuit model used to analyze effects of parasitic plasma on switch voltage and load current .....	182
5-24 Circuit model applied to ACE 4 Shot 1305, including parasitic plasma .....	183
5-25 Circuit model applied to ACE 4 Shot 1305, but without parasitic plasma .....	184
5-26 The effect of varying amounts of initial neutral concentration .....	185
5-27 The electron number density in the neutral plasma corresponding to 5-24 .....	186



## FIGURES (Continued)

Figure	Page
5-28 The electron temperature in the plasma corresponding to 5-24 .....	187
6-1 Simulation of the POS Current and Tube Voltage for DM1 Shot 1143 .....	198
6-2 Simulation of the POS Current and Transfer Capacitor Voltage for DM1 Shot 1322 .....	199
6-3 Simulation of the POS Current and POS Voltage for DM1 Shot 1353 .....	200
8-1 Steady-state electric field magnitude contours for 2-D TRIMAX PIC complex floating conductor emission test problem .....	254
8-2 Electron charge density contours at $t = 7, 14, 21$ , and $23$ ns for 2-D TRIMAX PIC simulation of ACE 4 with POS gap = $25$ mm .....	255
8-3 Electron charge density contours at $t = 42.5, 49.6, 56.6$ , and $63.8$ ns for 2-D TRIMAX PIC simulation of ACE 4 with POS gap = $25$ mm .....	256
8-4 Magnetic (top) and electric field (bottom) magnitudes for 2-D TRIMAX simulation of ACE 4 with POS gap = $25$ mm .....	257
8-5 Electron charge density contours at $t = 6.5$ ns for 2-D TRIMAX PIC simulation of ACE 4 with POS gap = $2.5$ mm .....	258
8-6 Electron charge density contours at $t = 11.75$ ns for 2-D TRIMAX PIC simulation of ACE 4 with POS gap = $2.5$ mm .....	259
8-7 Electron charge density contours at $t = 22$ ns for 2-D TRIMAX PIC simulation of ACE 4 with POS gap = $2.5$ mm .....	260

# SECTION 1

## EFFORTS LEADING TO AND A DESCRIPTION OF A NEW HALL EFFECT ALGORITHM FOR MACH2

### 1.1 INTRODUCTION.

Over the past several years, theory and computer simulations have indicated that the Hall effect may have a strong influence over the interaction between plasma and magnetic field in the plasma opening switch, particularly in the low density regime ( $n_e \leq 10^{14}$  per cc). More recently, experiments conducted in parallel plate geometry and simulations of those experiments, both performed at NRL, have suggested that the Hall effect can have a decided influence even in higher density regimes ( $n_e \cong 10^{15} - 10^{16}$  per cc). This is not surprising since the Hall parameter should satisfy the condition  $\omega_c \tau \gg 1$ , especially during the later part of the conduction phase and into the opening phase of microsecond conduction time switches. This result, along with the widely held suspicion that the Hall effect would be important in modeling the DECADE POS, have prompted an effort to outfit Mach2 with an improved algorithm for dealing with the Hall effect.

For a discussion of the Hall effect, the reader is referred to References 1 and 2. There the authors discuss the regions of parameter space where the Hall effect is significant and the peculiar response of plasma dominated by electron-magnetohydrodynamics which occur on time scales so short that ion motion can be neglected. A strong distinction is drawn between the Hall effect in cases where electrons and ions move together ( $\bar{v}_e \approx \bar{v}_i$ ) and where the velocity  $\bar{v}_e$  of electrons may differ strongly from the ion velocity  $\bar{v}_i$ . In plasma opening switches interest attaches primarily to the latter case.

The Hall effect causes magnetic field and plasma to couple in a manner which can be significantly different from that expected on the grounds of either ideal or non-ideal MHD. The primary difference is the development of a filamentary density structure. This is similar to the structure which develops in an accelerated fluid which is subject to growth of the Rayleigh-Taylor instability. This is important to POS modeling since the density in the low-density portions of the filamentary structure can become low enough to expect the switch to cease carrying the current supplied to it from the generator. In other words, the Hall effect can alter the time and place at which the switch is expected to open.

Mach2 is a very useful tool for modeling the POS as a quasi neutral plasma. Its geometric flexibility, its wide range of physics models, and its ease of modification help to make this so. The code has had provisions for including the Hall effect for some time, and this fact has made it an even more alluring tool for POS work. However, it has been discovered recently that the standard Hall effect algorithm in Mach2 is defective. It produces results quite dissimilar to those expected on theoretical grounds when exercised on problems simple enough to allow quantitative theoretical expectations. The algorithm has also exhibited instabilities which produce wildly nonphysical results. The algorithm has been exercised in POS modeling, but not to a great extent. While no virulent instabilities made themselves apparent in that work, the accuracy of the results must be questioned.

Thus, the situation at the onset of this effort was that on the one hand, there was the expectation of the importance of the Hall effect and a strong desire to include it in modeling efforts, and on the other hand, there was a very useful POS modeling tool, which just happened to fail catastrophically when it came to the Hall effect. So it seemed that some level of effort would be justified in correcting the deficiency in Mach2. This is the chronicle of that effort.

## **1.2 HISTORY OF THE HALL EFFECT IN MACH2.**

An algorithm for treating the Hall effect was not included within the scope of the initial Mach2 development effort. But sometime since that initial effort, as the code continued to evolve and develop in response to user demands, an algorithm for the Hall effect was implemented. In order to describe that algorithm, some background on the overall structure of Mach2 is in order.

Mach2 uses a technique known both as time-splitting and operator splitting to advance the equations of evolution. This technique is just a name for the simplest conceivable way of advancing a coupled set of partial differential equations. Specifically, each equation is advanced in time on its own, with the result of that advancement being fed into the next equation to be advanced. This is simple because it admits an open architecture into which new equations can be added with great ease. The counterexample would be a simultaneous solution of the entire set of evolution equations. This would require the solution of an equation matrix, and such an approach, in principle, makes the prospect of adding new equations more difficult than the operator splitting approach.

In a single time-step of operation, the main subroutine of Mach2 calls a number of other subroutines, each of which are the master subroutines for the set of subroutines responsible for

advancing a small set of equations corresponding to a given physical effect. Shown below is an excerpt from this main subroutine.

---

---

START MACH2 EXCERPT

---

---

```
      subroutine arun
c-----time-advance the physics equations and
c----- and write to the various output files
      100 continue
c=====BEGIN PHYSICS
c-----advance the time and cycle; compute a new time step
      call timstp
c-----compute the current from an external circuit
      if (ciron) call circuit
c-----compute edit quantities
      call budget
c-----radiation cooling model
      if (radiate) call radiant
c-----ion-electron splitting
      if (tsplit .ne. 0) call titecupl
c-----total or electron thermal conduction
      if (thmldif) call thmdiff('electron')
c-----ion thermal conduction
      if (thmldif .and. tsplit.ne.0) call thmdiff('ion')
c-----radiation field conduction
      if (radiate .and. radsplit) call thmdiff('radfld')
c-----resistive diffusion
      if (bdiff) call magdiff
c-----thermally-generated magnetic fields
      if (btherm) call thmag
c-----hall effect
      if (hallon) call halln
c-----lagrangian hydrodynamics
      if (hydron) call hydro
c-----lagrangian elastic dynamics
      if (hydron .and. strength) call elplastc
```

```

c-----advection and adaptive mesh generation
      if (hydron .or. meshon) call remesh
c-----attempt to zero the divergence of B
      if (brbzon) call potdivb(brbzon,itpot,potrelx)
c-----perform laser energy deposition
      if (laseron) call lasrdep
c-----evaluate detonation criteria for explosives
      if (explon) call explod
c-----evaluate equation of state and transport coefficients
      if (eoson) call eos
c=====END PHYSICS

.
.
.

c      loop until done
      go to 100

      return
      end

=====END MACH2 EXCERPT=====

```

The excerpt shows a number of subroutines being called, each of which is preceded by a comment indicating the nature of the physics being evaluated by that subroutine and its slaves. As new physical effects are added to the code, hooks for them are placed in this main subroutine.

The original Hall algorithm was based on the magnetic diffusion algorithm, but was substantially simpler. The magnetic diffusion algorithm is an implicit advance of:

$$\partial B / \partial t = -\text{curl}(\eta J) = -\text{curl}(\eta / \mu_0 \text{curl}(B)) \quad , \quad (1.1)$$

where B is the magnetic induction vector,  $\eta$  the resistivity and  $\mu_0$  the vacuum permeability. Moreover, this is done with a convergence accelerator known as the multigrid technique. This technique synthesizes a set of coarse grids which are based on the true computational grid, but each of which has only half as many cells in either direction as the grid from which it is based. Thus, the true grid might be a 16x32 grid; it would spawn coarse grids of 8x16, 4x8, 2x4, and 1x2. The magnetic diffusion equation is then solved on each of these coarse grids. Information

is passed between these solutions which is used to reduce the error in the solution on the finest grid.

The original Hall algorithm solved:

$$\partial B / \partial t = -\text{curl}(\mathbf{J} \times \mathbf{B} / \mu_0 n) , \quad (1.2)$$

where  $n$  is the plasma density. It used the same spatial differencing used by the magnetic diffusion solver. But it did so only on the finest grid, and with an explicit solve for the time-advance. In other words, it did not use the multigrid implicit time advance used by the magnetic diffusion equation solver, but it used the same finite difference scheme for the representing the spatial derivatives.

Because the original Hall algorithm was time-explicit, it was equipped with the ability to do temporal sub-cycling. This freed the rest of the code somewhat from the usually restrictive time step governing the Hall effect evolution of the magnetic field.

This algorithm has been used in the past, though to the knowledge of this author, its use has always been in the context of a full MHD simulation. Thus, the Hall algorithm may have been behaving poorly, but that behavior was masked by all the other things going on in the calculation. The current effort began with an explicit evaluation of the Hall algorithm operating on its own.

A simple problem was devised to exercise the Hall algorithm. The geometry was coaxial, with the inner boundary at 5 cm and the outer boundary at 7 cm. The space between inner and outer boundaries was filled with a uniform density medium with electron number density of  $2 \times 10^{13}$  per cc. The medium was not allowed to move. All physics models in the code were disabled, with the exception, of course, of the Hall effect, and the normal derivative of  $B$  was forced to vanish on the inner and outer boundaries. The magnetic field was driven with a current which instantly rose to a value of 500 kA and stayed at that level. The grid was 16x16. With the given current, the maximum magnetic field expected is 2 T. The standard Hall algorithm used a time step determined from:

$$dt|_{\text{hall}} = 0.1 e \mu_0 Z \rho (dx)^2 / \{B_{\text{max}} AM\} , \quad (1.3)$$

where  $e = 1.6 \times 10^{-19}$  C

$$\begin{aligned}\mu_0 &= 4\pi \times 10^{-7} \text{ H/m} \\ Z &= 2 \text{ (charge state)} \\ \rho &= 2 \times 10^{-7} \text{ kg/m}^3 \\ B_{\max} &= 2 \text{ T} \\ A &= 12 \text{ (atomic weight)} \\ M &= 1.67 \times 10^{-27} \text{ kg (proton mass)}.\end{aligned}$$

The factor of 0.1 ensures a conservative choice of time step. With the indicated parameters, the local Hall time step is  $3.14 \times 10^{-12}$  s. With the global time step of  $10^{-11}$  s, the subcyclor executes 32 subcycles per global time cycle. This places a fairly mild demand on the Hall algorithm, a situation which should not lead to numerical problems.

However, numerical problems did arise. Figures 1-1 and 1-2 illustrate the magnetic field contours at two times during the simulation. These plots indicate the development of an instability which causes the magnetic field to grow to physically implausible levels. In addition, the nature of the field propagation is quite different from that expected on theoretical grounds. The propagation should be as a curved front, with a propagation speed inversely proportional to the radius.

### 1.3 FIRST ATTEMPT - IMPLICIT MULTIGRID ALGORITHM (IMA).

The apparent dismal failure of the standard Hall algorithm prompted an investigation of the algorithm. It was found that the spatial part of the algorithm, that is, the differencing scheme used to calculate the current density from the magnetic field via Ampere's Law, and the difference scheme used to form the curl of a quantity for Faraday's Law, were identical to those used in the resistive-diffusion algorithm. Thus, the only difference that could be detected between the standard hall algorithm and the resistive-diffusion solver was in the treatment of time. The former was explicit, the latter was implicit, augmented with the multigrid convergence acceleration scheme. This observation led to the notion that putting the Hall algorithm under the auspices of the same implicit multigrid algorithm as used for resistive-diffusion might solve the problems described in the previous Section.

The prospect of putting the Hall effect into an algorithm as sophisticated as the implicit multigrid algorithm certainly sounds daunting, but it turns out to be not terribly difficult. The resistive diffusion algorithm identifies the resistive electric field explicitly. Thus, half the battle is won simply by augmenting every appearance of the resistive electric field with the Hall electric field.

The standard Hall algorithm already had provisions for calculating the Hall electric field, so that the code could be used directly. The other main challenge was to augment the IMA with the influence coefficients appropriate to the Hall effect (influence coefficients are part of the Euler scheme used for the implicit time advance of the equations). Again, this sounds daunting, but as the model for doing this already existed in the form of the resistive-diffusion equation, the actual task was not difficult.

The inclusion of the Hall effect in the resistive-diffusion IMA was done in such a way that either physical effect, resistive diffusion or Hall effect, could be toggled on and off independently of the other. This proved to be a valuable design choice as the IMA Hall algorithm would not run properly without the resistive diffusion, and with the independent toggles, this feature could be investigated.

The initial test of this new approach is shown in Figures 1-3, 1-4, and 1-5. This is the same test problem discussed in Section 1.2. The Hall effect is turned on; resistive diffusion is disabled. Figure 1-3 shows the sort of result to be expected, though the timing is quite a bit different from what theory predicts. But qualitatively, the broad front penetrating with a speed inversely proportional to radius is correct. Figures 1-4a, b, and c show the development and propagation from cathode to anode of vortical magnetic field structures. These "bubbles" are seen in PIC calculations, but no claim is made here that in the Mach2 calculation they are anything other than evidence of numerical instability. Figure 1-5 shows the instability once it has grown to intolerable levels. This result is quite similar to that described in Section 1.2, which resulted from the standard Hall algorithm.

The presence of essentially the same instability which provided motivation for developing a new algorithm was discouraging, but it prompted the effort to run the Hall algorithm in conjunction with resistive diffusion. There is precedence for resorting to this sort of approach. In computational fluid dynamics, shock waves are often accompanied by oscillatory behavior behind the shock. These oscillations can result in wildly nonphysical results, but they can be damped out and the general behavior of the calculation improved if a small amount of diffusion is added to the calculation. This technique is referred to as artificial viscosity, and is a widely accepted and practiced technique. This precedent provided rationalization for running the resistive diffusion alongside the Hall algorithm. A constant resistivity was chosen for the plasma



which was small enough to make the resistive-diffusion timescale much longer than the Hall timescale. The resistive-diffusion timescale is:

$$\tau_r = L^2/(\eta/\mu_0) = L^2/D \quad (1.4)$$

where  $D = \eta/\mu_0$  and  $\eta$  is the electrical resistivity. Mach2 deals directly with the diffusivity rather than with the electrical resistivity. A value of  $1.5625 \times 10^3 \text{ m}^2/\text{s}$  was chosen for the diffusivity. Using the domain length of 0.08 m as the scale length  $L$ , the resistive-diffusion timescale is  $4.1 \times 10^{-6} \text{ s}$ . The Hall timescale is  $2.01 \times 10^{-9} \text{ s}$ . Thus, diffusion acts roughly 2000 times more slowly than the Hall effect.

Figures 1-6 and 1-7 show the result of adding a little diffusion to the calculation. A broad front propagates axially, and reaches nearly to the end of the 8 cm long domain in 9.8 ns. This compares favorably with the theoretical prediction that the front should traverse 8 cm in 10 ns. Behind the front, one can still see the same bubbles which developed into an catastrophic instability in the previous calculation, but now, they remain a benign, if annoying, aspect.

Many tests of Mach2 with the implicit multigrid treatment of the Hall effect were performed. Overall, the results were good, but a few tests pointed to problems which led to the abandonment of this approach. The most revealing test was the following. The test was comprised of coaxial geometry and motionless plasma. The electron number density was:

$$\begin{aligned} ne(r) = & (6 \times 10^{15} \text{ per cc}) \exp[-(\ln(3))(r-5\text{cm})] \text{ for } 5 \text{ cm} < r < 6 \text{ cm;} \\ & 2 \times 10^{15} \text{ per cc for } 6 \text{ cm} < r < 7 \text{ cm.} \end{aligned} \quad (1.5)$$

i.e., the density profile decreases exponentially from  $6 \times 10^{15} \text{ per cc}$  at the cathode to  $2 \times 10^{15} \text{ per cc}$  at the midpoint of the AK gap, then maintains a constant value of  $2 \times 10^{15} \text{ per cc}$  from the AK gap midpoint out to the anode. The theoretical expectation is for a shock to propagate in the outer, uniform density region, and for no field to develop in the inner, negative density gradient region. The shock should propagate with a speed of  $9.67 \times 10^6 \text{ cm/s}$  along the line  $r=6 \text{ cm}$ ; this speed should scale with the inverse square of the radius.

Figure 1-8 shows the results for this test problem obtained with the implicit multigrid Hall algorithm. The theoretical shock speed quoted above implies that the disturbance should traverse the 8 cm length of the domain in 827 ns. As the figures show, the development of magnetic field

in the outer, uniform density region is not very shock-like, nor does it exhibit either the expected propagation speed or the expected dependence of the speed upon radius. Moreover, field is evolving in the inner, negative density gradient region, contrary to theoretical expectations. This field has the puzzling characteristic of being the polarity opposite to that impinging upon the plasma from the vacuum. Upon comparison of these results with those obtained by Grossmann using the Huba code, the suggestion was made that these undesirable features might be "cured" by implementing an upwind differencing scheme. The difficulty with this suggestion was that the implicit multigrid algorithm did not provide any opportunities for implementing an upwind differencing scheme.

The implicit multigrid algorithm had the strength of providing an implicit solution to the Burger's equation. However, the balance of pros and cons swung in favor of upwind differencing due in part to the sort of performance described in this test problem, but more significantly due to mismatch between the IMA algorithm and the desire to implement an upwind scheme. This approach does, despite these particular problems, merit to be revisited, particularly for application to problems involving poloidal magnetic fields. But this is not within the scope of the current effort.

#### 1.4 NEW ALGORITHM DEVELOPMENT.

The inability of the implicit multigrid Hall algorithm to perform acceptably on all test problems lead to an effort to develop a one-dimensional algorithm which would not only perform adequately, but could also be generalized to a two-dimensional algorithm for Mach2.

Over the course of a few days, several candidate one-dimensional algorithms were tested. A review of the various candidates and their performance is not in the scope of this report. The name algorithm C, or algoC for short, has been adopted for the algorithm chosen for use. AlgoC takes the following form in one dimension:

Consider the equation:

$$dB/dt = a B dB/dx \quad (1.6)$$

AlgoC then provides the numerical solution as:

$$B(n+1,j) = B(n,j) + (dt/dx) a \langle B \rangle (B1 - B2) \quad (1.7)$$

$$\begin{aligned}
& (1/2) [B(n,j-1) + B(n,j)] \text{ if } V_{\text{eff}} > 0 \\
\text{where } \langle B \rangle = & \\
& (1/2) [B(n,j+1) + B(n,j)] \text{ if } V_{\text{eff}} < 0 \\
& B(n,j-1) \text{ if } V_{\text{eff}} > 0 \\
\text{and } B1 = & \\
& B(n,j) \text{ if } V_{\text{eff}} < 0 \\
& B(n,j) \text{ if } V_{\text{eff}} > 0 \\
\text{and } B2 = & \\
& B(n,j+1) \text{ if } V_{\text{eff}} < 0.
\end{aligned}$$

This is a simple upwind differencing scheme; no claim is made here at developing a new and revolutionary technique. This was simply an algorithm which appeared to work adequately and appeared to be workable within the context of Mach2.

An example of the simple sort of test problem used to judge the various candidate one-dimensional algorithms is the propagation of a square pulse. Figures 1-9a and b show results from an AlgoC calculation of square pulse propagation. The parameter “a” has the value  $1 \times 10^4$  m/T-s. A Rankine-Hugoniot-type analysis indicates that the front should propagate with the speed  $(1/2)aB$ , where B is the value of the magnetic field immediately behind the shock front. Comparing the position of the shock front at time  $t=0.2$  ns to that at time  $t=5.4$  ns indicates that during that time, the shock has traversed a distance of 0.255 cm in 5.2 ns. This is a speed of  $4.91 \times 10^7$  cm/s, which differs from the theoretically expected value of  $5.00 \times 10^7$  cm/s by a relative error of 1.8%. This level of difference can easily be ascribed to grid-size effects. As time proceeds, the maximum value of the magnetic field eventually begins to decrease and the square wave profile is distorted. This is because in the finite simulation medium a rarefaction wave catches up to the shock front. As this occurs, the shock slows in accordance to the dependence of the speed on the value of the field immediately behind the front. The algorithm appears to have found a solution which depends linearly on the coordinate “x” for the rarefaction wave. Assuming a solution of the form  $B(x,t) = h(t)x$  and putting this into Burger’s equation results in the following differential equation for  $h(t)$ :

$$dh/dt = a h^2, \quad (1.8)$$

which has solution  $h(t) = h(0)/[1 + h(0)at]$ . This gives a good qualitative match to the AlgoC results, but since there is no prediction for  $h(0)$ , a quantitative assessment of the rarefaction wave cannot be made.

Having found an algorithm which appears to perform adequately, the next task was to fit it into an algorithmic framework compatible with Mach2. For the Mach2 algorithm aficionado, this required construction of a face-centered gradient using the adjacent vertex-centered magnetic field values.

A test problem demonstrates the algorithm, first on an orthogonal grid, then on a non-orthogonal grid. The problem is coaxial geometry with inner radius of 5 cm and outer radius of 7 cm. The medium is static, and of all the possible Mach2 physics modules, only the Hall algorithm is allowed to operate. The density is uniform between the inner electrode and a radius of 5.8 cm with a value of  $2 \times 10^{13}$  per cc. Between the outer electrode and 6.2 cm, the density is also constant, but at a value of  $8 \times 10^{13}$  per cc. These two uniform density regions are interpolated by an error function. The sharp positive density gradient in this interpolation region should allow rapid field propagation. In the uniform density regions, field will propagate, but not as rapidly. The driving current is 700 kA.

Figure 1-10 shows the grid for the orthogonal grid trial. Figure 1-11 shows contours of  $rB\{\theta\}$  at time  $t=2.5$  ns. Figure 1-12 shows the density contours on the orthogonal grid. At this time, the field has already traversed the length of the domain in the interpolation region. Figure 1-13 shows the grid used for the non-orthogonal grid trial. Figure 1-14 shows  $rB\{\theta\}$  contours at 2.5 ns. The density contours on the non-orthogonal grid are depicted in Figure 1-15. The field in the uniform density regions appears to be quite similar in the non-orthogonal trial as in the orthogonal trial. A large difference is exhibited between the two in how the field propagates in the interpolation region. This is probably due to the difference in the resolution of density gradients between the two grids. The most noteworthy feature of the non-orthogonal trial is in how the propagating field follows the density gradient rather than the grid. The reduction of grid features from the calculation is a worthy goal in any computational physics pursuit, but complete elimination of grid aspects is next to impossible. The non-orthogonal grid is simply a poor choice for the given circumstances; nonetheless, the Hall algorithm performs on it in a quite adequate manner.

## 1.5 GROSSMANN TEST PROBLEMS.

In anticipation of several competing Hall effect algorithms being presented at the Hall effect workshop he was organizing for mid-December 1995, John Grossman of the Naval Research Laboratory developed a suite of five test problems. These problems were designed around analytically tractable problems, and with the exception of problem 2, involve Hall-effect field propagation in a static medium. Problem 2, which is not analytically tractable, involves the coupling of hydrodynamic motion and the magnetic field due to the Hall effect. The results of the new Hall algorithm in Mach2 are presented here.

All problems use coaxial geometry with the cathode being the inner electrode and the anode being the outer. The equation governing the Hall effect evolution of the magnetic field is :

$$dB/dt = p B dB/dz + q B dB/dz \quad (1.9)$$

where

$$p = (2/r)/[ne \mu_0] + [d(\ln(ne)/dr)]/[ne \mu_0]$$

and

$$q = [d(\ln(n)/dz)]/[ne \mu_0]$$

For all but problem 1.2, the parameter  $q$  vanishes. Application of Rankine-Hugoniot technique to this equation indicates that the shock propagates with a speed:

$$V_f = (1/2) p B \quad , \quad (1.10)$$

where  $B$  is the magnitude of the magnetic field just behind the shock (Reference 3). This result is used to determine the expected front speed for the test problems.

### Problem 1

This is the same problem as described in Section 1.3 as the problem which uncovered significant flaws in the implicit multigrid algorithm approach.

Cathode radius	= 5 cm
Anode radius	= 7 cm
Domain length	= 8 cm
No. radial zones	= 20
No. axial zones	= 40

**Current:**

$$I(t) = \begin{cases} (700 \text{ kA}/2 \text{ ns}) t; & 0 < t < 2 \text{ ns} \\ 700 \text{ kA}; & t > 2 \text{ ns} \end{cases}$$

**Electron number density:**

$$n(r) = \begin{cases} (6 \times 10^{15} \text{ per cc}) \exp[-(\ln(3))(r-5\text{cm})] & \text{for } 5 \text{ cm} < r < 6 \text{ cm}; \\ 2 \times 10^{15} \text{ per cc} & \text{for } 6 \text{ cm} < r < 7 \text{ cm}. \end{cases}$$

This density profile is depicted in Figure 1-16.

**Theoretical expectation:**

At  $r=6 \text{ cm}$ , after converting to mks units in Equation 1.9, the parameter  $p$  takes on the value:

$$p = 8.29 \times 10^4 \text{ m/T-s}$$

With the indicated current, the magnetic field at  $r=6 \text{ cm}$  takes the value 2.33 T. Thus, the expected shock speed, Equation 1.10, is:

$$V/f = 9.67 \times 10^6 \text{ cm/s.}$$

**Mach2 result:**

The two dimensional results of Figures 1-17a and 1-17b show contours of  $rB\{\theta\}$  at times  $t=501 \text{ ns}$  and  $t=851 \text{ ns}$ , respectively. The latter shows that the shock traverses the 8 cm long domain at 851 ns. With the indicated speed at that radius, the theoretically expected propagation time is 827 ns. The difference represents a 2.9% error, but this neglects the initial linear ramp of the driving current. Thus, the Mach2 calculation is in agreement with the theoretical expectation to within a relative error of less than 2.9%. The shock front also exhibits a distinct radial dependence. Scaling the theoretical front speed with the inverse square of the radius gives a penetration distance of 6.04 cm. Figure 1-17b shows the shock front at the radius 7 cm having traversed 6.37 cm. This represents a relative error of 5.5%, but again, this neglects the early non-constant portion of the driving current.

## **Problem 2**

This problem is distinctly different from the other problems in the suite in that it involves the coupling between hydro motion and the magnetic field, and how the Hall effect alters that coupling. The atomic weight used for the plasma is 1/20 – this ensures that hydromotion will take place on a rapid timescale.

Cathode radius = 4.5 cm

Anode radius = 9 cm

Domain length = 5 cm

No. radial zones = 40

No. axial zones = 50

### **Current:**

$$I(t) = \begin{cases} (600 \text{ kA}/2 \text{ ns}) t; & 0 < t < 1 \text{ ns} \\ 600 \text{ kA}; & t > 1 \text{ ns}. \end{cases}$$

### **Electron number density:**

$$n_e(r) = \begin{cases} 1 \times 10^{14} \exp[-(\ln(10))((r-4.5 \text{ cm})/1.5 \text{ cm})] & \text{for } 4.5 \text{ cm} < r < 6 \text{ cm}; \\ 1 \times 10^{13} \exp[(\ln(2))((r-6 \text{ cm})/3 \text{ cm})] & \text{for } 6 \text{ cm} < r < 9 \text{ cm}. \end{cases}$$

This density profile is depicted in Figure 1-18.

### **Theoretical expectation:**

At  $r=6$  cm, the parameter  $p$  takes on the value:

$$\begin{aligned} p &= 1.658 \times 10^7 \text{ m/T-s} + 1.149 \times 10^7 \text{ m/T-s} \\ &= 2.807 \times 10^7 \text{ m/T-s} \end{aligned}$$

and the magnetic field takes the value 2T. Thus, the Hall effect should propagate field into the plasma at a speed 2.807 cm/ns. But since hydromotion is allowed in this problem, the Hall speed must be compared to the Alfven speed. At  $r=6$  cm, the Alfven speed is:

$$V_{\text{Alfven}} = B / (2\mu_0\rho)^{1/2} \quad (1.11)$$

where  $\rho$  is the mass density and has the value:

$$\rho = \frac{nm}{20} = 8.35 \times 10^{-10} \text{ kg/m}^3. \quad (1.12)$$

Thus, the Alfven speed is 4.26 cm/ns. This is of the same magnitude as the Hall speed, but about 50% greater. Thus, theoretically, one would expect to see hydromotion dominating the problem, but for the Hall effect to have a significant impact. Comparison between a pure hydro, ideal MHD run, and the same run including the Hall effect is required to test this expectation.

#### **Mach2 result:**

Figure 1-19 and Figure 1-20 show the electron number density and  $rB\{\theta\}$  contours for the run which includes the Hall effect at time  $t=1.8$  ns. These results are to be compared with analogous results from the calculation which did not include the Hall effect; these are shown Figure 1-21 and Figure 1-22. The snowplow front is of essentially the same shape at the indicated time in both calculations, and has traversed roughly the same distance. This is evidence of the dominance of Alfvenic, rather than Hallish, effects. However, two features in the Hall effect calculation are noticeably different from those in the ideal MHD run. The first is the width of the snowplow front. With the Hall effect, the width is greater, and the peak density in the snowplow front is less than that in the ideal MHD front. This is probably due to the propagation of the magnetic field into the snowplow front. In this respect, the Hall effect acts quite similarly to resistive diffusion; the driving force slowly becomes diffuse as it relaxes into the snowplow front, allowing the density profile to relax, also. The second feature of note is the structuring of the density along the line of the snowplow front. Without the Hall effect, the density decreases from the cathode to a mid-gap point, then increases to the anode. With the Hall effect, several local density maxima in the snowplow front develop.



### **Problem 3**

This problem uses a special density profile formulated by requiring the parameter  $p$  to be constant. The inner, exponential part of the profile is used to suppress instabilities that in Huba's code develop at the cathode.

Cathode radius	= 1 cm
Anode radius	= 7 cm
Domain length	= 8 cm
No. radial zones	= 20
No. axial zones	= 40

Current:

$$I(t) = \begin{cases} (5 \text{ kA}/0.1 \text{ ns}) t; & 0 < t < 0.1 \text{ ns} \\ 5 \text{ kA}; & t > 0.1 \text{ ns} \end{cases}$$

Electron number density:

$$n(r) = \begin{cases} 1 \times 10^{13} \exp[-(\ln(1.812))((r-1 \text{ cm})/0.4 \text{ cm})] & \text{for } 1 \text{ cm} < r < 1.4 \text{ cm}; \\ 5 \times 10^{12} (1.0 \text{ cm}/r)^2 / [1 - (1/2)\ln(r/1.0 \text{ cm})] & \text{for } 1.4 \text{ cm} < r < 7 \text{ cm} \end{cases}$$

This density profile is depicted in Figure 1-23.

**Theoretical expectation:**

The theoretical predictions are currently under dispute. Grossmann of NRL claims a domain traversal time of 40 ns. For the present, we will accept that value, but we suspect that 40 ns is not the exact value of the theoretical prediction, so the comparison between theory and computation must factor in that uncertainty.

**Mach2 result:**

Figure 1-24 and Figure 1-25 show the propagating magneto-shock at times  $t=16$  ns and  $t=32$  ns, respectively. The latter indicates that the time required for the shock to reach the end of the domain is 32 ns.

**Problem 4**

This is identical to problem 2 with the exception that hydromotion is not allowed, i.e. the medium is static.

**Theoretical expectation:**

From the discussion of Problem 2, the Hall speed is 2.807 cm/ns, and the domain length is 5 cm. The time require to cross this distance at the indicated speed is 1.78 ns. There is a difficulty in applying this prediction alone, since this time is comparable to the time during which the driving current is linearly increasing to its constant value. However, the Rankine-Hugoniot analysis still applies to that part of the problem, despite the time-dependent current. The shock speed is  $(1/2)\rho B(t)$ , where the appropriate time-dependent magnetic field must be used. Using  $B(t) = \mu_0 I(t)/(2\pi r)$  at  $r=6$  cm gives:

$$\begin{aligned} V_f &= 0.5 (2.807 \times 10^7 \text{ M/T-s}) (2 \times 10^9 \text{ T/s}) t \\ &= 2.807 t \text{ m/s}^2 . \end{aligned} \quad (1.13)$$

Thus, at the time the linear-ramp portion of the driving current is through, i.e. at time  $t=1$  ns, the front has propagated a distance of 1.403 cm. The remaining distance of 3.596 cm takes the constant speed shock 1.28 ns to traverse. Thus, the total time required for the shock to traverse the 5 cm domain length is 2.28 ns.

**Mach2 result:**

Figure 1-26 and Figure 1-27 show  $rB\{\theta\}$  contours at times  $t=1$  ns and  $t=2.5$  ns. Figure 1-26 shows that during the linearly rising phase of the driving current, the shock has traversed a distance of 1.11 cm. Figure 1-25 indicates that to traverse the remaining 3.89 cm of the domain, the calculated shock requires 1.4 ns. This implies a constant speed of 2.779 cm/ns. The relative difference between this and the theoretical constant shock speed of 2.807 cm/ns is 1.01%.

**Problem 5**

This problem is designed to show Hall effect magnetic field penetration due solely to a density gradient. To achieve this, a large radius was chosen for the inner electrode, with an AK gap much smaller than that radius.

Cathode radius = 200 cm  
Anode radius = 202 cm  
Domain length = 8 cm  
No. radial zones = 20  
No. axial zones = 40

Current:

$$I(t) = \begin{cases} (700 \text{ kA}/2 \text{ ns}) t; & 0 < t < 2 \text{ ns} \\ 700 \text{ kA}; & t > 2 \text{ ns} \end{cases}$$

**Electron number density:**

$$n_e(r) = \begin{cases} 6 \times 10^{14} \exp[-\ln(6)((r-200)/0.5)] & \text{for } 200 \text{ cm} < r < 200.5 \text{ cm;} \\ 1. \times 10^{14} \exp[+\ln(20)((r-200.5)/1.5)] & \text{for } 200.5 \text{ cm} < r < 202 \text{ cm.} \end{cases}$$

This density profile is depicted in Figure 1-28.

**Theoretical expectation:**

At  $r=200.5$  cm, neglecting the  $1/r$  term, the parameter  $p$  takes on the value  $p = 9.932 \times 10^6$  m/T-s and the magnetic field has the value  $B = 0.07$  T. Thus, the expected shock speed  $V_f = 2.47 \times 10^7$  cm/s. To cross the 8 cm long domain at this speed requires 324 ns.

### **Mach2 result:**

Figure 1-29 and Figure 1-30 show  $rB\{\theta\}$  contours at times  $t=100$  ns and  $t=300$  ns, respectively. Figure 1-30 shows that the time required for the calculated shock to traverse the 8 cm domain length is 300 ns. This represents an average speed of  $2.667 \times 10^7$  cm/s, which is a relative difference of 8% from the theoretical speed of  $2.47 \times 10^7$  cm/s.

### **1.6 SUMMARY – THEORY VS MACH2.**

The table below shows the theoretically expected Hall speed and the speed observed in the corresponding Mach2 simulation. The relative error is calculated from

$$RE(\%) = 100 * (\text{Theory} - \text{Mach2}) / \text{Theory}$$

so a positive relative error indicates that the observed Mach2 speed is lower than that expected theoretically. Speeds are quoted in cm/s.

<u>Problem No.</u>	<u>Theory</u>	<u>Mach2</u>	<u>Relative Error (%)</u>
1	$9.67 \times 10^6$	$9.40 \times 10^6$	2.79
2	NA	NA	NA
3*	$2. \times 10^8$	$2.5 \times 10^8$	-25%*
4	$2.807 \times 10^9$	$2.779 \times 10^9$	0.998
5	$2.47 \times 10^7$	$2.67 \times 10^7$	-8.10

\* Theoretical prediction for problem 3 currently under dispute.

The new Hall algorithm thus appears to perform quite adequately on this suite of test problems. Indeed, comparison of these results with those obtained with the Huba code puts Mach2 in a favorable position. This, with the apparent ability of the new Hall algorithm to perform on multiblock problems (not discussed in this report), as well as to perform well on non-orthogonal grids, suggests that the algorithm is worthy of use in the POS problems currently of interest to the DSWA community.

IDEAL MHD/HALL HAWK - OLD HALL ALGO  
 EXHALL6 V9403.  
 T = 2.500E-10 CYCLE = 25  
 MAGNETIC FIELD - THETA COMPONENT

-=-9.7163E-01

A=-7.1810E-01

B=-4.6457E-01

C=-2.1103E-01

D= 4.2500E-02

E= 2.9603E-01

F= 5.4957E-01

H= 1.0536E+00

I= 1.3102E+00

+= 1.5637E+00

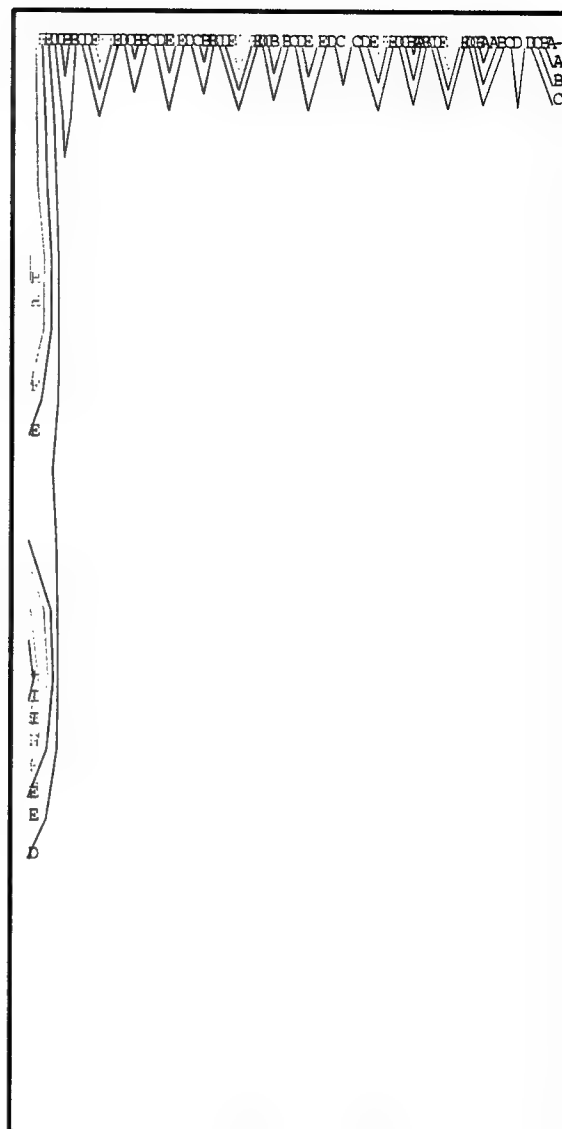


Figure 1-1. Standard Hall algorithm results on coaxial test problem at  $t=0.25$  ns. Note the finger-like penetration along the cathode and the oscillatory feature along the generator side of the domain. (The generator is toward the top in this calculation).

IDEAL MHD/HALL HAWK - OLD HALL ALGO  
 EXHALL6 V9403.  
 T = 6.904E-10 CYCLE = 150  
 MAGNETIC FIELD -- THETA COMPONENT

--1.7806E+01

A=-1.5813E+01

B=-1.3820E+01

C=-1.1827E+01

D=-9.8343E+00

E=-7.8414E+00

F=-5.8485E+00

H=-1.8628E+00

I= 1.3008E-01

+= 2.1230E+00

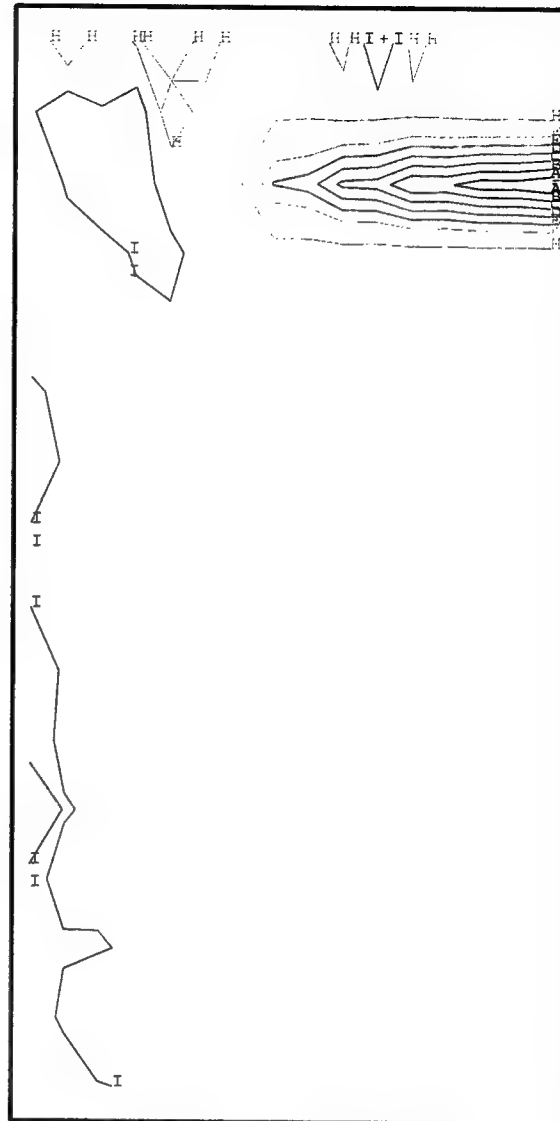


Figure 1-2. The standard Hall algorithm develops a numerical instability which causes growth of the magnetic field to physically untenable levels. Here, the field has grown negative to a level two orders of magnitude greater than that expected on physical grounds.

HALL EFFECT TEST: HALL ONLY -  
 CONVERGE MODE  
 H92795B V9403.  
 T = 1.900E-08 CYCLE = 384  
 MAGNETIC FIELD -- THETA COMPONENT

--9.1621E-03

A= 2.6947E-01

B= 5.4811E-01

C= 8.2675E-01

D= 1.1054E+00

E= 1.3840E+00

F= 1.6627E+00

H= 2.2199E+00

I= 2.4986E+00

+= 2.7772E+00

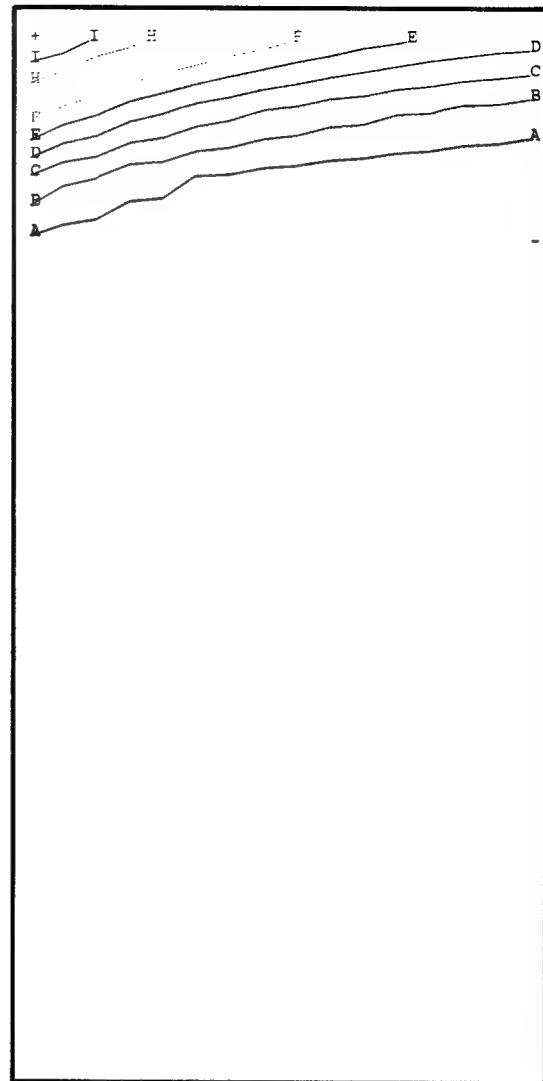
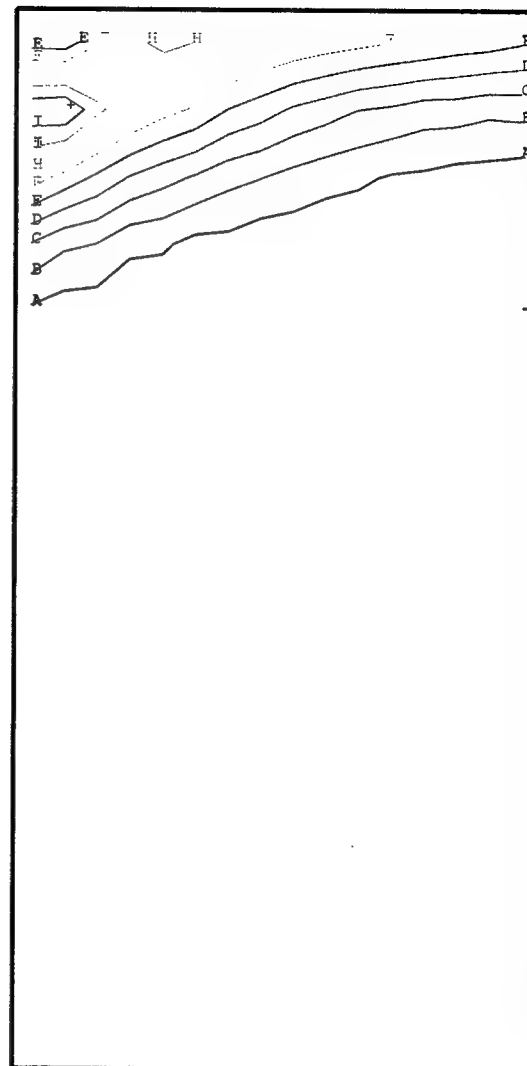


Figure 1-3. The IMA algorithm gives qualitatively correct penetration of the magnetic field at early times.

HALL EFFECT TEST: HALL ONLY -  
 CONVERGE MODE  
 H92795B V9403.  
 T = 2.500E-08 CYCLE = 504  
 MAGNETIC FIELD -- THETA COMPONENT

--2.2903E-03  
 A= 3.4099E-01  
 B= 6.8427E-01  
 C= 1.0275E+00  
 D= 1.3708E+00  
 E= 1.7141E+00  
 F= 2.0574E+00  
 G= 2.4007E+00  
 H= 2.7439E+00  
 I= 3.0872E+00  
 += 3.4305E+00



(a) T = 25 ns

Figure 1-4. The IMA algorithm leads to the development and propagation from cathode to anode of magnetic vortices.



HALL EFFECT TEST: HALL ONLY -  
 CONVERGE MODE  
 H92795B V9403.  
 T = 2.700E-08 CYCLE = 544  
 MAGNETIC FIELD -- THETA COMPONENT

--2.2827E-03

A= 3.7648E-01

B= 7.5525E-01

C= 1.1340E+00

D= 1.5128E+00

E= 1.8915E+00

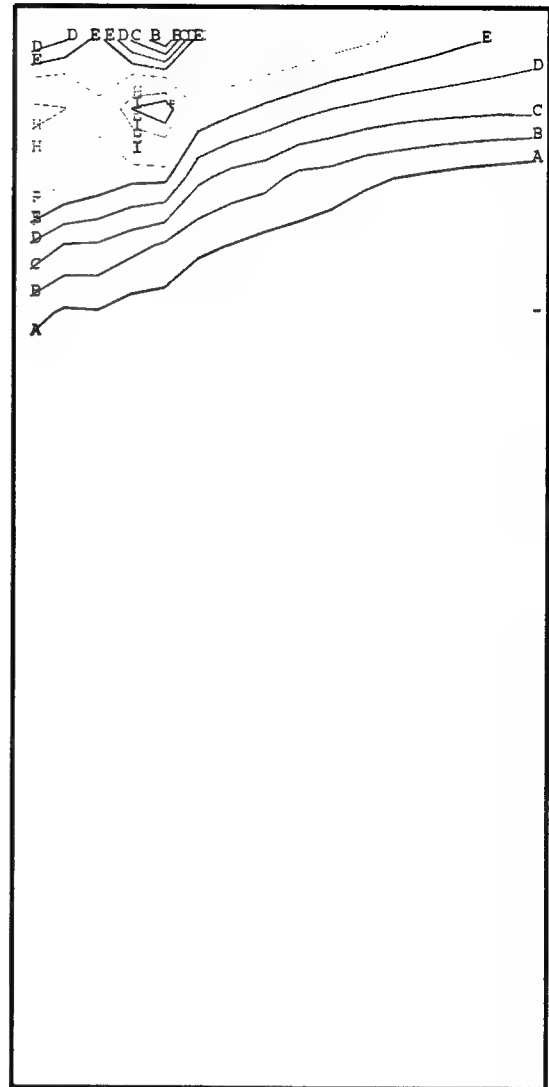
F= 2.2703E+00

G= 2.6491E+00

H= 3.0278E+00

I= 3.4066E+00

+= 3.7854E+00



(b) T = 27 ns

Figure 1-4. The IMA algorithm leads to the development and propagation from cathode to anode of magnetic vortices (Continued).

HALL EFFECT TEST: HALL ONLY -  
 CONVERGE MODE  
 H92795B V9403.  
 T = 2.900E-08 CYCLE = 584  
 MAGNETIC FIELD - THETA COMPONENT

-=-2.1181E-03

A= 3.6973E-01

B= 7.4158E-01

C= 1.1134E+00

D= 1.4853E+00

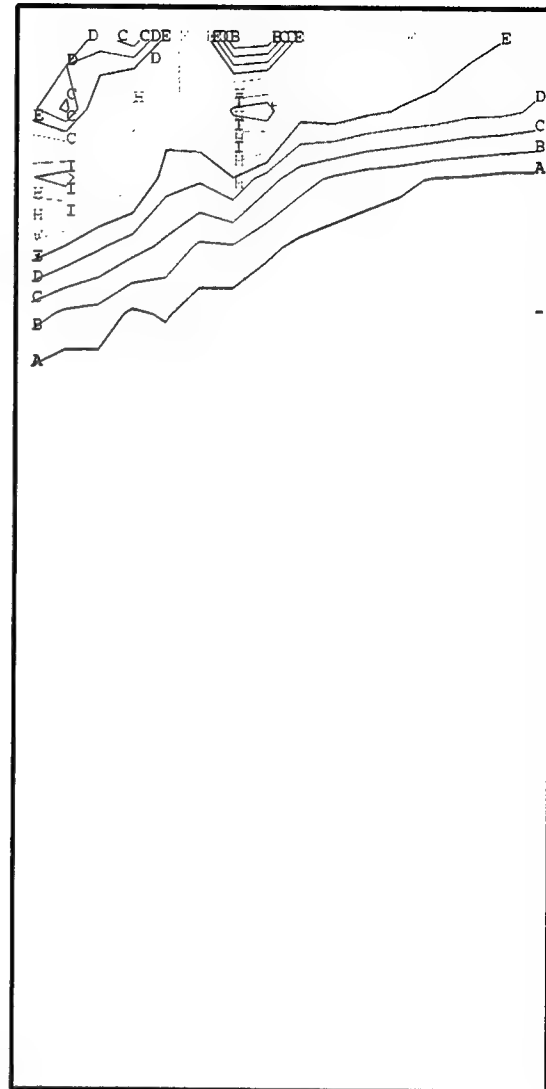
E= 1.8571E+00

F= 2.2290E+00

H= 2.9727E+00

I= 3.3445E+00

+= 3.7164E+00



(c) T = 29 ns

Figure 1-4. The IMA algorithm leads to the development and propagation from cathode to anode of magnetic vortices (Continued).

HALL EFFECT TEST: HALL ONLY -  
 CONVERGE MODE  
 H92795B V9403.  
 T = 3.600E-08 CYCLE = 724  
 MAGNETIC FIELD - THETA COMPONENT

-=-9.8029E+00

A=-7.7458E+00

B=-5.6887E+00

C=-3.6316E+00

D=-1.5746E+00

E= 4.8250E-01

F= 2.5396E+00

H= 6.6537E+00

I= 8.7108E+00

+= 1.0768E+01

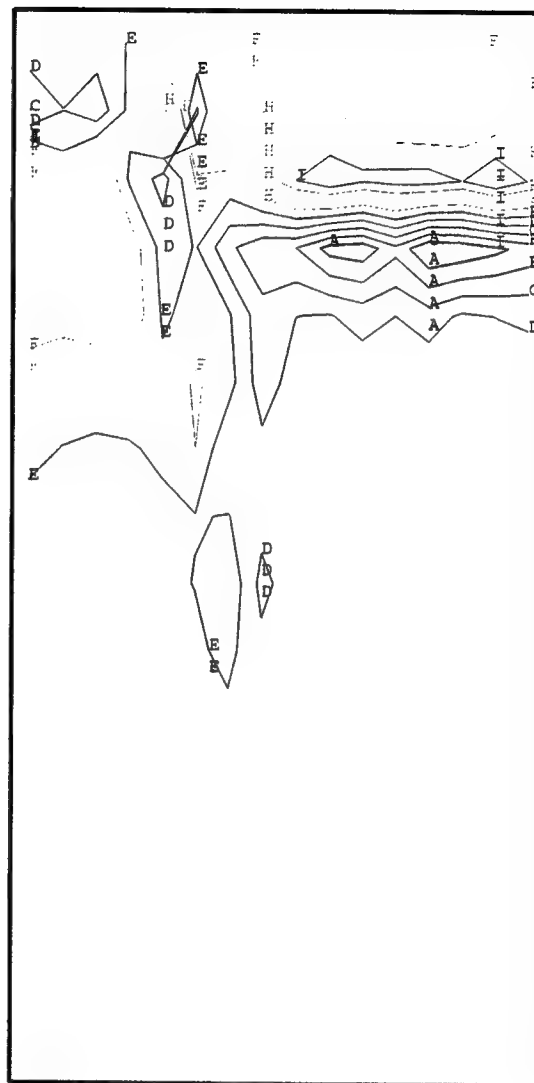


Figure 1-5. At this time the presumed numerical instability has grown to intolerable levels.

HALL EFFECT TEST:HALLEBCF, INEG ON TOP,  
 SMALL DIFFN  
 H92895E V9403.  
 T = 5.001E-09 CYCLE = 104  
 MAGNETIC FIELD – THETA COMPONENT

--2.9783E-04

A= 2.3806E-01

B= 4.7642E-01

C= 7.1477E-01

D= 9.5313E-01

E= 1.1915E+00

F= 1.4298E+00

H= 1.9066E+00

I= 2.1449E+00

+= 2.3833E+00

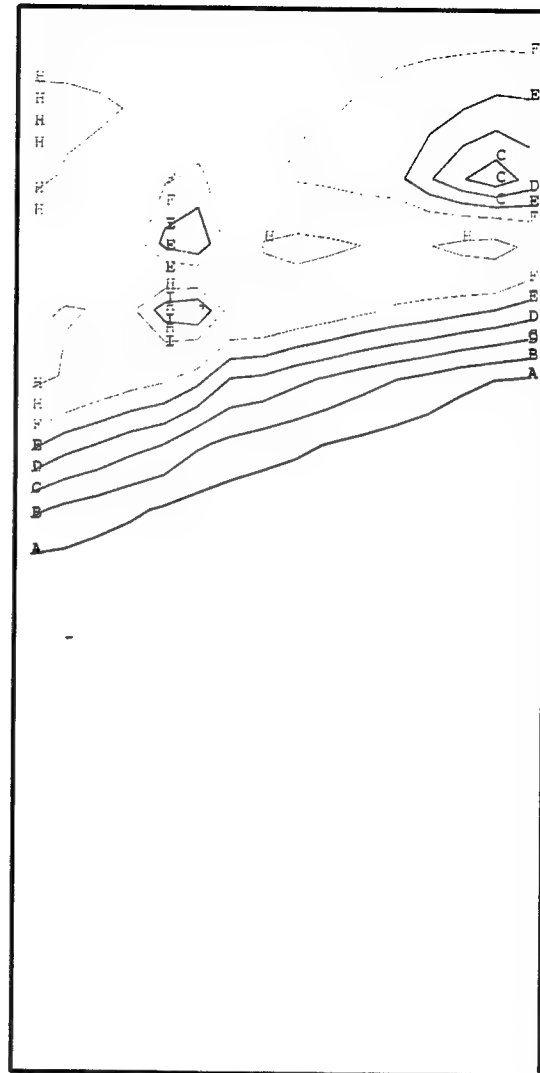


Figure 1-6. The effect of adding a small amount of resistive diffusion to the calculation is to quench the numerical instability. The bubbles remain as a benign, if annoying, aspect of calculation.

HALL EFFECT TEST:HALLEBCF, INEG ON TOP,  
 SMALL DIFFN  
 H92895E V9403.  
 T = 9.801E-09 CYCLE = 200  
 MAGNETIC FIELD – THETA COMPONENT

-=-2.4176E-06  
 A= 2.4094E-01  
 B= 4.8189E-01  
 C= 7.2283E-01  
 D= 9.6377E-01  
 E= 1.2047E+00  
 F= 1.4457E+00  
  
 H= 1.9275E+00  
 I= 2.1685E+00  
 += 2.4094E+00

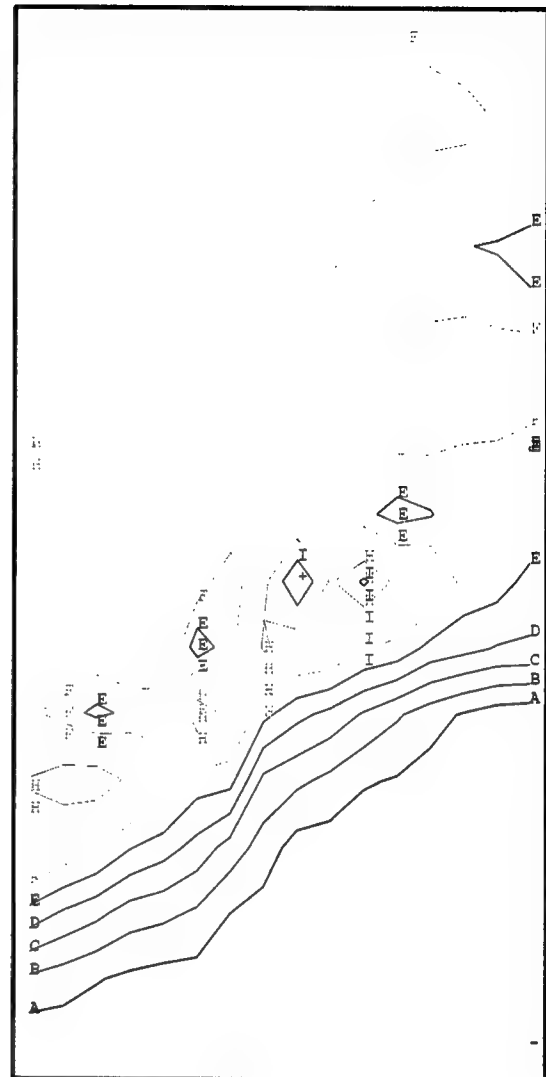
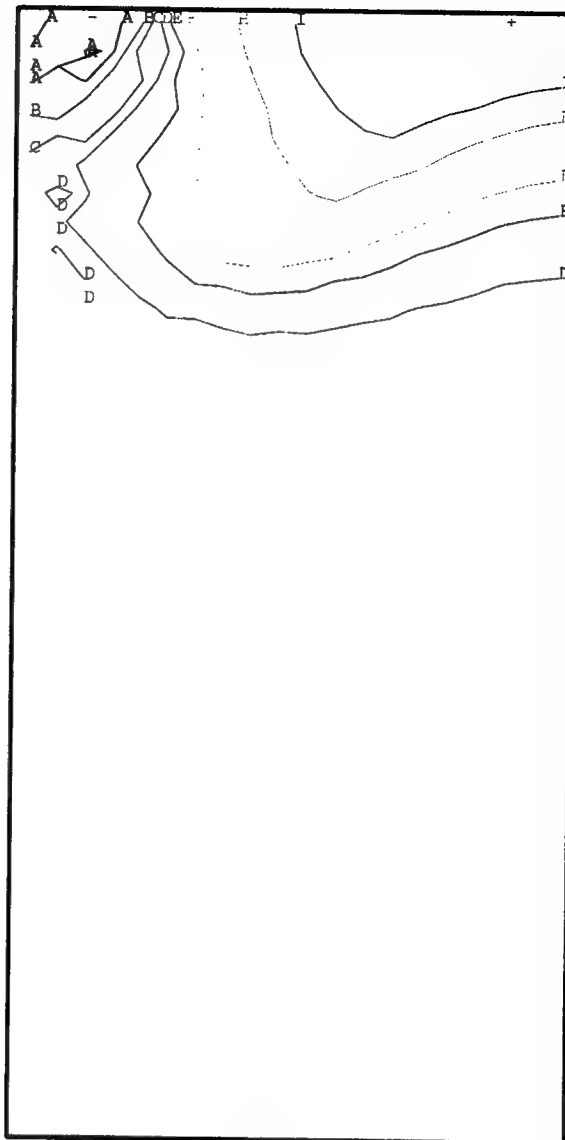


Figure 1-7. The effect of adding a small amount of resistive diffusion to the calculation is to quench the numerical instability. The bubbles remain as a benign, if annoying, aspect of calculation.

HALL: 2ND GROSSMANN TEST  
H111695B V9403.  
T = 2.501E-07 CYCLE = 1578  
RB (AMPS)

--3.9054E+05  
A=-2.8291E+05  
B=-1.7527E+05  
C=-6.7634E+04  
D= 4.0002E+04  
E= 1.4764E+05  
F= 2.5528E+05  
H= 4.7055E+05  
I= 5.7819E+05  
+= 6.8582E+05

CURRENT(1) = 7.0E+05



(a) T = 250 ns

Figure 1-8. For the variable density case (see text) field propagation with the IMA algorithm does not follow the theoretical expectation.

HALL: 2ND GROSSMANN TEST  
H111695B V9403.  
T = 5.001E-07 CYCLE = 2414  
RB (AMPS)

--3.9151E+05

A=-2.8315E+05

B=-1.7479E+05

C=-6.6432E+04

D= 4.1928E+04

E= 1.5029E+05

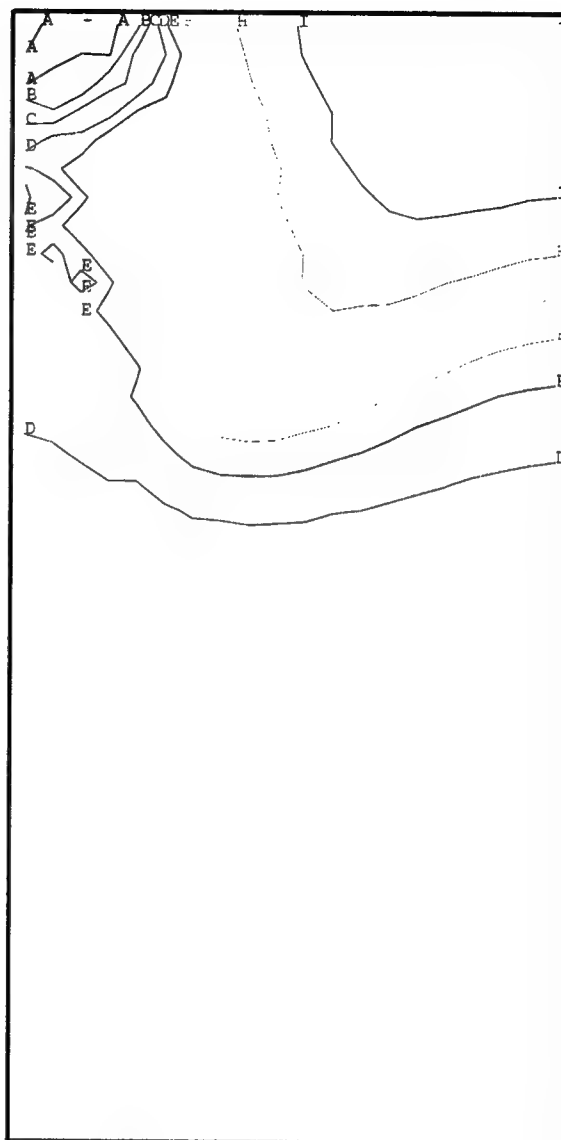
F= 2.5865E+05

H= 4.7537E+05

I= 5.8373E+05

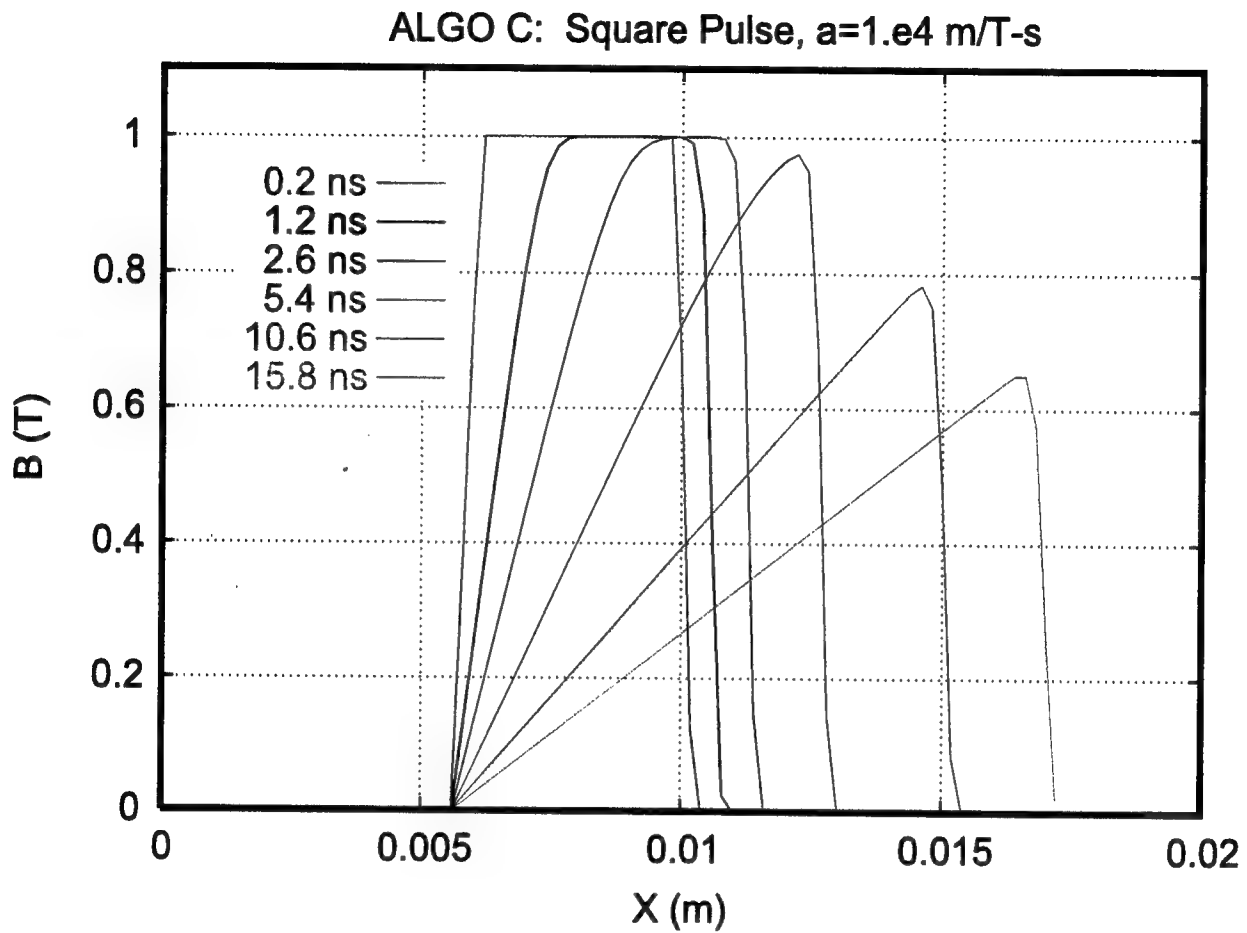
+= 6.9209E+05

CURRENT(1) = 7.0E+05



(b) T = 500 ns

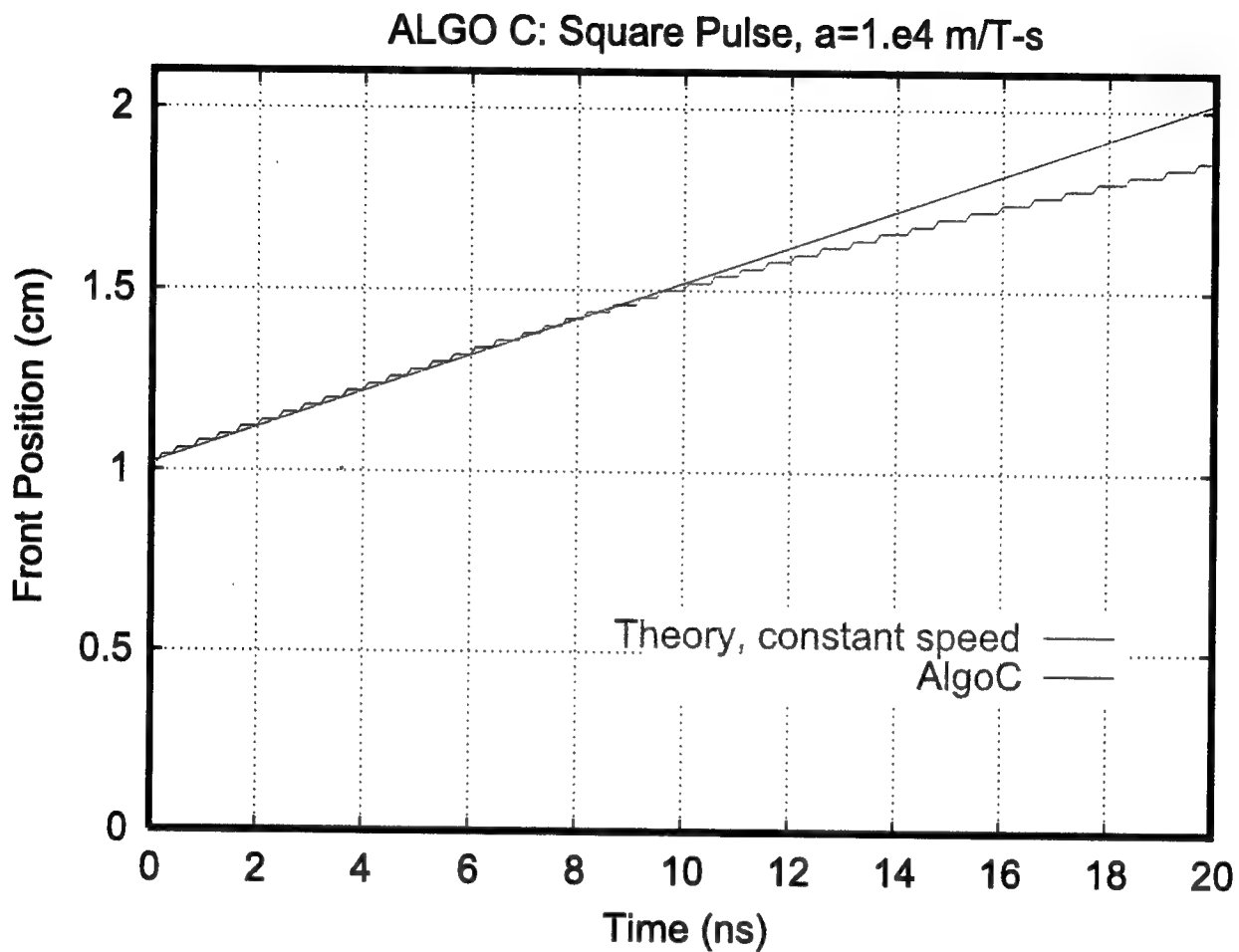
**Figure 1-8. For the variable density case (see text) field propagation with the IMA algorithm does not follow the theoretical expectation (Continued).**



(a)  $B(T)$  vs. Position at Several Times

Figure 1-9. Results for AlgoC propagation of a square pulse in a finite medium. The results conform well to theoretical expectations.





(b) Comparison of Theoretical and Computed Magnetic Shock Front Position

**Figure 1-9. Results for AlgoC propagation of a square pulse in a finite medium. The results confirm well to theoretical expectations (Continued).**

NHA - ERROR FUNC INCREASING PROFILE  
NHA1218B V9403.1  
T = 0.000E+00 CYCLE = 0  
CALCULATION MESH  
1ST X = 5.00E-02  
X INC = 5.00E-03  
1ST Y = -4.00E-02  
Y INC = 1.00E-02

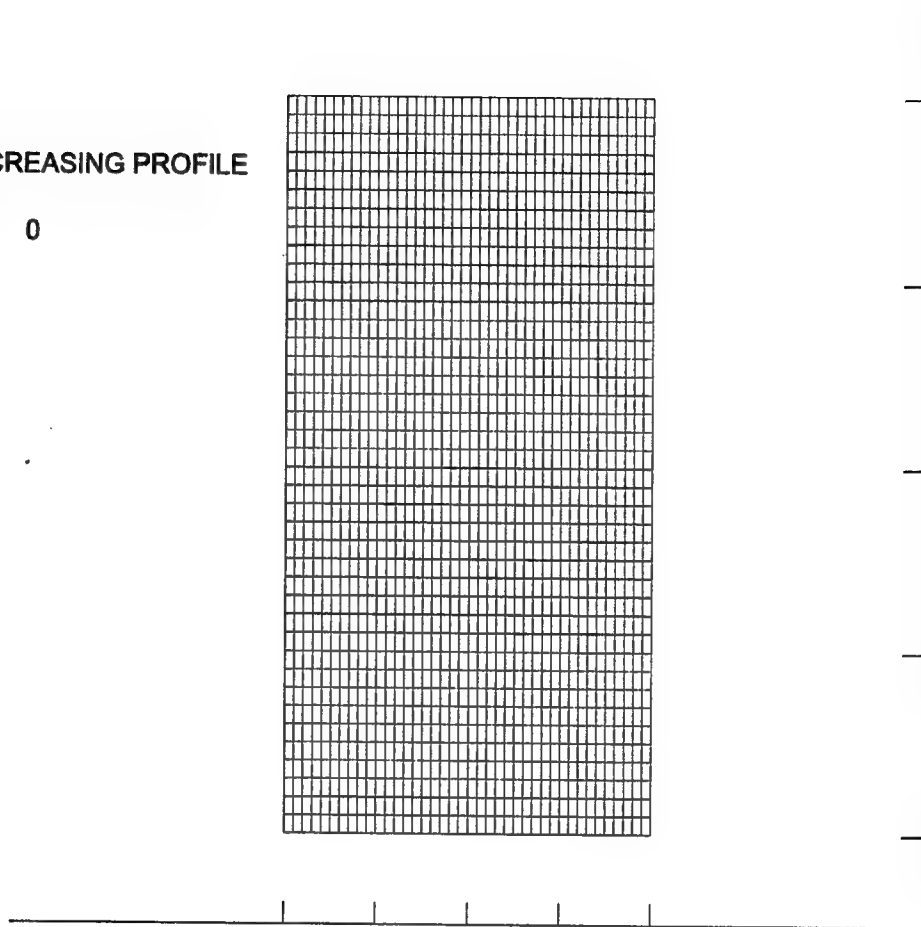


Figure 1-10. Orthogonal grid used to compare with calculations on a non-orthogonal grid.

NHA - ERROR FUNC INCREASING PROFILE  
 NHA1218B V9403.1  
 T = 2.500E-09 CYCLE = 1252  
 MAGNETIC FIELD - THETA COMPONENT

- = 0.0000E+00

A = 2.7861E-01

B = 5.5721E-01

C = 8.3582E-01

D = 1.1144E+00

E = 1.3930E+00

F = 1.6716E+00

H = 2.2289E+00

I = 2.5075E+00

+ = 2.7861E+00

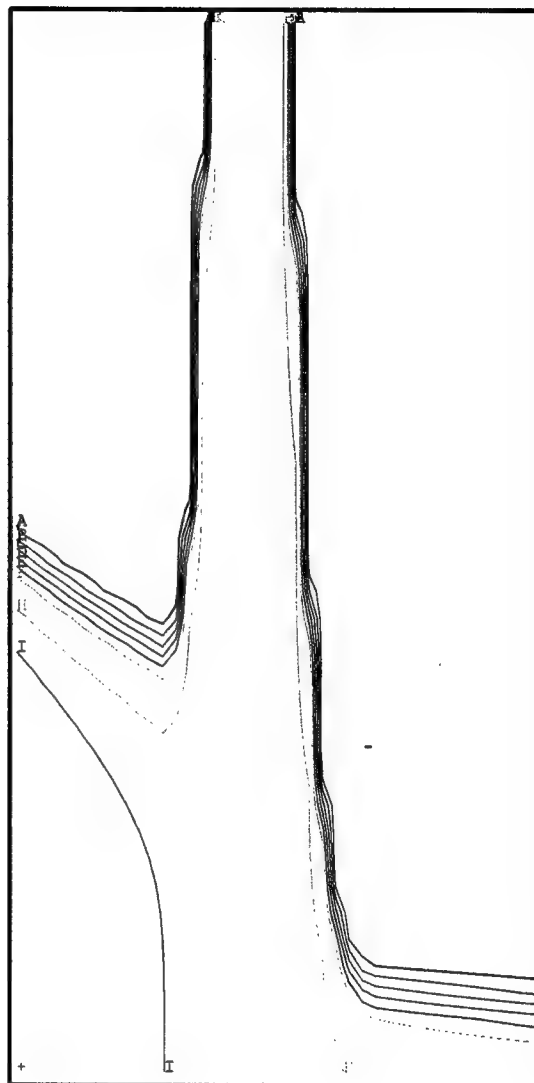


Figure 1-11. Contours of  $rB_\theta$  at  $t=2.5$  ns for orthogonal grid calculation.

NHA - ERROR FUNC INCREASING PROFILE  
NHA1218B V9403.1  
T = 0.000E+00 CYCLE = 0  
ELECTRONS / CC

- = 1.9970E+13

A = 2.5961E+13

B = 3.1952E+13

C = 3.7943E+13

D = 4.3934E+13

E = 4.9925E+13

F = 5.5916E+13

H = 6.7898E+13

I = 7.3889E+13

+ = 7.9880E+13

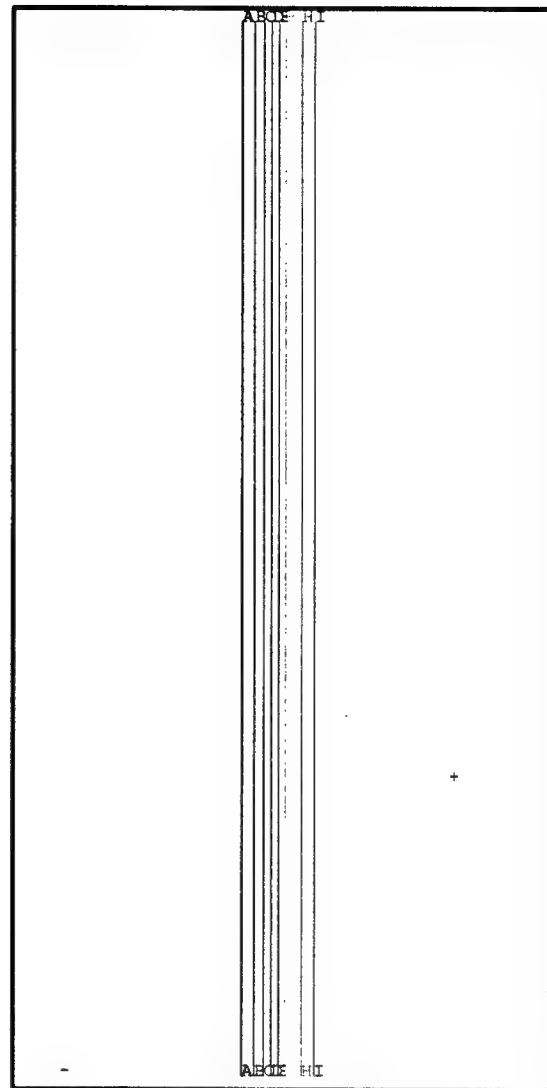


Figure 1-12. Density contours on the orthogonal grid.

NHA - VGA, ERROR FUNC INCREASING PROFILE  
NHA0104F V9403.1  
T = 0.000E+00 CYCLE = 0  
CALCULATION MESH

1ST X = 5.00E-02  
X INC = 5.00E-03  
1ST Y = -4.00E-02  
Y INC = 1.00E-02

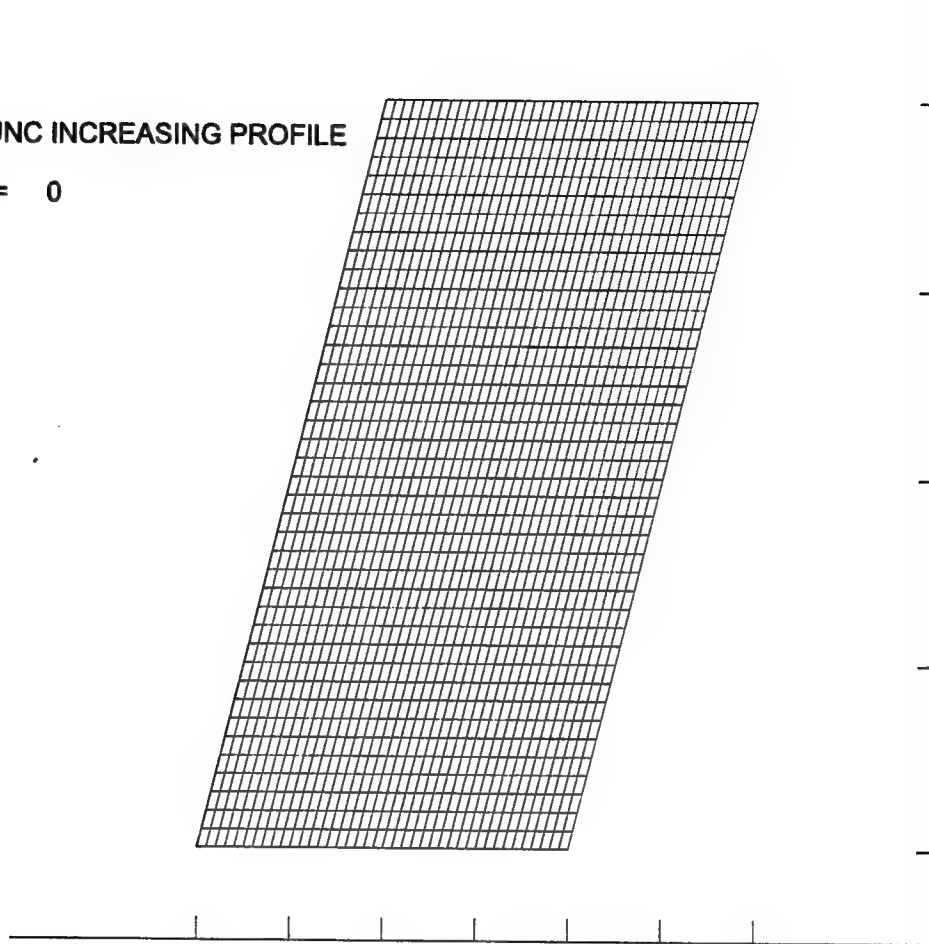


Figure 1-13. Non-orthogonal grid used to compare with calculations on an orthogonal grid.

NHA - VGA, ERROR FUNC INCREASING PROFILE  
NHA0104F V9403.1  
T = 2.500E-09 CYCLE = 1252  
RB (AMPS)

- = 0.0000E+00

A = 7.7195E+04

B = 1.5439E+05

C = 2.3159E+05

D = 3.0878E+05

E = 3.8598E+05

F = 4.6317E+05

H = 6.1756E+05

I = 6.9476E+05

+ = 7.7195E+05

CURRENT(1) = 7.0E+05

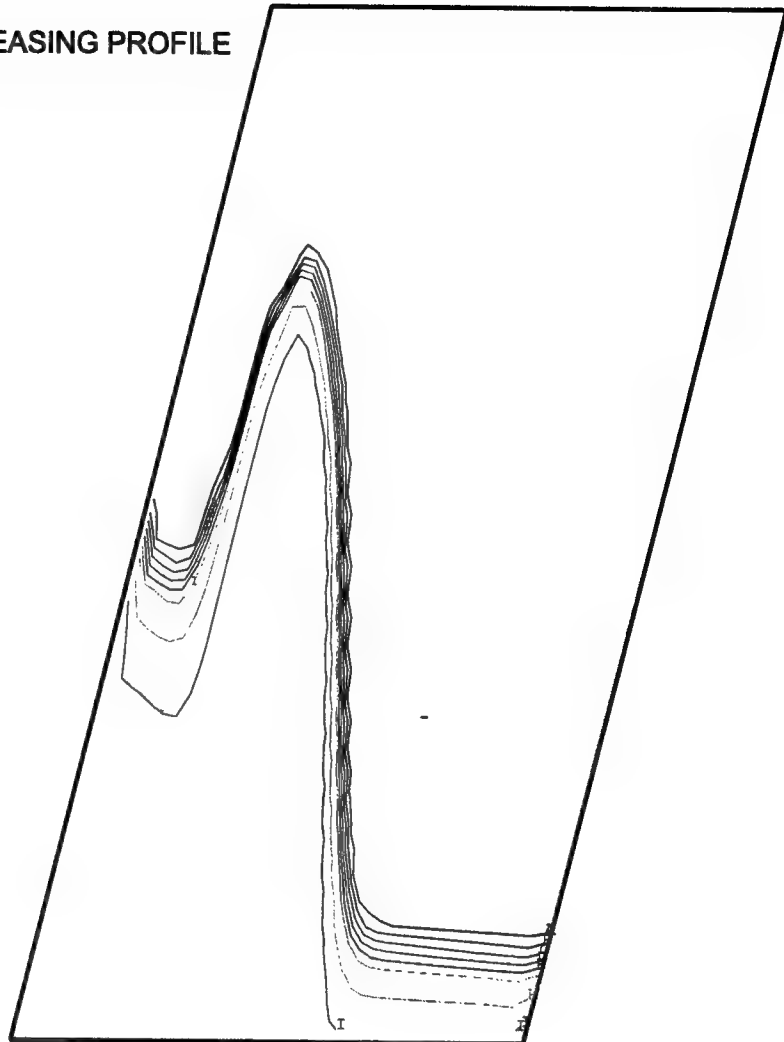


Figure 1-14. Contours of  $rB_0$  at 2.5 ns for non-orthogonal grid calculation.

NHA - VGA, ERROR FUNC INCREASING PROFILE  
 NHA0104F V9403.1  
 T = 0.000E+00 CYCLE = 0  
 ELECTRONS / CC

- = 1.9970E+13

A = 2.5961E+13

B = 3.1952E+13

C = 3.7943E+13

D = 4.3934E+13

E = 4.9925E+13

F = 5.5916E+13

H = 6.7898E+13

I = 7.3889E+13

+ = 7.9880E+13

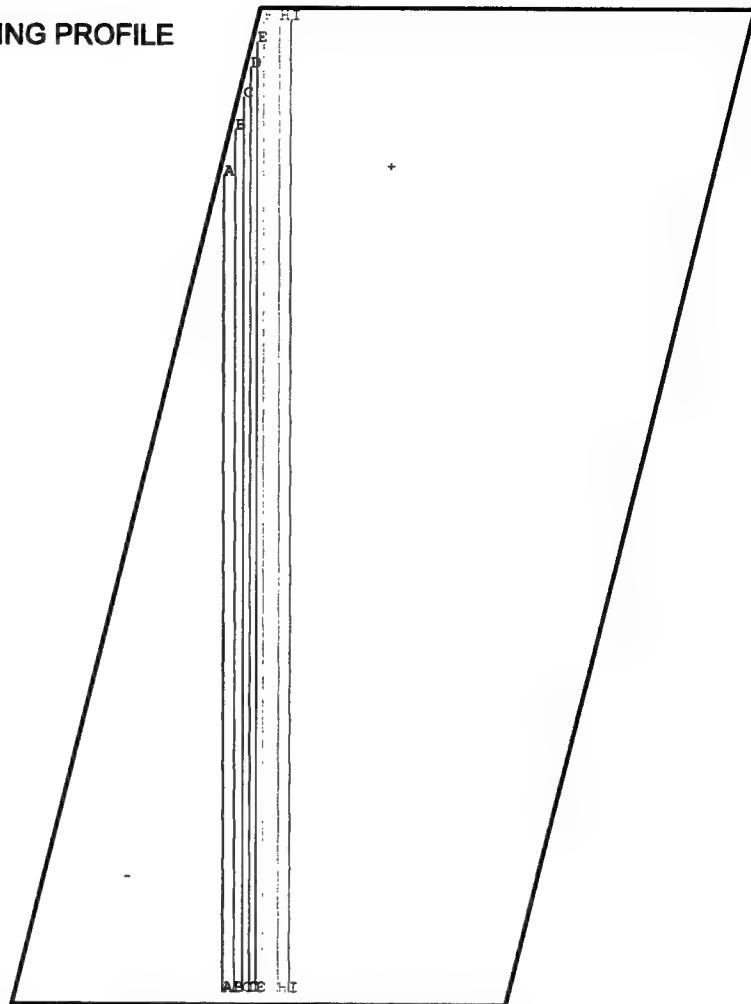


Figure 1-15. Density contours on non-orthogonal grid.

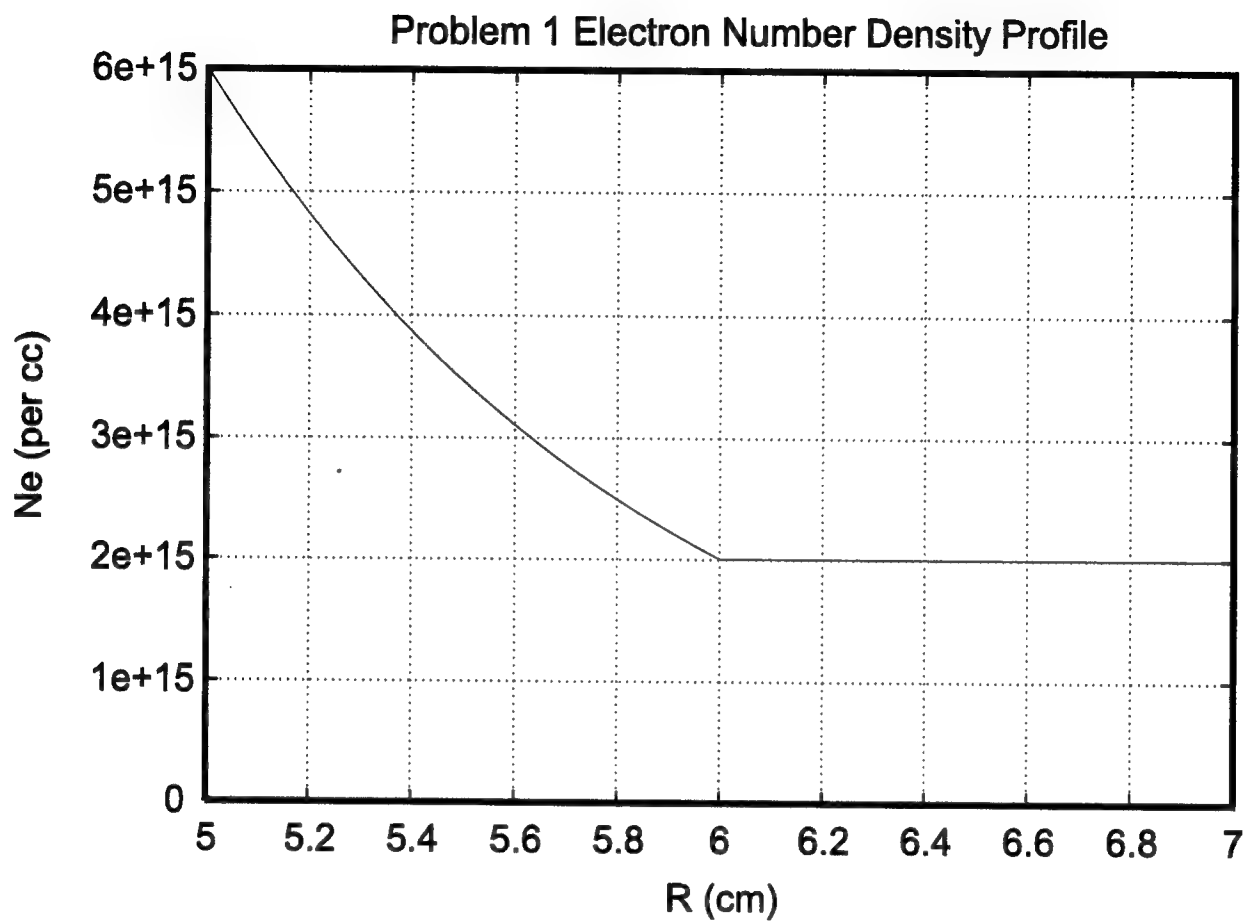


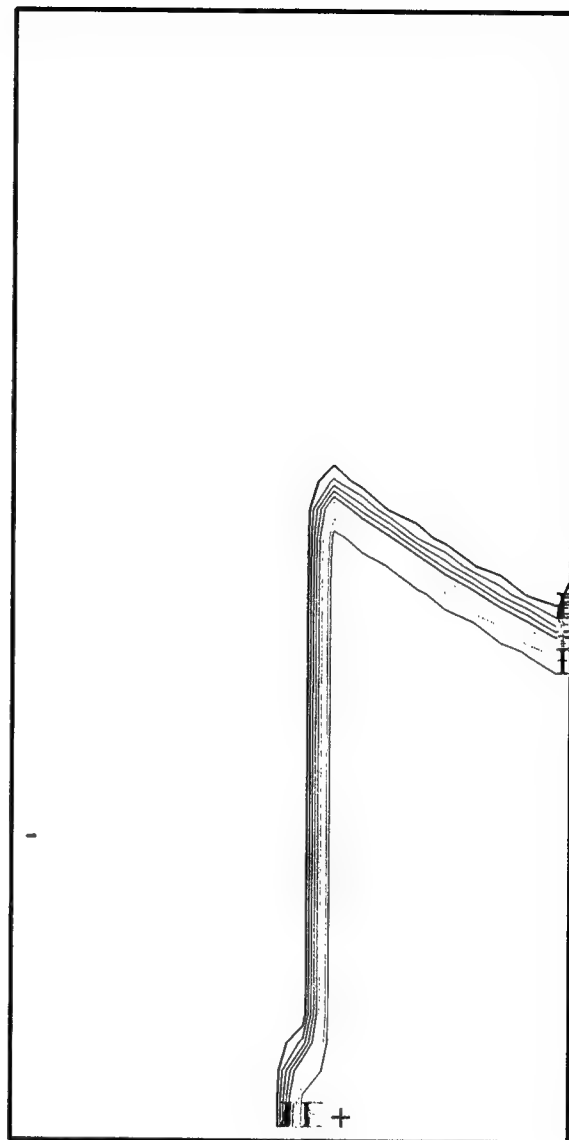
Figure 1-16. Problem 1 electron number density profile.



NHA - GROSSMANN PROBLEM 1  
 NHA0118F V9403.1  
 T = 5.010E-07 CYCLE = 182  
 RB (AMPS)

- = 0.0000E+00  
 A = 7.0000E+04  
 B = 1.4000E+05  
 C = 2.1000E+05  
 D = 2.8000E+05  
 E = 3.5000E+05  
 F = 4.2000E+05  
 G = 4.9000E+05  
 H = 5.6000E+05  
 I = 6.3000E+05  
 J = 7.0000E+05

CURRENT(1) = 7.0E+05



(a) T = 501 ns

Figure 1-17. Mach2 results for  $rB_0$  contours of Problem1 at (a) 501 ns and (b) 851 ns.

NHA - GROSSMANN PROBLEM 1  
 NHA0118F V9403.1  
 T = 8.513E-07 CYCLE = 311  
 RB (AMPS)

- = 0.0000E+00

A = 7.0000E+04

B = 1.4000E+05

C = 2.1000E+05

D = 2.8000E+05

E = 3.5000E+05

F = 4.2000E+05

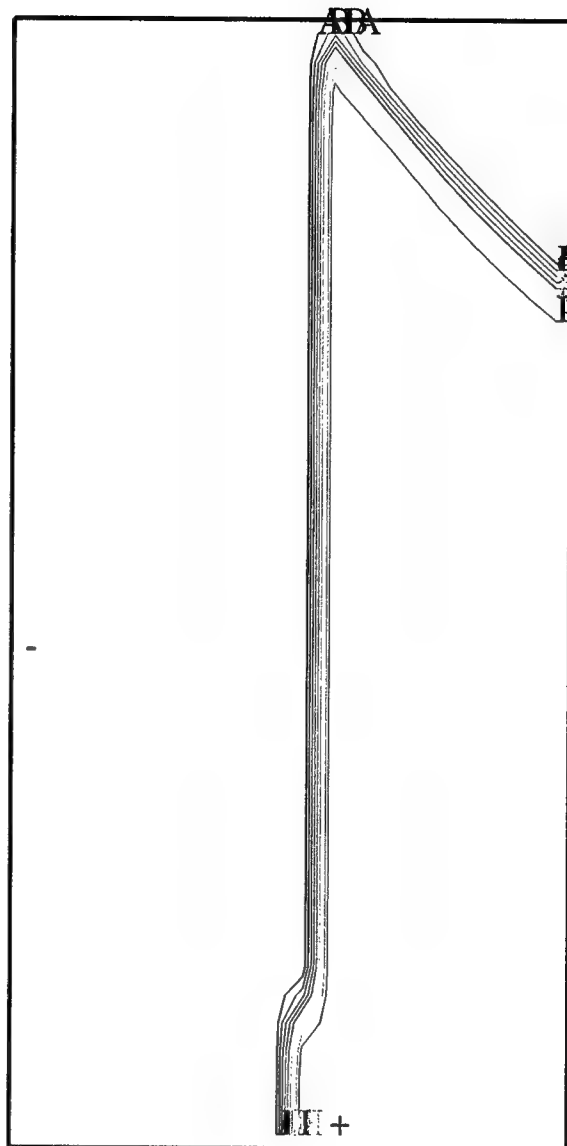
G = 4.9000E+05

H = 5.6000E+05

I = 6.3000E+05

+ = 7.0000E+05

CURRENT(1) = 7.0E+05



(b) T = 851 ns

Figure 1-17. Mach2 results for  $rB_\theta$  contours of Problem 1 at (a) 501 ns and (b) 851 ns (Continued).

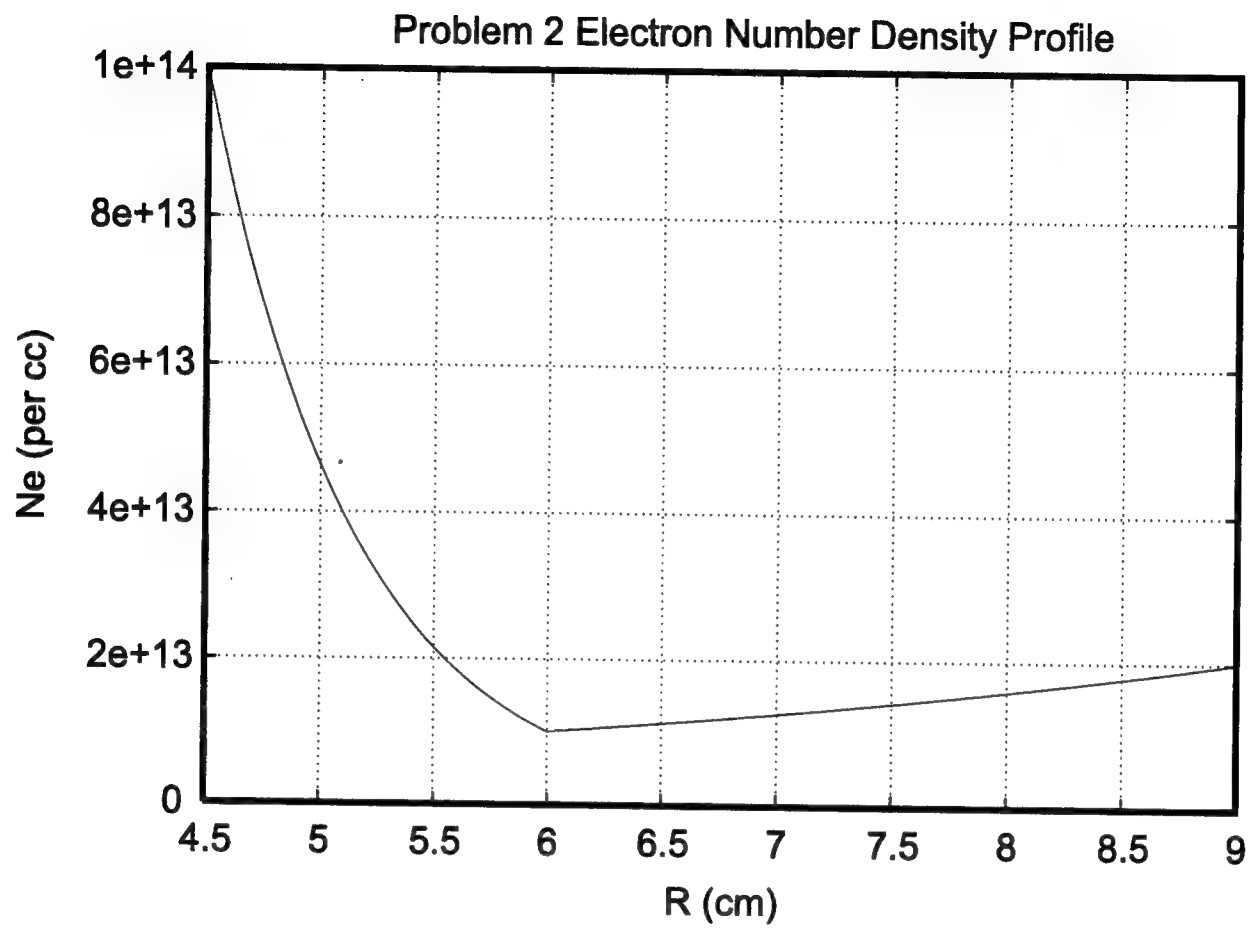


Figure 1-18. Problem 2 electron number density profile.

NHA - GROSSMANN PROBLEM 2A - HALL  
 NHAX0118A V9403.1  
 T = 1.801E-09 CYCLE = 2038  
 ELECTRONS / CC

- = 9.5665E+12    H = 1.2328E+14  
 A = 1.3168E+13    I = 1.6969E+14  
 B = 1.8125E+13    J = 1.0167E+14  
 C = 2.4949E+13  
 D = 3.4341E+13    L = 4.4254E+14  
 E = 4.7270E+13    M = 6.0914E+14  
 F = 6.5066E+13    N = 8.3846E+14  
 G = 8.9561E+13    + = 1.1541E+15

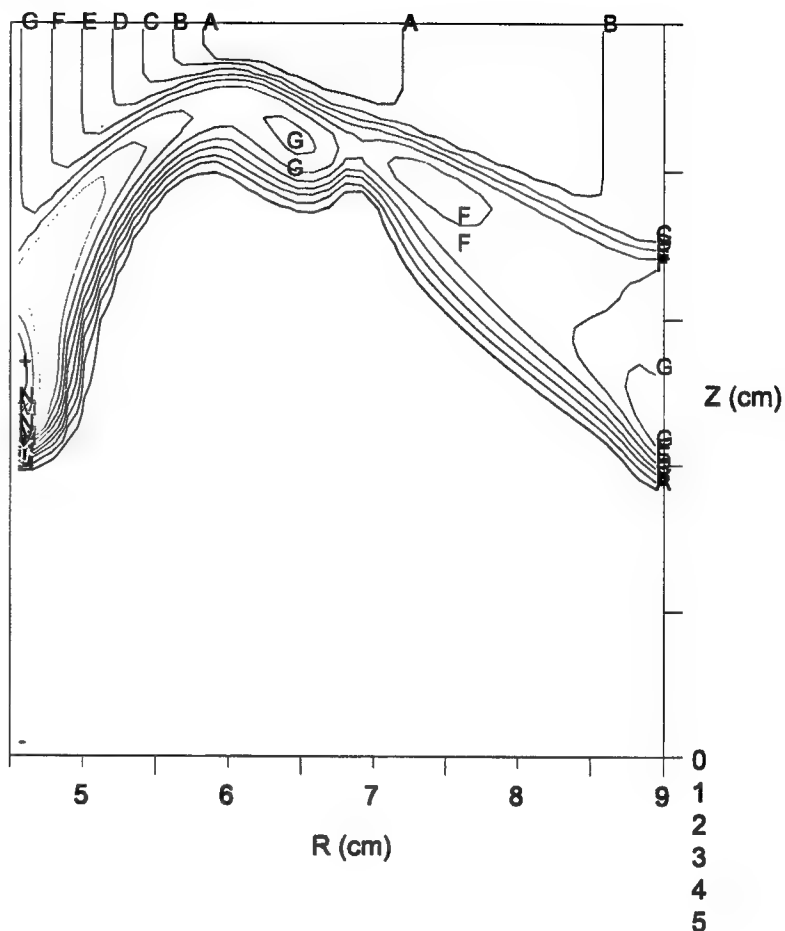


Figure 1-19. Mach2 results including Hall effect for electron number density contours in Problem 2 at 1.8 ns.

NHA - GROSSMANN PROBLEM 2A - HALL  
 NHAX0118A V9403.1  
 T = 1.801E-09 CYCLE = 2038  
 RB (AMPS)

- = 8.5574E-02 H = 3.4027E+05  
 A = 4.2534E+04 I = 3.8280E+05  
 B = 8.5068E+04 J = 3.8514E+05  
 C = 1.2760E+05  
 D = 1.7014E+05 L = 5.1041E+05  
 E = 2.1267E+05 M = 5.5294E+05  
 F = 2.5520E+05 N = 5.9547E+05  
 G = 2.9774E+05 + = 6.3801E+05

CURRENT(1) = 6.0E+05

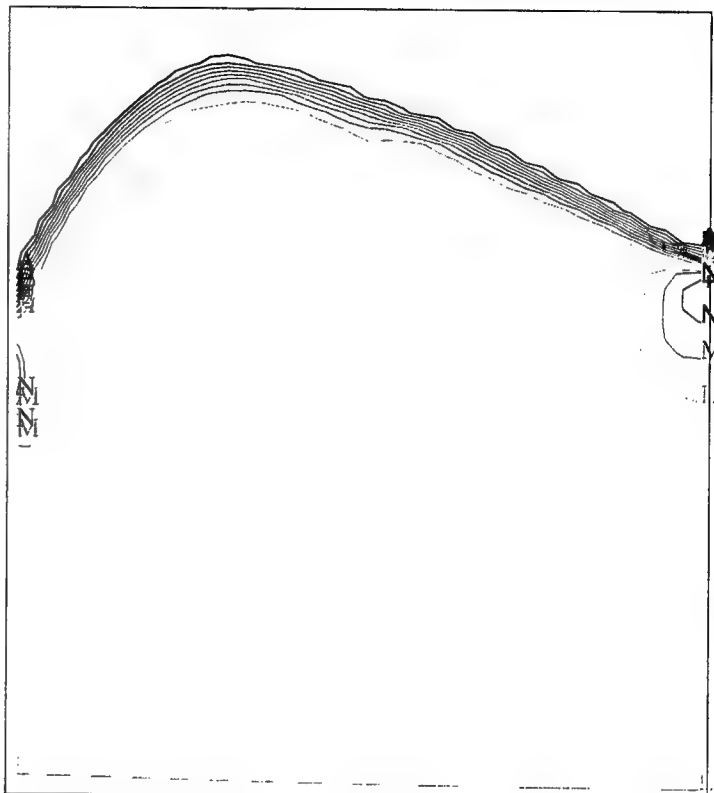


Figure 1-20. Mach2 result including Hall effect for  $rB_\theta$  contours in Problem 2 at 1.8 ns.

NHA - GROSSMANN PROBLEM 2B - NO HALL  
 NHAX0122A V9403.1  
 T = 1.801E-09 CYCLE = 285  
 ELECTRONS / CC

-= 9.5665E+12    H= 1.3534E+14  
 A= 1.3323E+13    I= 1.8848E+14  
 B= 1.8553E+13    J= 2.8249E+14  
 C= 2.5838E+13  
 D= 3.5983E+13    L= 5.0907E+14  
 E= 5.0111E+13    M= 7.0894E+14  
 F= 6.9786E+13    N= 9.8730E+14  
 G= 9.7185E+13    O= 1.3749E+15

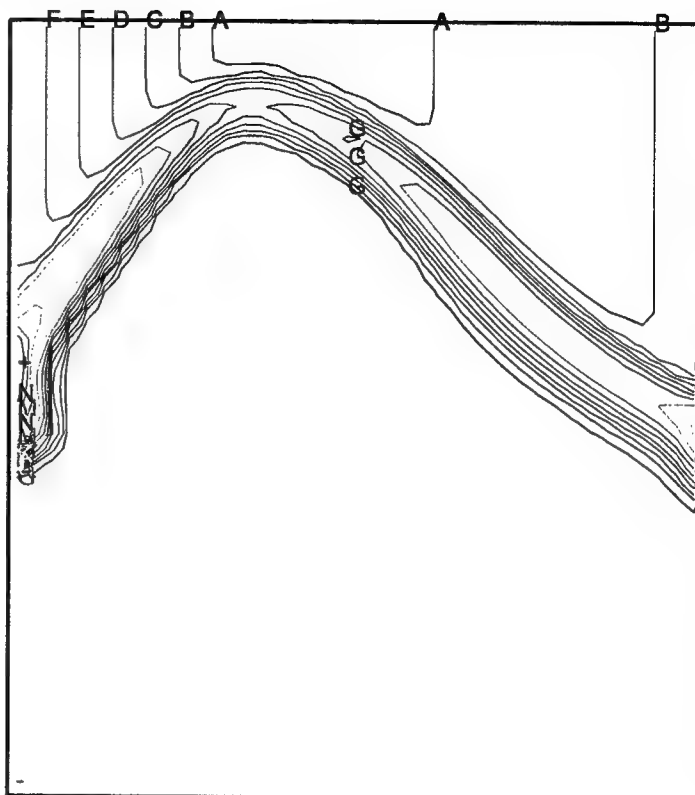


Figure 1-21. Mach2 result without Hall effect for electron number density contours in Problem 2 at 1.8 ns.

NHA - GROSSMANN PROBLEM 2B - NO HALL  
 NHAX0122A V9403.1  
 T = 1.801E-09 CYCLE = 285  
 RB (AMPS)

-= 0.0000E+00    H= 2.9185E+05  
 A= 3.6481E+04    I= 3.2833E+05  
 B= 7.2962E+04    J= 3.5471E+05  
 C= 1.0944E+05  
 D= 1.4592E+05    L= 4.3777E+05  
 E= 1.8241E+05    M= 4.7425E+05  
 F= 2.1889E+05    N= 5.1074E+05  
 G= 2.5537E+05    O= 5.4722E+05

CURRENT(1) = 6.0E+05

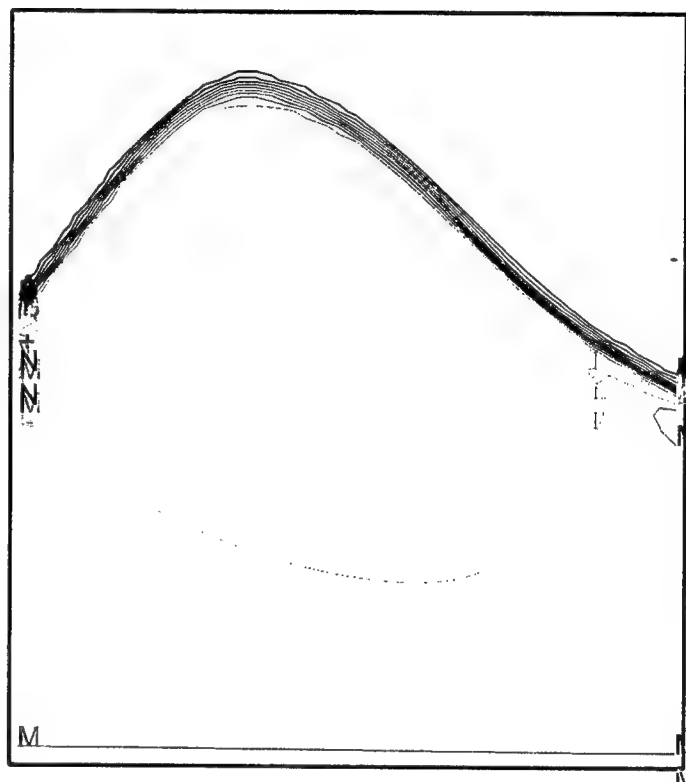


Figure 1-22. Mach2 result without Hall effect for  $rB_\theta$  contours in Problem 2 at 1.8 ns.

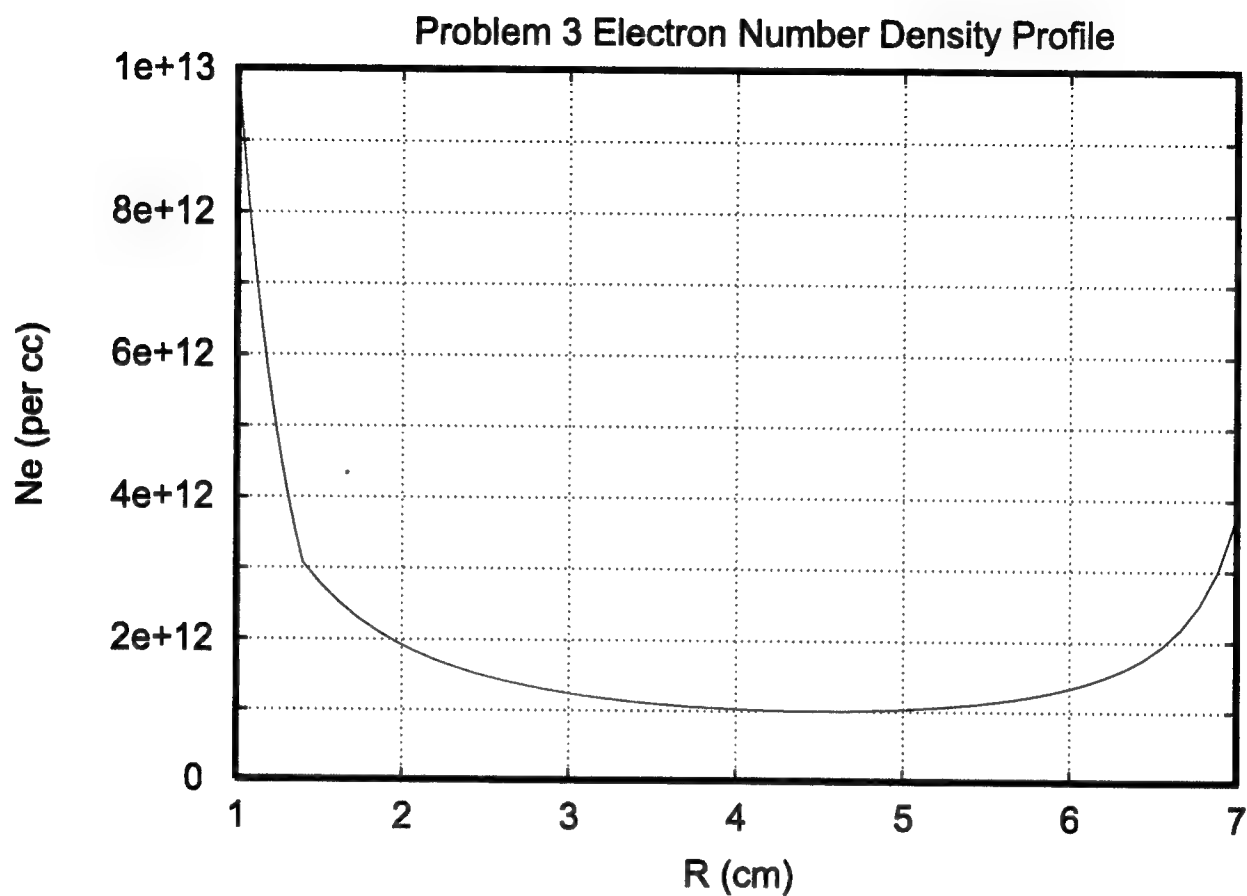


Figure 1-23. Problem 3 electron number density profile.



0117 TWEAK - GROSSMANN PROBLEM 3 - HALL, NO HYDRO

NHA0118B V9403.1

T = 1.600E-08 CYCLE = 320

RB (AMPS)

--1.3499E+00

A= 4.9879E+02

B= 9.9892E+02

C= 1.4991E+03

D= 1.9992E+03

E= 2.4993E+03

F= 2.9995E+03

H= 3.9997E+03

I= 4.4999E+03

+= 5.0000E+03

CURRENT(1) = 5.0E+03

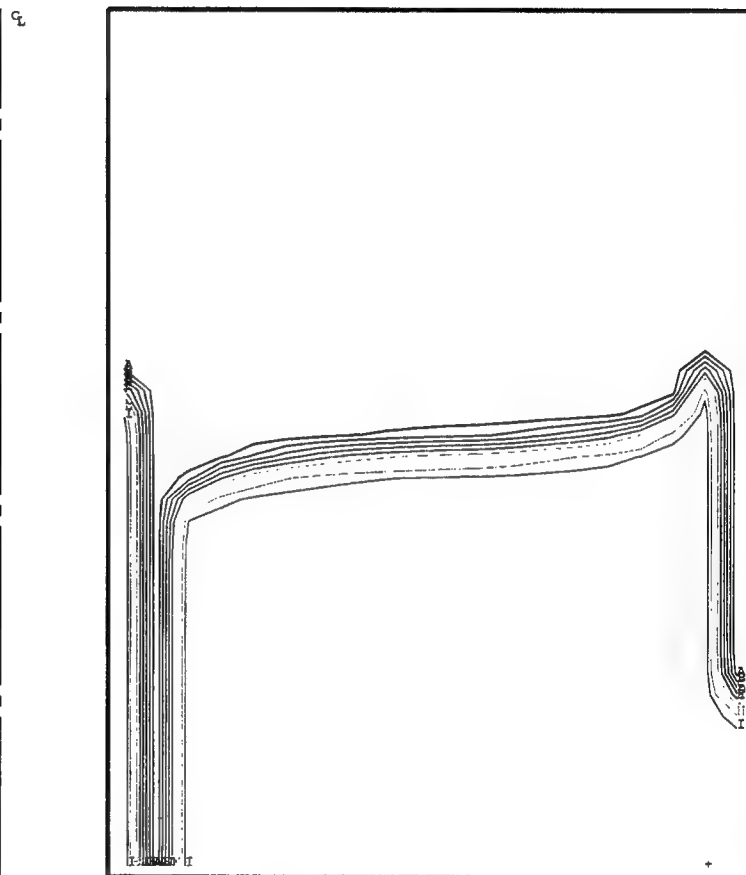


Figure 1-24. The magnetoshock for Problem 3 at 16 ns.

0117 TWEAK - GROSSMANN PROBLEM 3 - HALL, NO HYDRO

NHA0118B V9403.1

T = 3.200E-08 CYCLE = 640

RB (AMPS)

--2.4330E+00

A= 4.9781E+02

B= 9.9805E+02

C= 1.4983E+03

D= 1.9985E+03

E= 2.4988E+03

F= 2.9990E+03

H= 3.9995E+03

I= 4.4998E+03

+= 5.0000E+03

CURRENT(1) = 5.0E+03

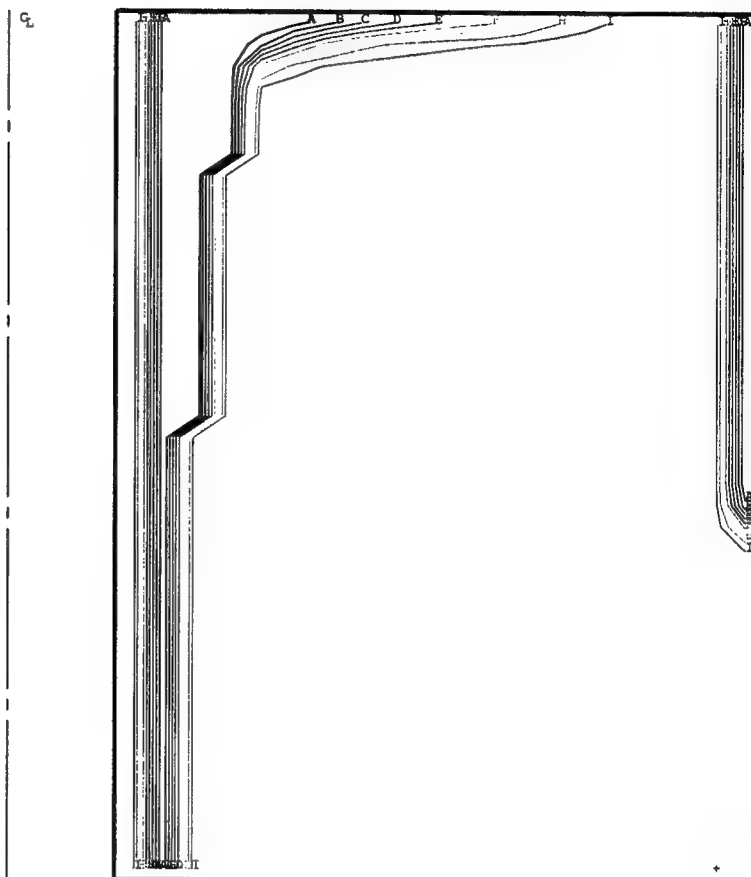


Figure 1-25. The magnetoshock for Problem 3 has reached the end of the computational domain at 32 ns.

NHA - GROSSMANN PROBLEM 4  
NHA0118A V9403.1  
T = 1.003E-09 CYCLE = 48  
RB (AMPS)

-= 0.0000E+00

A= 5.9271E+04

B= 1.1854E+05

C= 1.7781E+05

D= 2.3708E+05

E= 2.9635E+05

F= 3.5562E+05

H= 4.7417E+05

I= 5.3344E+05

+= 5.9271E+05

CURRENT(1) = 6.0E+05

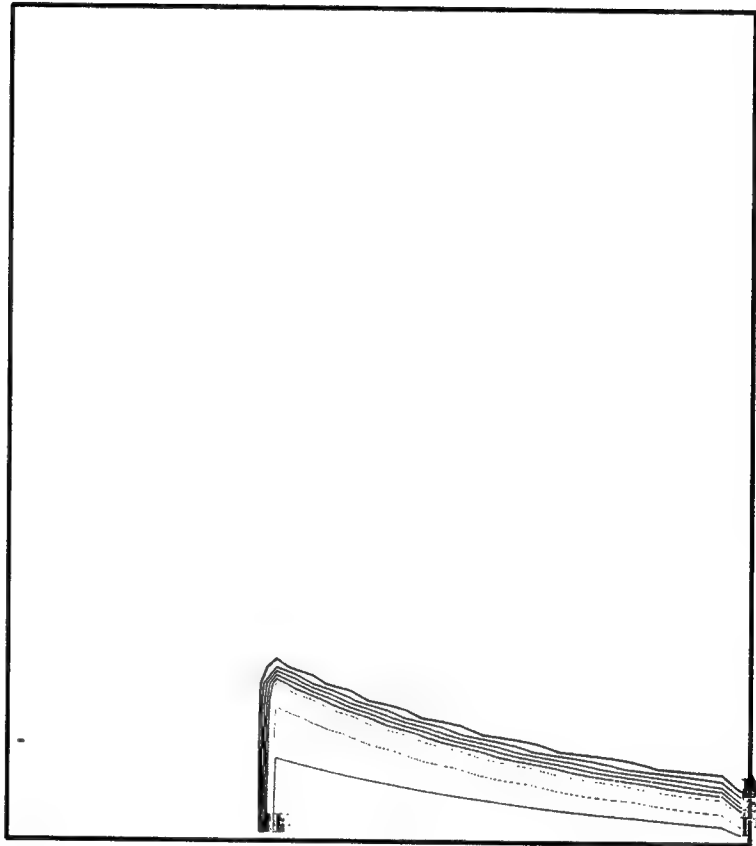


Figure 1-26. Mach2 results for  $rB_\theta$  contours in Problem 4 at 1 ns.

NHA - GROSSMANN PROBLEM 4  
NHA0118A V9403.1  
T = 2.504E-09 CYCLE = 206  
RB (AMPS)

--6.9046E-02

A= 6.0000E+04

B= 1.2000E+05

C= 1.8000E+05

D= 2.4000E+05

E= 3.0000E+05

F= 3.6000E+05

H= 4.8000E+05

I= 5.4000E+05

+= 6.0000E+05

CURRENT(1) = 6.0E+05

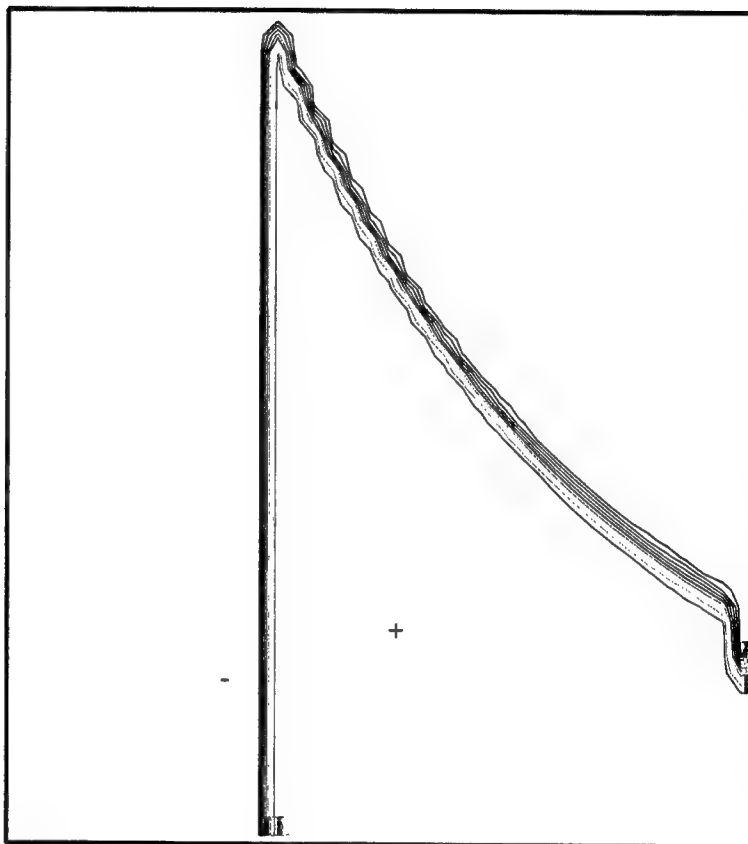


Figure 1-27. Mach2 results for  $rB_\theta$  contours in Problem 4 at 2.5 ns.

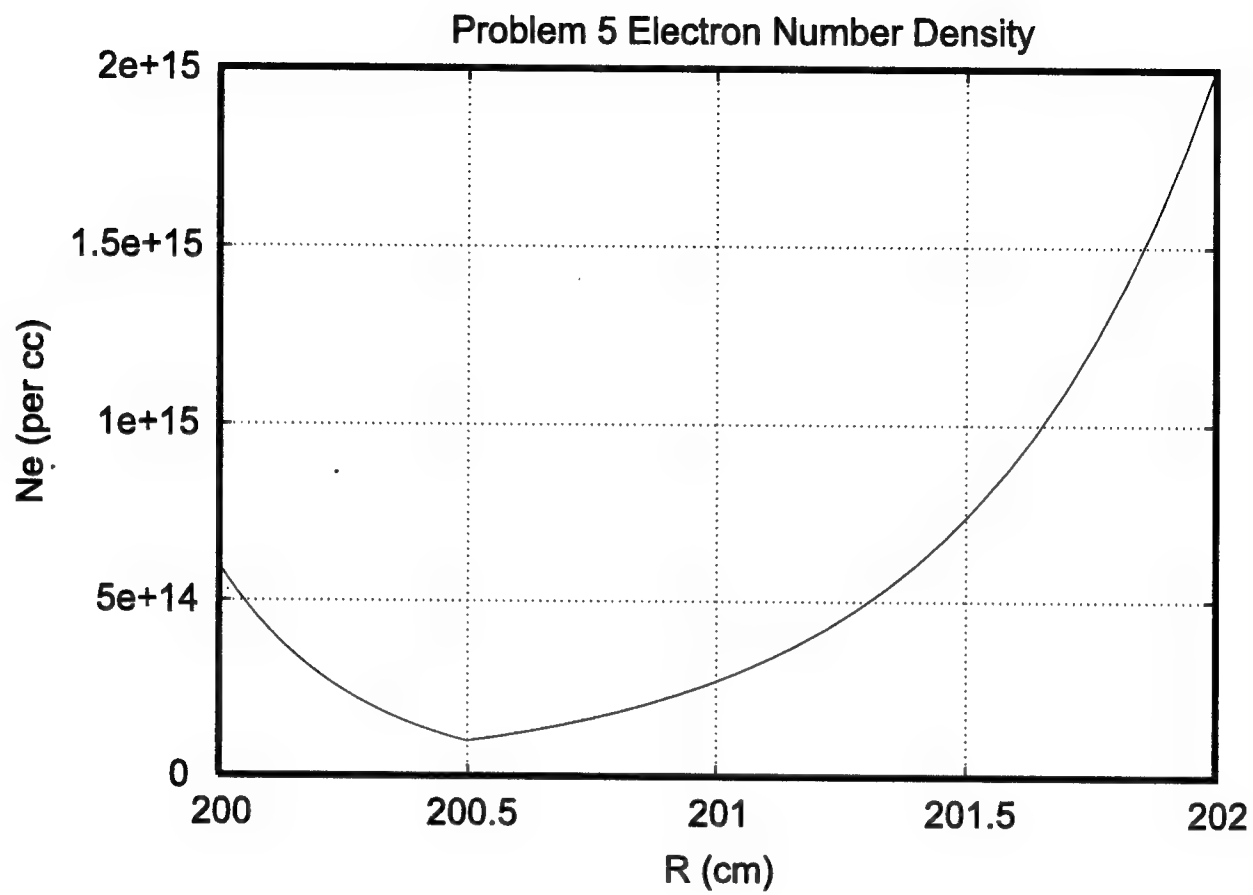


Figure 1-28. Problem 5 electron number density.

NHA - GROSSMANN PROBLEM 5  
NHA0118C V9403.1  
T = 1.002E-07 CYCLE = 503  
RB (AMPS)

- = 0.0000E+00

A = 7.0000E+04

B = 1.4000E+05

C = 2.1000E+05

D = 2.8000E+05

E = 3.5000E+05

F = 4.2000E+05

G = 4.9000E+05

H = 5.6000E+05

I = 6.3000E+05

+ = 7.0000E+05

CURRENT(1) = 7.0E+05

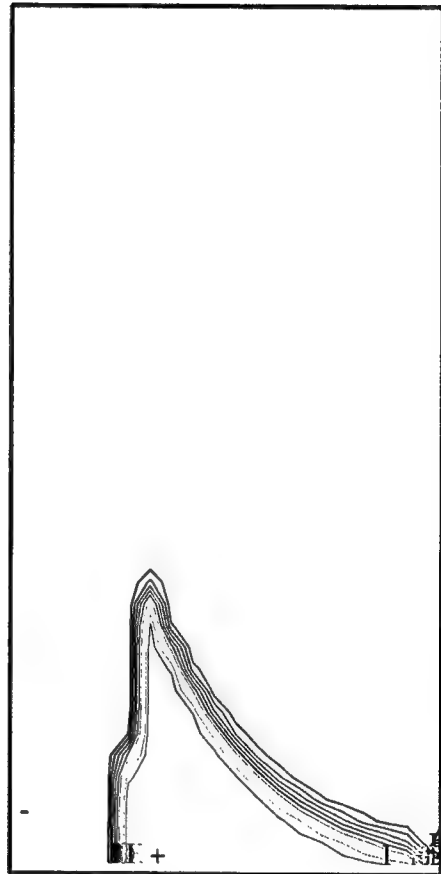


Figure 1-29. Mach2 results for  $rB_\theta$  contours in Problem 5 at 100 ns.

NHA - GROSSMANN PROBLEM 5  
NHA0118C V9403.1  
T = 3.001E-07 CYCLE = 1503  
MAGNETIC FIELD -- THETA COMPONENT

- = 0.0000E+00

A = 6.9808E-03

B = 1.3962E-02

C = 2.0942E-02

D = 2.7923E-02

E = 3.4904E-02

F = 4.1885E-02

H = 5.5846E-02

I = 6.2827E-02

+ = 6.9808E-02

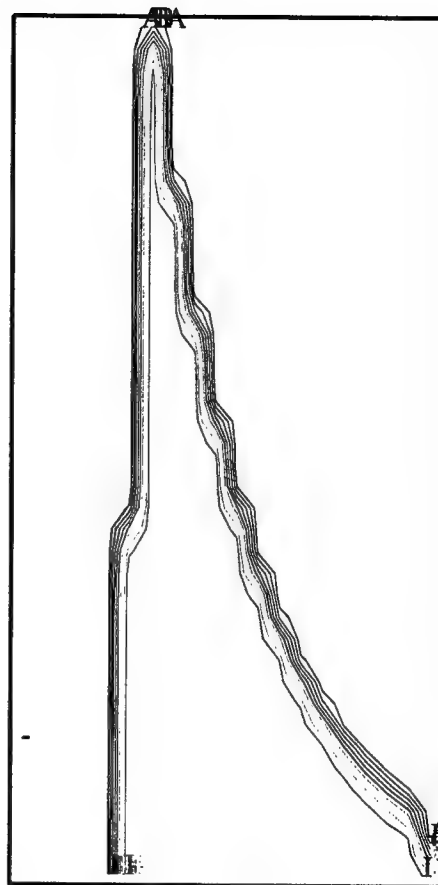


Figure 1-30. Mach2 results for  $rB_\theta$  contours in Problem 5 at 300 ns.

## **SECTION 2**

### **HAWK PARALLEL PLATE POS MODELING**

Arguably the most fully diagnosed POS experiment in the U.S. pulsed power community is the parallel plate Hawk experiment conducted by the Pulsed Power Physics Group of the Naval Research Laboratory (References 4 and 5). This experiment was designed explicitly for diagnostic access. A typical shot has a set of 8 interferometric lines of sight integrating the electron number density along the ignorable direction. A number of identical shots are taken, moving this set of 8 lines-of-sight from one position to another. In this manner, a matrix of 96 different line-of-sight data is constructed. The typical spacing between lines-of-sight is half-a-centimeter in the axial direction, and a quarter of a centimeter in the radial direction. Along with diagnostic access, the experiment was designed to allow studies of the Hall effect. This then, was an ideal experiment to attempt to model with the newly created Hall effect algorithm in Mach2.

#### **2.1 DESCRIPTION OF EXPERIMENTS.**

Exhaustive descriptions of the Hawk parallel plate POS experiment can be found elsewhere (References 4 and 5). A brief description will suffice for present purposes. The plates are arranged to form a gap of 2.5 cm. Plasma is introduced into the AK gap through an opening in what will be referred to here as the outer plate (the actual configuration consists of three parallel plates with plasma flowing in toward the center plate from openings in the two exterior plates). Cable guns are used as the plasma source; a number of guns are arranged in a line along the ignorable direction (the ignorable direction is that which is analogous to the azimuthal direction in cylindrical geometry). The opening in the outer plate is 5-cm in length in the upstream/downstream direction; this sets the nominal length of the switch region to be 5 cm. The current pulse which HAWK provides creates a magnetic field which rises to 2.932T in 1.4  $\mu$ s, following a sinusoidal time-behavior. Experimentally, the conduction time is observed to be about 600 ns. Figure 2-1 shows the experimentally observed electron number density distribution at the time quite close to the time chosen for the initiation of pulsed power.

The parallel-plate experiment was designed so that the polarity of the pulsed current could be changed readily. This allows the importance of the Hall effect to be tested. In the absence of the Hall effect, MHD has no sensitivity to the polarity of the current, just its magnitude. But the Hall effect is sensitive to the current polarity. So performing the same experiment with different



polarities should indicate whether or not the Hall effect has significance. Other experimental parameters were chosen so that, at least according to theory, the Hall effect would be significant. Specifically, the densities and magnetic field strengths were chosen so the Hall timescale would be comparable to the Alfven timescale.

To demonstrate this, one needs an estimate for the electrode-to-electrode electron number density gradient. Experimentally, it is observed that the inflow of cable gun plasma produces a distribution of plasma in the gap which, in grossest terms, increases from the inner electrode to the outer electrode. Specific values are:

$$\begin{aligned} n(r=3.8 \text{ mm}) &= 1.3 \times 10^{15} \text{ per cc} \\ n(r=22.7 \text{ mm}) &= 3.7 \times 10^{15} \text{ per cc.} \end{aligned}$$

Here,  $r$  is used to measure distance from the inner electrode in a manner analogous to the use of  $r$  in cylindrical geometry. The theoretical results of Section 1 can be used here, despite the fact that they were posed for cylindrical geometry, by considering their behavior as  $r$  increases toward infinity. Using:

$$V_f = (1/2) p B \quad (2.1)$$

where  $p = (2/r)/[e \mu_0 n e] + [d(\ln(ne)/dr)/[e \mu_0 n]]$  one obtains, for  $r$ -infinity,

$$V_f = (1/2) B [d(\ln(ne)/dr)/[e \mu_0 n]] \quad (2.2)$$

$$\begin{aligned} &\approx (0.5)(1.5T) \\ &[\{\ln(3.7 \times 10^{21}) - \ln(1.3 \times 10^{21})\}/(0.0227\text{m} - 0.0038\text{m})] * \\ &1./[(1.6 \times 10^{-19} \text{ C})(4\pi 10^{-7} \text{ H/m})(2.5 \times 10^{21} \text{ m}^{-3})] \\ &= (0.75T)(55.34 \text{ m}^{-1})(1.990 \times 10^3 \text{ m}^4/\text{C-H}) \\ &= 8.26 \times 10^4 \text{ m/s.} \end{aligned}$$

This speed, combined with the nominal switch length of 5 cm, gives a Hall timescale of 600 ns. Note that this coincides with the stated value of the experimentally observed conduction time.

The Alfven speed is:

$$V_{\text{Alfven}} = B / (2\mu_0 \rho) , \quad (2.3)$$

where  $\rho$  is the mass density. Using an electron number density of  $2.5 \times 10^{15}$  per cc, assuming an average charge state of 2, and assuming the average atomic weight to be 16.7 (from the chemical composition of teflon, two fluorines per carbon, teflon being the dielectric in the cable guns), the mass density is  $3.49 \times 10^{-5}$  kg/m<sup>3</sup>. Using a magnetic field strength of 1.5 T, the Alfven speed is:

$$V_{\text{Alfven}} = 2.27 \times 10^5 \text{ m/s} . \quad (2.4)$$

This speed, combined with the 5-cm nominal length of the POS region, gives an Alfven timescale of 221 ns.

## 2.2 DESCRIPTION OF SIMULATION SETUP.

The principle task in simulating the Hawk-driven parallel plate POS experiment was to reproduce in the simulation the conditions observed in the experiment in the absence of pulsed power. The richness of the experimental data allows comprehensive comparison of experiment and simulation.

Two tasks needed to be accomplished in order to model the guns-only case faithfully. First, the observed initial electron number density distribution had to be translated into mass density. Second, boundary conditions had to be developed which allowed the continued inflow of plasma into the AK gap in a manner which mimicked the experiment. What is referred to here as "the initial" electron number density distribution is actually the distribution which occurs at the time which was chosen for the firing of the pulsed power generator. Of course, in the guns-only case, the generator is not fired.

The first task, translation of electron number density into mass density, is done with the help of the Saha equilibrium ionization model. This model requires two pieces of information to be used in this manner; the composition of the plasma, and the plasma temperature. Since the dielectric in the cable gun is the primary source of plasma, and since that dielectric is composed of teflon, the plasma is assumed to consist of two fluorines per carbon. The matter of plasma temperature is not so trivial, but the experimental data is of help.

The data from the pulsed-power case suggests that the snowplow increases the average ionization state from its initial value to a value roughly three times greater. This factor of three increase, along with the Saha model for how  $Z_{\text{eff}}$  varies with temperature, gives a fairly strong indication for the likely range of initial temperatures. Figure 2-2 shows how for a plasma with the composition CF<sub>2</sub> and at an ion number density of  $2 \times 10^{15}$  per cc, the average ionization state varies with temperature. A plateau in  $Z_{\text{eff}}$  of  $Z_{\text{eff}}=6$  exists for the temperature range 12-20 eV. Assuming that the snowplow does not heat the plasma to a temperature above this range then restricts the initial temperature to below roughly 3 eV. Higher initial temperatures would require that the snowplow heat the plasma to above the 12-20 eV range; not an impossible occurrence, but not likely, either.

Thus, the Saha model and the experimental observation of the increase in average ionization state suggest a range for the initial temperature, but as Figure 2-2 shows, a small change in temperature results in a large change in  $Z_{\text{eff}}$ , and thus in a large change in the mass density inferred from the electron number density. A solid grasp on the initial temperature can be obtained by a comparison of the observed evolution of the electron number density distribution with the simulated evolution. The point here is that different assumptions on the plasma temperature will lead to different time-dependent behaviors, and comparison to experiment will indicate which assumption is the best. Here, the grossly simplifying assumption of uniform temperature is made, and is made with no more justification than it does allow for a huge simplification of the modeling task.

Figures 2-3, 2-4 and 2-5 show the experimental data, the penultimate, and ultimate guns-only simulations, respectively. Here, the electron number density distribution at 1  $\mu$ s (relative to the yet-to-come firing of the capacitor bank) as observed is compared to those simulated assuming plasma temperatures of 1 eV and 2 eV. These assumed temperatures are used for the initial temperature as well as the temperature of the plasma introduced at the inflow boundary. The temperature is allowed to change in response to pdV work and to radiative cooling as the simulation proceeds. As the figures indicate, the assumption of 2 eV gives quite good agreement with the experimentally observed data.

A useful result of this effort to faithfully model the guns-only situation is that the simulation models the pile-up of plasma against the inner electrode. While this is not directly observed experimentally, it is difficult to imagine a way for it not to happen. Moreover, it has been observed in other experiments (References 6 and 7). The lack of direct experimental observation of this phenomenon in the parallel plate experiment must be due to the fact the interferometric

lines-of-sight nearest the inner electrode are simply not sufficiently near the inner electrode to observe the pile-up. As will be seen in the pulsed-power simulations, this pile-up of plasma gives rise to behavior significantly different from what would occur had that pile-up not been present.

One feature of the guns-only experimental data which proved to be less than trivial to capture in the simulations was the axial structure. As yet, no compelling explanation is offered for how such structure results from what is effectively a line source, but the data show it to be there nonetheless. The means by which this feature eventually was captured in the simulations was to use a segmented boundary condition. Thus, rather than to use a single boundary condition for the entire section through which plasma flows into the AK gap, this part of the boundary was divided into four segments, each of which used their own boundary condition. It was found that four such segments were adequate.

Given a technique for faithfully modeling the guns-only case, the next task was to use this set-up for assessing whether and to what degree the Hall effect affected the plasma during the conduction phase. This was merely a matter of turning on the current. Here a minor detail should be reported. The experiments were in slab geometry, however the Hall effect algorithm was applicable to cylindrical geometry only. However, by doing the calculation in cylindrical geometry, but at very larger radius, cylindrical effects all but disappear. But in so doing, one must magnify the driving current by a factor proportional to the radius in order to get the desired magnetic field values. The simulations reported here were performed at a radius of 2.0 m. The current used to drive them is shown below:

<u>Time (s)</u>	<u>Current (A)</u>
0.000E+00	0.000E+00
0.200E-06	0.652E+07
0.400E-06	1.272E+07
0.600E-06	1.828E+07
0.800E-06	2.292E+07
1.000E-06	2.641E+07
1.200E-06	2.858E+07
1.400E-06	2.932E+07

### **2.3 DISCUSSION OF SIMULATION RESULTS AND COMPARISON TO EXPERIMENTS.**

Experimentally observed electron number density distributions at various times throughout the conduction phase are shown in Figures 2-6, 2-7, 2-8, 2-9, and 2-10. These experiments are run in positive polarity. In the figures the cathode is on the left and power flows from bottom to top. Analogous results for three different simulations, corresponding to ideal MHD (no Hall effect), Hall MHD in positive polarity, and Hall MHD in negative polarity, are shown in Figures 2-11, 2-12, and 2-13, respectively.

The degree to which the Hall effect affected the conduction phase can be assessed by comparing the simulation results to one another as well as the experimental results. The ideal MHD and positive polarity Hall calculations give results which are roughly similar to one another; both share qualitative features with the experimental data, particularly the development of a low density region near the left-hand (AKA inner) electrode. The negative polarity calculation, however, develops in a manner distinctly different from either ideal MHD, positive polarity Hall MHD, or the experiment.

The negative polarity simulation is interesting inasmuch as it shows that while the simplest theoretical prediction concerning Hall would lead one to believe that Hall should have no effect in this polarity, it does indeed have a profound effect. The zeroth order prediction says that when the flow of electrons is down the density gradient, as it is in the negative polarity case, the Hall effect does not enhance magnetic field penetration into the plasma. At early times, this is indeed the prevailing condition. But as discussed above, the simulation of in flowing plasma leads to a pile-up of plasma near the inner electrode. That is, as time passes, the density gradient near the inner electrode reverses sign and becomes such as to allow Hall penetration of the plasma to occur. What follows is a subtle interaction between the standard picture of the magnetic field pushing the plasma around, and the not-so-standard picture of Hall penetration into the plasma. Early on, say from around 200 ns to around 300 ns, a finger-like region of magnetic-flux-occupied plasma pushes into the plasma just above the plasma which has piled-up on the inner electrode. The Hall effect allows the magnetic field then to propagate along electron number density contours, which brings the field more or less into the center of the switch plasma. And concurrent with this penetration is the standard magnetic pushing, causing plasma to be thrust aside, away from the central switch region. Eventually, the flux-filled "void" breaks through the plasma near the outer electrode. This is distinctly different from the behavior observed in ideal MHD, positive polarity Hall MHD, or experimentally. Moreover, it is

distinctly different from what the simplest prediction of the importance of the Hall effect in this case would have lead one to expect. This point cannot be under-emphasized as it leads one to wonder where else in the grand history of MHD might the Hall effect have been an important, if neglected, player.

As the experiment against which comparisons are being made here was run in positive polarity (with electrons being emitted from the inner or left-hand electrode and traveling to the outer or right-hand electrode), it is the positive polarity and ideal MHD calculations which ought to be considered as contenders for accurate depictions of reality. The negative polarity case, and its difference with the other cases, shows that Hall certainly does make a difference. The question then is whether or not Hall, in the correct polarity, can make a simulation behave more like that which is observed experimentally.

Figures 2-11 and 2-12 display features of qualitative similarity shared by the ideal MHD and positive polarity Hall MHD calculations, which also are similar to features seen in the experimental data. In particular, a region of vacuum grows along the inner (left-hand) electrode. Comparing the electron number density plots at time  $t = 400$  ns shows a great deal of similarity between ideal MHD and positive polarity Hall MHD. In both cases, there is a low density or vacuum region near the inner electrode, the bulk of the plasma has been pushed a little bit downstream, and there is a high-density ridge where the snowplow is pushing on the bulk of the plasma. Looking back earlier in time, however, shows that these evacuated regions developed in grossly different manners. In the case of ideal MHD, the snowplow has simply pushed its way furthest where the mass density was lowest. In the case of positive polarity Hall, the density gradient was such as to allow a finger-like penetration of magnetic field into the plasma along the inner electrode; this field then began to push plasma away from the inner electrode. A clear difference in how plasma is distributed in the vicinity of the inner electrode is clear between the ideal MHD calculation and the positive polarity Hall calculation. In the former, plasma gets pushed up against the inner electrode as the snowplow pushes through the switch plasma. In the latter case, plasma is lifted up and away from the inner electrode. Unfortunately, this difference cannot be seen experimentally, since it occurs between the inner electrode and the innermost row of interferometric lines-of-sight.

In order to answer the question as to whether or not including the Hall effect in a calculation affords greater fidelity to the experiment, experimentally discernible features must be found which are observed in the Hall effect calculation, but are not observed in the no-Hall calculation. An appeal to the quantitative values of electron number density logically is not sufficient, and

regardless of logic, does not help much in this case as most of the experimental numbers lie somewhere between the ideal MHD and the positive polarity Hall MHD numbers. The strongest piece of evidence is in the size and behavior of the gap which forms between the inner electrode and the main body of switch plasma. In the case of the ideal MHD calculation, this gap is wider and extends closer to the outer electrode than in either the case of the positive polarity Hall MHD calculation or the experimental data. This is most clearly seen by comparing the electron number density plots at times  $t = 500$  ns, 550 ns, and 575 ns. In the ideal MHD case, while the snowplow is rapidly moving plasma downstream, it is also pushing plasma in the main body of the switch outward toward the outer (right-hand) electrode. Over the 75 ns covered by these three plots, the evacuated region grows to cover more than half of the distance of the A-K gap. Over this same period, the gap seen in the positive polarity Hall MHD calculation, as well as that seen in the experimental data, stays more or less the same size, remains situated near the inner (right-hand) electrode, and maintains a size which is significantly smaller than half the AK gap.

Two pieces of evidence then suggest that the Hall effect is important and that its inclusion in a simulation allows the simulation to agree better with experiment. The first is the polarity effect. Changing the polarity of current flow in the simulations lead to significant differences in how the electron number density distribution evolved throughout the conduction phase. The second is the comparison of the evolution of electron number density as obtained in an ideal MHD simulation, in a positive polarity Hall MHD simulation, with that observed experimentally. The growth of the evacuated region between the inner electrode and the main body of plasma, in particular, is modeled much more faithfully with the positive polarity Hall MHD calculation than with the ideal MHD calculation. Further pieces of compelling evidence would likely be obtained by an examination of the experiment in which current polarity was reversed, but at the time of these investigations, the data for that experiment had not yet been sufficiently processed to be useful for such purposes.

# HAWK-DRIVEN PARALLEL PLATE: EXPERIMENTAL DATA AT 10NS

ELECTRONS / CC

J= 1.5227E+14	J= 1.0821E+15
A= 1.8526E+14	K= 1.3165E+15
B= 2.2540E+14	L= 1.6018E+15
C= 2.7423E+14	M= 1.9172E+15
D= 3.3364E+14	N= 2.2847E+15
E= 4.0592E+14	O= 2.6847E+15
F= 4.9387E+14	P= 3.5096E+15
G= 6.0086E+14	Q= 4.2700E+15
H= 7.3104E+14	R= 5.1951E+15
I= 8.8942E+14	S= 6.3206E+15

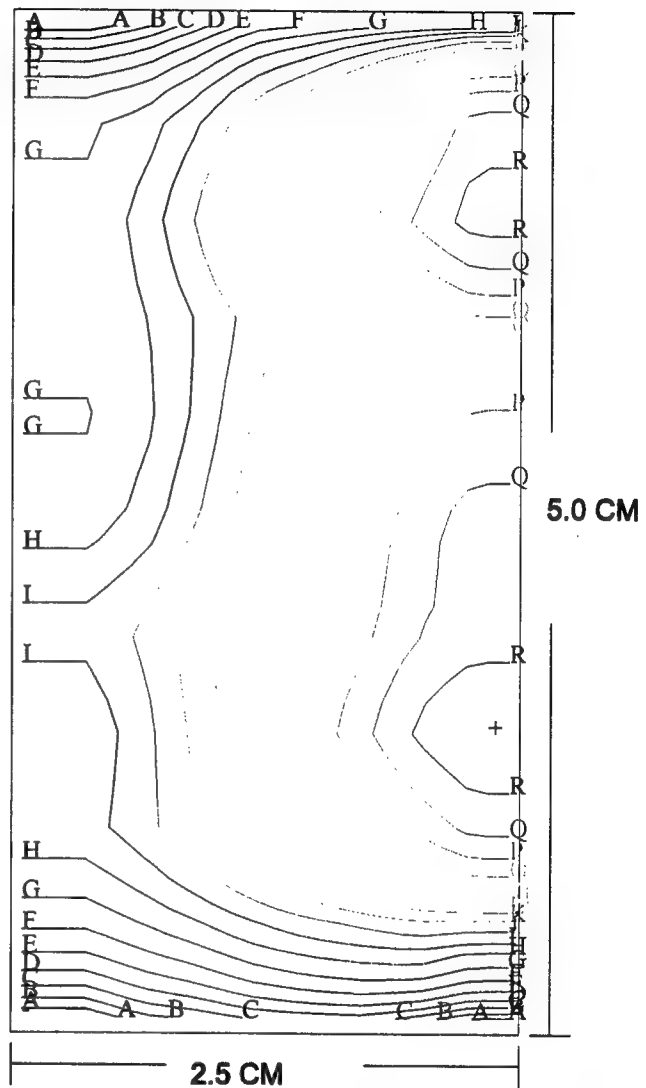


Figure 2-1. Observed electron number density at time close to that of initiation of pulsed power.



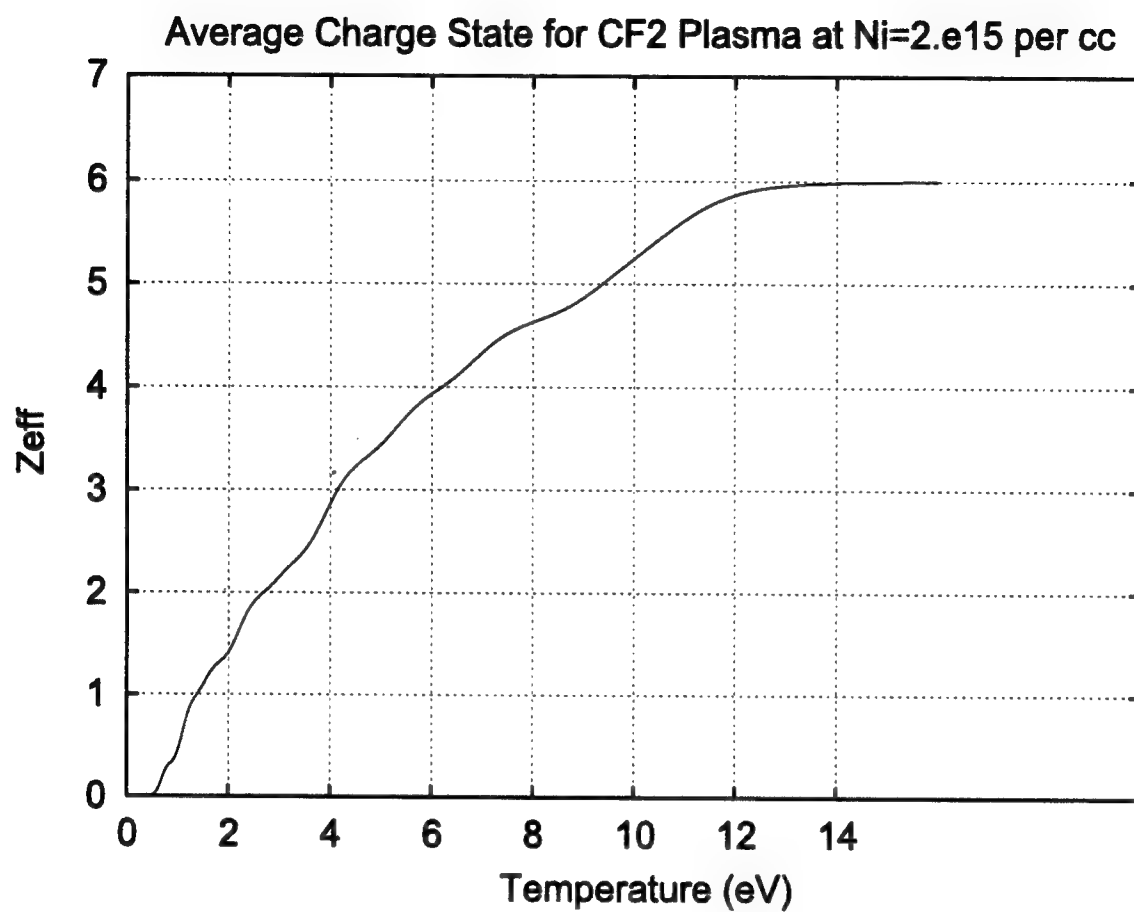


Figure 2-2. Mean degree of ionization versus temperature for a CF<sub>2</sub> plasma at an ion density of  $2 \times 10^{15} \text{ cm}^{-3}$ .

## ELECTRONS / CC

**G= 1.9980E+14,      += 6.1480E+15**

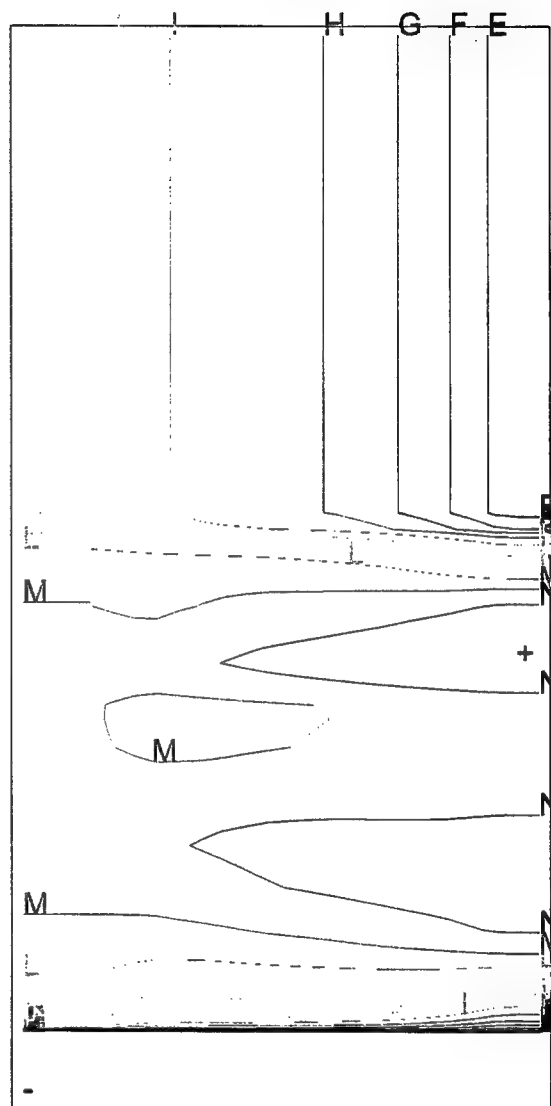


Figure 2-3. Measured electron density contour with guns only at 1  $\mu$ s before firing Marx.

HAWK-DRIVEN ||-PLATE: SEGMENTED INFLOW , 1 EV  
 PPHWK2 S3JW96J  
 T = 1.009E-06 CYCLE = 78  
 ELECTRONS / CC

-= 1.2913E+12	H= 2.2901E+14
A= 2.4668E+12	I= 4.3748E+14
B= 4.7123E+12	J= 5.3573E+14
C= 9.0019E+12	K= 5.5135E+14
D= 1.7196E+13	L= 3.0498E+15
E= 3.2851E+13	M= 5.8261E+15
F= 6.2755E+13	N= 1.1130E+16
G= 1.1988E+14	+= 2.1261E+16

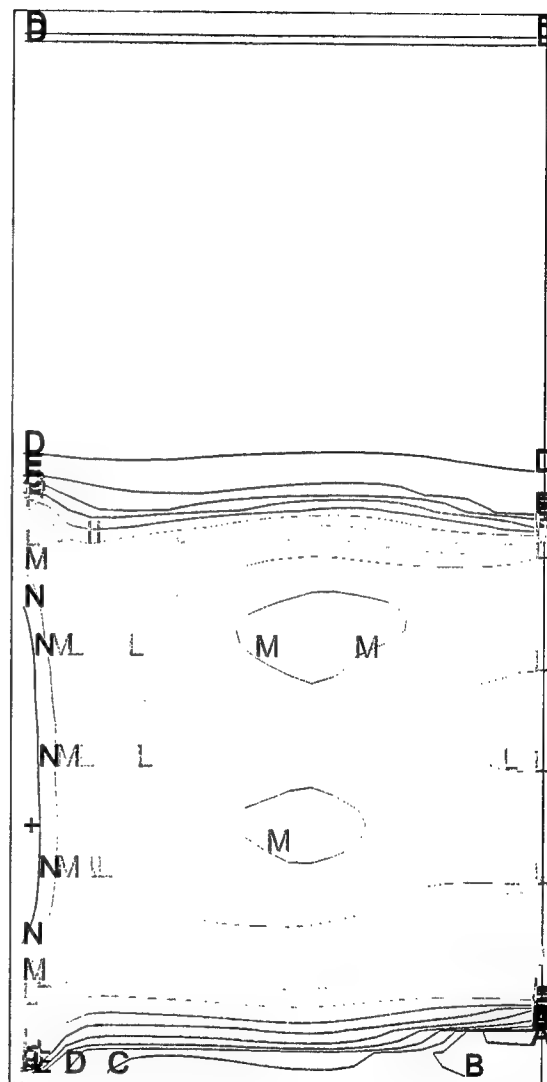


Figure 2-4. Simulated electron density contours (T=1 eV) with guns only at 1  $\mu$ s before firing Marx.

HAWK-DRIVEN ||-PLATE: SEGMENTED, 2 EV, RAMPED INFLOW  
 PPHWK3 S3JW96J  
 T = 1.012E-06 CYCLE = 84  
 ELECTRONS / CC

-= 8.9074E+11	H= 1.1680E+14
A= 1.6386E+12	I= 2.1487E+14
B= 3.0142E+12	J= 3.3513E+14
C= 5.5448E+12	K= 4.5262E+15
D= 1.0200E+13	L= 1.3375E+15
E= 1.8764E+13	M= 2.4605E+15
F= 3.4517E+13	N= 4.5262E+15
G= 6.3495E+13	+ = 8.3262E+15

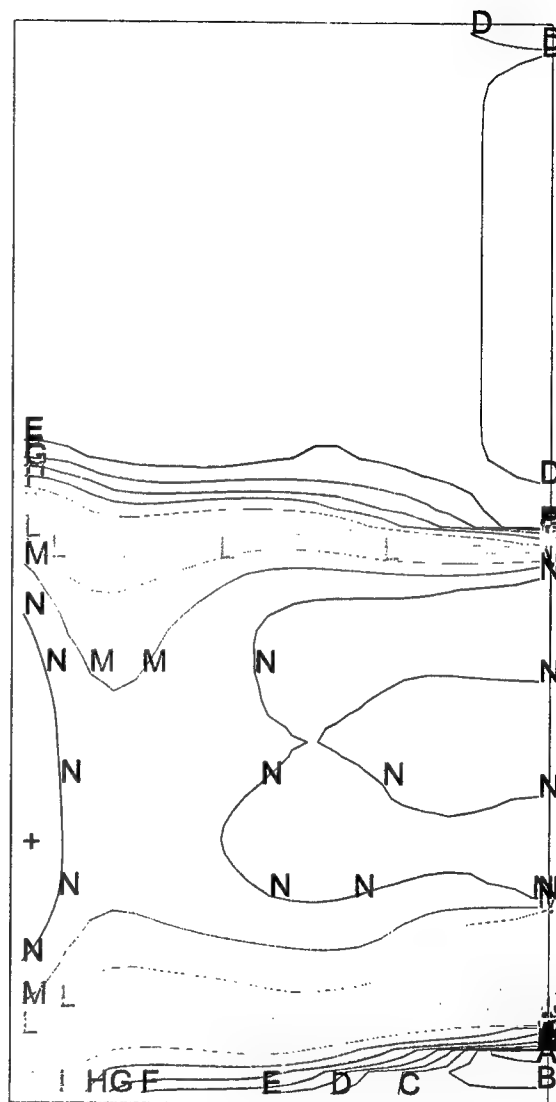


Figure 2-5. Simulated electron density contours (T = 2 ev) with guns only at 1  $\mu$ s before firing Marx.

# HAWK-DRIVEN PARALLEL PLATE: EXPERIMENTAL DATA

T = 500 ns  
ELECTRONS / CC

- = 9.9651E+12	H = 7.2955E+14
A = 1.7043E+13	I = 1.2478E+15
B = 2.9149E+13	J = 1.1347E+15
C = 4.9854E+13	K = 1.1177E+15
D = 8.5265E+13	L = 6.2423E+15
E = 1.4583E+14	M = 1.0676E+16
F = 2.4941E+14	N = 1.8259E+16
G = 4.2656E+14	+ = 3.1229E+16

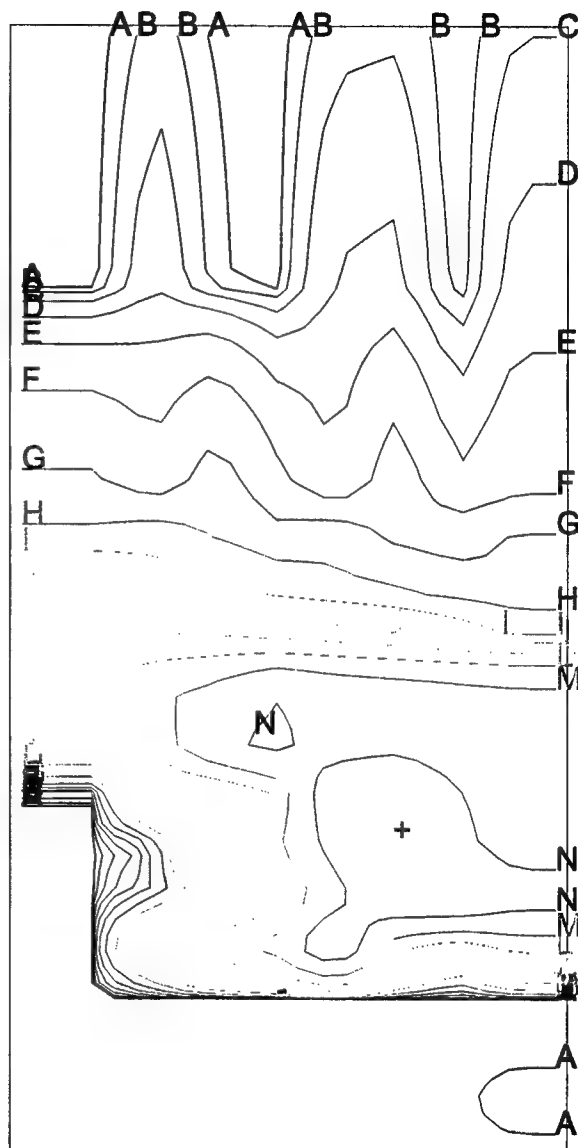


Figure 2-6. Measured electron density contours at 500 ns.

# HAWK-DRIVEN PARALLEL-PLATE: EXPERIMENTAL DATA

T = 550 ns  
ELECTRONS / CC

-= 9.9651E+12	H= 1.0950E+15
A= 1.7931E+13	I= 1.9702E+15
B= 3.2263E+13	J= 3.5450E+15
C= 5.8053E+13	K= 6.0112E+15
D= 1.0446E+14	L= 1.1478E+16
E= 1.8795E+14	M= 2.0652E+16
F= 3.3819E+14	N= 3.7160E+16
G= 6.0853E+14	+= 6.6864E+16

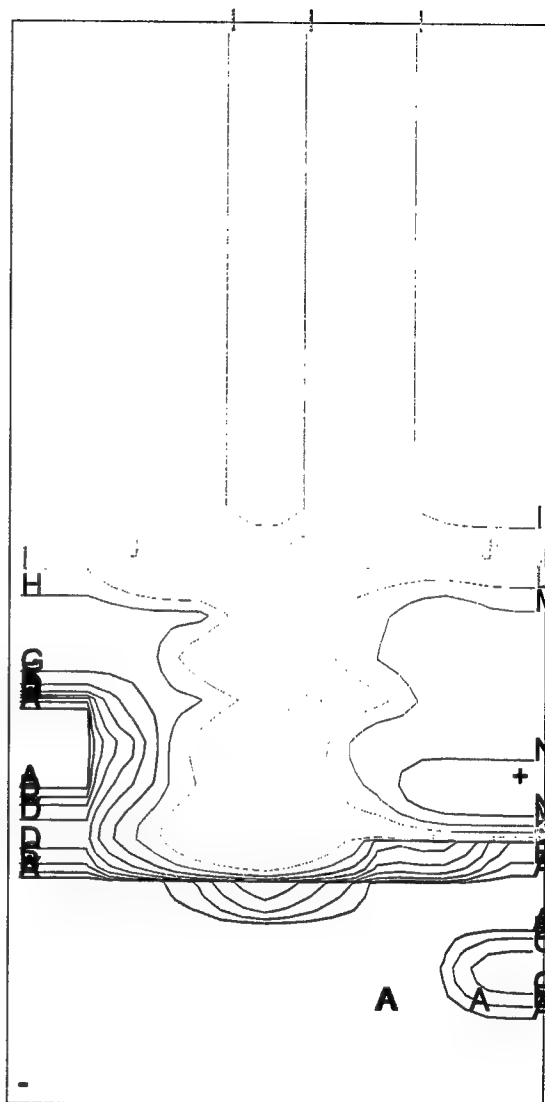


Figure 2-7. Measured electron density contours at 550 ns.

# HAWK-DRIVEN PARALLEL-PLATE: EXPERIMENTAL DATA

T = 575 ns  
ELECTRONS / CC

-= 9.9651E+12	H= 1.1260E+15
A= 1.7993E+13	I= 2.0331E+15
B= 3.2490E+13	J= 3.1771E+15
C= 5.8664E+13	K= 4.3211E+15
D= 1.0593E+14	L= 1.1969E+16
E= 1.9127E+14	M= 2.1611E+16
F= 3.4536E+14	N= 3.9022E+16
G= 6.2359E+14	= 7.0460E+16

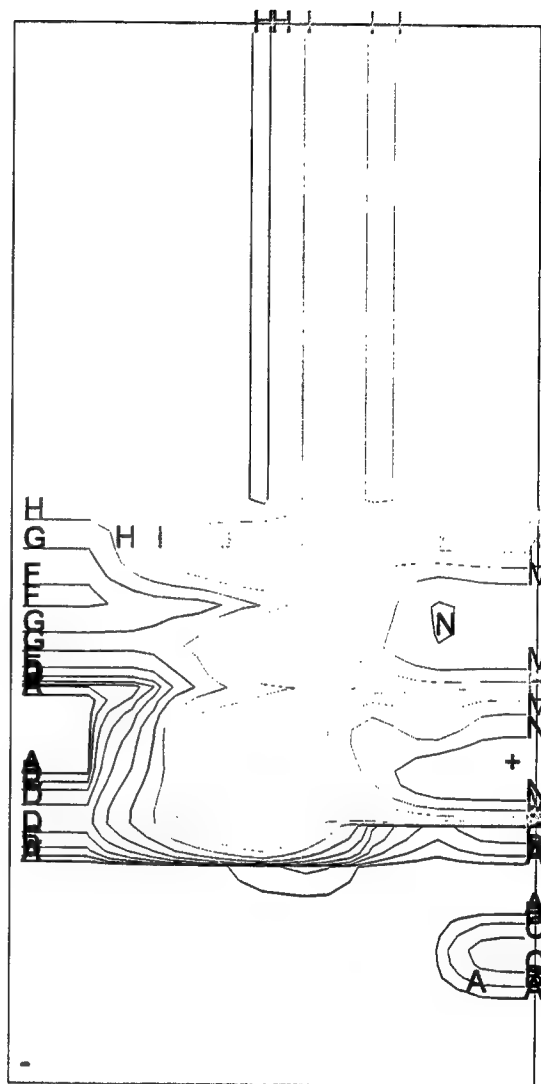


Figure 2-8. Measured electron density contours at 575 ns.

# HAWK-DRIVEN PARALLEL PLATE: EXPERIMENTAL DATA

T = 600 ns  
ELECTRONS / CC

- = 9.9651E+12	H = 9.7677E+14
A = 1.7677E+13	I = 1.7326E+15
B = 3.1355E+13	J = 3.0734E+15
C = 5.5619E+13	K = 5.5619E+15
D = 9.8659E+13	L = 9.6705E+15
E = 1.7501E+14	M = 1.7154E+16
F = 3.1043E+14	N = 3.0428E+16
G = 5.5065E+14	+ = 5.3975E+16

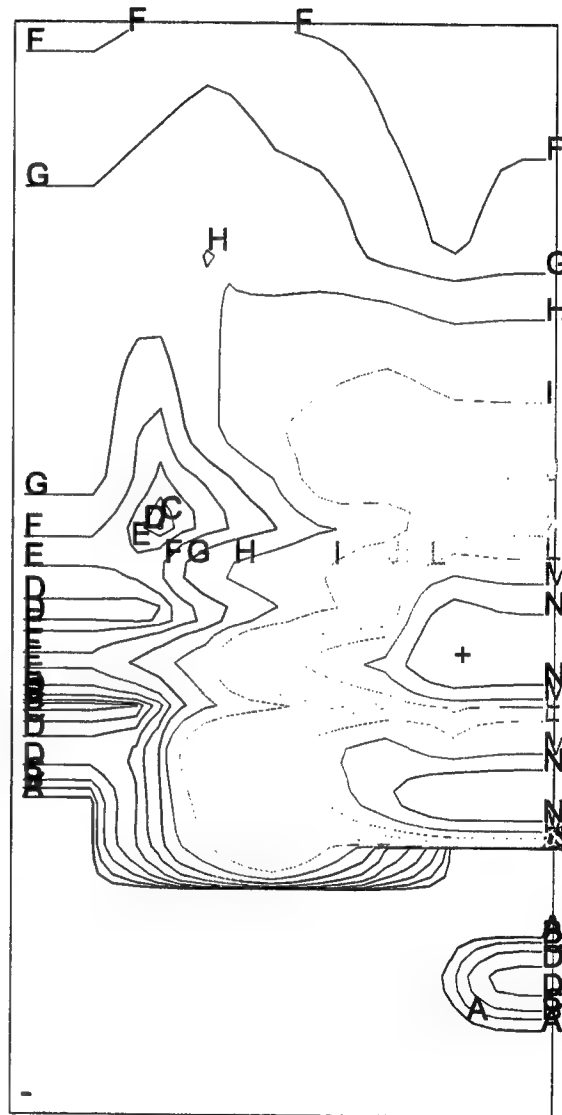


Figure 2-9. Measured electron density contours at 600 ns.



# HAWK-DRIVEN PARALLEL PLATE: EXPERIMENTAL DATA

T = 700 ns  
ELECTRONS / CC

H= 9.9651E+12	H= 8.4944E+14
A= 1.7371E+13	I= 1.4807E+15
B= 3.0279E+13	J= 2.5810E+15
C= 5.2781E+13	K= 3.6812E+15
D= 9.2004E+13	L= 7.8425E+15
E= 1.6038E+14	M= 1.3671E+16
F= 2.7956E+14	N= 2.3830E+16
G= 4.8730E+14	O= 4.1538E+16

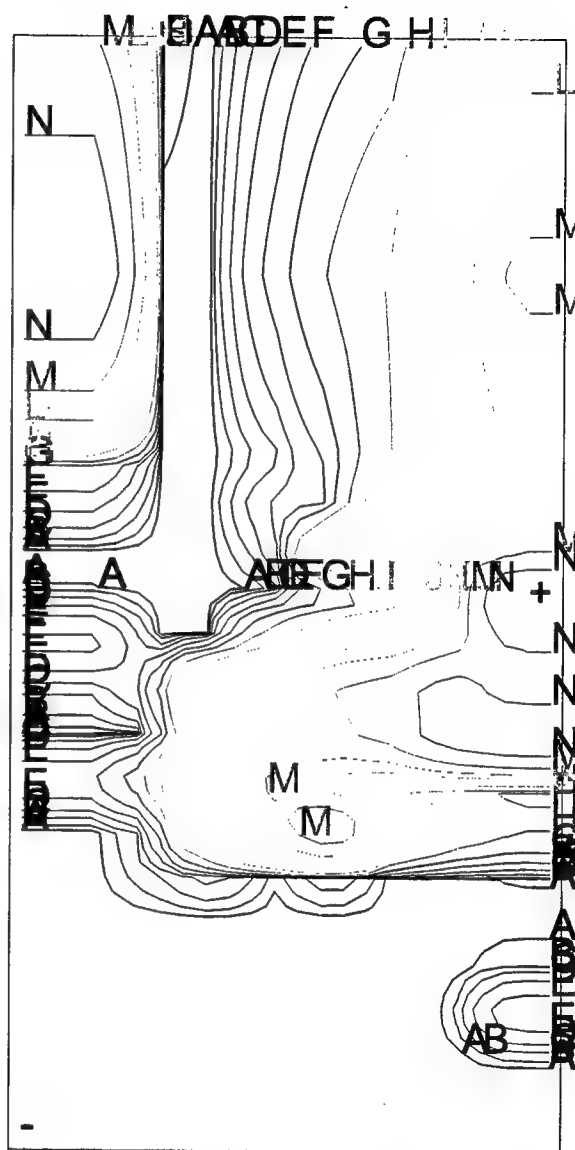
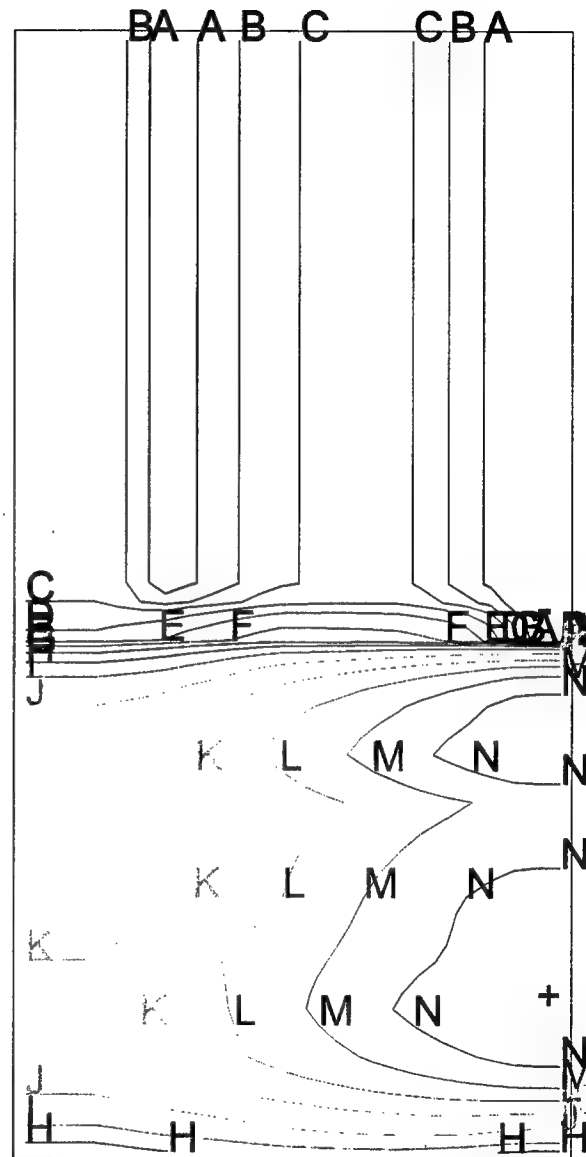


Figure 2-10. Measured electron density contours at 700 ns.

HAWK-DRIVEN ||-PLATE: IDEAL MHD  
 PPHALL2 S3JW96J  
 T = 0.000E+00 CYCLE = 0  
 ELECTRONS / CC

- = 4.9219E+12	H = 2.2371E+14
A = 7.9309E+12	I = 3.6048E+14
B = 1.2780E+13	J = 5.8086E+14
C = 2.0593E+13	K = 9.3597E+14
D = 3.3182E+13	L = 1.5082E+15
E = 5.3469E+13	M = 2.4303E+15
F = 8.6158E+13	N = 3.9160E+15
G = 1.3883E+14	+ = 6.3102E+15

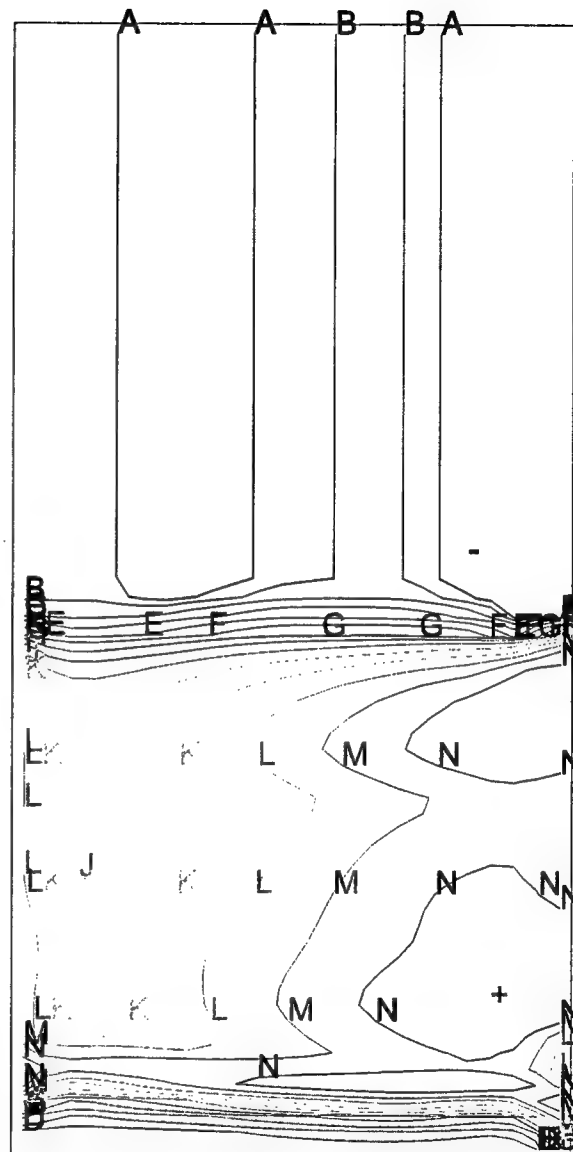


(a) T = 0 (Initial Electron Densities)

Figure 2-11. Mach2 ideal MHD (no Hall effect) simulation.

HAWK-DRIVEN ||-PLATE: IDEAL MHD  
 PPHALL2 S3JW96J  
 T = 2.015E-07 CYCLE = 54  
 ELECTRONS / CC

$- = 9.6830E+12$	$H = 3.0445E+14$
$A = 1.4900E+13$	$I = 4.6850E+14$
$B = 2.2929E+13$	$J = 7.2093E+14$
$C = 3.5284E+13$	$K = 1.1094E+15$
$D = 5.4296E+13$	$L = 1.7071E+15$
$E = 8.3551E+13$	$M = 2.6270E+15$
$F = 1.2857E+14$	$N = 4.0425E+15$
$G = 1.9785E+14$	$+ = 6.2207E+15$

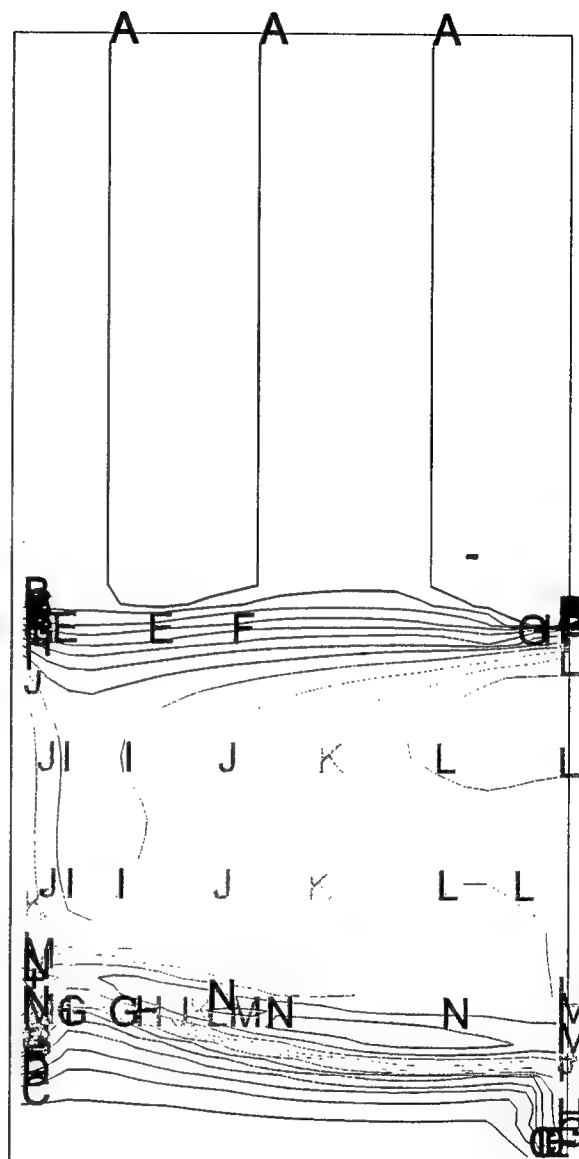


(b) T = 202 ns

Figure 2-11. Mach2 ideal MHD (no Hall effect) simulation (Continued).

HAWK-DRIVEN ||-PLATE: IDEAL MHD  
 PPHALL2 S3JW96J  
 T = 3.017E-07 CYCLE = 99  
 ELECTRONS / CC

- = 9.6830E+12	H = 5.7027E+14
A = 1.6116E+13	I = 9.4916E+14
B = 2.6824E+13	J = 1.5798E+15
C = 4.4646E+13	K = 2.6294E+15
D = 7.4310E+13	L = 4.3764E+15
E = 1.2368E+14	M = 7.2841E+15
F = 2.0586E+14	N = 1.2124E+16
G = 3.4263E+14	+ = 2.0179E+16

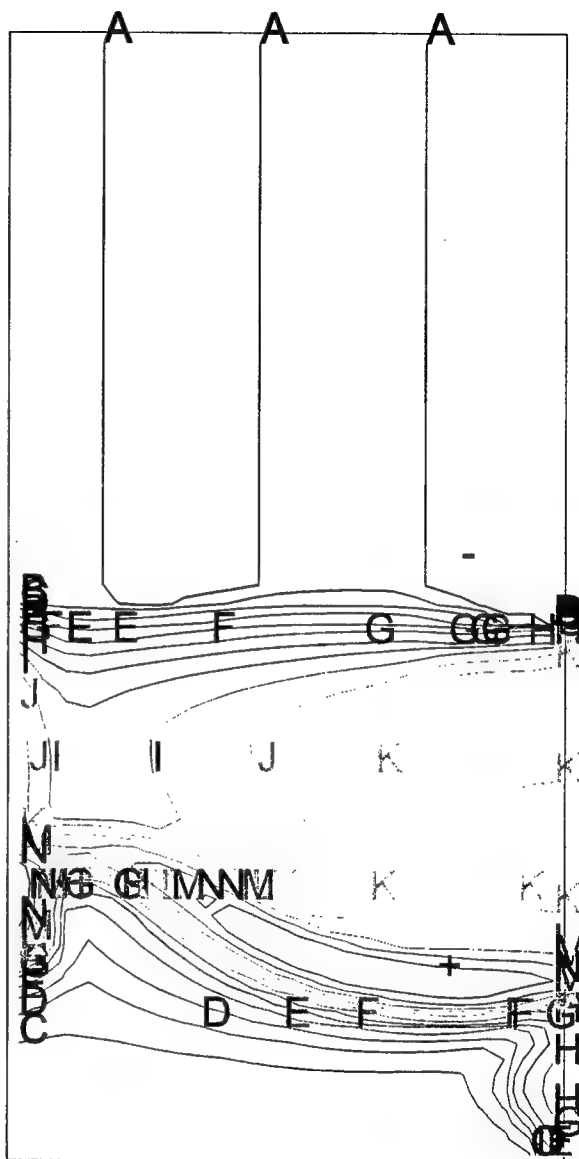


(c) T = 302 ns

Figure 2-11. Mach2 ideal MHD (no Hall effect) simulation (Continued).

HAWK-DRIVEN  $\parallel$ -PLATE: IDEAL MHD  
 PPHALL2 S3JW96J  
 T = 4.001E-07 CYCLE = 163  
 ELECTRONS / CC

$= 9.6830\text{E}+12$	H = 7.3789E+14
A = 1.6644E+13	I = 1.2683E+15
B = 2.8609E+13	J = 2.1801E+15
C = 4.9176E+13	K = 3.7474E+15
D = 8.4528E+13	L = 6.4414E+15
E = 1.4529E+14	M = 1.1072E+16
F = 2.4974E+14	N = 1.9032E+16
G = 4.2928E+14	+ = 3.2713E+16



(d) T = 400 ns

Figure 2-11. Mach2 ideal MHD (no Hall effect) simulation (Continued).

HAWK-DRIVEN ||-PLATE: IDEAL MHD  
 PPHALL2 S3JW96J  
 T = 5.002E-07 CYCLE = 257  
 ELECTRONS / CC

$- = 9.6830E+12$	$H = 9.9239E+14$
$A = 1.7272E+13$	$I = 1.7702E+15$
$B = 3.0809E+13$	$J = 3.1575E+15$
$C = 5.4956E+13$	$K = 5.6323E+15$
$D = 9.8027E+13$	$L = 1.0047E+16$
$E = 1.7486E+14$	$M = 1.7921E+16$
$F = 3.1190E+14$	$N = 3.1966E+16$
$G = 5.5635E+14$	$+ = 5.7019E+16$

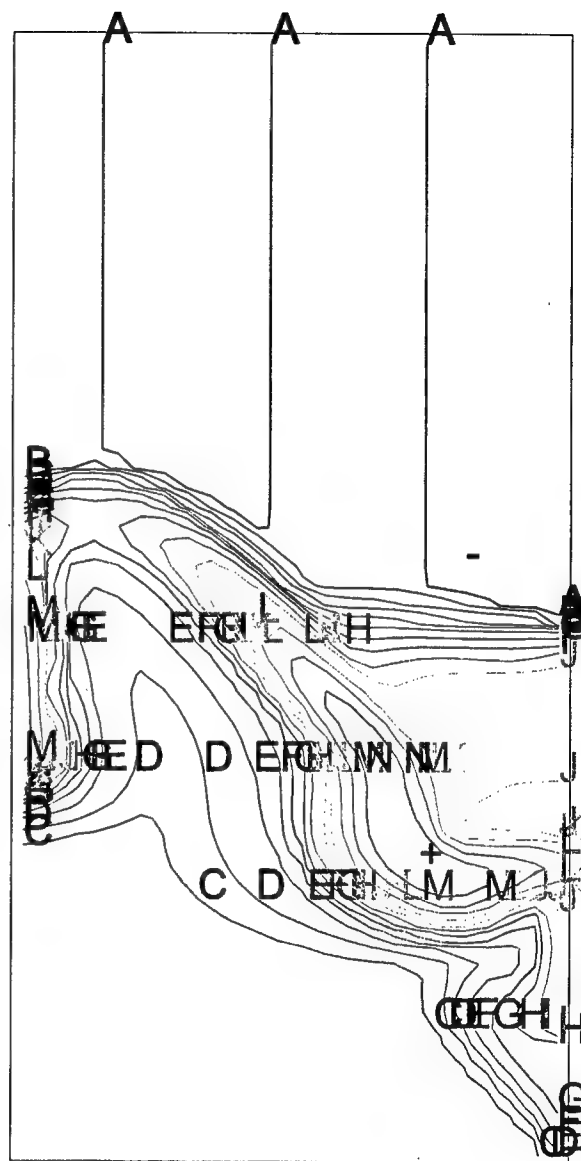


(e) T = 500 ns

Figure 2-11. Mach2 ideal MHD (no Hall effect) simulation (Continued).

HAWK-DRIVEN  $\parallel$ -PLATE: IDEAL MHD  
 PPHALL2 S3JW96J  
 T = 5.501E-07 CYCLE = 319  
 ELECTRONS / CC

$\rho = 9.6830\text{E}+12$	H = 1.1756E+15
A = 1.7642E+13	I = 2.1418E+15
B = 3.2142E+13	J = 3.9022E+15
C = 5.8560E+13	K = 7.1095E+15
D = 1.0669E+14	L = 1.2953E+16
E = 1.9438E+14	M = 2.3599E+16
F = 3.5415E+14	N = 4.2996E+16
G = 6.4524E+14	O = 7.8336E+16

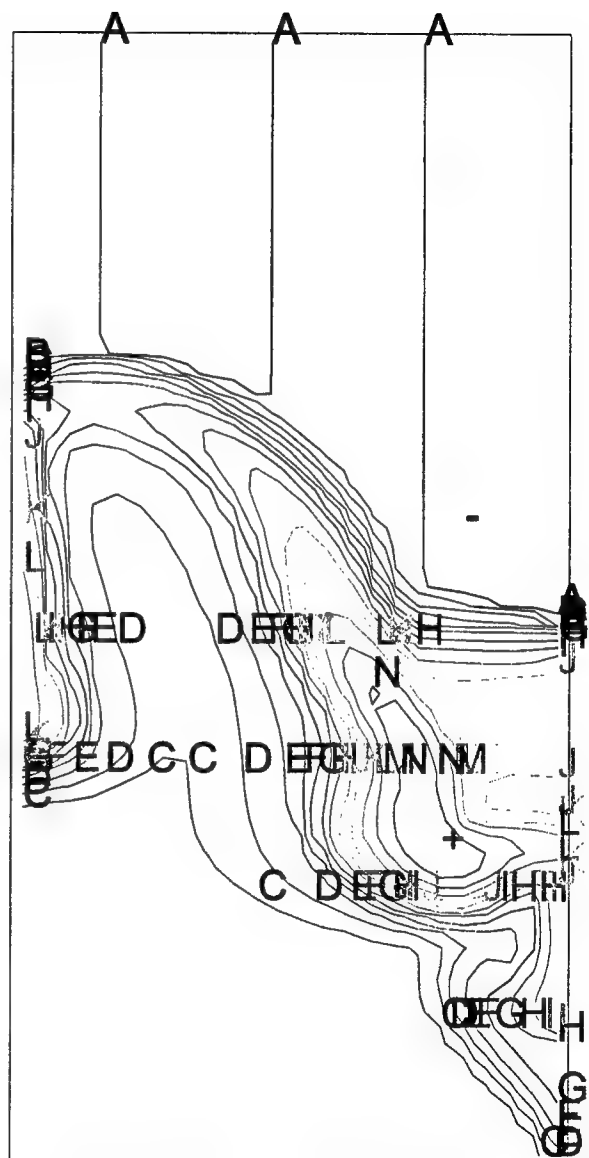


(f) T = 550 ns

Figure 2-11. Mach2 ideal MHD (no Hall effect) simulation (Continued).

HAWK-DRIVEN ||-PLATE: IDEAL MHD  
 PPHALL2 S3JW96J  
 T = 5.752E-07 CYCLE = 358  
 ELECTRONS / CC

$\rho = 9.6830\text{E}+12$	$H = 1.3250\text{E}+15$
$A = 1.7907\text{E}+13$	$I = 2.4503\text{E}+15$
$B = 3.3118\text{E}+13$	$J = 4.5316\text{E}+15$
$C = 6.1247\text{E}+13$	$K = 3.3806\text{E}+15$
$D = 1.1327\text{E}+14$	$L = 1.5499\text{E}+16$
$E = 2.0947\text{E}+14$	$M = 2.8663\text{E}+16$
$F = 3.8740\text{E}+14$	$N = 5.3009\text{E}+16$
$G = 7.1644\text{E}+14$	$\pm = 9.8033\text{E}+16$



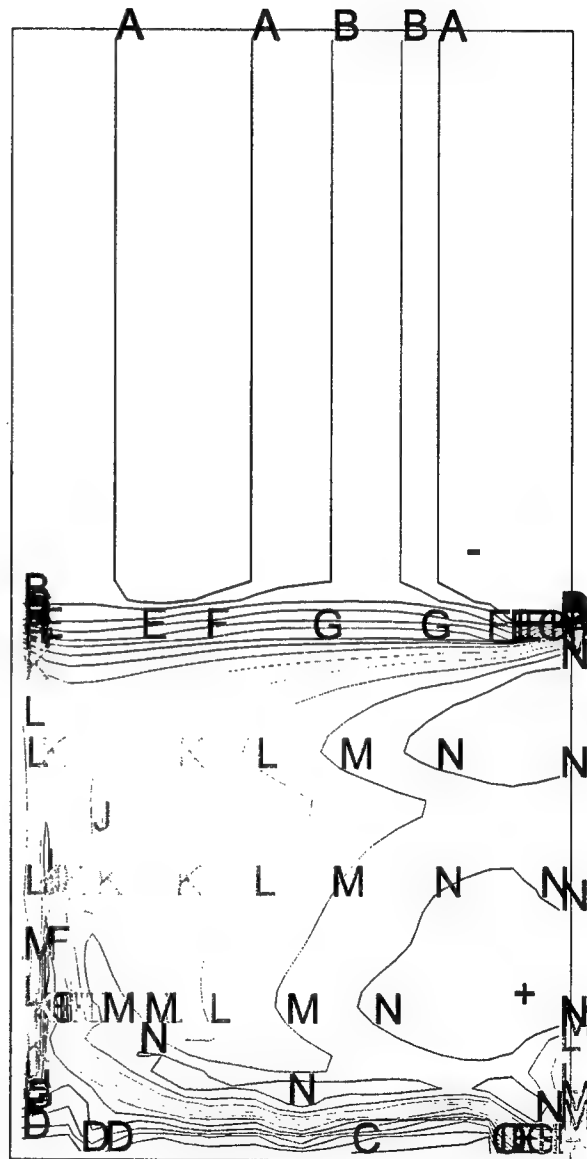
(g) T = 575 ns

Figure 2-11. Mach2 ideal MHD (no Hall effect) simulation (Continued).



## ELECTRONS / CC

<b>== 9.6830E+12</b>	<b>H= 3.0388E+14</b>
<b>A= 1.4897E+13</b>	<b>I= 4.6751E+14</b>
<b>B= 2.2918E+13</b>	<b>J= 7.1924E+14</b>
<b>C= 3.5259E+13</b>	<b>K= 1.1065E+15</b>
<b>D= 5.4245E+13</b>	<b>L= 1.7023E+15</b>
<b>E= 8.3453E+13</b>	<b>M= 2.6190E+15</b>
<b>F= 1.2839E+14</b>	<b>N= 4.0292E+15</b>
<b>G= 1.9752E+14</b>	<b>+= 6.1988E+15</b>

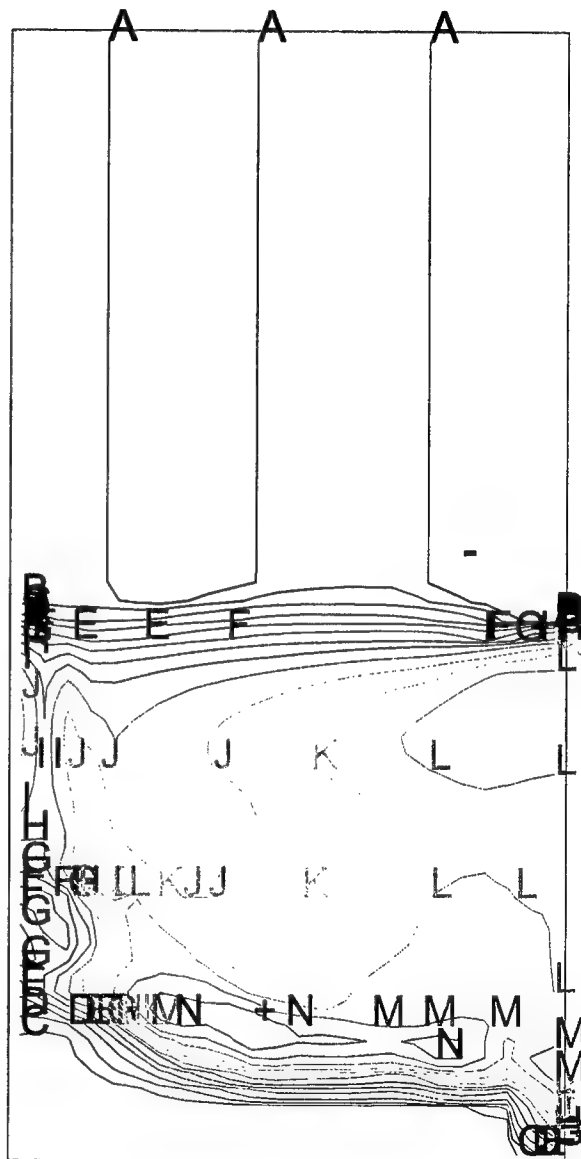


(a)  $T = 200 \text{ ns}$

**Figure 2-12. Mach2 Hall MHD simulation in positive polarity.**

HAWK-DRIVEN  $\parallel$ -PLATE: POSITIVE POLARITY WITH HALL  
 PPHALL1 S3JW96J  
 T = 3.000E-07 CYCLE = 19583  
 ELECTRONS / CC

-= 9.6830E+12	H= 5.6158E+14
A= 1.6086E+13	I= 9.3291E+14
B= 2.6722E+13	J= 1.5498E+15
C= 4.4390E+13	K= 2.5745E+15
D= 7.3742E+13	L= 4.2768E+15
E= 1.2250E+14	M= 7.1046E+15
F= 2.0350E+14	N= 1.1802E+16
G= 3.3806E+14	+ = 1.9606E+16

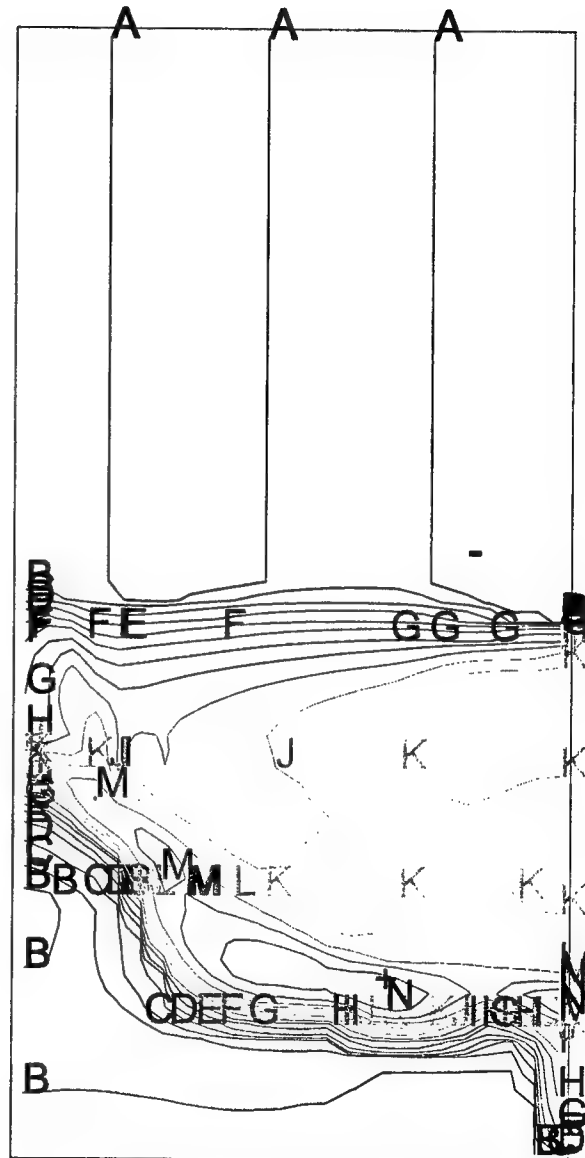


(b) T = 300 ns

Figure 2-12. Mach2 Hall MHD simulation in positive polarity (Continued).

HAWK-DRIVEN ||-PLATE: POSITIVE POLARITY WITH HALL  
 PPHALL1 S3JW96J  
 T = 4.000E-07 CYCLE = 30053  
 ELECTRONS / CC

-= 9.6830E+12	H= 7.7800E+14
A= 1.6755E+13	I= 1.3462E+15
B= 2.8990E+13	J= 2.3293E+15
C= 5.0162E+13	K= 4.0303E+15
D= 8.6795E+13	L= 6.9737E+15
E= 1.5018E+14	M= 1.2067E+16
F= 2.5986E+14	N= 2.0879E+16
G= 4.4963E+14	+ = 3.6126E+16



(c) T = 400 ns

Figure 2-12. Mach2 Hall MHD simulation in positive polarity (Continued).

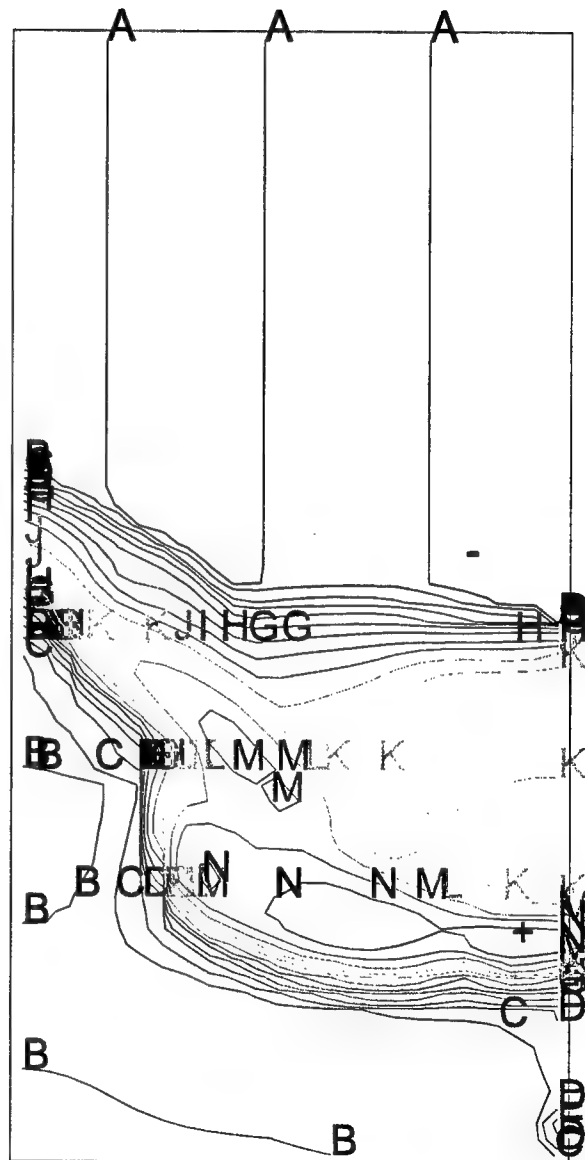
# HAWK-DRIVEN $\parallel$ -PLATE: POSITIVE POLARITY WITH HALL

PPHALL1 S3JW96J

T = 5.000E-07 CYCLE = 39163

ELECTRONS / CC

$- = 9.6830\text{E}+12$	H = $7.8648\text{E}+14$
A = $1.6777\text{E}+13$	I = $1.3627\text{E}+15$
B = $2.9069\text{E}+13$	J = $2.3611\text{E}+15$
C = $5.0366\text{E}+13$	K = $4.0909\text{E}+15$
D = $8.7267\text{E}+13$	L = $7.0881\text{E}+15$
E = $1.5120\text{E}+14$	M = $1.2281\text{E}+16$
F = $2.6198\text{E}+14$	N = $2.1279\text{E}+16$
G = $4.5392\text{E}+14$	+ = $3.6869\text{E}+16$

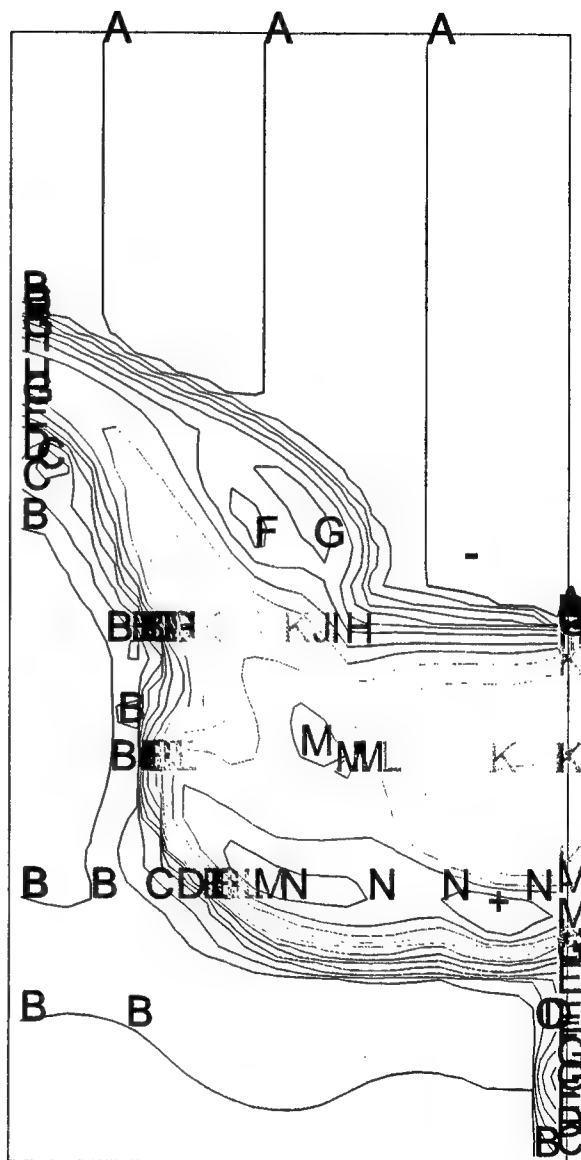


(d) T = 500 ns

Figure 2-12. Mach2 Hall MHD simulation in positive polarity (Continued).

HAWK-DRIVEN  $\parallel$ -PLATE: POSITIVE POLARITY WITH HALL  
 PPHALL1 S3JW96J  
 T = 5.500E-07 CYCLE = 42941  
 ELECTRONS / CC

$- = 9.6830\text{E}+12$	$H = 8.9308\text{E}+14$
$A = 1.7046\text{E}+13$	$I = 1.5722\text{E}+15$
$B = 3.0008\text{E}+13$	$J = 2.7676\text{E}+15$
$C = 5.2825\text{E}+13$	$K = 4.8721\text{E}+15$
$D = 9.2993\text{E}+13$	$L = 8.5768\text{E}+15$
$E = 1.6370\text{E}+14$	$M = 1.5099\text{E}+16$
$F = 2.8818\text{E}+14$	$N = 2.6579\text{E}+16$
$G = 5.0732\text{E}+14$	$+ = 4.6790\text{E}+16$

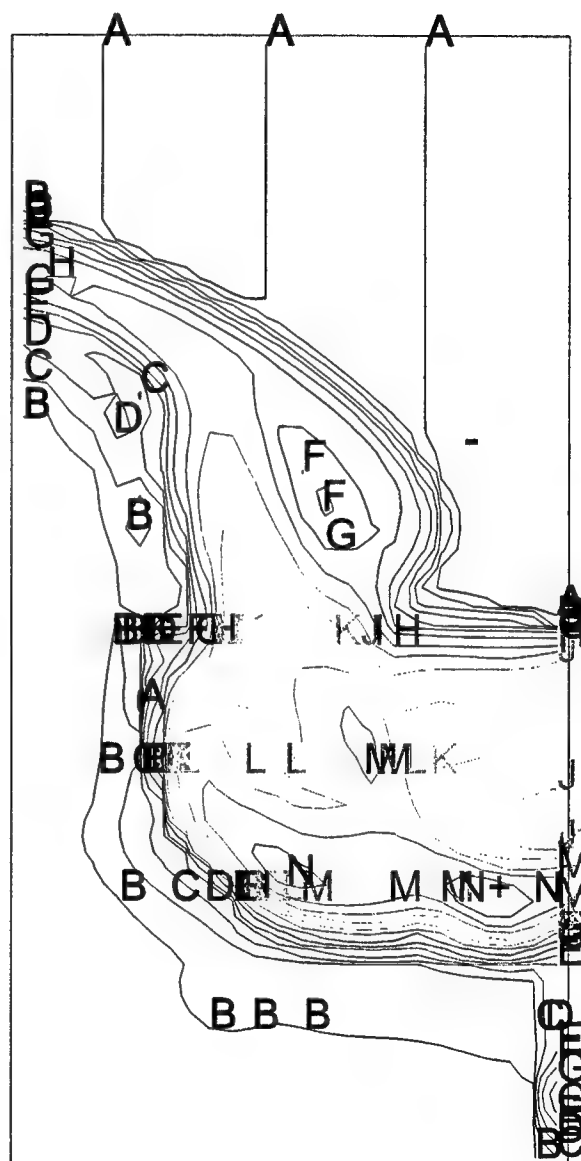


(e) T = 550 ns

Figure 2-12. Mach2 Hall MHD simulation in positive polarity (Continued).

HAWK-DRIVEN  $\parallel$ -PLATE: POSITIVE POLARITY WITH HALL  
 PPHALL1 S3JW96J  
 T = 5.750E-07 CYCLE = 46148  
 ELECTRONS / CC

$- = 9.6830\text{E}+12$	H = 1.0009E+15
A = 1.7291E+13	I = 1.7873E+15
B = 3.0875E+13	J = 3.1915E+15
C = 5.5132E+13	K = 5.6939E+15
D = 9.8447E+13	L = 1.0176E+16
E = 1.7579E+14	M = 1.8171E+16
F = 3.1391E+14	N = 3.2448E+16
G = 5.6053E+14	$+ = 5.7941\text{E}+16$

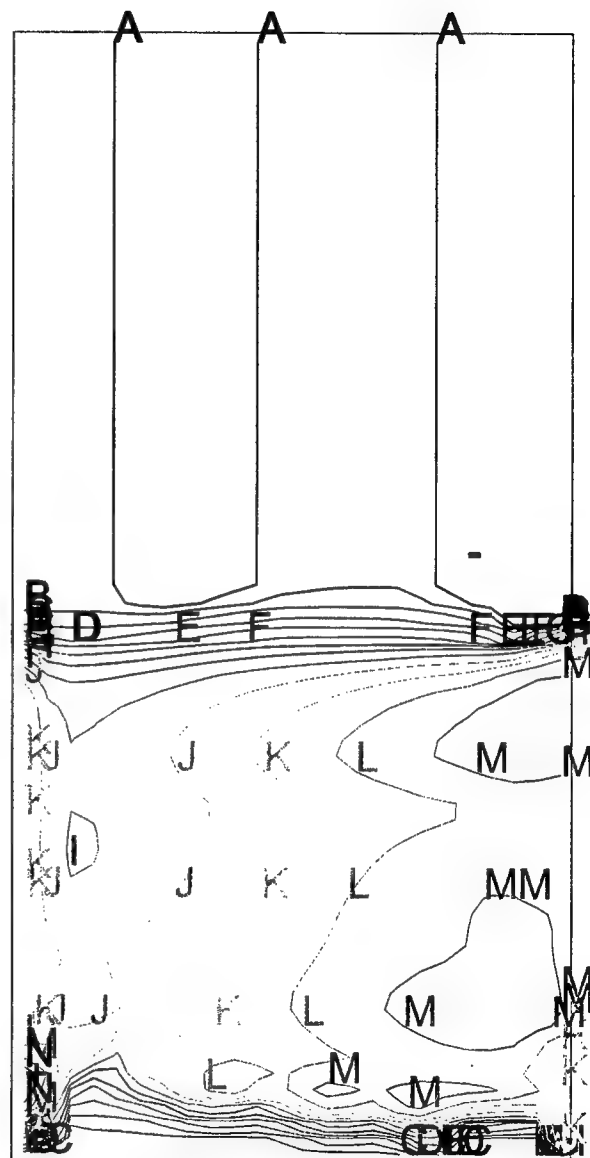


(f) T = 575 ns

Figure 2-12. Mach2 Hall MHD simulation in positive polarity (Continued).

HAWK-DRIVEN  $\parallel$ -PLATE: NEGATIVE POLARITY WITH HALL  
 PPHALL0 S3JW96J  
 T = 2.000E-07 CYCLE = 7886  
 ELECTRONS / CC

$- = 9.6830\text{E}+12$	H = $4.2631\text{E}+14$
A = $1.5541\text{E}+13$	I = $6.8421\text{E}+14$
B = $2.4942\text{E}+13$	J = $1.0981\text{E}+15$
C = $4.0032\text{E}+13$	K = $1.7625\text{E}+15$
D = $6.4249\text{E}+13$	L = $2.8287\text{E}+15$
E = $1.0312\text{E}+14$	M = $4.5399\text{E}+15$
F = $1.6550\text{E}+14$	N = $7.2863\text{E}+15$
G = $2.6562\text{E}+14$	$+ = 1.1694\text{E}+16$

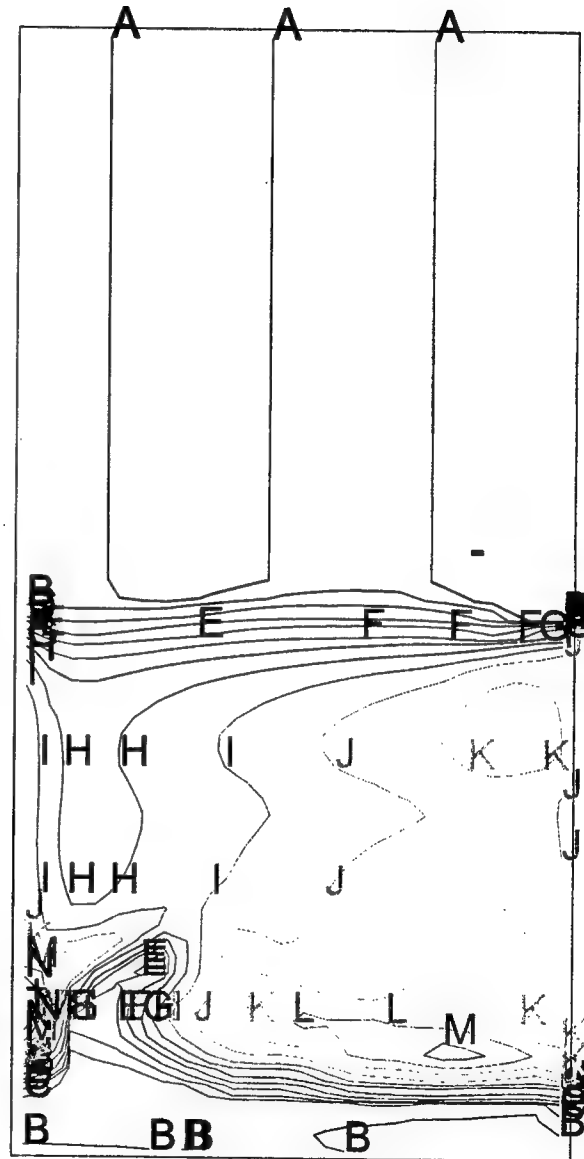


(a) T = 200 ns

Figure 2-13. Mach2 Hall MHD simulation in negative polarity.

HAWK-DRIVEN  $\parallel$ -PLATE: NEGATIVE POLARITY WITH HALL  
 PPHALLO S3JW96J  
 T = 3.000E-07 CYCLE = 14392  
 ELECTRONS / CC

$- = 9.6830\text{E}+12$	H = 9.0912E+14
A = 1.7084E+13	I = 1.6040E+15
B = 3.0141E+13	J = 2.8299E+15
C = 5.3179E+13	K = 4.9929E+15
D = 9.3825E+13	L = 8.8090E+15
E = 1.6554E+14	M = 1.5542E+16
F = 2.9206E+14	N = 2.7421E+16
G = 5.1528E+14	+ = 4.8379E+16



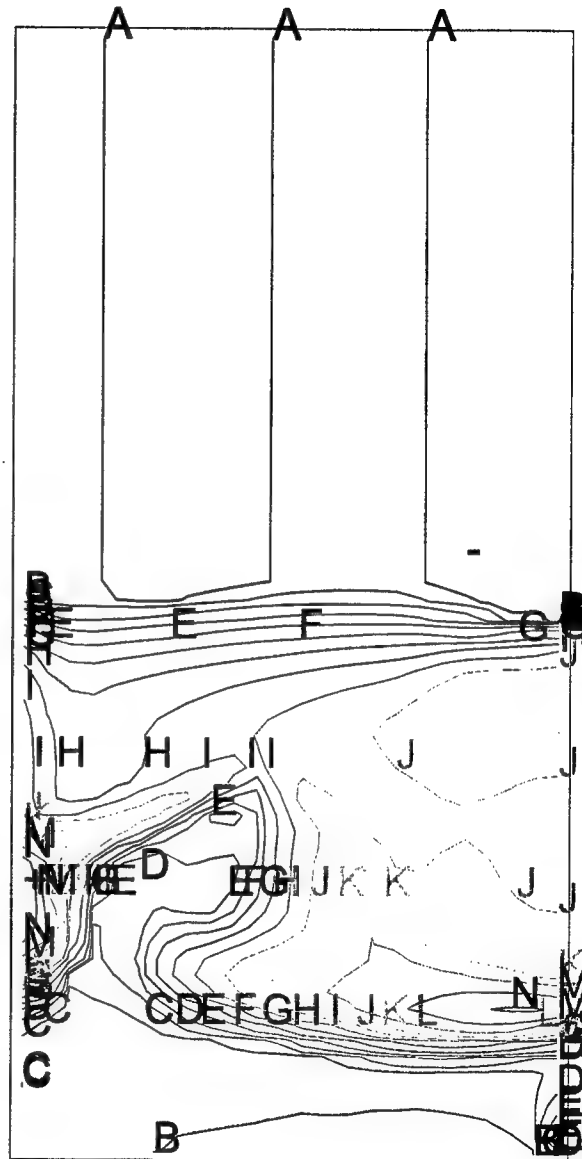
(b) T = 300 ns

Figure 2-13. Mach2 Hall MHD simulation in negative polarity (Continued).



HAWK-DRIVEN  $\parallel$ -PLATE: NEGATIVE POLARITY WITH HALL  
 PPHALLO S3JW96J  
 T = 4.000E-07 CYCLE = 22363  
 ELECTRONS / CC

$\rho = 9.6830\text{E}+12$	H = 1.1963E+15
A = 1.7680E+13	I = 2.1844E+15
B = 3.2283E+13	J = 3.9885E+15
C = 5.8945E+13	K = 7.2826E+15
D = 1.0763E+14	L = 1.3297E+16
E = 1.9652E+14	M = 2.4280E+16
F = 3.5883E+14	N = 4.4333E+16
G = 6.5519E+14	$\pm = 8.0947\text{E}+16$

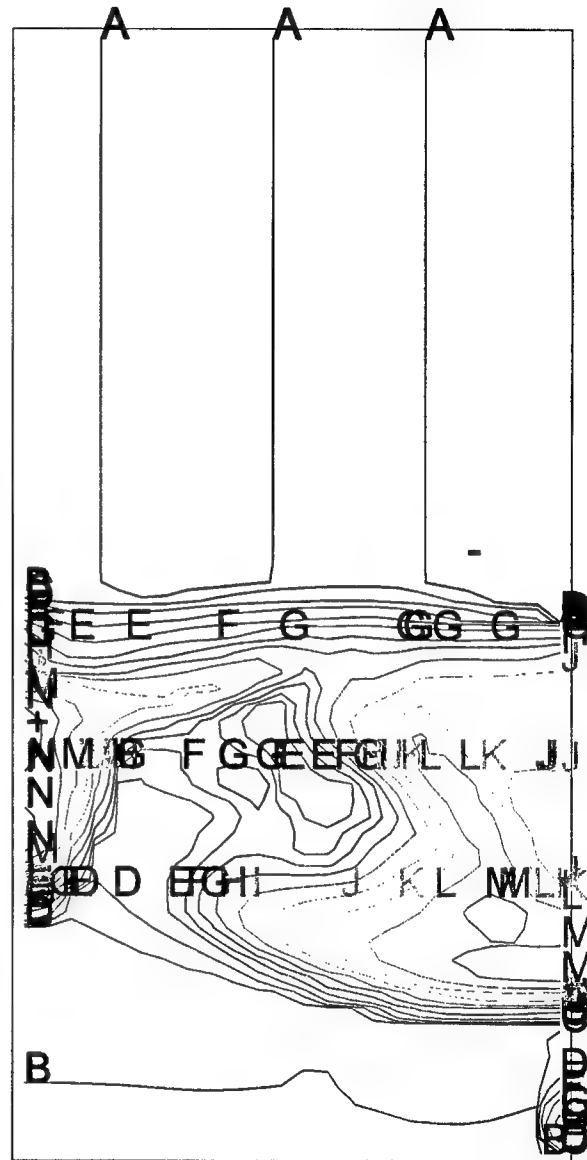


(c) T = 400 ns

Figure 2-13. Mach2 Hall MHD simulation in negative polarity (Continued).

HAWK-DRIVEN ||-PLATE: NEGATIVE POLARITY WITH HALL  
 PPHALLO S3JW96J  
 T = 5.000E-07 CYCLE = 33475  
 ELECTRONS / CC

- = 9.6830E+12	H = 1.3553E+15
A = 1.7958E+13	I = 2.5136E+15
B = 3.3306E+13	J = 4.6618E+15
C = 6.1769E+13	K = 8.6458E+15
D = 1.1456E+14	L = 1.6035E+16
E = 2.1246E+14	M = 2.9738E+16
F = 3.9404E+14	N = 5.5153E+16
G = 7.3079E+14	+ = 1.0229E+17

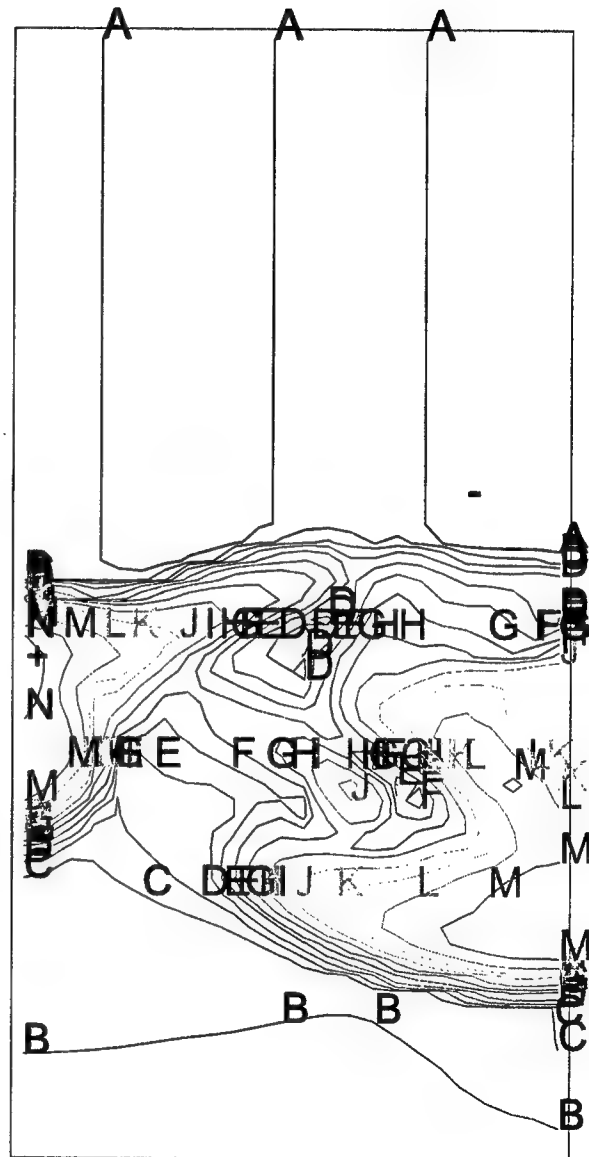


(d) T = 500 ns

Figure 2-13. Mach2 Hall MHD simulation in negative polarity (Continued).

HAWK-DRIVEN  $\parallel$ -PLATE: NEGATIVE POLARITY WITH HALL  
 PPHALLO S3JW96J  
 T = 5.500E-07 CYCLE = 38813  
 ELECTRONS / CC

$- = 9.6830\text{E}+12$	H = $1.3398\text{E}+15$
A = $1.7932\text{E}+13$	I = $2.4813\text{E}+15$
B = $3.3210\text{E}+13$	J = $4.5953\text{E}+15$
C = $6.1504\text{E}+13$	K = $8.5102\text{E}+15$
D = $1.1390\text{E}+14$	L = $1.5761\text{E}+16$
E = $2.1094\text{E}+14$	M = $2.9188\text{E}+16$
F = $3.9065\text{E}+14$	N = $5.4054\text{E}+16$
G = $7.2347\text{E}+14$	$+ = 1.0011\text{E}+17$

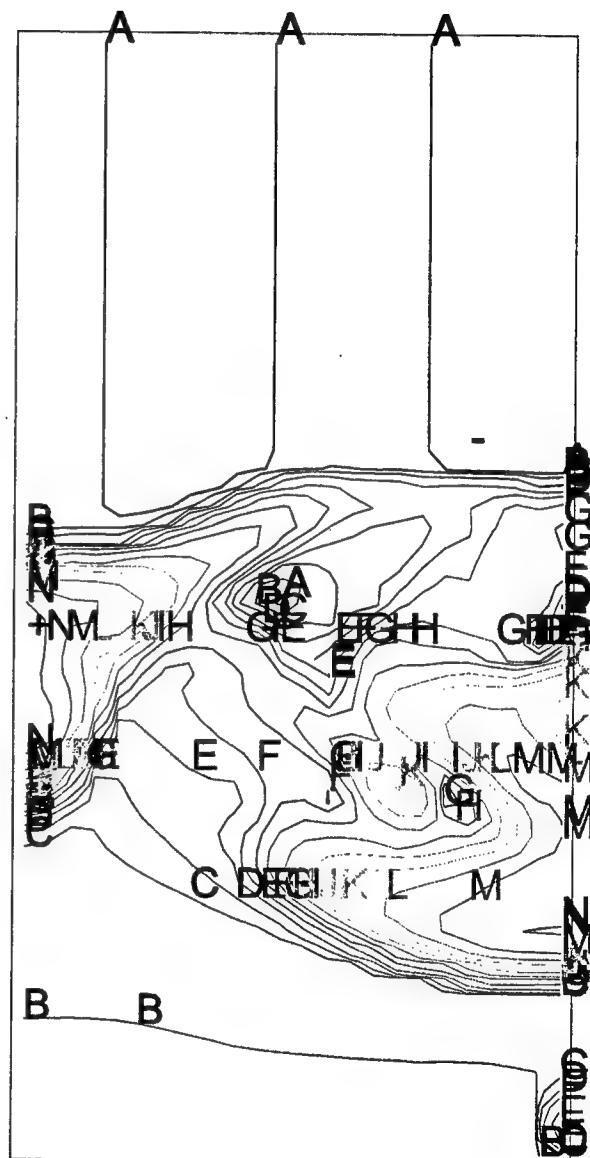


(e) T = 550 ns

Figure 2-13. Mach2 Hall MHD simulation in negative polarity (Continued).

HAWK-DRIVEN  $\parallel$ -PLATE: NEGATIVE POLARITY WITH HALL  
 PPHALLO S3JW96J  
 T = 5.750E-07 CYCLE = 42442  
 ELECTRONS / CC

$\approx 9.6830\text{E}+12$	H= 1.2526E+15
A= 1.7782E+13	I= 2.3002E+15
B= 3.2656E+13	J= 4.2242E+15
C= 5.9970E+13	K= 7.7575E+15
D= 1.1013E+14	L= 1.4246E+16
E= 2.0225E+14	M= 2.6162E+16
F= 3.7141E+14	N= 4.8044E+16
G= 6.8206E+14	$\approx 8.8230\text{E}+16$

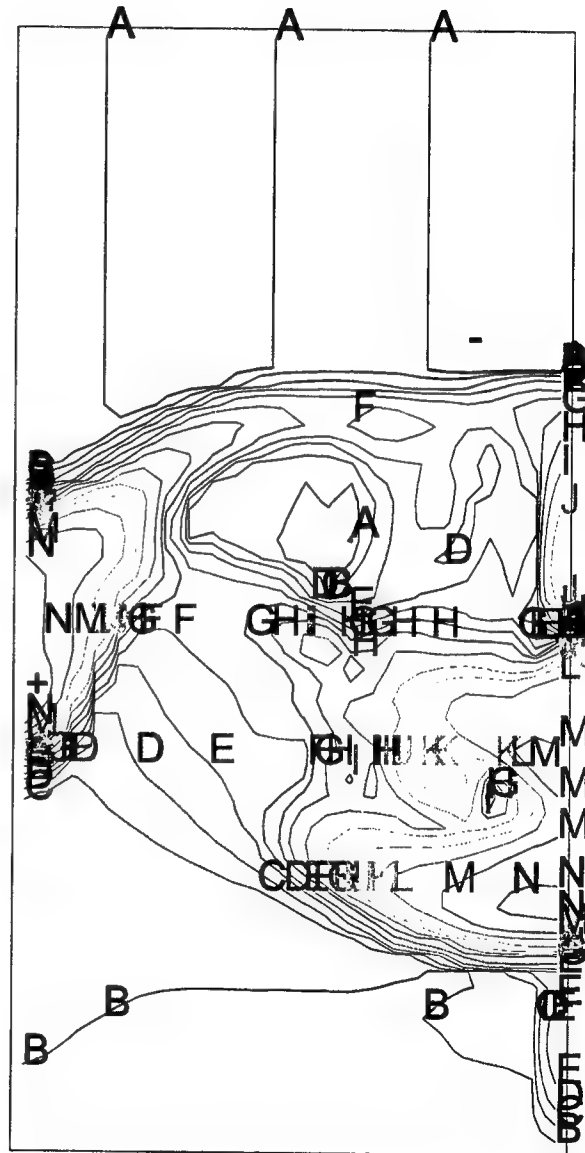


(f) T = 575 ns

Figure 2-13. Mach2 Hall MHD simulation in negative polarity (Continued).

HAWK-DRIVEN  $\parallel$ -PLATE: NEGATIVE POLARITY WITH HALL  
 PPHALL0 S3JW96J  
 T = 6.000E-07 CYCLE = 47802  
 ELECTRONS / CC

-= 9.6830E+12	H= 1.2177E+15
A= 1.7719E+13	I= 2.2283E+15
B= 3.2426E+13	J= 4.0777E+15
C= 5.9338E+13	K= 7.4619E+15
D= 1.0859E+14	L= 1.3655E+16
E= 1.9871E+14	M= 2.4988E+16
F= 3.6362E+14	N= 4.5727E+16
G= 6.6541E+14	+ = 8.3678E+16



(g) T = 600 ns

Figure 2-13. Mach2 Hall MHD simulation in negative polarity (Continued).

### SECTION 3

#### FLASHBOARD PLASMA INTERACTION WITH ANODE VANES

An important feature of the ACE 4 experimental configuration is the means by which the flashboard plasma enters the AK gap. The flashboards are positioned so that the plasma which they produce flows directly toward the outer surface of the anode. In the region of the switch, the anode has an open structure which allows the flashboard plasma to flow into the AK gap. But this flow is not completely unimpeded by the anode, for while the anode is mostly open, there is structure. Three different types of structure have been used in experiments: anode rods, anode vanes, and a mesh. In all three cases, this open structure replaces a section of otherwise solid cylindrical anode material. The rods are circular; various radii have been used as well as various rod-to-rod spacings. The vanes have a rectangular cross-section and are oriented to present their narrowest side to the incoming plasma. The mesh is a structure with thickness of half a centimeter having square holes three quarters of a centimeter on a side with hole-to-hole spacing of a quarter of an inch in both directions. The mesh will be discussed under the section pertaining to shot 1727. Here, the focus will be on the rods and the vanes.

The interaction of the flashboard plasma with the open anode structure would be relatively simple were it not for the fact that the flashboard plasma carries magnetic field. As discussed in the 1995 Annual Report (Reference 6), free space flashboard measurements made by John Thompson indicate that the plasma carries magnetic field of appreciable strength for several tens of centimeters away from the flashboard surface. This shows that the flowing flashboard plasma has a relatively high electrical conductivity. The magnetic field embedded in the plasma will then, to some degree, impede the progress of the plasma as it attempts to flow through the gaps between the anode rods or vanes. The ability of the embedded magnetic field to impede the plasma flow depends on the electrical resistivity of the plasma, the magnetic pressure relative to the plasma pressure, or probably more importantly, the ram pressure, and the length and time scales.

If the Spitzer model is assumed for the electrical resistivity, and if a temperature and density of 2 eV and  $10^{16}$  per cc are assumed, the numerical value for the resistivity is  $2.22 \times 10^{-4} \Omega\text{-m}$ . The electrical diffusivity ( $\eta/\mu_0$ ) is then  $176 \text{ m}^2/\text{s}$ . Assuming a length scale of 2 cm then gives a resistive timescale of 2.3  $\mu\text{s}$ . This is comparable to the observed hydrodynamic timescale and thus suggests that the plasma will not readily flow across magnetic field lines due to resistive

effects. If peak values are used to estimate and compare ram pressure and magnetic pressure, one obtains:

$$\begin{aligned} p_{\text{ram}} &= (1/2) \rho v^2 \\ &= (1/2) (2.8 \times 10^{-4} \text{ kg/m}^3) (8 \times 10^{-4} \text{ m/s})^2 = 8.9 \times 10^{-5} \text{ J/m}^3 \end{aligned} \quad (3.1)$$

and for B = 0.4 T

$$\begin{aligned} p_{\text{mag}} &= B^2/(2 \mu_0) \\ &= 6.4 \times 10^{-4} \text{ J/m}^3. \end{aligned} \quad (3.2)$$

This suggests that the plasma will have little trouble in overwhelming the force of the embedded magnetic field and thus flow wherever it would in the absence of an embedded magnetic field. This, however, overlooks a number of important features of the flow. First, the leading edge of the plasma flow is not well represented by these peak values. One could imagine that the lower density leading edge will be much more dominated by magnetic pressure effects than this simple calculation would suggest. In that case, the anode structure could act as a flux excluder, preventing magnetic field and thus plasma from entering very far into the AK gap. As the flow continues and the density builds, the plasma pressure, ram as well as kinetic, could then begin to overpower the magnetic pressure and begin to push its way into the AK gap. The difficulty is that these back-of-the-envelope calculations, for this particular case, leave one in a gray area where no one effect overwhelms all others. Thus, detailed MHD calculations are in order.

The starting point for such calculations is the flashboard model reported on in the 1995 Annual Report (Reference 6). This model resulted from attempts to reproduce the electron number density and magnetic field measurements taken by John Thompson in his free-space flashboard experiments. Another essential ingredient is the geometry of the anode structure. Figure 3-1 shows the mesh used to simulate the case of circular rods, Figure 3-2 shows the mesh used to simulate the case of rectangular vanes. The plots show that two rods or vanes, as the case may be, were used in the simulations. This was done because earlier simulations using just one rod were found to be too strongly influenced by interactions with the boundary. As it turns out, the two-rod simulations were also strongly influenced by boundary conditions, and in a manner which might not be an accurate depiction of reality. But this point will be reserved for later discussion.

The principal purpose for this study was to learn the effect of the shape and spacing of the anode rods and vanes on the distribution of plasma in the AK gap. Figures 3-3 and 3-4 show that the plasma distribution is affected by such details. Both figures show electron number density histories at various positions in the AK gap as measured by interferometry. The interferometric lines-of-sight were positioned on a common radius located azimuthally midway between two vanes. The lines-of-sight measure electron line density at various radial locations between the cathode and the innermost point of the anode vanes. The vanes result in electron number densities which are a half to a third that which result when circular rods are used, and result in a time-behavior more slowly paced than that seen with the circular rods. Following the prevailing convention, the lines-of-sight are numbered from innermost to outermost.

Figure 3-3 shows another feature which simulations might be able to explain. If one examines the individual curves carefully, and compares the curves labeled LOS 9, LOS 8, and LOS 7 to each other, one will see that, at least up until the time  $t=500$  shakes (1 shake = 10 ns), these three curves are similar to one another. In fact, they appear to be related to one another via a single parameter mapping. Similarly, the curves labeled LOS 1, LOS 2, and LOS 3 also appear to be similar to each other, though quite different from the curves LOS 9, LOS 8, and LOS 7. The curves appear to be separated into two distinct families according to whether they are near the cathode or near the outer edge of the AK gap. Were this apparent separation to be unique to a single shot, it would not warrant much attention, but it appears to be a feature shared by a large number of shots. The details of the two curve-families are not always the same, but this separation into two distinct families can be seen over and over again. Two other examples are included in Figures 3-5 and 3-6.

A one-dimensional explanation for the development of two distinct families of curves can be imagined. One would ascribe the family of curves corresponding to the outermost lines-of-sight to the inflowing plasma, and to the innermost lines-of-sight, the development and outward motion of a body of plasma stagnated against the cathode. Various effects, such as an embedded magnetic field, thermal conductivity, and radiative cooling, just to mention a few, could be at play to make such a one-dimensional scenario possible. However, the two-dimensional simulations done in this study provide an alternative explanation, at least in a qualitative sense; quantitative agreement has proven elusive.

Figure 3-7 shows electron number density contour plots from the circular rod simulation at times  $t=2501$  ns and  $t=3501$  ns. Figure 3-8 shows a zoom-in of plasma velocity vectors from the lower left-hand corner of the simulation domain during this time. These plots help to show that



a prominent feature of the flow is the development of a high-density region along the side boundaries of the simulation domain. These jets develop as plasma from the flashboard impinges on the boundary. The boundary condition is that which is appropriate for a wall, so plasma accumulates along the wall, and its velocity becomes parallel to the wall. This is not an entirely nonphysical result. The underlying reality would have plasma from neighboring flashboards converging. There are certainly questions concerning the details of how this confluence would behave, and some aspects of that will be discussed below. But the consequence of the development of these jets is that plasma flows into the AK gap in two entirely distinct manners. The first is from these high momentum jets. The second is from the plasma which has flowed in a straight-line from the flashboards. This direct flow involves a much stronger interaction of the embedded magnetic field with the anode rods than does the jet flow since the jets have much higher ram pressure and are thus able to push the magnetic field on past the rods. Figure 3-9 shows the magnetic field at time  $t=3001$  ns. Figure 3-10 shows a blow-up of this from the lower left-hand corner of the simulation domain. These magnetic field plots show that the embedded magnetic field does indeed interact strongly with the anode rods, piling up behind them and impeding the direct portion of the flow. The anode rods act somewhat like flux-excluders, and since the plasma is fairly conductive, like plasma-excluders, as well.

A result of the division of the plasma flow into two distinct parts is that the simulated interferometric signals fall into two distinct categories of behavior. As in the experimental configuration, the simulated interferometric lines-of-sight are placed on a radius midway between two rods and at varying distances from the cathode. Figure 3-11 shows the simulated interferometric line-of-sight signals. The lines-of-sight nearest the cathode (innermost lines-of-sight) peak earlier than the outermost lines-of-sight, then dip down while the signals from the outermost lines-of-sight are on the increase, then rapidly increase to very high levels just as the outermost lines-of-sight are in a decreasing phase. This simulation should be compared with shot 1317 (Figure 3-6) as both the geometry and model of the flashboard are appropriate for that particular experimental set-up. The comparison indicates that the simulation is producing electron number densities which are in the same ballpark as those seen experimentally, and that there are similarities in the overall timing. The details are considerably different. But despite the numerous differences which a detailed comparison will reveal, the division of the curves into two distinct families in accordance with the line-of-sight location is a feature which the simulation shares with experiment. This prompts the question as to whether or not the observed division of curves into two distinct families occurs in the experiment for the same reason as seen in the simulation. Experimentally, this question could be answered by measuring the electron

number density in a gap aligned not with the centerline of a flashboard, as was the case in the experiments discussed here, but in a gap aligned with the gap between two flashboards. According to the simulation, much higher electron number densities would be observed in such a gap, the result of the confluence of the plasma flows from neighboring flashboards.

The simulations also predict that the electron number density measured in the AK gap will be lower for the case of rectangular vanes than for the case of circular rods. This is illustrated in Figure 3-12, which shows electron number density contours at time  $t=4 \times 10^{-6}$  s. Note that this shows a density profile across the gap which at the midplane has a mid-gap depression. The highest density along that radius occurs at the cathode with a value in the low  $1 \times 10^{15}$  per cc's. The rectangular vanes, being more closely spaced to one another than are the circular rods, as well as being considerably longer in the flow direction, appear to restrict the flow much more effectively than did the circular rods. The decrease in electron number density predicted by the simulation is greater than that seen in the simulations. This leads to speculation that the Spitzer resistivity model may be underestimating the electrical resistivity.

In summary, the comparison of simulations and experimental measurements shows that a number of important features of the observed behavior are captured in the simulations. In particular, the division of the line-of-sight traces into two distinct families, with the division made according to the radial position, and the trend in the change of the line-of-sight signal with changes in geometry, are features which the simulations capture. The fairly large quantitative differences between simulation and experimental results lead to speculation that the Spitzer resistivity model is underestimating electrical resistivity.

The most challenging result of the simulations is the explanation they offer of how the flow becomes divided into two distinct parts. The feature which leads to that behavior is the manner in which the gap between neighboring flashboards is modeled. The flashboards are not simple devices; the plasma is produced by breakdown from pea-sized copper grommets. These grommets are placed in five nearly parallel lines on along the length of the board. The lines are more closely spaced at one end of the board than at the other. The line-to-line spacing is roughly a centimeter, and that distance happens to be also a fair measure of the gap between neighboring flashboards. This points out a potential problem with these simulations. The output of plasma from a single flashboard was modeled as having no variation across the width of the board. This implies that over length scales of relevance to these simulations the plasma flowing from the five individual grommet-lines flows together and washes out any variation due to the discrete nature of the grommet-lines. But if this is the case, then it is not logically

consistent to include the inter-flashboard gap in the model. That is, if the plasma from the five individual grommet-lines flows together and washes out the line-source nature of plasma generation within a centimeter or two, then the plasma from neighboring flashboards ought to flow together as well, and wash out the separation between neighboring flashboards. Continued modeling of the flashboards to resolve these questions could be quite useful for revealing the nature of the plasma they produce and their interaction with structures.

TWO ROD SIM  
DUOROD0 S3JW96J  
T = 0.000E+00 CYCLE = 0  
CALCULATION MESH  
1ST X = -5.00E-02  
X INC = 5.00E-02  
1ST Y = 6.00E-02  
Y INC = 2.00E-02

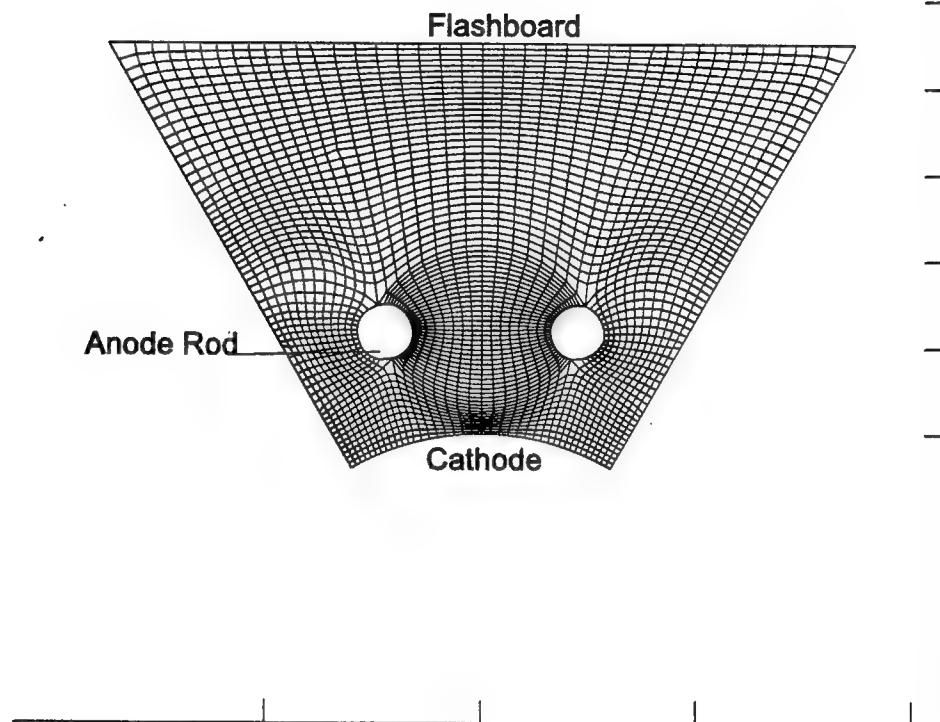


Figure 3-1. Simulation mesh for case of circular rods.

TWO ROD SIM: 1IN X 0.25IN, 18 VANES  
DUAL2 S3JW96J  
T = 0.000E+00 CYCLE = 0  
CALCULATION MESH  
1ST X = -4.00E-02  
X INC = 2.00E-02  
1ST Y = 6.00E-02  
Y INC = 2.00E-02

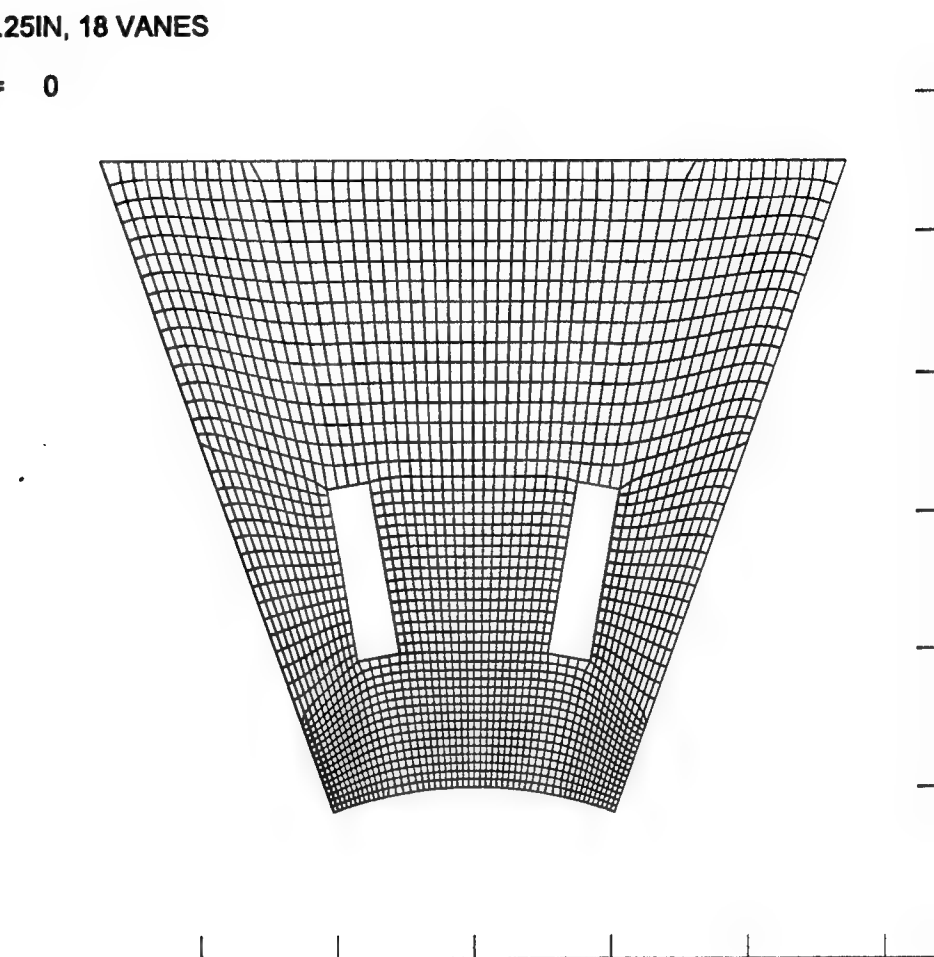


Figure 3-2. Simulation mesh for case of rectangular vanes.

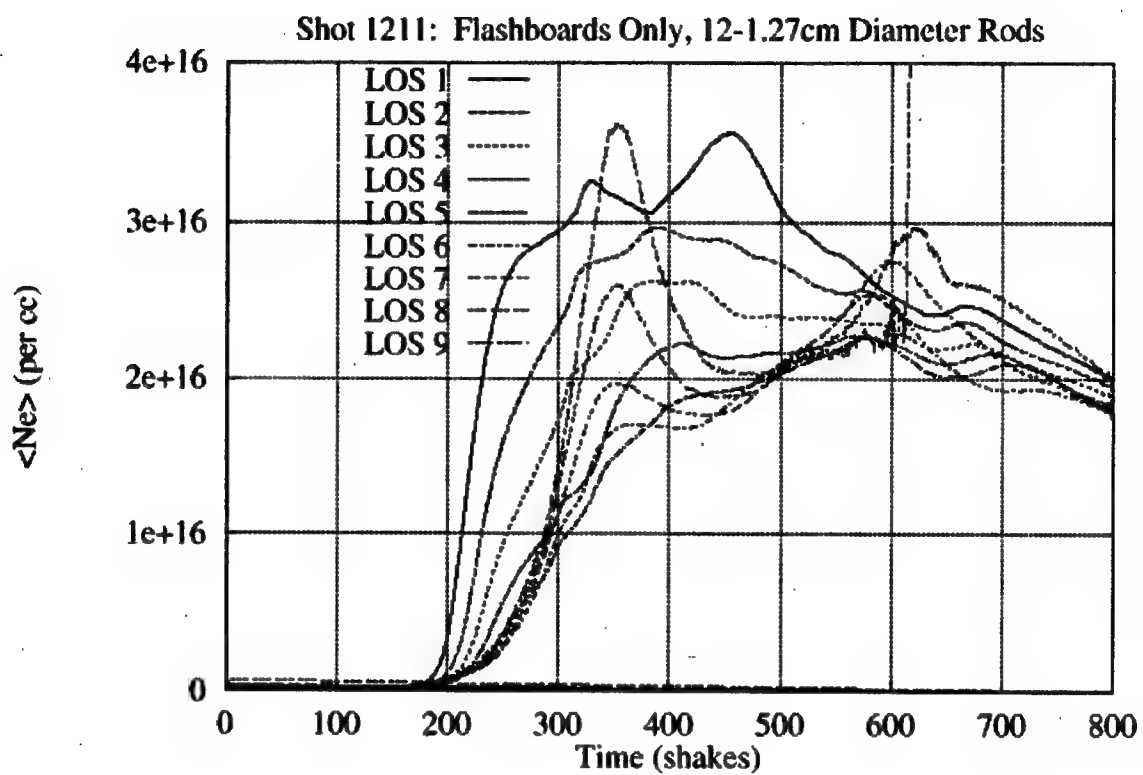


Figure 3-3. Measured electron density for rodded case.

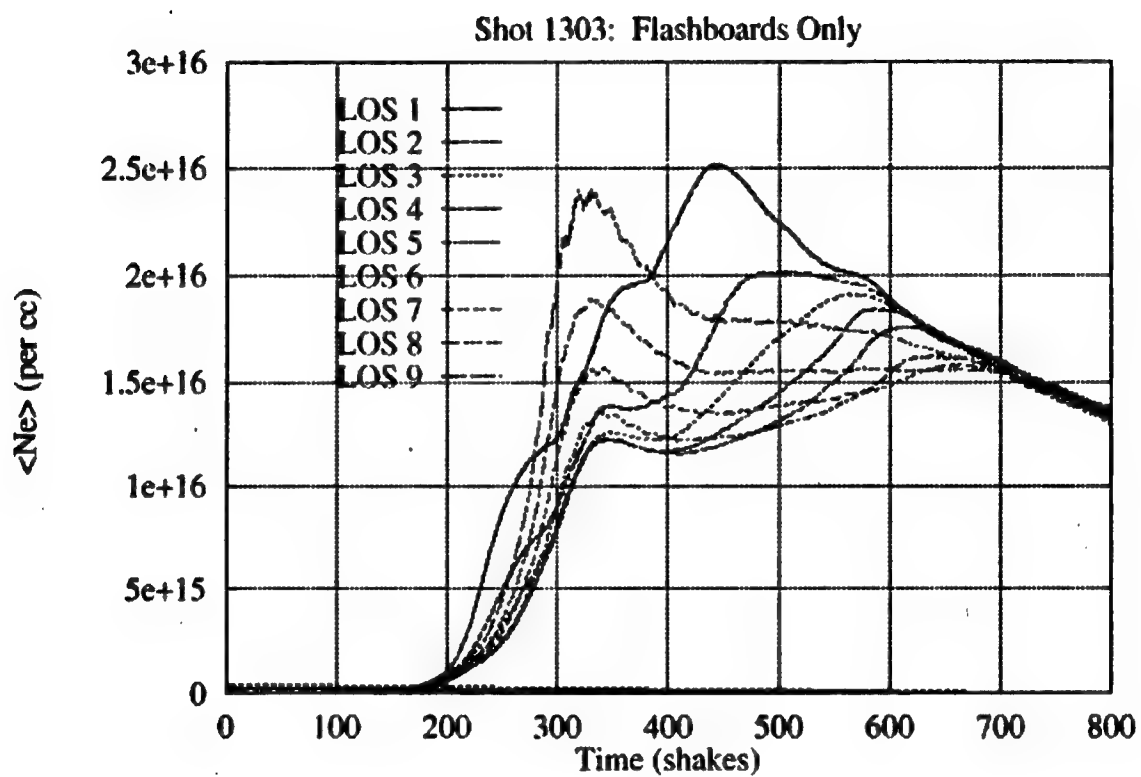


Figure 3-4. Measured electron density distribution for vaned case.

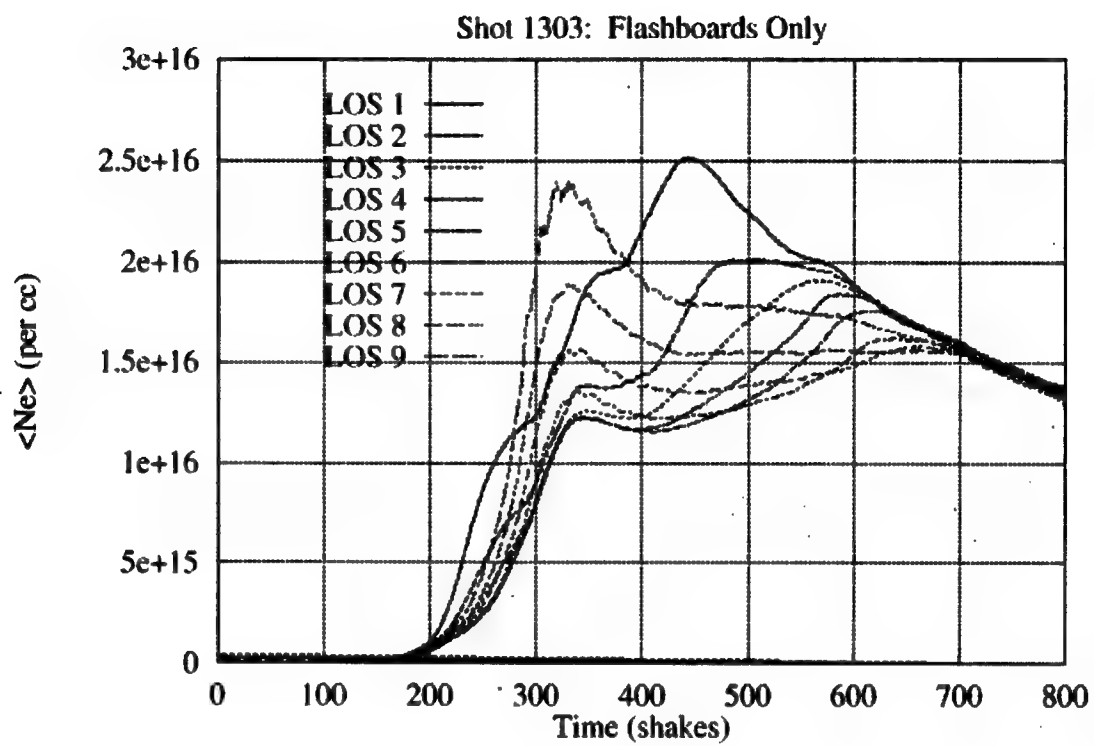


Figure 3-5. Measured electron densities for flashboard only, shot 1303.



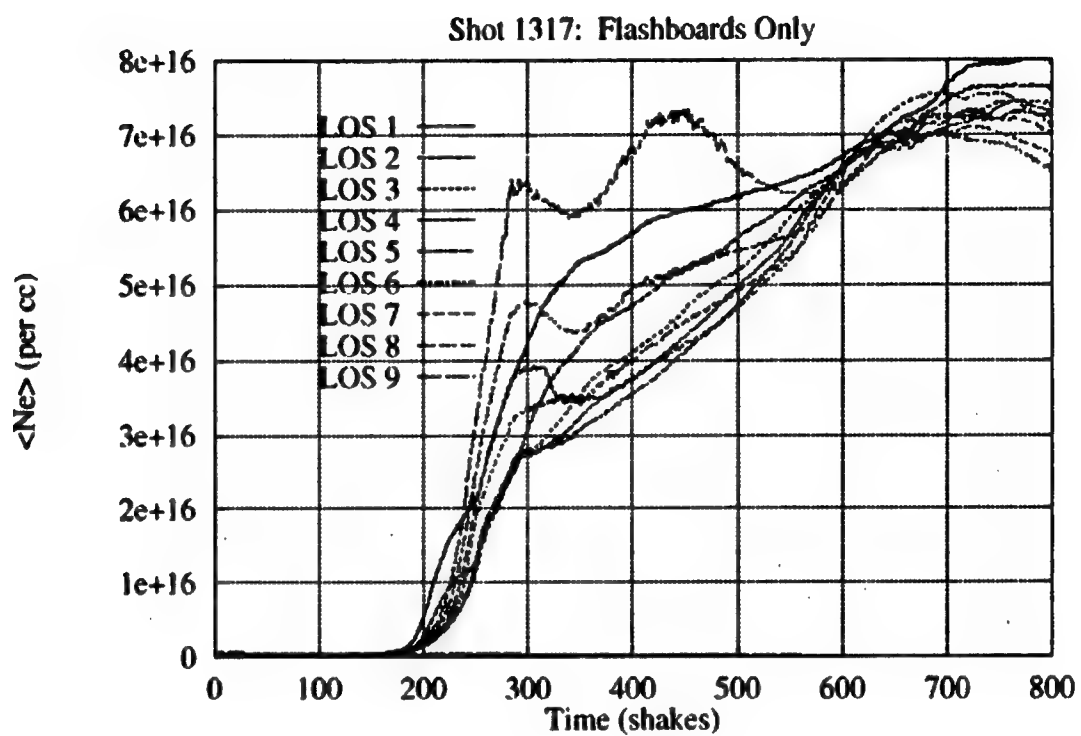
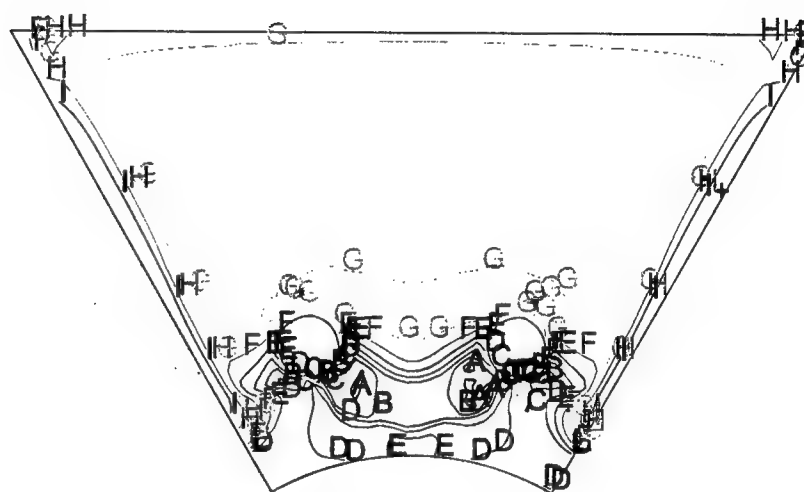


Figure 3-6. Measured electron densities for flashboard only, shot 1317.

TWO ROD SIM  
 DUOROD0 S3JW96J  
 T = 2.501E-06 CYCLE = 2501  
 ELECTRONS / CC

-= 1.7439E+14  
 A= 3.2670E+14  
 B= 6.1203E+14  
 C= 1.1466E+15  
 D= 2.1479E+15  
 E= 4.0238E+15  
 F= 7.5381E+15  
 G= 1.4122E+16  
 H= 2.6455E+16  
 I= 4.9559E+16  
 += 9.2842E+16



(a) T = 2501 ns

Figure 3-7. Electron number density contour plots from the circular rod simulation at times  $t = 2501$  ns and  $t = 3501$  ns.

TWO ROD SIM  
DUOROD0 S3JW96J  
T = 3.501E-06 CYCLE = 3501  
ELECTRONS / CC

-= 1.4765E+15

A= 2.4063E+15

B= 3.9216E+15

C= 6.3911E+15

D= 1.0416E+16

E= 1.6975E+16

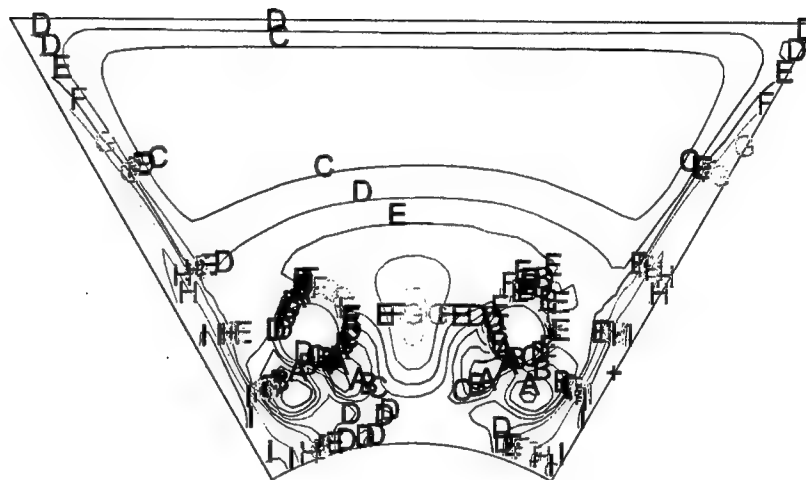
F= 2.7665E+16

G= 4.5087E+16

H= 7.3479E+16

I= 1.1975E+17

+= 1.9516E+17



(b) T = 3501 ns

Figure 3-7. Electron number density contour plots from the circular rod simulation at times  $t = 2501$  ns and  $t = 3501$  ns (Continued).

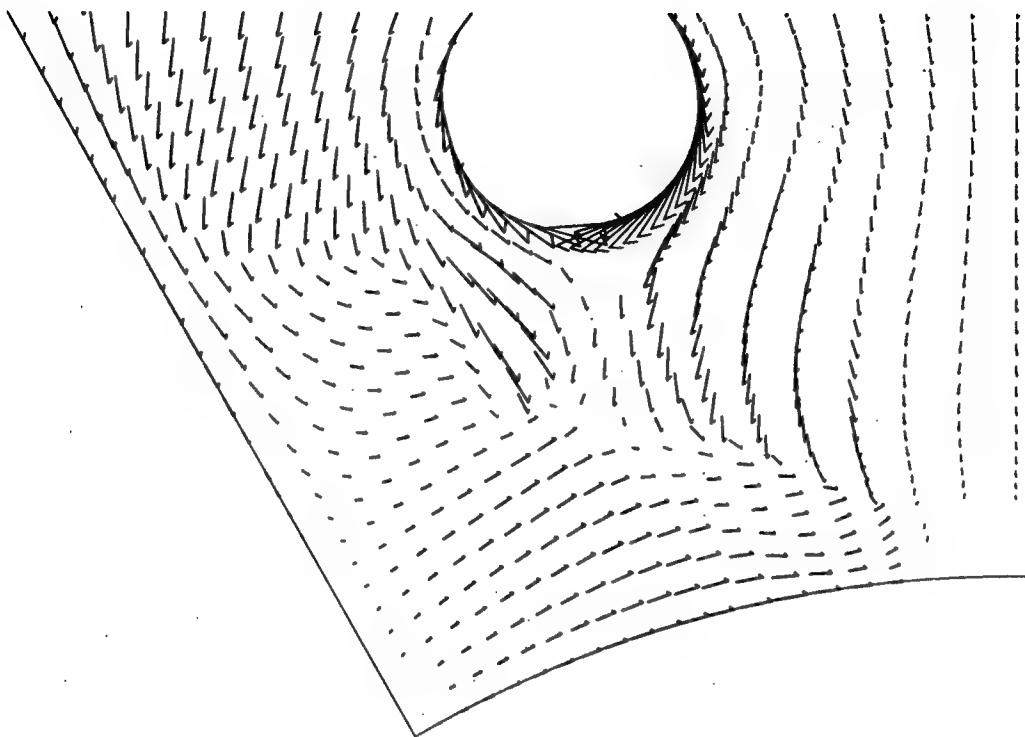


**Figure 3-8.** Plasma velocity vector from the lower left hand corner of simulation domain at a time between 2501 ns and 3501 ns.

TWO ROD SIM  
DUOROD0 S3JW96J  
T = 3.001E-06 CYCLE = 3001  
MAGNETIC FIELD  
MAX = 1.738E+00

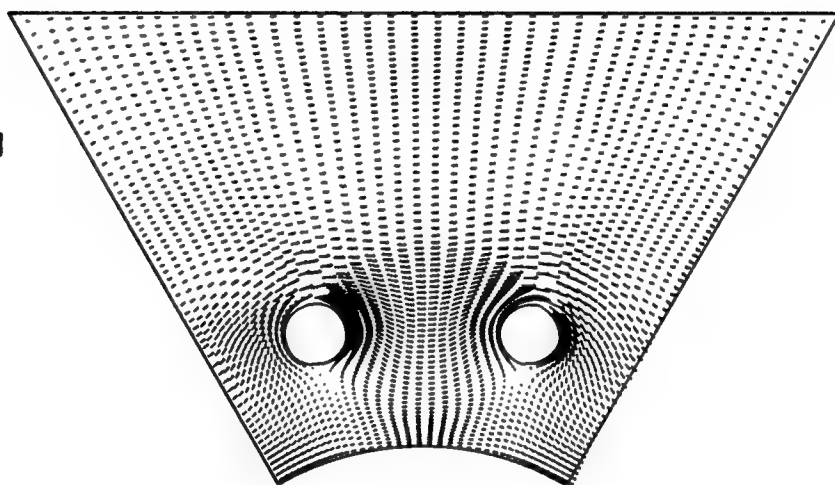


Figure 3-9. Magnetic field at 3001 ns.

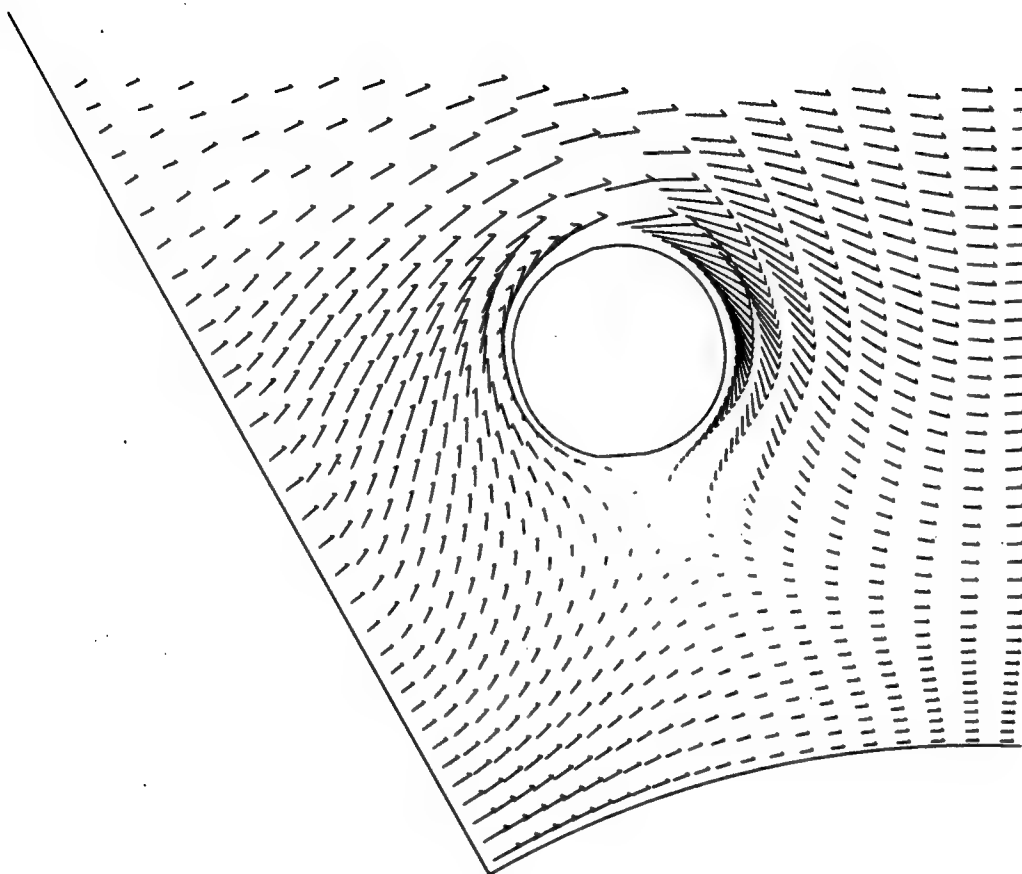


Figure 3-10. Blowup of left hand corner of Figure 3-9.

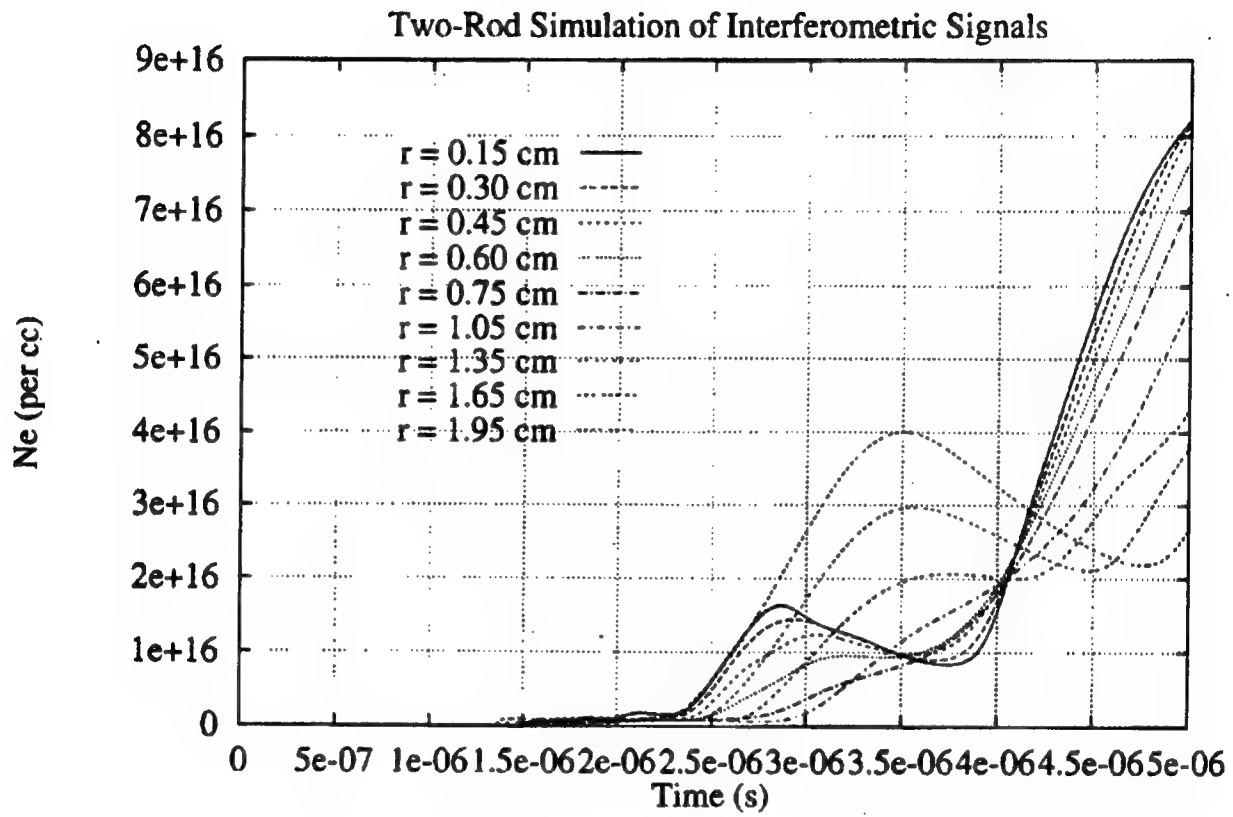
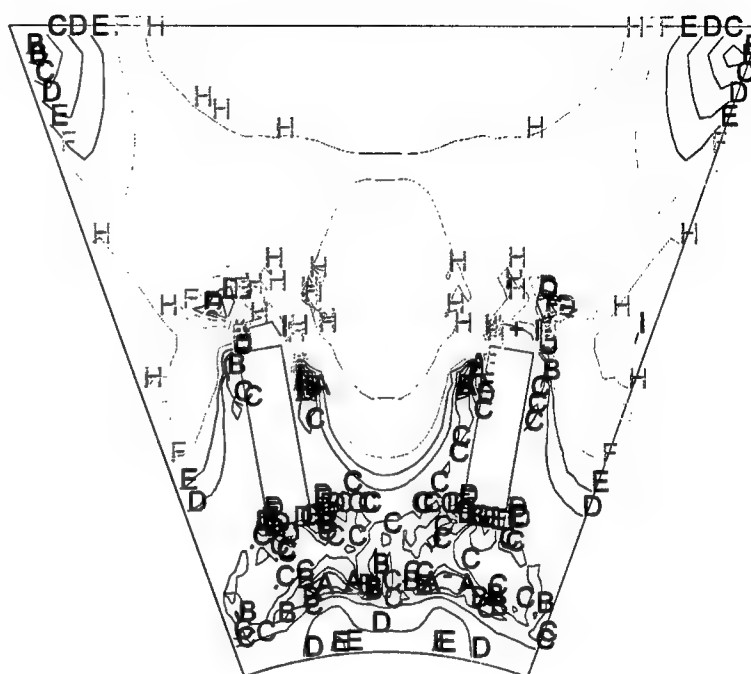


Figure 3-11. Simulated interferometric line-of-sight signals.

**+= 8.6693E+16**



111



## **SECTION 4**

### **OPENING SWITCH SIMULATIONS**

A difficulty in modeling opening switches which has been recognized for the past several years is that the interferometric measurements of the plasma's electron number density strongly suggest that the plasma becomes more ionized as the magnetic field starts to sweep plasma up before it. In order to perform accurate modeling of the conduction phase, this ionization effect must be included. The Saha equilibrium ionization model discussed in our 1995 Annual Report (Reference 5) has proven to be very useful in this regard. Not only does this model allow for a great deal of flexibility in translating the measured electron number density into the mass density, it appears to give a fairly accurate depiction of the magnetically driven shock-heating which causes the early increase in ionization observed experimentally.

#### **4.1 SIMULATION OF EXTENDED TRANSPARENT ANODE EXPERIMENT – SHOT 1037.**

Detailed comparisons of ACE 4 switch experiments and Mach2 simulations have been conducted and are beginning to show promise in their ability to reveal hitherto unfathomed details in the nature of the conduction phase. The extended transparent anode experiment series was one set of experiments chosen for detailed modeling. Shot 1037 in particular was chosen for modeling. This shot was chosen since, amongst other reasons, the interferometric measurements of the electron number density revealed that in the absence of pulsed power, the plasma in the AK gap was relatively quiescent during the time-interval which, with pulsed power, would be the conduction phase. This makes the modeling task much easier as there is no need to contrive dynamic boundary conditions and such, as was the case for the Hawk parallel-plate experiment. This is good not just because it makes the modeling task easier, but in that it removes a layer of uncertainty from the creation of the initial condition. Figure 4-1 shows the interferometric signals from channels 3-8 for the no-pulsed power case. Here time  $t=0$  is defined as the time at which the generator would be fired. Figure 4-2 shows the responses from channels 3 and 4 for the flashboard-only case as well as for the pulsed-power case. The comparison shows that the shot-to-shot reproducibility of the flashboard plasma is quite good – a point not of great relevance here, but always of general interest when dealing with experimental matters.

The procedure in setting up the simulation is to create an initial density distribution which gives the same line-integrated electron number density signals in each channel as observed

experimentally. This is done by assuming the plasma to be uniform in the axial direction, assuming the plasma composition to be  $\text{CF}_2$  (since the flashboards are teflon), and an initial temperature. This allows the measured electron number density profile to be translated into a mass density profile. A temperature of 2 eV appears to give fairly good agreement between experiment and simulation.

The line-integrated electron number density as obtained experimentally is compared with that from the simulations channel-by-channel in Figures 4-3, 4-4, 4-5, 4-6, 4-7 and 4-8. The signals from channels 1, 2, and 9 were considered not reliable, and so are not included in this comparison. The comparison shows that the initial rise in the signals is predicted fairly well by the Saha model, both in terms of the relative increase in the signals as well as in the timing. The time at which the signals approach zero is also predicted quite closely. All the signals show a rapid change in their slope just before their rapid approach to zero – the simulated signals show this somewhat more clearly than do the experimental signals, but it can be seen in all signals, with fairly good agreement between simulation and experiment. The agreement in timing is quite important for this feature. The simulations reveal that this change in slope is due to the more rapid decrease in the line-integrated density of the plasma which occurs when the snowplow has reached the nominal end of the switch region and has no more switch plasma to accrete. Getting agreement of the timing of this phenomena indicates that the translation between electron number density and mass density was done correctly.

A systematic discrepancy between simulation and experiment is the second peak seen in the simulated signals for channel 7 and 8. The plots shown in Figure 4-9 show a sequence of ion number density plots which help to reveal the cause for this second peak. The initial density profile has a weak mid-gap minimum. Near the cathode, the density profile is essentially flat, so the  $\sim r^{-2}$  magnetic force tends to push plasma away from the cathode and toward the center of the AK gap. At the same time, the mid-gap density minimum allows the snowplow to push ahead in that region. This creates a density peak between the initial density minimum and the cathode. As the snowplow continues to push its way down the switch length, this action continues. The snowplow is eventually able to push the plasma in this peak all the way across the AK gap. As it passes across the various lines-of-sight, it registers as a peak in the line-integrated electron number density signals. At early times, say before 800 ns, this peak is coincident with the increase in signals due to the increase in ionization, and thus does not appear as a discrete peak. But eventually, this blob gets pushed across the outermost lines-of-sight, and this occurs at a time sufficiently late that it is no longer part of the initial ionization increase. This can be seen occurring in the ion number density contour plots at times  $t=700, 800$ , and  $900$  ns. The reason

for this phenomenon not being visible in the experimental signals is not known, but one can speculate that the initial condition of a uniform temperature is not sufficient, and that greater fidelity to the observations could be obtained with a spatially dependent temperature profile.

The later time ion number density contour plots in Figure 4-9 gives a picture as to how the switch opens. At time  $t=1100$  ns, the snowplow is just starting to push plasma into the downstream vacuum. At time  $t=1150$  ns, the shape of the snowplow is seen to be rapidly distorting as the inner portion accelerates unimpeded into the vacuum while the outer portion still is slogging through the plasma ahead of it. Between times  $t=1150$  ns and  $t=1200$  ns, the plasma which remains in the gap is pushed violently into the anode, clearing the AK gap of nearly all of the initially present plasma. This picture is at odds with that suggested by the experimentalists, whose view is that the plasma is propelled to much greater distances downstream before opening. This difference has not yet been adequately resolved.

#### 4.2 SIMULATION OF MESH SHOT – SHOT 1727.

A series of shots was taken with an anode structure specifically designed to minimize azimuthal variations in the switch plasma. The goal was to create a database against which simulations could be benchmarked more convincingly, and for which the nagging question of the effect of azimuthal variations would be absent.

The anode structure, referred to as a mesh, was comprised of a fairly thin sheet of stainless, rolled into cylindrical form, in which roughly rectangular holes had been stamped. The holes, square save for radiused corners, were three-quarters of an inch on a side and spaced with an edge-to-edge spacing of a quarter inch. In this series of shots, the anode radius was 11.9 cm (4.69 inches). The circumference of the anode was thus 29.44 inches, permitting 30 holes (the deviation from exactly 30 inches is due to the difference between inside and outside circumference, the thickness of the sheet being 2.28 mm). Taking a nominal electric resistivity of  $7 \times 10^{-7} \Omega\text{-m}$  for stainless steel, the diffusion time through the sheet is:

$$\tau = dx^2/(2\eta/\mu_0) = 9.33 \times 10^{-6} \text{ s} , \quad (4.1)$$

so over the 4-8  $\mu\text{s}$  time scale which characterizes the flashboard-only experiments, the mesh should prevent the penetration of magnetic field into the AK gap. This neglects the holes in the anode, off course, which could admit magnetic flux into the AK gap, but given the degree to which the anode vanes appear to restrict flow into the gap, it's likely that the plasma which

flows through the mesh does so by virtue of resistively shedding the magnetic field which it carried from the flashboard to the exterior surface of the mesh. This turns into a fairly complicated situation to model, but a vast simplification is afforded if the assumption is made that once past the anode mesh, the plasma flow is one-dimensional and carries no magnetic field. This is justified in part by hope, but primarily due to the close spacing of the holes.

The experimental flashboard-only data is shown in Figure 4-10. A curious feature of the data is the behavior of channel 1. While all the channels behave similarly to one another, channel 1 has a curious dip which starts at about time  $t = -750$  ns and persists until about time  $t = 1000$  ns. The same feature is present in the data for the shot with pulsed power (pulsed power current pulse starts at time  $t = 0$ ), so this feature cannot be relegated to the ranks of irreproducible results. It may, however, be an artifact of the interferometric measurement technique, specifically a slight corruption of the signal due to beam refraction by a density gradient. This suggests that the abrupt change in slope seen at time  $t = 750$  ns in channel 1 is not an accurate depiction of how the electron number density is actually changing. This is mere speculation, however, and for modeling purposes, the signals have been taken as accurate representations of reality.

For modeling, the same strategy used for the parallel plate experiment and for the extended transparent anode experiment is followed. The measured electron number density profile is converted into mass density under assumptions regarding the plasma composition and the plasma temperature. Again, a plasma composition of two fluorines per carbon is used, but here, a more detailed examination of the issue of plasma temperature has been carried out. Specifically, the simulated line-integrated electron number density signals were compared to the experimental signals for several different initial plasma temperatures. The results are shown in Figures 4-11 through 4-18.

Initial temperatures of 1.0, 1.5, and 2.5 eV were used. In using the Saha model to translate electron number density to mass density, a lower temperature corresponds to a higher mass density since to get the same number of electrons at a lower charge state requires more ions, and the charge state increases with temperature. The simulations were driven with a simple LRC circuit model which produced a current pulse quite similar to that observed experimentally.

A trend is visible in the experimental data. The increase in signals over the first 200-400 ns of the conduction phase varies in a systematic manner with the radial position of the line-of-sight. Channel 8 violates this trend, and channels 1 and 2 go off scale, but channels 3 through 7 seem to fit the pattern. The pattern is: the closer the line-of-sight is to the cathode, the larger is the

ionization step. This suggests that the temperature is not spatially uniform as is assumed in initializing the simulations. It suggests that the temperature decreases from anode to cathode. This could be the case if the plasma were resistively heated as it sheds the flashboard's magnetic field on its way through the anode holes, and if the plasma then cooled, by expansion or radiation or both, as it flows into the AK gap. But this is speculative grist for future simulations. The simulations described here used an initial uniform temperature profile.

A trend of a similar nature is seen in how the simulations compare with the experiment: the inner channels show better agreement for the lower temperature simulation, while the outer channels show better agreement for the higher temperature simulations. But this trend is restricted to the ionization step only. The agreement between experiment and simulation on the basis of the duration of the conduction phase is best for the 1.5 eV simulation, regardless of channel. Channels 3, 4, and 5 show remarkably good agreement in when the signals take their abrupt plunge to zero – as discussed in connection with the extended transparent anode study, the sharp change in the slope of the signals and this quick drop to zero are signatures of the snowplow having pushed its way through the switch and entering the downstream vacuum. The 1.0 eV simulation, while having fairly good agreement on the basis of the ionization step in the inner channels, diverges widely from experiment on the basis of the duration of the conduction phase. This shows that the 1.0 eV simulation had far too much mass. The 2.5 eV simulation, on the basis of the ionization step, does not agree with the experiment much more poorly than does the 1.5 eV simulation, but, as with the 1.0 eV, quite clearly fails to give the correct duration for the conduction phase. This is not quite so clear in the line-integrated electron number density signals as it was for the 1.0 eV simulation; these traces have curious peaks at the end of the conduction phase. The cause of these peaks is revealed upon closer examination of the simulation results.

Figure 4-19 shows electron number density contour plots for times  $t=500$  ns and  $t=600$  ns for the 1.5 eV case; these times bookend the period during which the line-integrated electron number density signals are plunging rapidly to zero. As can be seen from these two plots, the snowplow is just beginning to push plasma into the downstream vacuum at 500 ns. At 600 ns, the plasma has been effectively cleared from the gap. In contrast, Figure 4-20, showing electron number density contours at times  $t=400$  ns, 500 ns, and 600 ns for the 2.5 eV case, shows that the main body of plasma is pushed into vacuum and out of the gap during the time interval from 400 ns to 500 ns. The plots also show the development of a feature not at all visible in those for the 1.5 eV case — this is the curling up of the plasma which had been against the cathode. Just like in a clumsy moment, someone will hook their toe under the edge of a carpet, the magnetic field

has caught the plasma and lifted it away from the cathode. The fact that this flow feature does not develop for the 1.5 eV case shows the importance of the details of the initial conditions.

The simulations, particularly the 1.5 eV case, do a fairly good job of matching the experimental data. In order to do better, a more complete, more accurate model of the switch plasma is needed. For this study, the plasma was given an initial distribution with uniform temperature and zero fluid velocity. Clearly, there should be a nontrivial distribution of temperature as well as velocity. The plasma distribution also evolves to a non-negligible degree over the time scale of the conduction phase – this can effect the manner in which the snowplow interacts with the switch plasma. Dimensional effects can also be important. For example, Figure 4-21 shows line-integrated electron number density signals from a flashboard-only simulation. At late times, the signals converge, suggesting that the plasma has become uniformly distributed across the AK gap. Figure 4-22 shows the two-dimensional distribution of electron number density at a time when the LOS-signals have converged – this shows that the convergence is not at all a signature of a uniform density plasma, but occurs as a result of the distribution of plasma in the axial direction as well as the radial direction. The sort of convergence seen in these simulated LOS signals is seen over and over again in the experimental data. The point here is that the experimental signals can be interpreted in more than one way, and modeling provides a useful manner in which to try to distinguish the right ways from the wrong ways. So dimensional effects can be important, but simple one-dimensional flow effects can be of importance, as well. Work is currently being done on modeling the mesh-shot flashboard-only data. The goal here is not to show that experiments can be post-predicted, an activity only slightly less useful than predicting last season's corn harvest, but by forcing the simulations to converge to the experimental observations, to reveal aspects of the experimental data in a different light than previously considered.

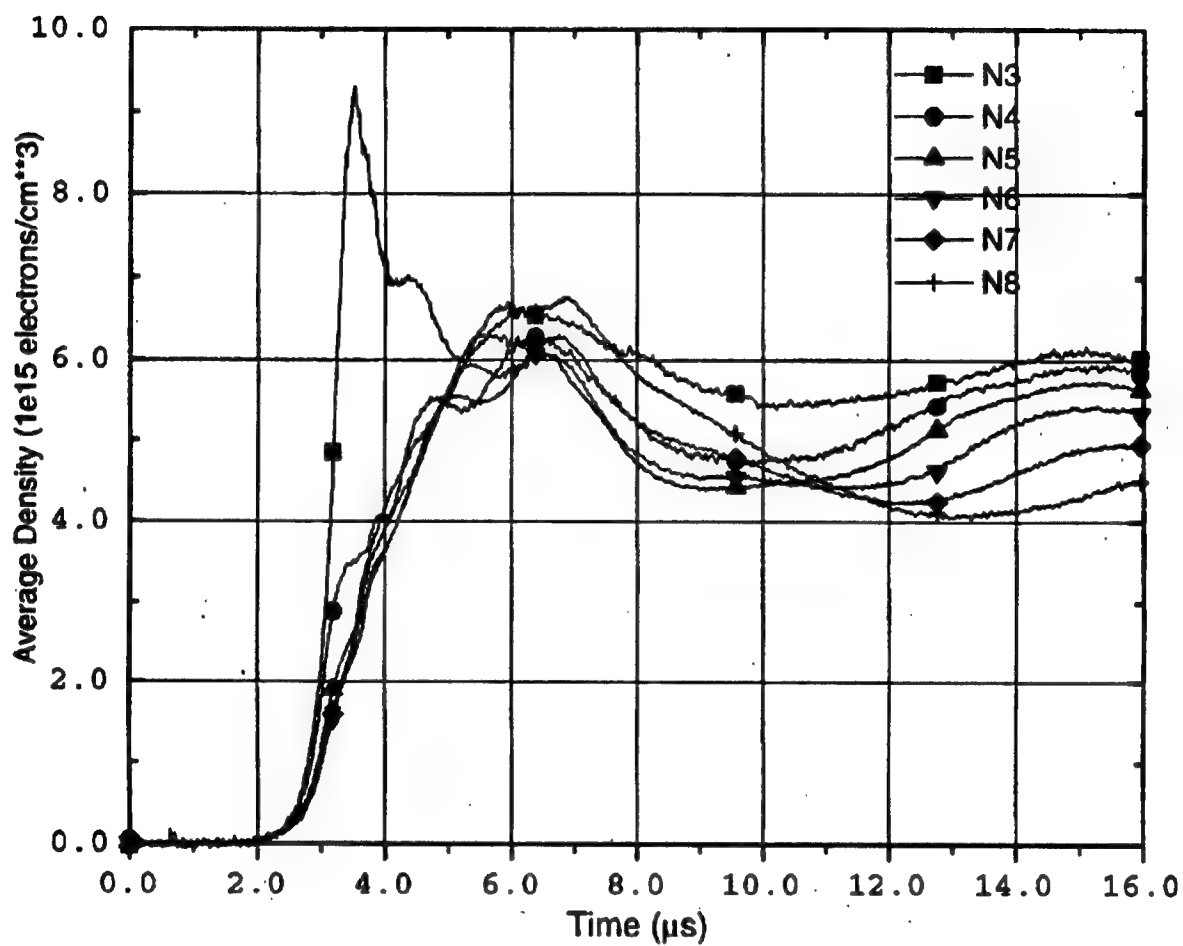


Figure 4-1. Interferometric signals for pre-shot 1037, channels 3-8.

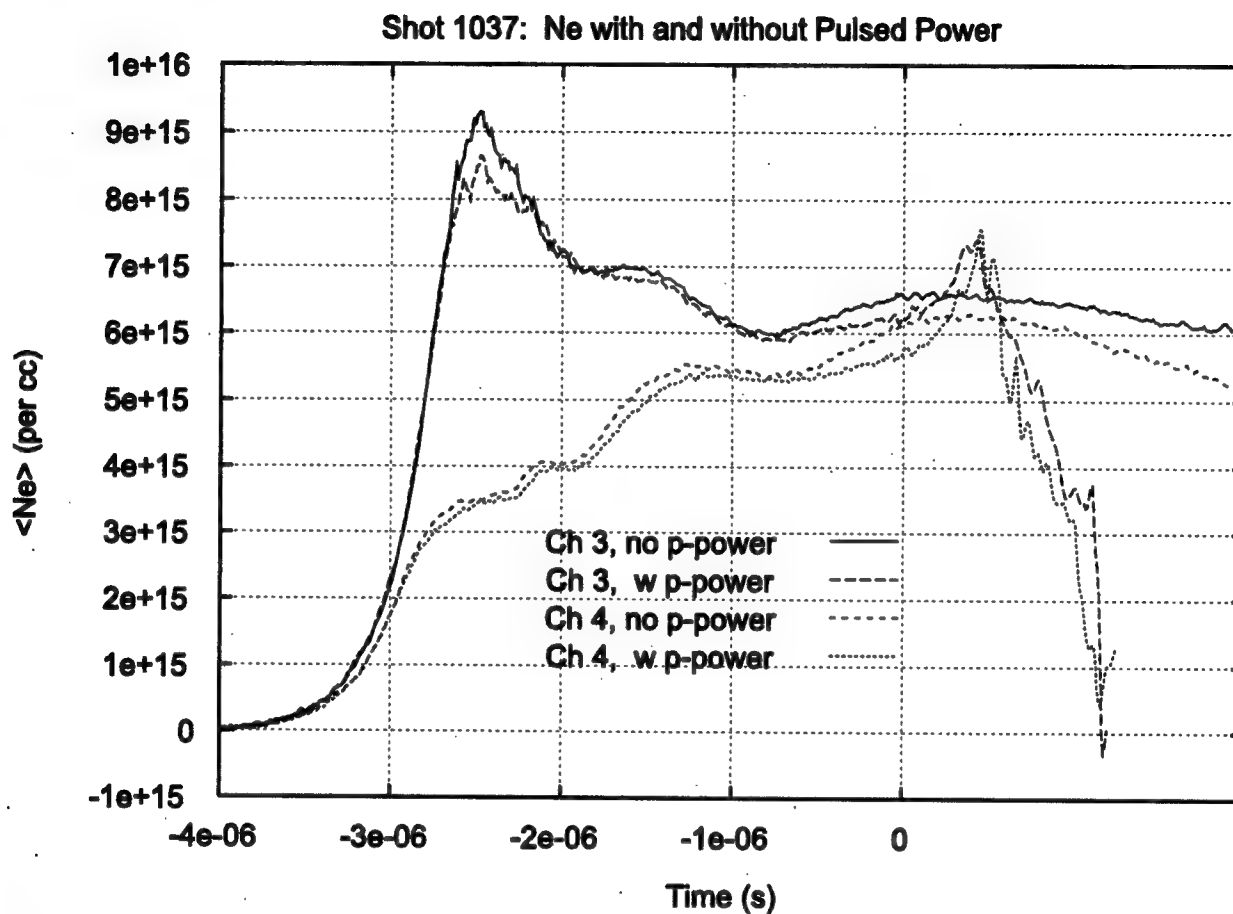


Figure 4-2. Responses from channels 3 and 4 for the flashboard only case as well as for the pulsed power case.



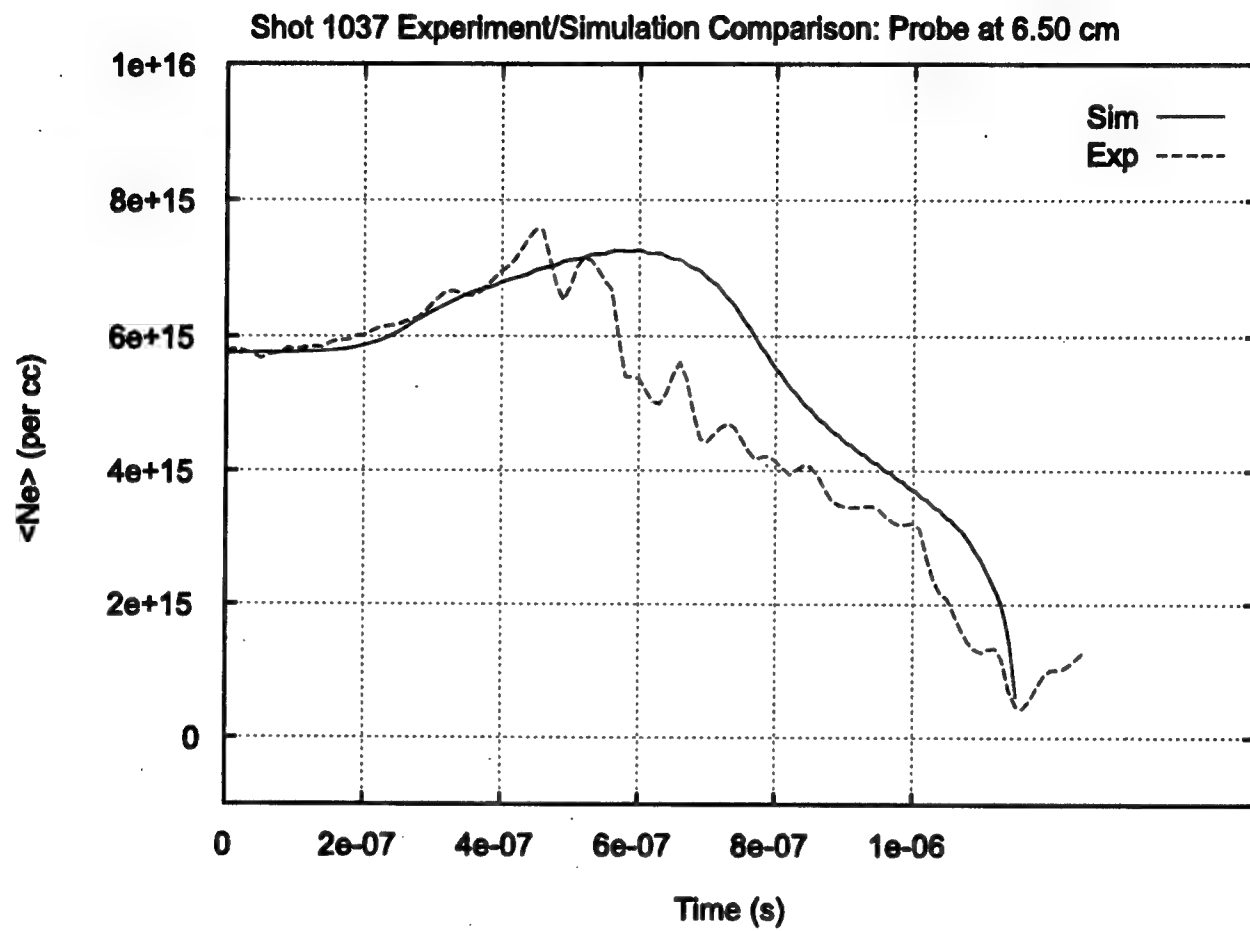


Figure 4-3. Comparison of experimental and simulated line electron densities for channel 3.

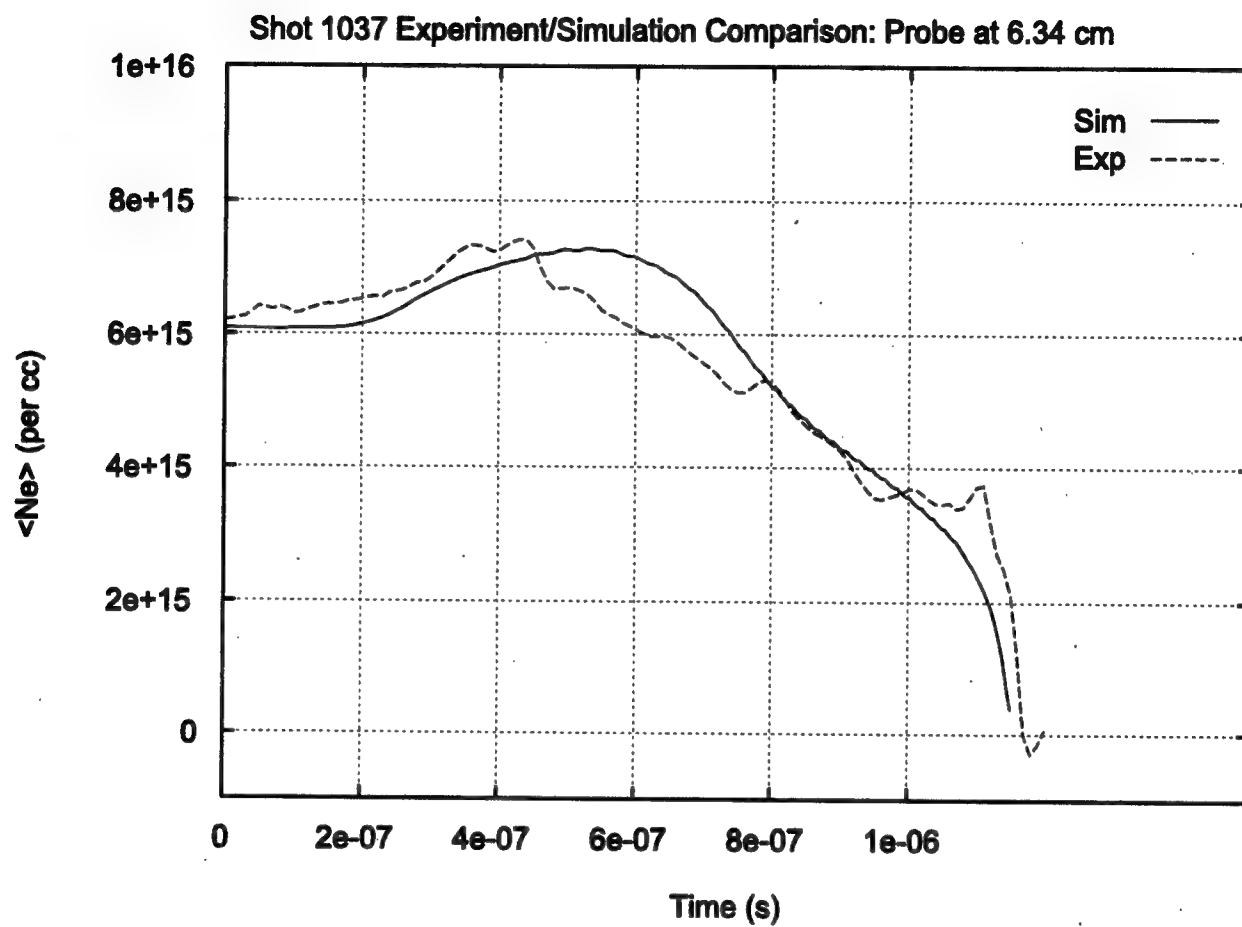


Figure 4-4. Comparison of experimental and simulated line electron densities for channel 4.

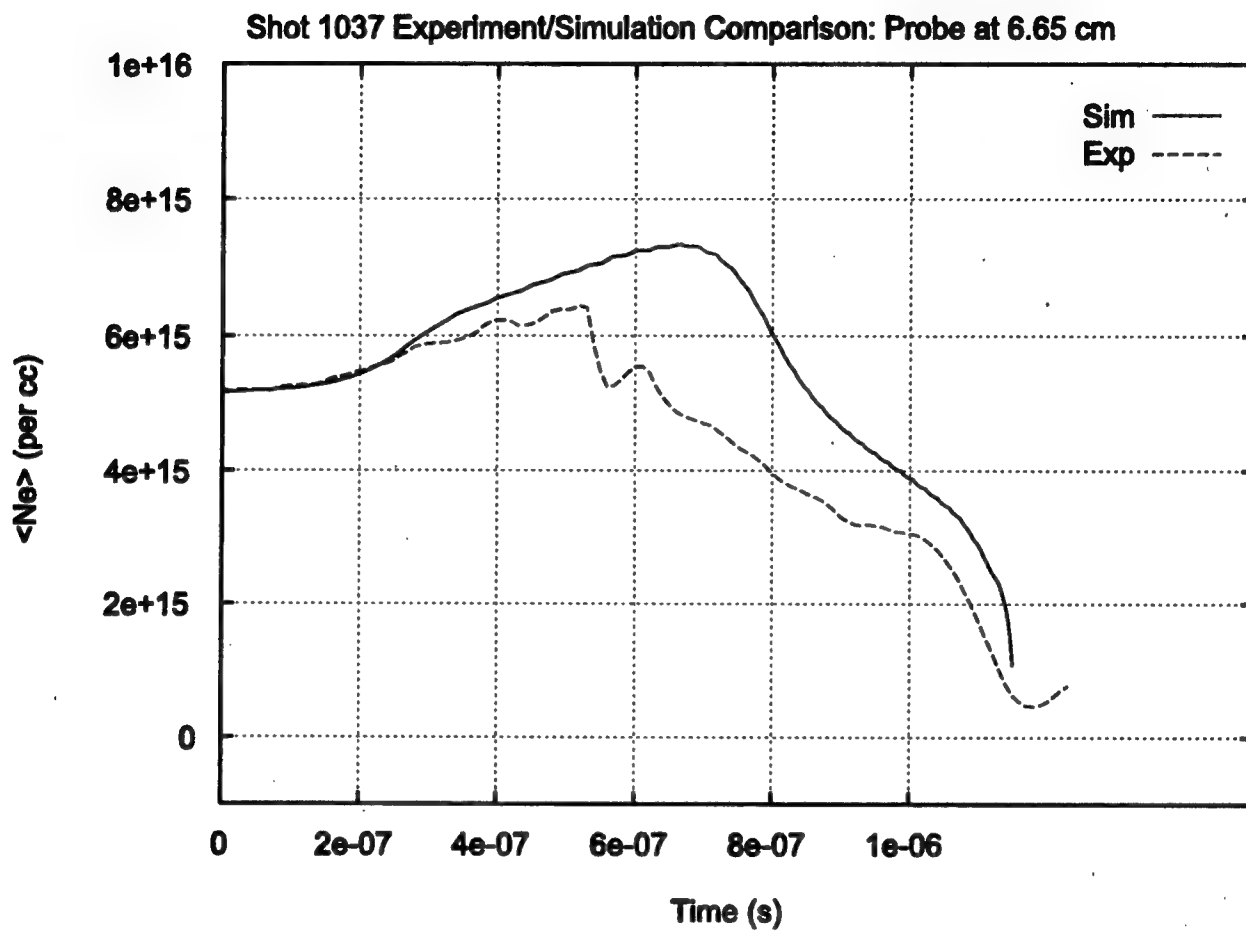


Figure 4-5. Comparison of experimental and simulated line electron densities for channel 5.

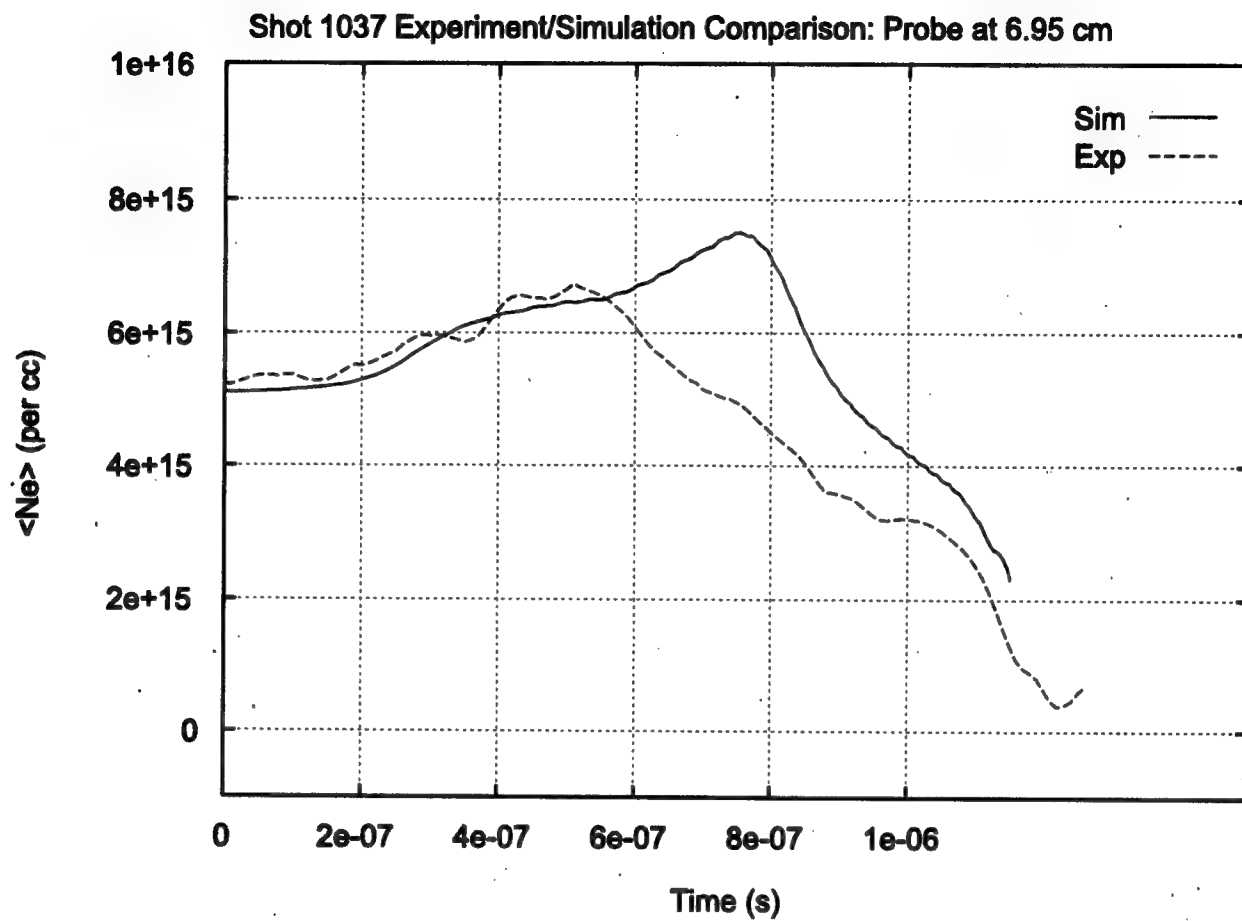


Figure 4-6. Comparison of experimental and simulated line electron densities for channel 6.

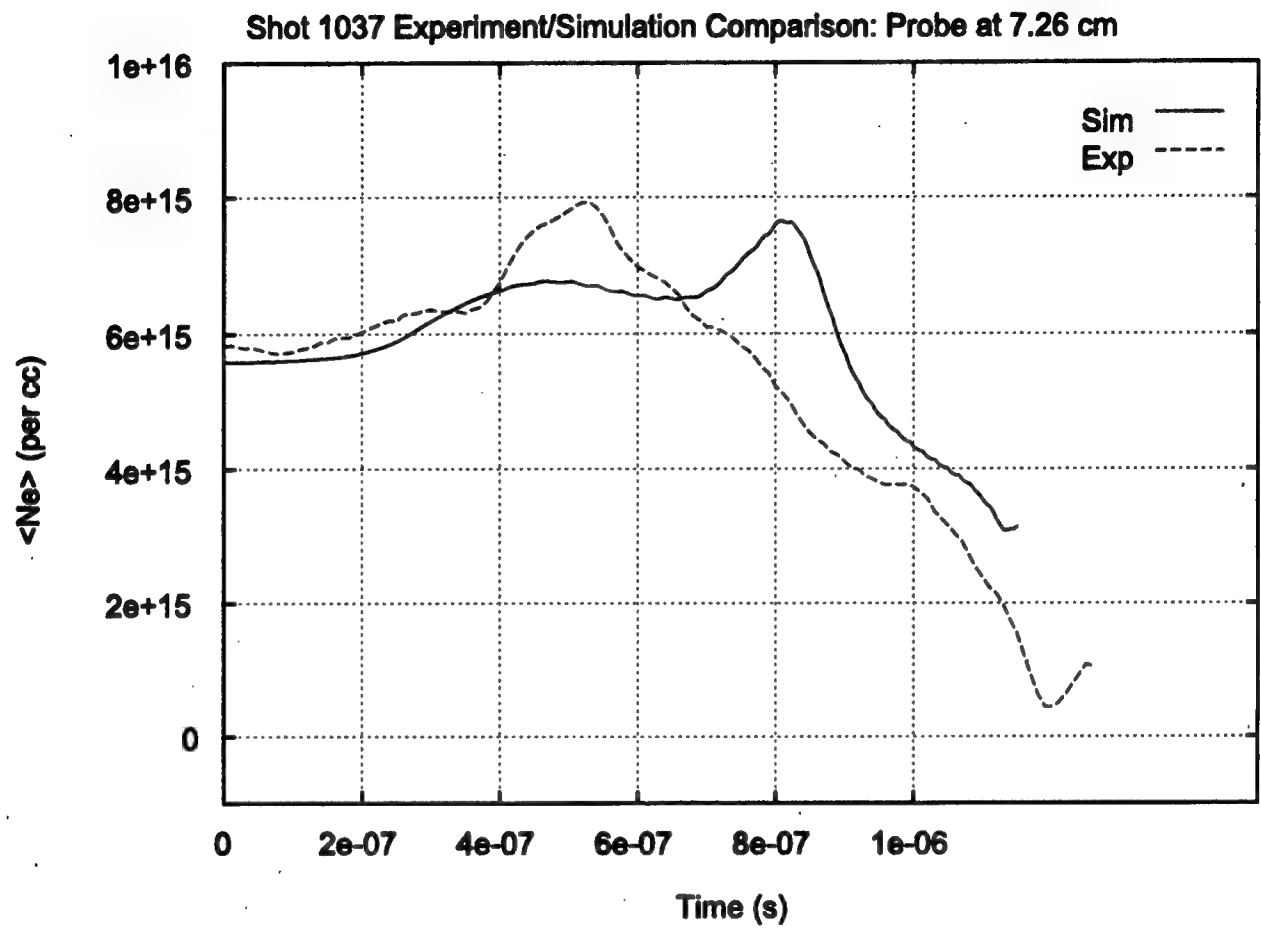


Figure 4-7. Comparison of experimental and simulated line electron densities for channel 7.

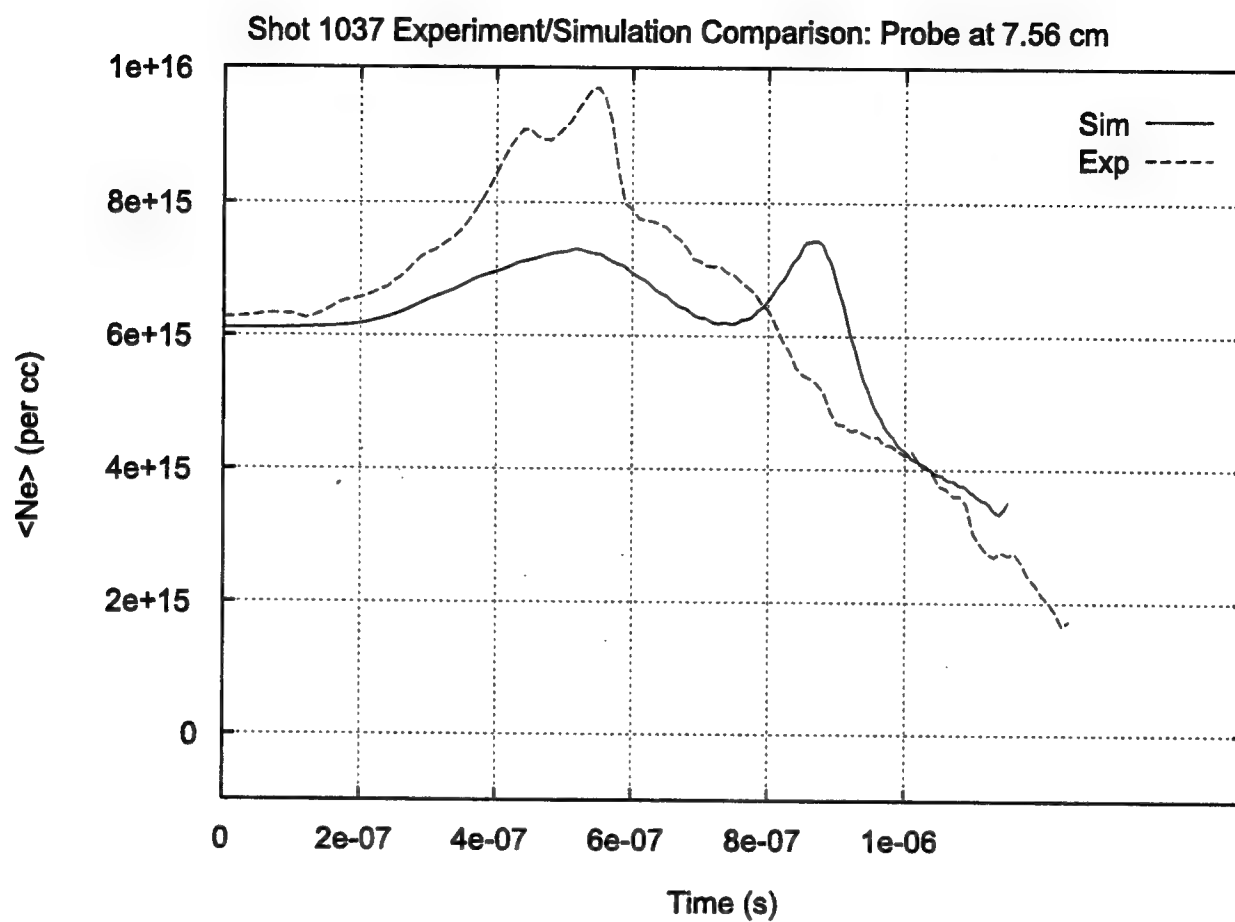


Figure 4-8. Comparison of experimental and simulated line electron densities for channel 8.

S1037 GEOM; CF2, 2EV, NITRO RADN  
 S1037H V9403.J  
 T = 1.000E-06 CYCLE = 9519  
 IONS / CC

- = 9.9851E+11

A = 2.6055E+12

B = 6.7989E+12

C = 1.7741E+13

D = 4.6294E+13

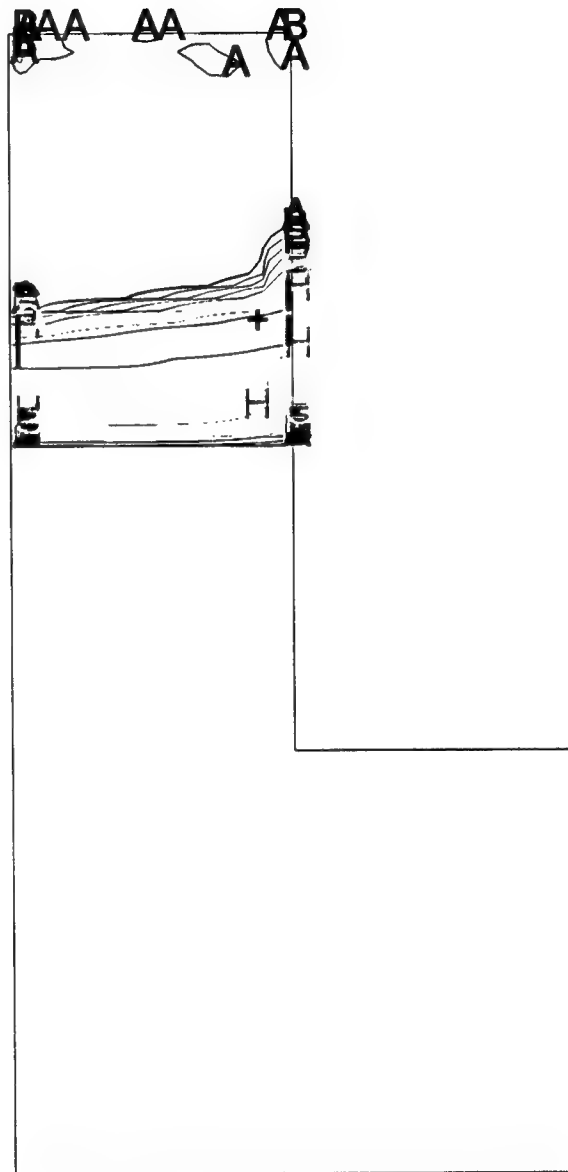
E = 1.2080E+14

F = 3.1522E+14

H = 2.1464E+15

I = 5.6008E+15

+ = 1.4615E+16



(a) T = 1.0  $\mu$ s

Figure 4-9. These ion density plots help reveal the cause for the shapes of the density profiles (see text).

S1037 GEOM; CF2, 2EV, NITRO RADN  
 S1037H V9403.J  
 T = 1.100E-06 CYCLE = 11612  
 IONS / CC

- = 9.9851E+11

A = 2.6100E+12

B = 6.8222E+12

C = 1.7832E+13

D = 4.6612E+13

E = 1.2184E+14

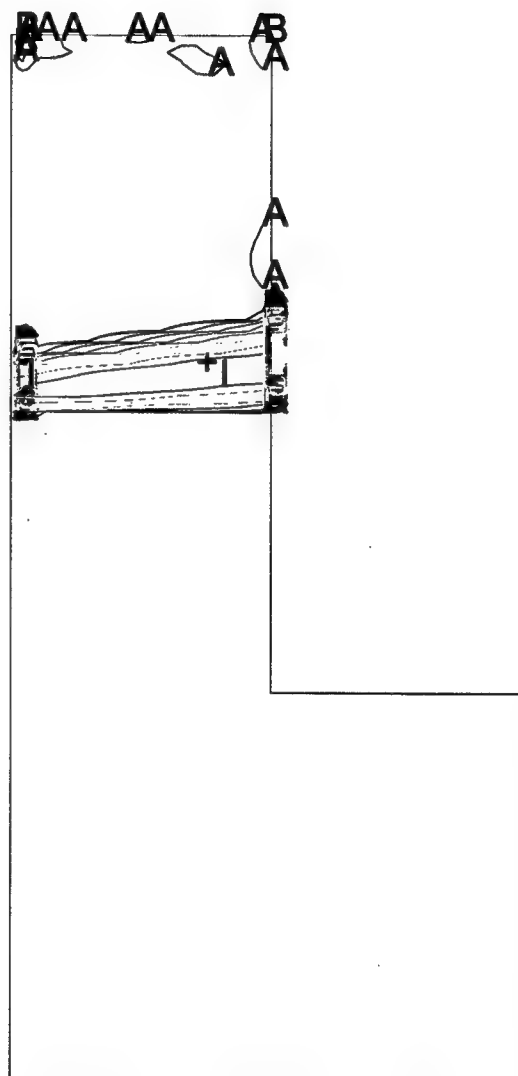
F = 3.1847E+14

G = 1.0000E+15

H = 2.1759E+15

I = 5.6875E+15

+ = 1.4867E+16



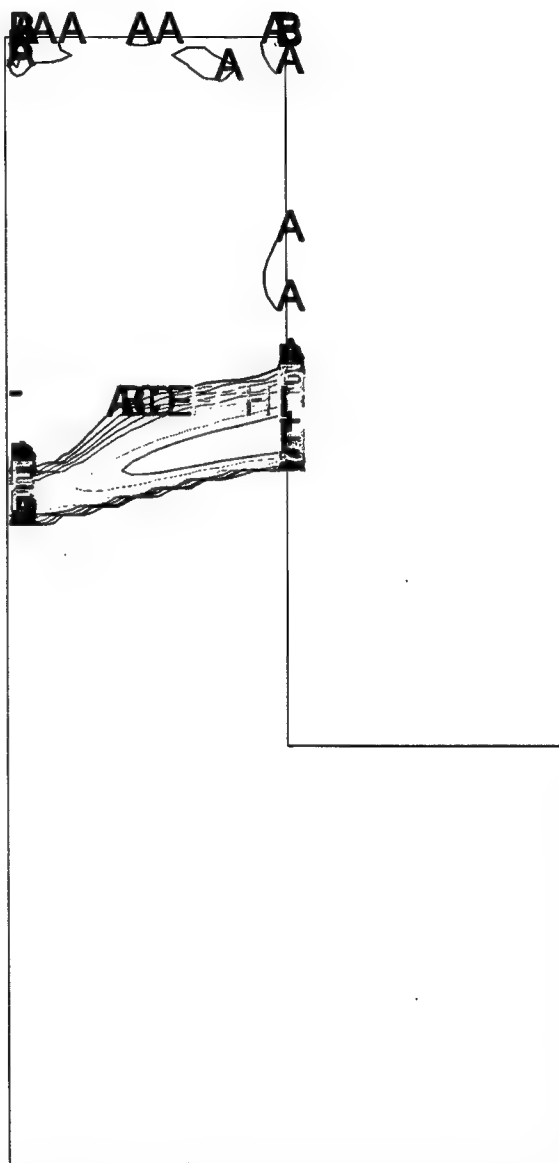
(b) T = 1.1  $\mu$ s

Figure 4-9. These ion density plots help reveal the cause for the shapes of the density profiles (see text) (Continued)



S1037 GEOM; CF2, 2EV, NITRO RADN  
 S1037H V9403.J  
 T = 1.150E-06 CYCLE = 12774  
 IONS / CC

- = 9.9851E+11  
 A = 2.5514E+12  
 B = 6.5192E+12  
 C = 1.6658E+13  
 D = 4.2564E+13  
 E = 1.0876E+14  
 F = 2.7790E+14  
 G = 6.9475E+14  
 H = 1.8144E+15  
 I = 4.6361E+15  
 + = 1.1846E+16



( c ) T = 1.15  $\mu$ s

Figure 4-9. These ion density plots help reveal the cause for the shapes of the density profiles (see text) (Continued)

S1037 GEOM; CF2, 2EV, NITRO RADN

S1037H V9403.J

T = 1.200E-06 CYCLE = 13357

IONS / CC

- = 9.9851E+11

A = 1.9138E+12

B = 3.6683E+12

C = 7.0310E+12

D = 1.3476E+13

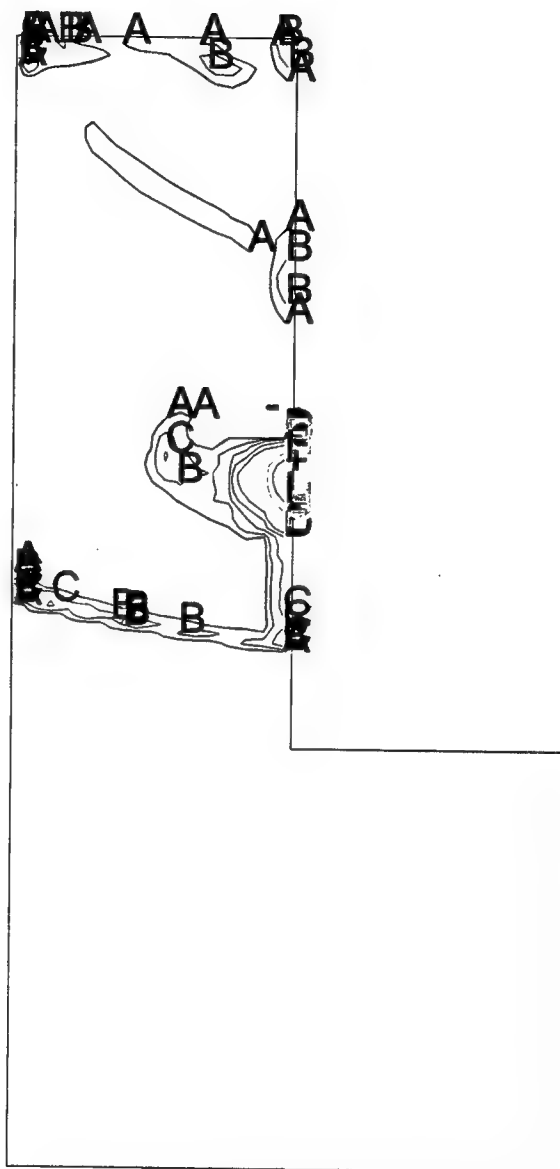
E = 2.5830E+13

F = 4.9510E+13

H = 1.8189E+14

I = 3.4862E+14

+ = 6.6821E+14



(d)  $T = 1.2 \mu\text{s}$

Figure 4-9. These ion density plots help reveal the cause for the shapes of the density profiles (see text) (Continued).

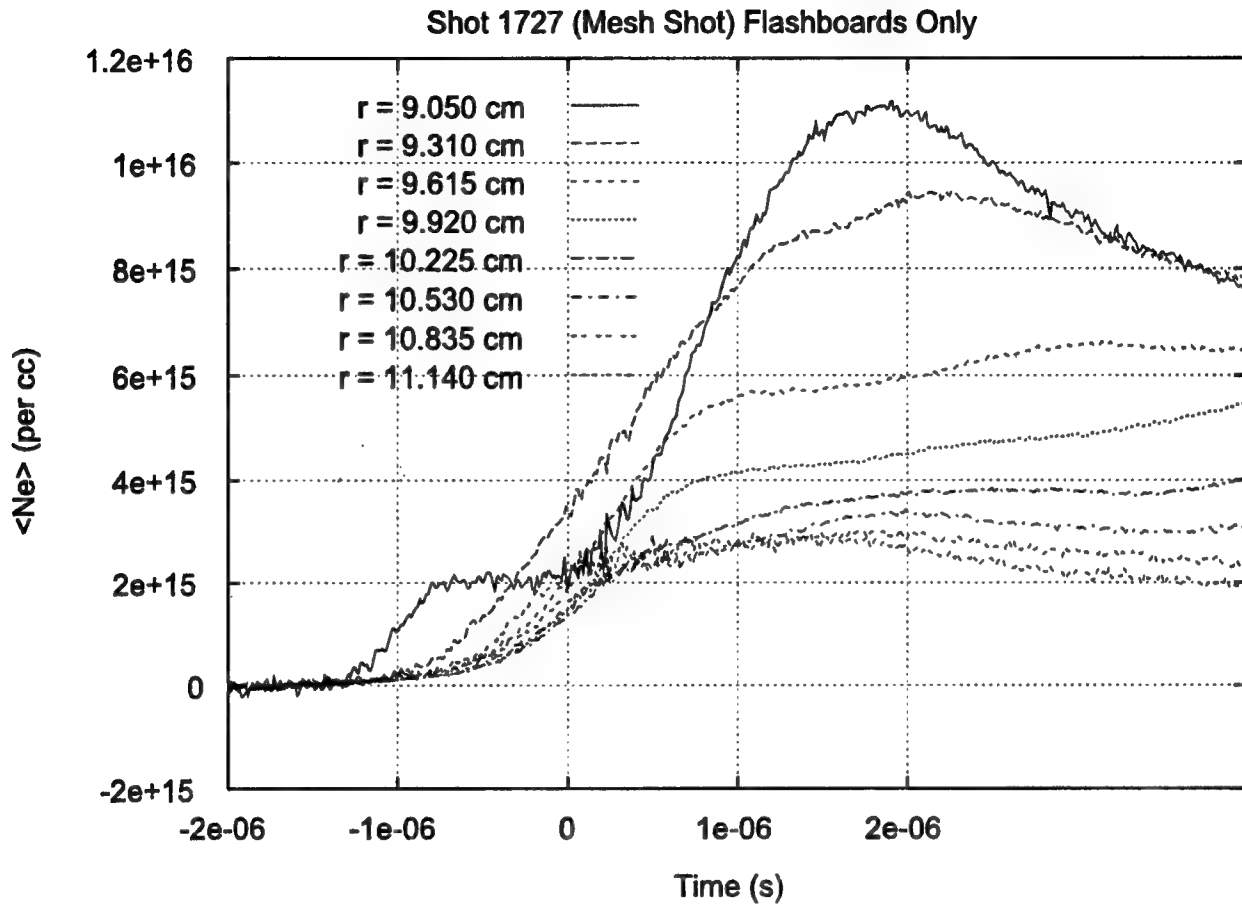


Figure 4-10. Experimental electron density for flashboard only case – no pulsed power.

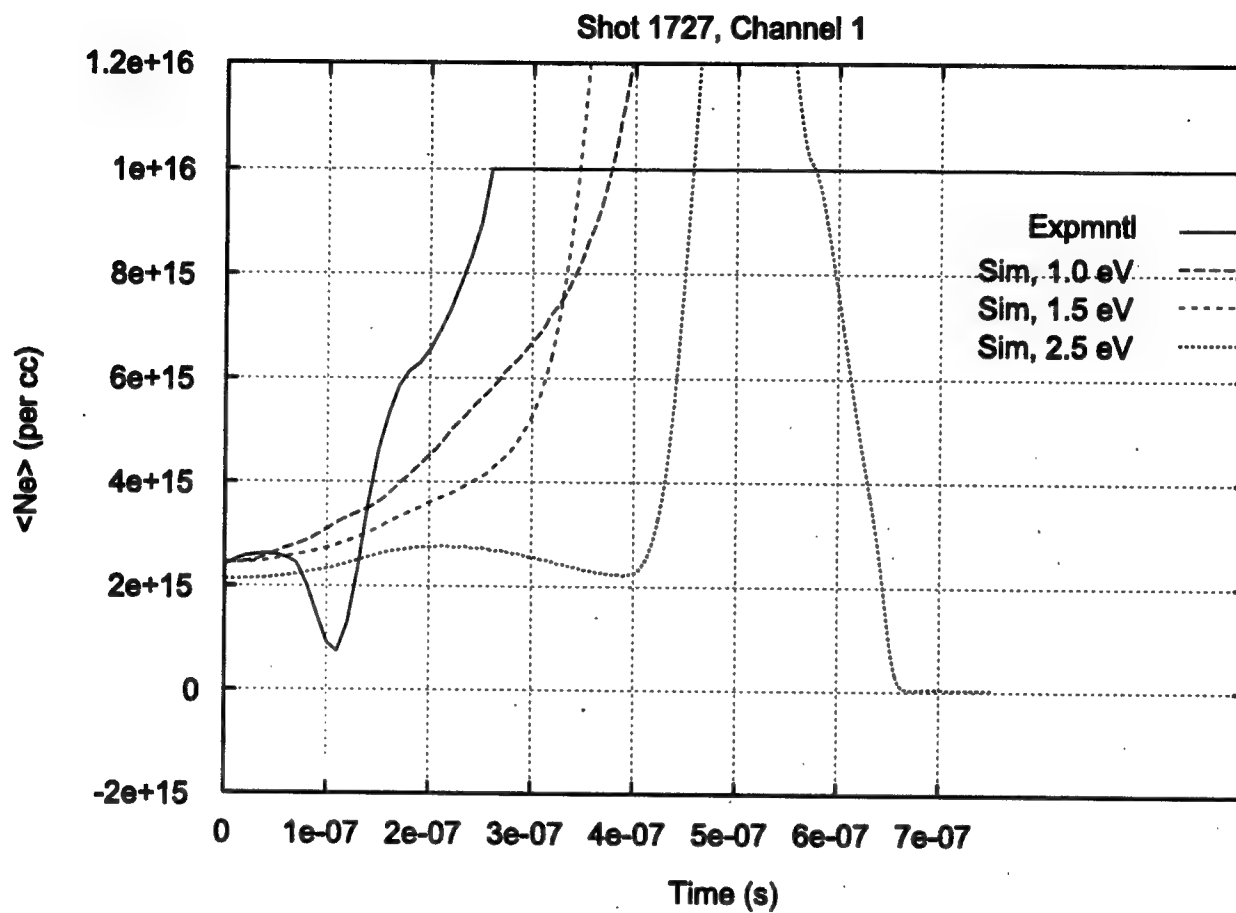


Figure 4-11. Comparison of measured and simulated electron densities for three simulation temperatures.

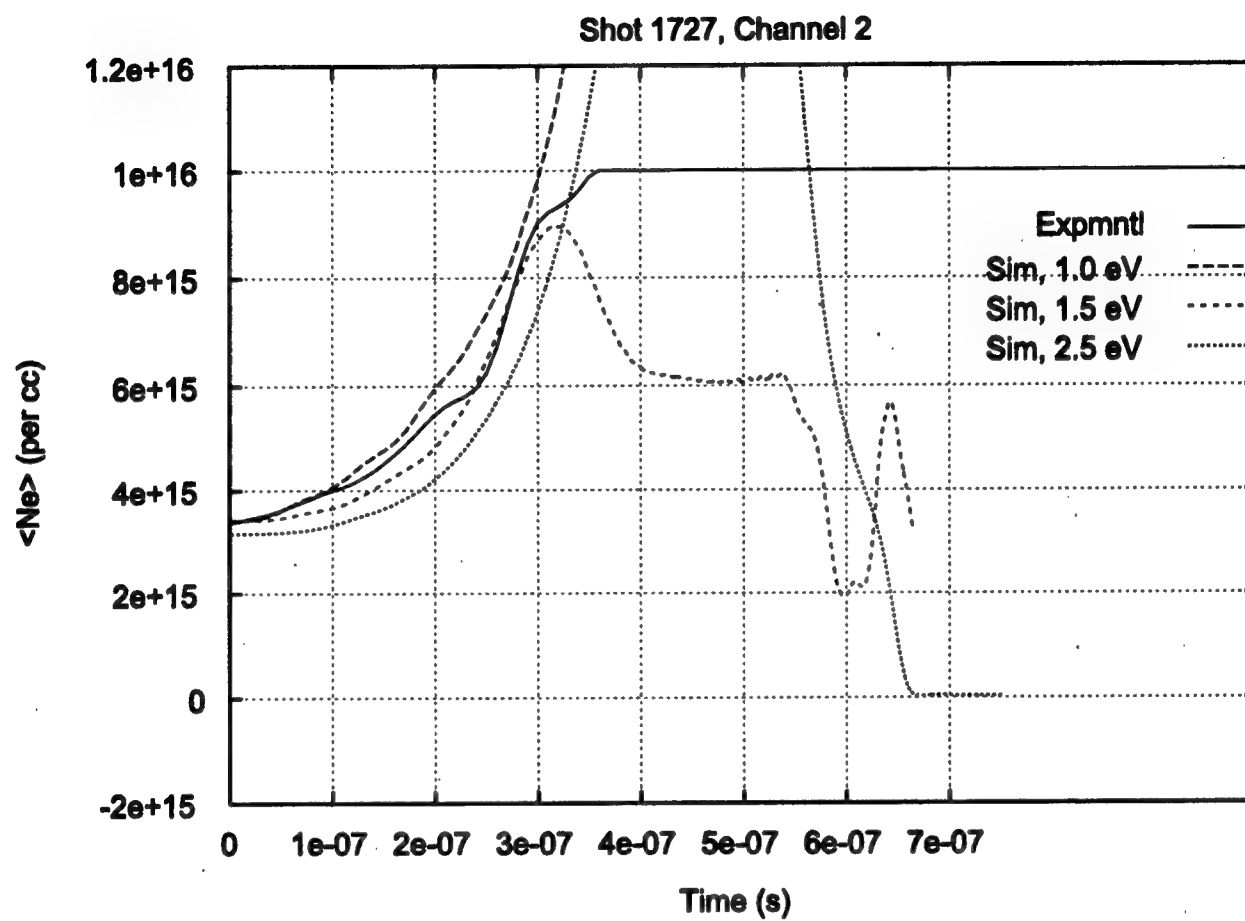


Figure 4-12. Comparison of measured and simulated electron densities for three simulation temperatures.

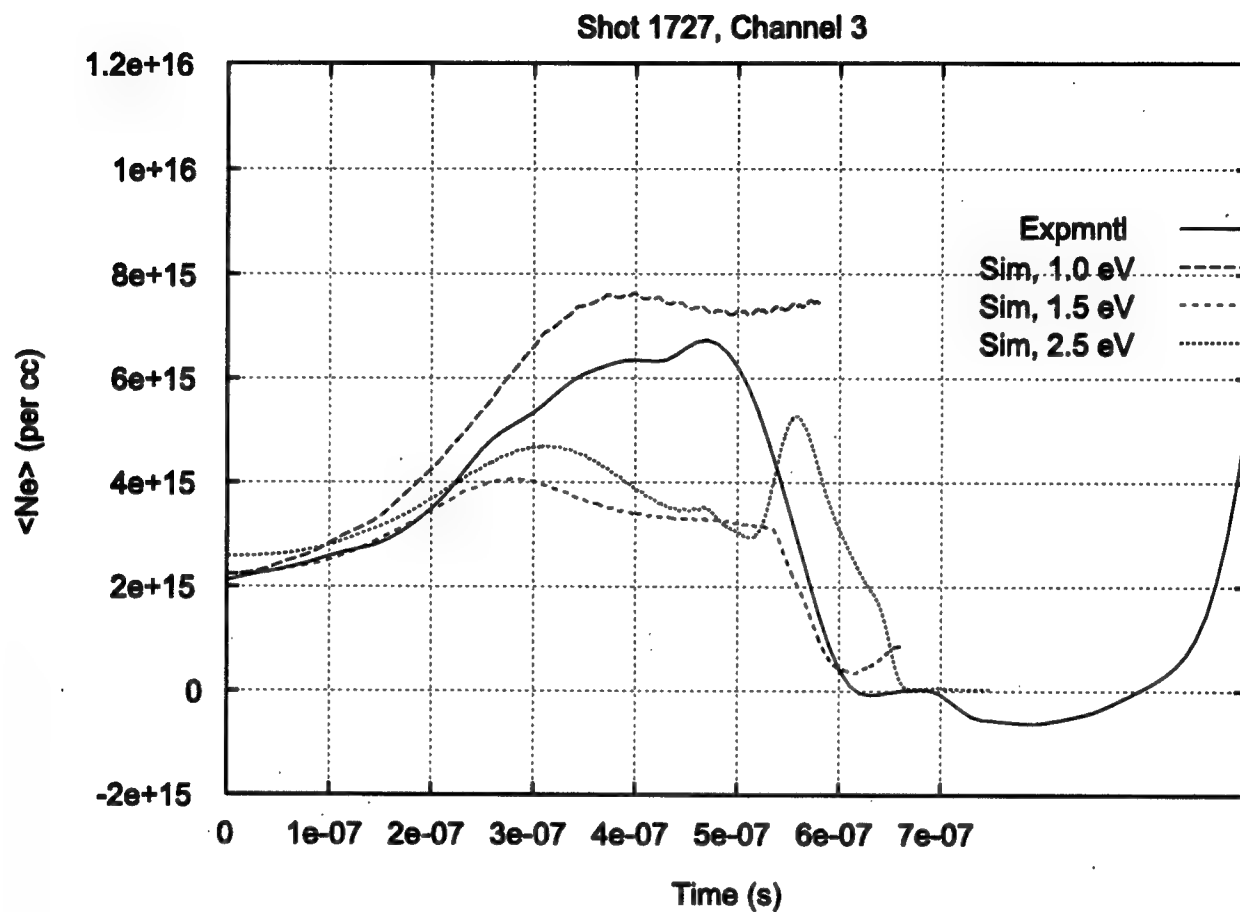


Figure 4-13. Comparison of measured and simulated electron densities for three simulation temperatures.

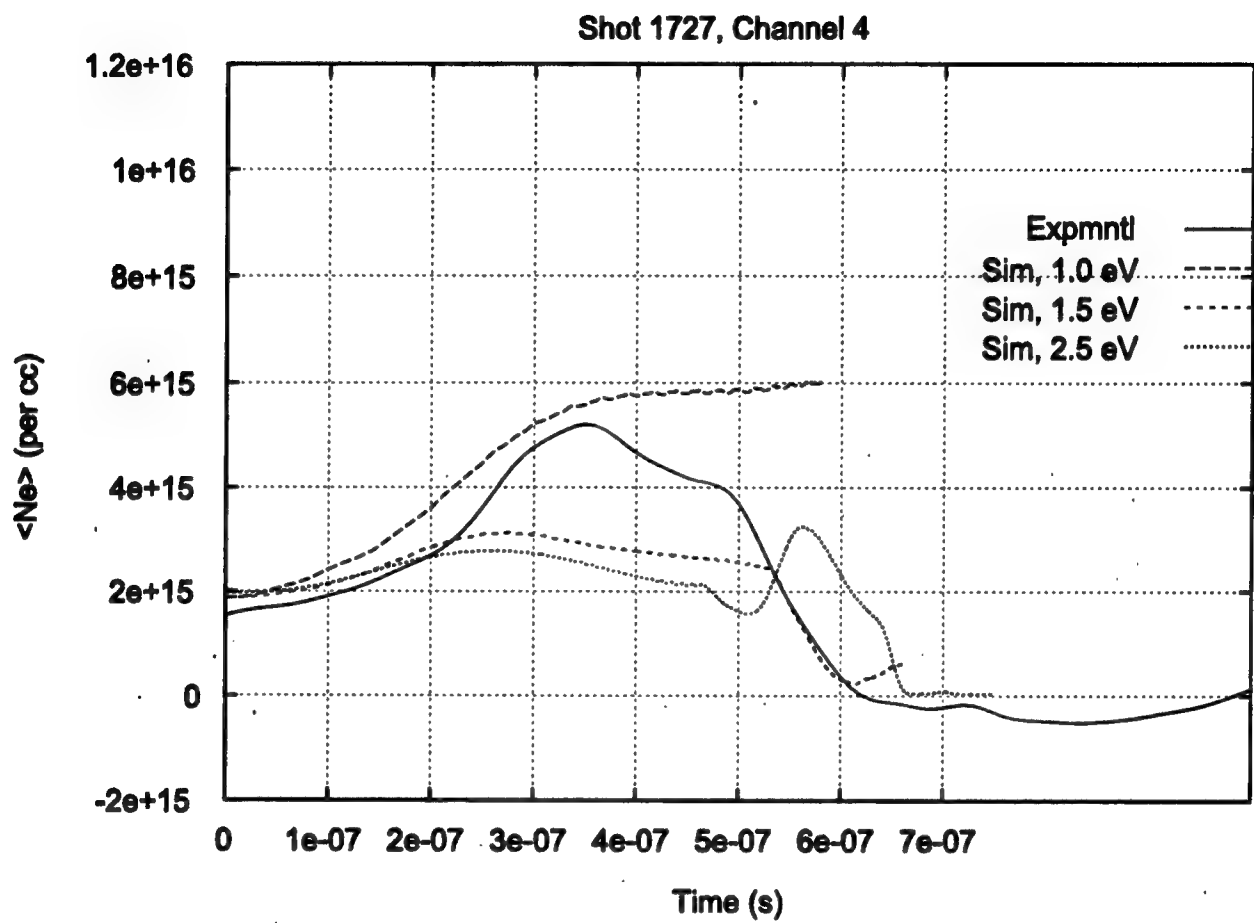


Figure 4-14. Comparison of measured and simulated electron densities for three simulation temperatures.

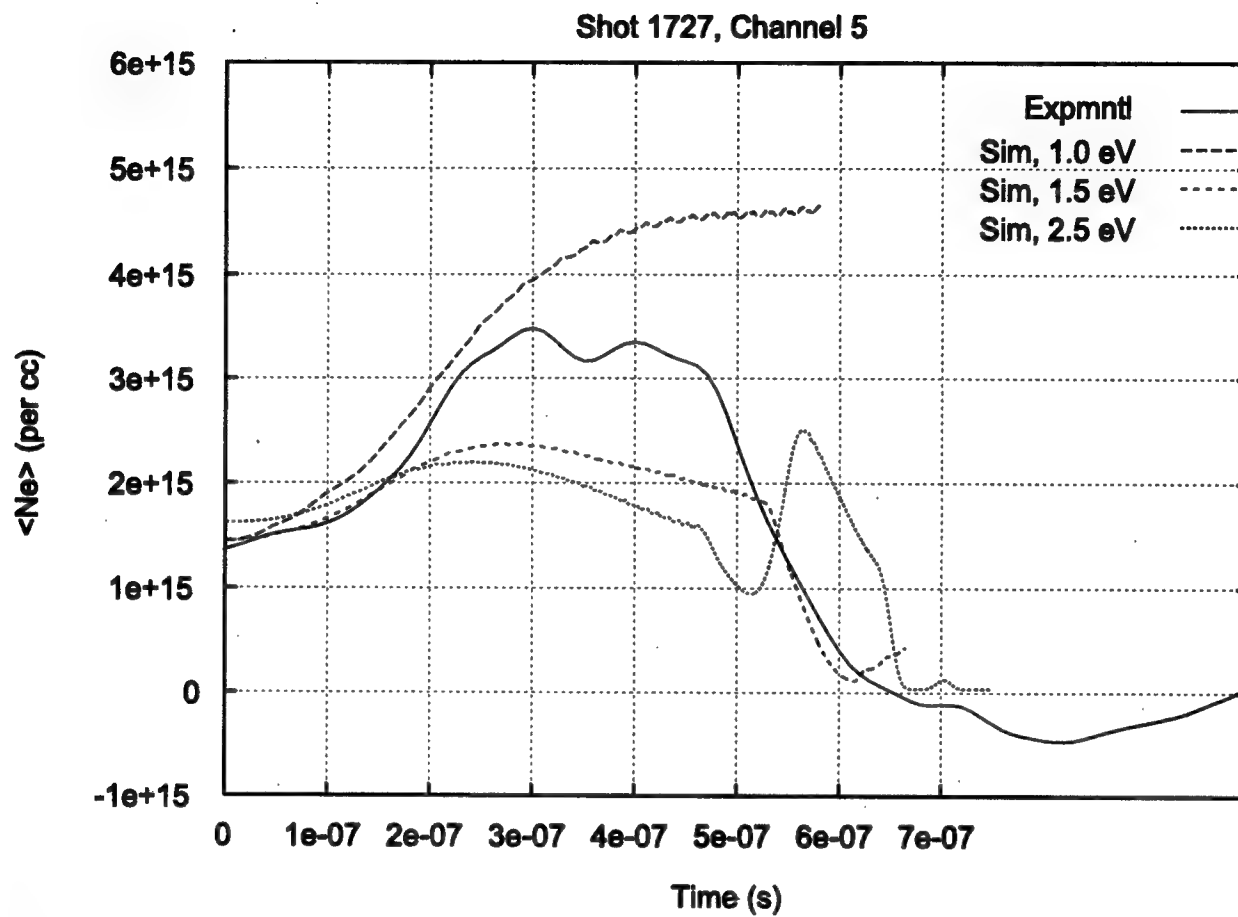


Figure 4-15. Comparison of measured and simulated electron densities for three simulation temperatures.



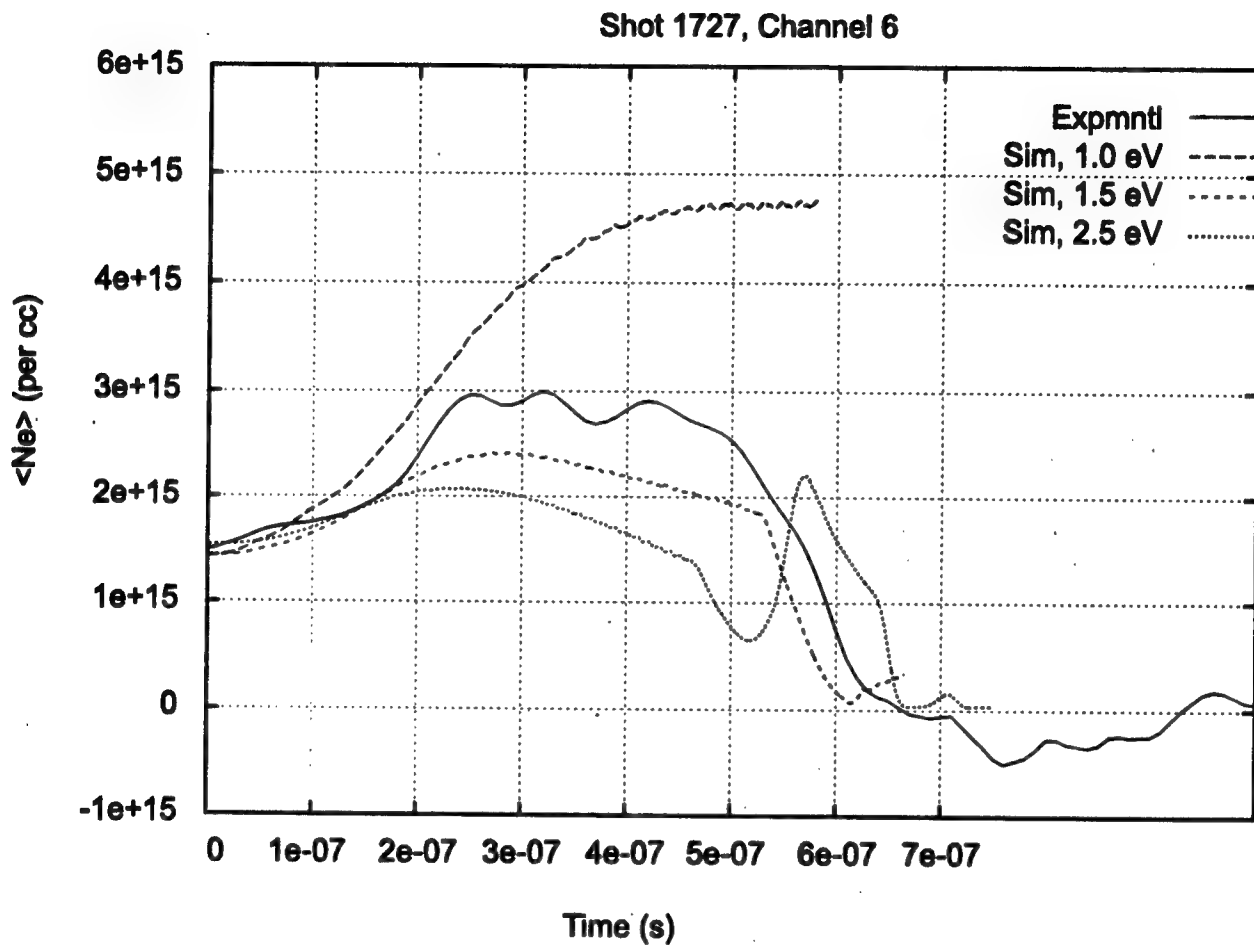


Figure 4-16. Comparison of measured and simulated electron densities for three simulation temperatures.

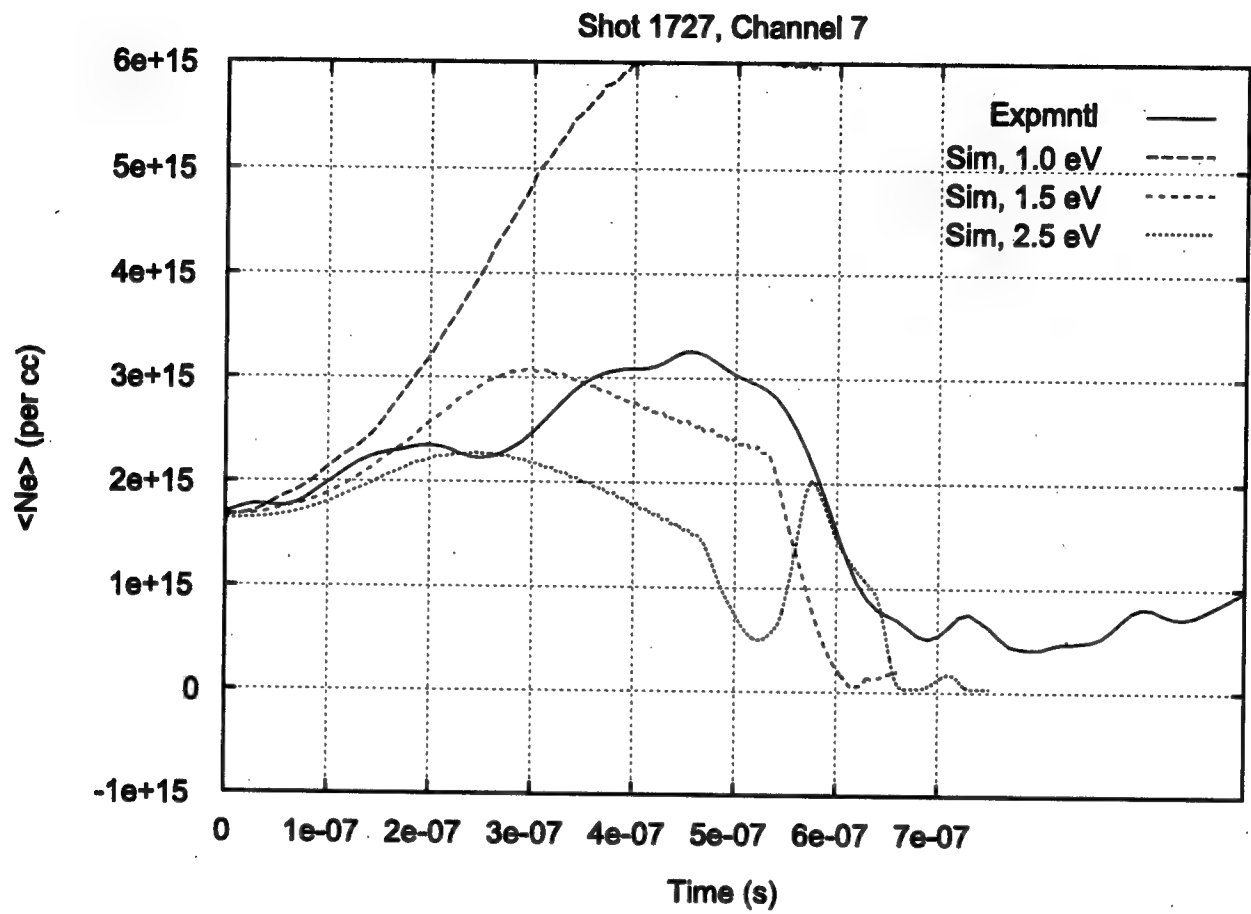


Figure 4-17. Comparison of measured and simulated electron densities for three simulation temperatures.

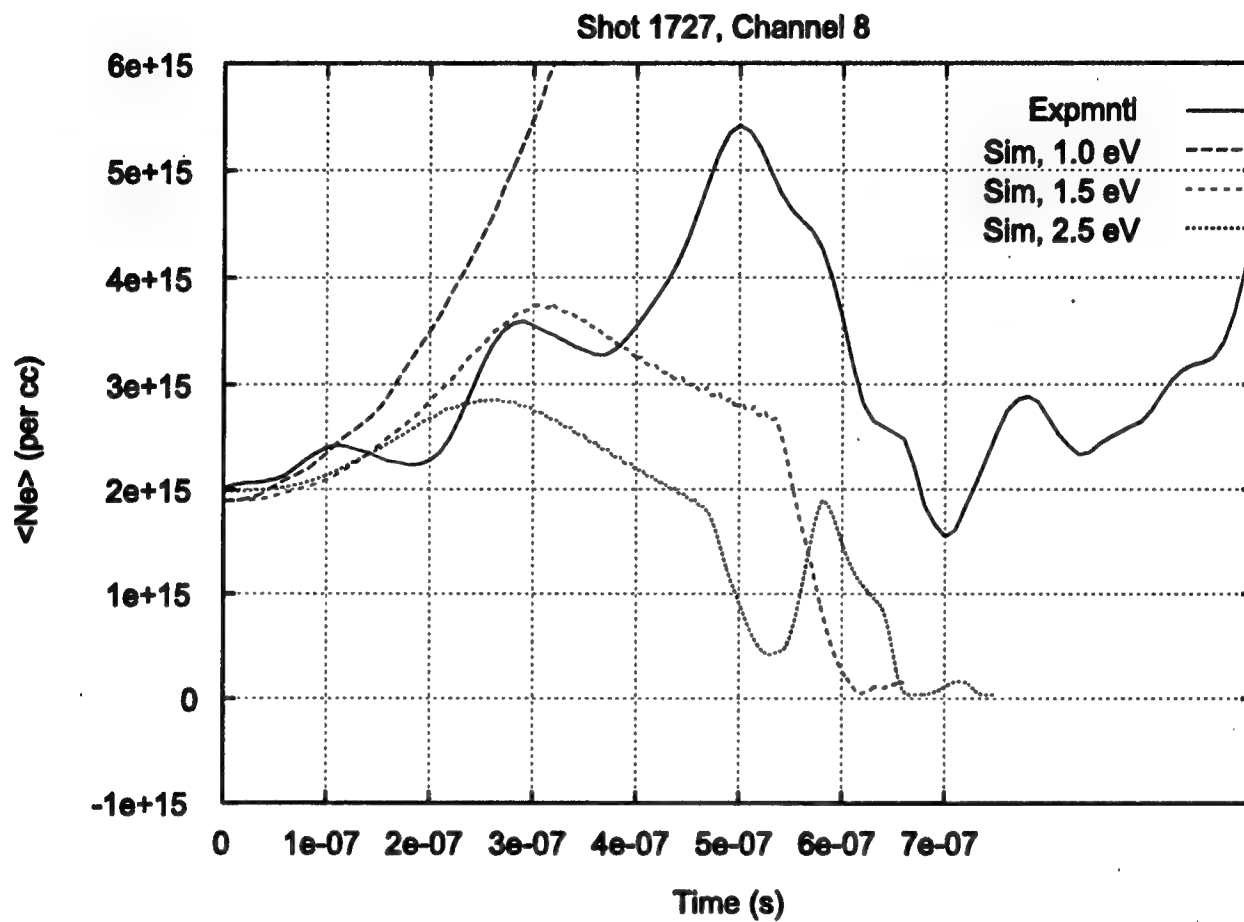
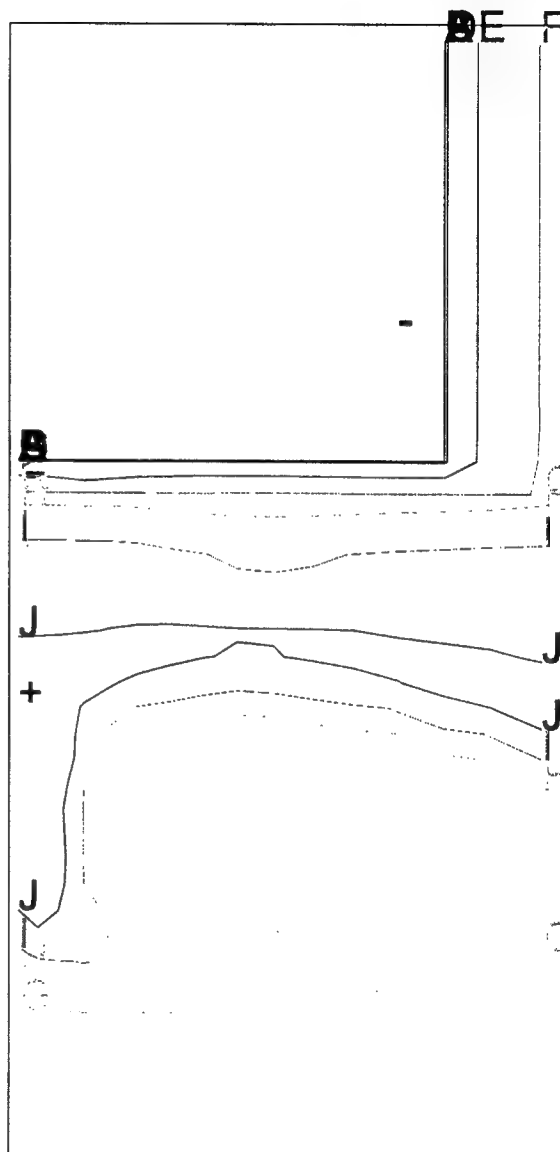


Figure 4-18. Comparison of measured and simulated electron densities for three simulation temperatures.

-= 2.1506E+05  
 A= 2.6514E+06  
 B= 3.2688E+07  
 C= 4.0299E+08  
 D= 4.9683E+09  
 E= 6.1251E+10  
 F= 7.5513E+11  
 G= 9.3099E+12  
 H= 1.1477E+14  
 I= 1.4150E+15  
 J= 1.7444E+16  
 += 2.1506E+17

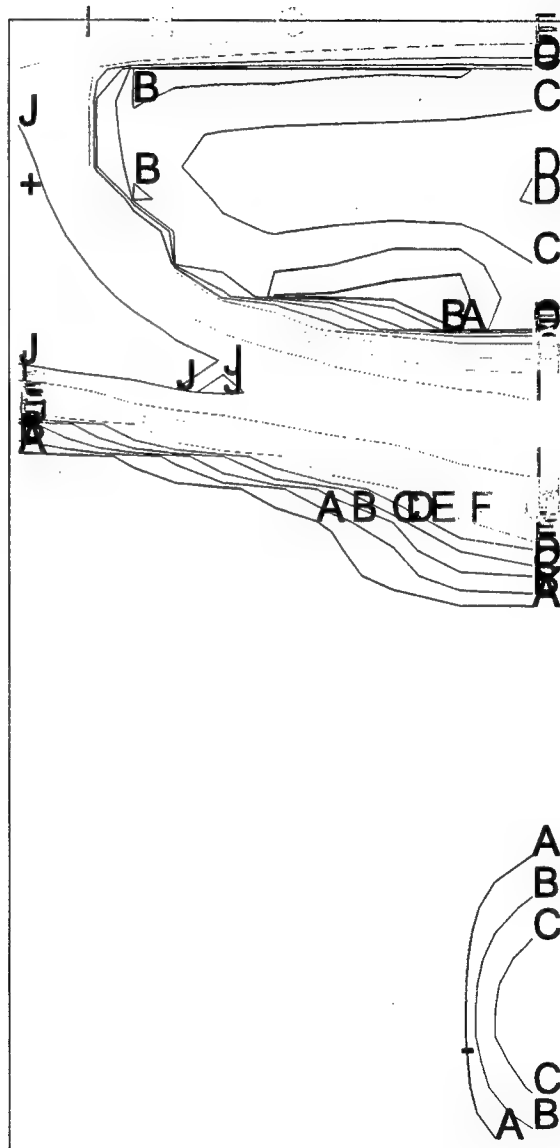


(a)  $T = 500$  ns

**Figure 4-19. Simulated electron density contours for a temperature of 1.5 eV at (a) 500 ns and (b) 600 ns.**

ACE4 SHOT 1727 (MESH ANODE): STILL PLASMA  
 S1727\_2 V9403.1  
 T = 6.000E-07 CYCLE = 4386  
 ELECTRONS / CC

- = 1.6109E+13  
 A = 3.1021E+13  
 B = 5.9737E+13  
 C = 1.1504E+14  
 D = 2.2153E+14  
 E = 4.2660E+14  
 F = 8.2151E+14  
 G = 1.5820E+15  
 H = 3.0435E+15  
 I = 5.8666E+15  
 J = 1.1297E+16  
 + = 2.1756E+16



(b) T = 600 ns

Figure 4-19. Simulated electron density contours for a temperature of 1.5 eV at (a) 500 ns and (b) 600 ns (Continued).

ACE4 SHOT 1727 (MESH ANODE): STILL PLASMA  
 S1727\_2 V9403.1  
 T = 4.001E-07 CYCLE = 1723  
 ELECTRONS / CC

= 8.9897E+04

A= 1.1083E+06

B= 1.3664E+07

C= 1.6845E+08

D= 2.0767E+09

E= 2.5603E+10

F= 3.1565E+11

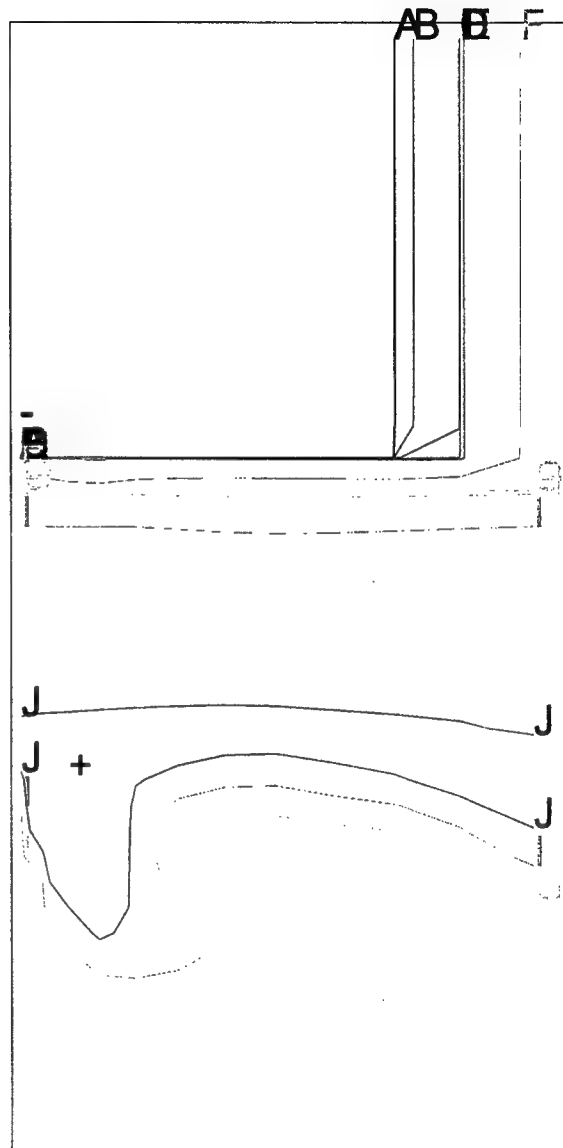
G= 3.8914E+12

H= 4.7313E+13

I= 5.9146E+14

J= 7.2919E+15

= 8.9897E+16

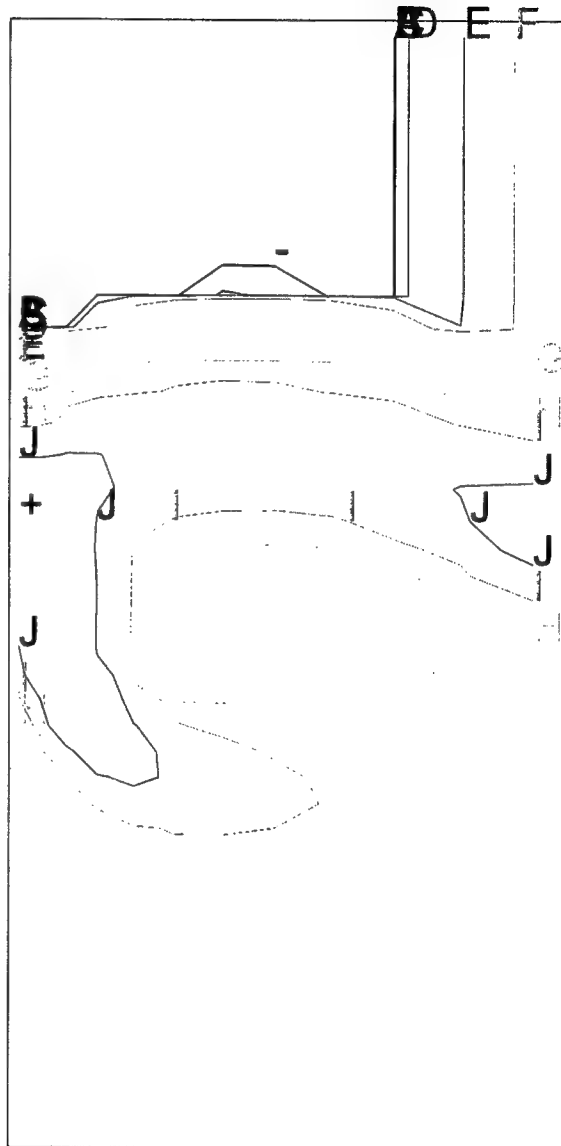


(a) T = 400 ns

Figure 4-20. Simulated electron number density contours for a temperature of 2.5 eV at (a) 400 ns (b) 500 ns and (c) 600 ns.

ACE4 SHOT 1727 (MESH ANODE): STILL PLASMA  
 S1727\_2 V9403.1  
 T = 5.000E-07 CYCLE = 2959  
 ELECTRONS / CC

- = 1.0801E+05  
 A = 1.3316E+06  
 B = 1.6417E+07  
 C = 2.0240E+08  
 D = 2.4952E+09  
 E = 3.0762E+10  
 F = 3.7925E+11  
 G = 4.6758E+12  
 H = 5.7343E+13  
 I = 7.1065E+14  
 J = 8.7612E+15  
 + = 1.0801E+17



(b) T = 500 ns

Figure 4-20. Simulated electron number density contours for a temperature of 2.5 eV at (a) 400 ns (b) 500 ns and (c) 600 ns (Continued).

ACE4 SHOT 1727 (MESH ANODE): STILL PLASMA

S1727\_2 V9403.1

T = 6.000E-07 CYCLE = 4386

ELECTRONS / CC

- = 1.6109E+13

A = 3.1021E+13

B = 5.9737E+13

C = 1.1504E+14

D = 2.2153E+14

E = 4.2660E+14

F = 8.2151E+14

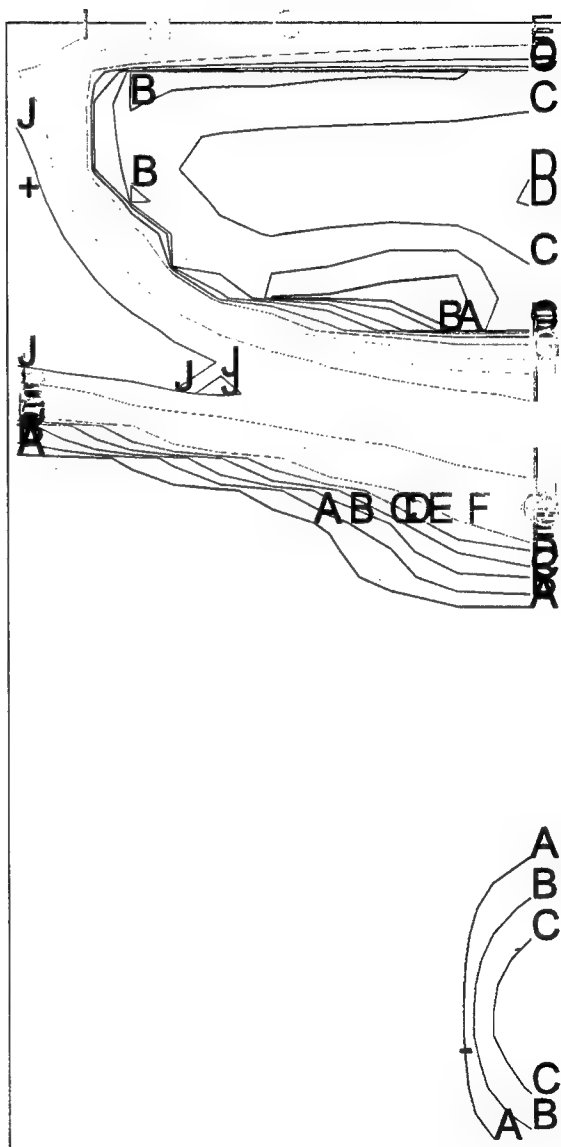
G = 1.5330E+15

H = 2.0455E+15

I = 5.8666E+15

J = 1.1297E+16

+ = 2.1756E+16



(c) T = 600 ns

Figure 4-20. Simulated electron number density contours for a temperature of 2.5 eV at (a) 400 ns (b) 500 ns and (c) 600 ns (Continued).



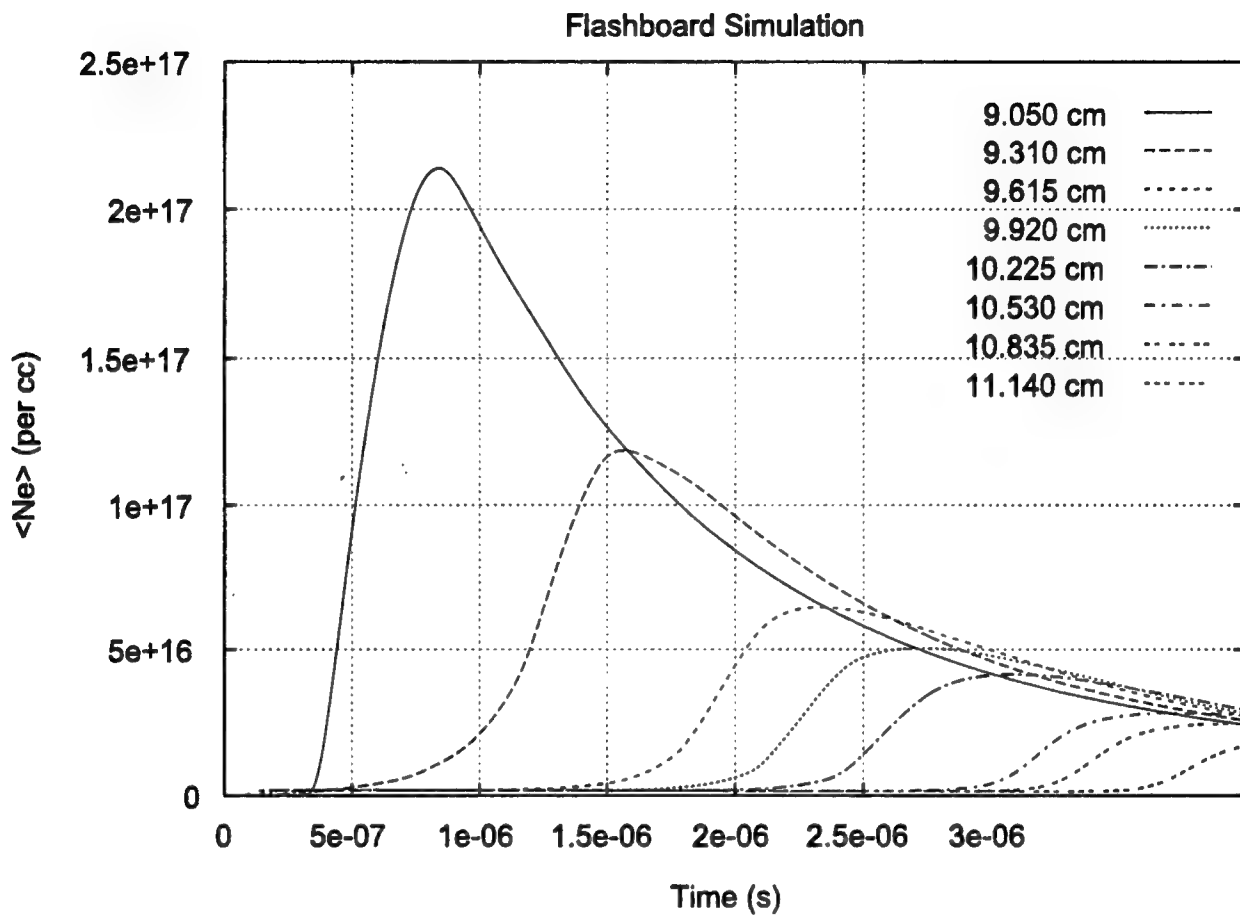


Figure 4-21. Line integrated electron densities for a flashboard only simulation.

ACE4 SHOT 1727 (MESH ANODE): PRESHOT TESTS  
 MESH\_1 V9403.1  
 T = 4.015E-06 CYCLE = 462  
 ELECTRONS / CC

- = 1.0398E+15  
 A = 4.2158E+15  
 B = 7.3918E+15  
 C = 1.0568E+16  
 D = 1.3744E+16  
 E = 1.6920E+16  
 F = 2.0096E+16  
 G = 2.3272E+16  
 H = 2.6448E+16  
 I = 2.9624E+16  
 J = 3.2800E+16  
 + = 3.5976E+16

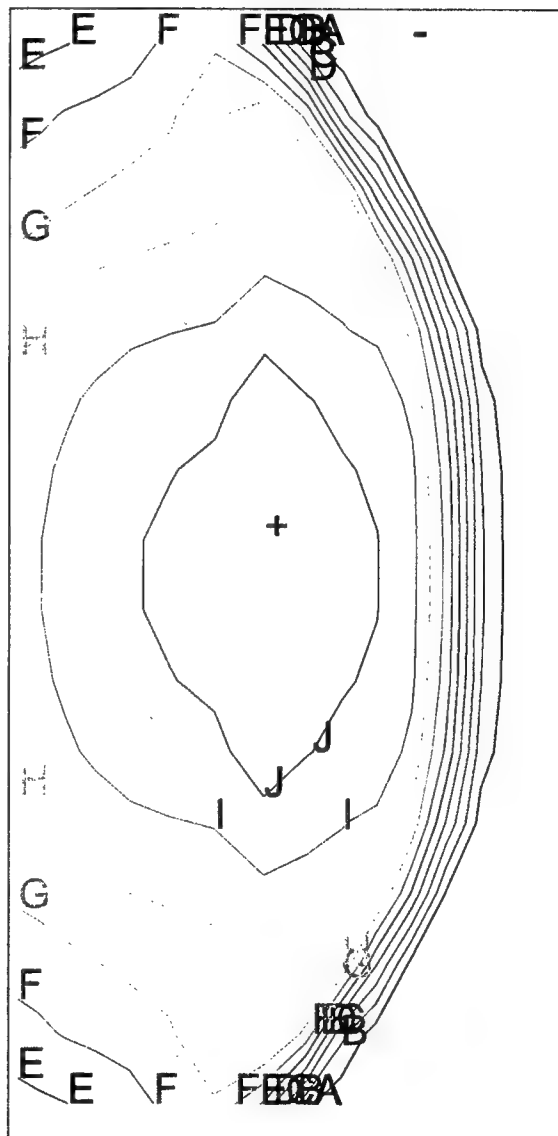


Figure 4-22. Simulated electron density contours at a time when different LOS-signals have converged (see text).

## SECTION 5

### THE ROLE OF NEUTRAL ATOMS IN PLASMA OPENING SWITCHES

During the past year substantial data has been obtained on the in-situ properties of plasmas in opening switch configurations in microsecond conduction time inductive energy store systems. The measurements have been made both during the injection phase of the plasma prior to the application of pulsed power and during current conduction. They include interferometric measurements of time dependent electron densities at the Hawk and ACE 4 facilities, and spectroscopic observations of time dependent and time integrated relative line intensities from various neutral and ionized species in the switch plasma. These measurements become especially valuable when correlated with the times of occurrence of electrical events, such as the onset of load current or of voltage at particular locations in a diode. Some of the salient experimental results are summarized below.

#### 5.1 SALIENT EXPERIMENTAL RESULTS.

Figure 5-1 shows the Ace 4 configuration used in a series of experiments carried out by Thompson, et al. (References 9 and 10). This configuration is essentially axisymmetric except for the anode structure that allows the flashboard generated plasma to enter the space between anode and cathode. In this configuration with a 6 cm cathode radius, the cylindrical istovepipe region downstream of the switch (in the direction of power flow) connects it to a 100 nH inductor. Nine thin beams of He-Ne laser light pass through the interelectrode space parallel to the axis of symmetry at the distances from the cathode indicated in Figure 5-2. This figure shows a typical electron density distribution across the anode-cathode gap as a function of time after firing the flashboards, but before the flow of any current through the switch. The densities are extracted from the measured line integrated densities assuming invariance with respect to axial location over the nominal 20 cm length of the switch. Figures 5-3, 5-4 and 5-5 show generator and load current wave forms simultaneously with the switch voltage and electron density at the indicated radial positions of the laser beams. These three sets of results differ in the delay time between the firing of the flashboards and the firing of the Marx banks. Shot 1305 with the shortest delay time, 2.3  $\mu$ s, yields the largest peak voltage; observe that relative to shots 1304 and 1303, the density remains low during the rise of voltage to its peak value.

Figures 5-6 and 5-7 show two configurations with a 20 cm. cathode and flashboards located 17.3 cm from the cathode. A neon gas is puffed into these configurations at the top most

position in the vicinity of the center line. The electrical boundary of each configuration is defined roughly by a coarse wire grid at the top of each configuration. The openings of the grid are sufficiently large that any switch plasma reaching them would pass freely through them. The second configuration, Figure 5-7, extends 25 cm beyond the uppermost position of the configuration without an extension. Figures 5-8 through 5-14 show density profiles at positions extending from 0.4 to 2.5 cm from the cathode for two shots, shot 1937 with no extension and shot 1959 with the extension. Each figure also shows the voltage waveforms for the two shots. As in the experiments with the 6 cm cathode strong temporal variations in density are correlated with the development of voltage. First there is a rapid fall in density preceding or coincident with the onset of voltage, except for the probes which are nearest the electrodes. Following the fall there is in general a rapid increase of density during the voltage pulse. However, near the middle of the gap in the case without the extension, a minimum of density corresponding to the limit of detection of the interferometry lasts for several hundred nanoseconds before the density again increases.

It is instructive to compare the above results with corresponding results obtained by Weber, et al. at the Hawk facility (Reference 11). Generator and load current wave forms are shown in Figure 5-15 together with density measurements along axial lines of sight at distances from the cathode ranging from 3 to 17 mm. The most significant feature of this sequence for our purposes is that except for the probe nearest the cathode the late time increase of density occurs only after current transfer to the load is complete. Since we expect that the switch voltage is generated during the current transfer, the rather late appearance of the density increase is in contrast to what is observed generally in the ACE 4 experiments, but is similar to what is observed at the center of the gap in the ACE 4 shot 1937. Perhaps another significant feature of the Hawk results is the apparent saturation of electron density between 1.3 and 1.5  $\mu\text{s}$  exhibited in the last three frames of Figure 5-15. Possible reasons for the similarities and differences in the data obtained from Hawk and ACE 4 will be considered in Section 3.

The behavior of the density profiles in relation to the current and voltage wave forms leads us to hypothesize that neutral gas is being ionized as the voltage develops across the switch. If this gas is located behind the primary conduction front of the POS as indicated in Figure 5-16, then potentially it can lead to shorting of the switch before current transfer to the load is complete. For this to occur the ionization must take place more rapidly than the switching, and must constitute a current path of sufficiently low impedance. This view is supported by recent observations by Coleman showing H $\alpha$  radiation late in the power pulse from the middle of the region occupied initially by the injected switch plasma. The 440 angstrom bandpass used in the

experiment also accepts continuum radiation. It seems likely that the increase of intensity observed beyond  $1.1 \mu\text{s}$  is associated with radiation from free electrons following complete ionization of the hydrogen. The experimental arrangement used for the measurements is shown in Figure 5-17. The lens is apertured to view a region whose radial extent is about 2 mm. Figure 5-18 shows the relative  $\text{H}\alpha$  and high photon energy ( $>5 \text{ keV}$ ) intensities as a function of time together with the voltage at the position of the POS obtained by inductively correcting the voltage measured in oil near the insulator stack. The line profiles shown in Figure 5-19 are for time intervals ranging from  $0.6\mu\text{s}$  to  $0.8\mu\text{s}$  for shot 1937. The figure also shows preshot profiles for hydrogen and singly ionized carbon. The asymmetries in the line profiles with a clear bias toward the blue with pulsed power indicate that the hydrogen atoms are moving in the direction of power flow with speeds in excess of  $10 \text{ cm}/\mu\text{s}$ .

In the following sections we shall consider the significance of the preceding interferometric and spectroscopic observations as well as possible sources of neutral gas on the generator side of the POS, mechanisms for ionizing the gas, and the mechanism leading to a low impedance current path through the gas.

## 5.2 POSSIBLE SOURCES OF NEUTRALS.

Three mechanisms are considered which can lead to the presence of neutral atoms behind the conduction front in a microsecond POS. First, neutral atoms may be left behind as charged components of the plasma are coupled into the hydrodynamic disturbance that accompanies the rising switch current coming from the generator. To analyze this situation let us suppose that the conduction phase of the switch is dominated by MHD effects, rather than by electron magnetohydrodynamic effects. We therefore imagine that the disturbed mass and current are carried in a thin layer of thickness  $T$ . Viewed from the frame of reference of the snowplow the undisturbed plasma approaches it with a speed  $v$ . We suppose that all ions and electrons are coupled into the plow, but that ion neutral collisions are required to couple neutral atoms to the moving mass. The cross section for ion-neutral collisions is given by:

$$\sigma = 2.210\pi Z e \sqrt{\frac{\alpha}{\mu M_H}} / v \quad (5.1)$$

where  $\alpha$  is the polarizability of the neutral atom,  $e$  the charge on a proton,  $Z$  the mean charge state of ions in the snowplow,  $\mu$  the reduced mass of the colliding particles in units of the

hydrogen mass,  $M_H$  the mass of hydrogen, and  $v$  the relative velocity, all in cgs units (Reference 12). As a condition that the neutral atom not be swept up we adopt the criterion:

$$NT\sigma < 1 \quad , \quad (5.2)$$

where  $N$  is the density of ions in the snowplow. For a snowplow with a uniform acceleration  $a$ , corresponding to a linearly rising current,

$$NT = N_0 \frac{1}{2} at^2 \quad , \quad (5.3)$$

where  $N_0$  is the ion density in the undisturbed plasma and  $t$  is the time that current has been flowing. Since  $v=at$ , neutrals are left behind for times satisfying

$$N_0 \sigma v t < 2 \quad .$$

For fluorine, the dominant element in Thompson's experiments,  $\alpha=0.557 \times 10^{-24} \text{ cm}^3$  (Reference 13) and the preceding inequality reduces to:

$$9.6 \times 10^{-10} N_0 t < 2 \quad ,$$

giving  $t < 0.4 \mu\text{s}$  for an initial ion density equal to  $5 \times 10^{15}/\text{cc}$ . Thus for a conduction time of one microsecond one might expect that a substantial fraction of the neutrals originally in the switch would be left behind. In a more general vein, neutrals will be more efficiently swept up the higher the polarizability and the smaller the reduced mass.

So far we have ignored the possibility that neutrals may become ionized by electron impact while crossing the "snowplow." To evaluate this possibility we consider the ionization rate of atoms with ionization potential  $I$  electron volts (NRL formulary):

$$S(\Theta) = 10^{-5} \frac{(\Theta/I)^{1/2}}{I^{3/2} (6 + \frac{\Theta}{I})} \exp(-\frac{I}{\Theta}) \text{ cm}^3 / \text{sec} \quad (5.4)$$

produced by a maxwellian distribution of electrons at a temperature  $\Theta$  electron volts.

The table below summarizes ionization rate constants for fluorine over a range of temperatures.

Table 5-1. Ionization rates for neutral fluorine.

$\Theta$ eV	$S(\Theta)$ cc/sec
1	2.3(-16)
5	3.9(-10)
10	3.0(-9)
50	1.8(-8)

The time a neutral atom spends in the snowplow is given by:

$$\delta t = T/v = N(0)x/N(t)v = 0.5tN(0)/N(t) = 0.5tN(0)Z/n, \quad (5.5)$$

where  $x$  is the distance the snowplow has moved.

The pertinent quantity for estimating the probability of ionization is:

$$f = nS(\Theta)\delta t = N(0)S(\Theta)Zt/2, \quad (5.6)$$

where  $Z$  is the mean degree of ionization per ion. For temperatures less than about 5 eV relatively few of the neutrals would be ionized for  $t < 0.5 \mu s$ , but for temperatures larger than 5 to 10 eV very few neutrals would escape ionization as the snowplow passed over them.

Let us now consider how Teflon flashboards may compare with other types of plasma sources. The most obvious feature of Teflon ( $CF_2$ ) is the large ionization potential of fluorine, 17.418 eV. In comparison, the ionization potential of other atoms found in POS plasmas are 11.256 eV(C), 13.614 eV(O), 14.53 eV(N), and 13.595 eV(H). Thus for similar conditions of temperature and density, neutral fluorine will be more abundant than neutral species of the other components listed here.

The second means by which neutrals may appear behind the swept up plasma is by means of continued injection from the plasma source. Even as the magnetic field in the switch gap builds up plasma will continue to be injected at least until the magnetic pressure exceeds the stagnation

pressure of the impinging plasma. Ionized components should be swept up, but neutral components may be left behind much as described in the preceding paragraph. Neutrals may continue to enter even when the magnetic pressure exceeds the stagnation pressure. The continued injection of neutrals would require temperatures of several electron volts so that the neutrals may separate from the ions by virtue of a large ion-neutral mean free path, perhaps of the order of a centimeter, and have sufficient velocity to cross the interelectrode space in less than a microsecond. Reliable estimates of neutral densities associated with this effect are difficult to make.

The third mechanism leading to the presence of neutrals behind the snowplow consists in the neutralization and scattering of ions in the snowplow impacting on electrode surfaces and the sputtering of material from the surface. This may occur even before the onset of pulsed power as injected ions that scatter as neutrals from the surface, or eject neutrals from the surface, in the direction toward the generator. Such neutrals should not participate at all in the snowplow. Among the sputtered materials we consider hydrocarbons, which may be weakly bound to the surface. It is known that ions with speeds  $\leq$  approximately 10 cm/ $\mu$ s neutralize with a near unit probability when they strike a metallic surface (Reference 14). This could be the most copious source of neutrals with speeds sufficient to fill the space between electrodes. The yield Y of neutral densities arising from these processes may be obtained from Figures 5-20 through 5-22 (References 15 and 16, respectively). The reflected energy R allows the speed v of particles emanating from the surface to be determined from:

$$1/2mv^2 = 1/2(R/Y)MV^2$$

where m (M) and v(V) are the mass and speed of the particle leaving(striking) the surface. In the case of hydrogen with a surface binding energy of 0.25 eV and an incident ion energy of 1 keV the speed of the sputtered hydrogen is 3 cm/ $\mu$ s. The snowplow speeds V achieved in a 20 cm long switch conducting for 1  $\mu$ s, typical of ACE 4 operation, are between 2 cm/ $\mu$ s and 4 cm/ $\mu$ s in the last half of the conduction phase. With about one half of this energy directed toward the electrode surfaces it is reasonable to expect that sputtered hydrogen could extend throughout the anode-cathode gap. The contribution to switch impedance by hydrogen or any other neutral species in the gap would depend on whether it becomes ionized.



### 5.3 IONIZATION AND HEATING OF THE GAS.

#### 5.3.1 Seeding of the Gas by Photoionization.

Given an initial supply of electrons in the gas, it would eventually ionize rapidly as a result of joule heating once the voltage associated with switch opening develops. One possibility for providing an initial electron seed is ionization by photons emitted from the snowplow.

Resonance line photons from FII, for example, have sufficient energy to ionize FI or hydrogen. To estimate the photon flux carried in the line we suppose that the snowplow is optically thick over much of the breadth of this line. The optical depth at line center for a Doppler broadened line is given by:

$$d = 5.4 \times 10^{-9} \lambda (\mu / \Theta)^{1/2} N_F l \quad (5.7)$$

where  $N_F$  is the concentration of ground state FII ions and  $l$  is the thickness of the snowplow. The product of these two quantities is equal to the product of the initial concentration and the distance  $x$  the snowplow has moved assuming that the ionization has not significantly depleted the amount of FII in the plow. If such depletion has occurred then radiation from higher ion stages would ionize the neutral gas. For  $N_F(0) = 5 \times 10^{15} \text{ cm}^{-3}$ ,  $x=4\text{cm}$ , a mass  $\mu = 19$  for fluorine, a wavelength  $\lambda=6 \times 10^{-6} \text{ cm}$ , and a temperature  $\Theta = 10 \text{ ev}$ ,  $d=902$ . The optical depth reduces to one at frequencies from the line center given by:

$$\Delta \nu / \nu = 7.7 \times 10^{-5} (\Theta / \mu)^{1/2} (\ln d)^{1/2} \quad (5.8)$$

The bandwidth over which the emission from this layer is saturated at the black body level is approximately twice  $\Delta \nu$ . The flux of photons radiated by the snowplow in this frequency band is approximately:

$$f = \frac{4 \pi \nu^2 \Delta \nu}{c^2 \frac{h \nu}{e^{\frac{h \nu}{\Theta}} - 1}} \quad (5.9)$$

Using a wavelength of 606 angstroms and a temperature of 10 ev gives:

$$f = 3.6 \times 10^{22} \text{ photons/cm}^2 \text{ sec}$$

as a rough estimate of the radiation flux in the resonance line. This estimate is rather insensitive to the number of ground state ions and to the thickness  $l$ . The photoelectrons produced from neutral fluorine by this flux have a mean energy of about three electron volts, which is about 20% of the ionization threshold of FI. Assuming that the photoionization cross section does not differ markedly from its threshold value of 6 megabarns (Reference 17), this flux, if not substantially diluted by distance or by absorption at surfaces, would produce electrons at a rate:

$$S_p = N_F(0) f \sigma_p \text{ electrons} \cdot \text{cm}^{-3} \cdot \text{sec}^{-1} \quad (5.10)$$

For the chosen values of parameters this amounts to  $10^{21} \text{ electrons cm}^{-3} \text{ sec}^{-1}$ , a rate sufficient to provide seed electrons in the quantity and on the time scale required to enable rapid gas breakdown to occur with the onset of voltage. In Section 5.3.2 we incorporate photoionization in a more complete model of neutral gas breakdown.

### 5.3.2 Joule Heating and Collisional Ionization.

The partially ionized gas resulting from photoionization, or any other process, exists in the magnetic field arising from the current conducted by the well ionized snowplow. One such other process is collisional ionization once the electrons already present in the plasma are heated by electric fields to temperatures of 5 or 10 eV. To describe this process we assume that the electron's dynamics is described by ohm's law;

$$\nu V = -\frac{e}{m} \left( E + \frac{V \times B}{c} \right) \quad (5.11)$$

where  $\nu$  is the electron collision frequency,  $V$  is the velocity of the electron fluid,  $E$  is the electric field, and  $B$  the magnetic field in the plasma. The electric field is taken to be uniform in the anode cathode gap and to be in the radial direction, that is in the direction from anode to cathode. The magnetic field is in the direction of the ignorable  $\phi$  coordinate describing rotations about the axis of symmetry of the axisymmetric system. The collision frequency  $\nu$  is assumed to

arise primarily from electron-ion collisions, a good assumption once the degree of ionization exceeds a few tenths of 1%. We approximate  $\nu$  by:

$$\nu = 2.9 \cdot 10^{-6} n \lambda_c \Theta^{-\frac{3}{2}} \approx 2.9 \cdot 10^{-5} n \Theta^{-\frac{3}{2}} \text{ sec}^{-1} , \quad (5.12)$$

where the Coulomb logarithm  $\lambda_c$  has been set equal to ten and  $\Theta$  is in electron volts.

From Equation 5-11 the current density due to electrons can be expressed as:

$$\vec{j} = \frac{ne^2 \tau_c}{m(1 + \omega_c^2 \tau_c^2)} (\vec{E} + \vec{E} \times \frac{e\vec{B} \tau_c}{mc}) . \quad (5.13)$$

Here  $\tau_c = 1/\nu$  and  $\omega_c$  is the electron cyclotron frequency. The first term in Equation 5-13 is the part leading to joule heating of the electrons and to further ionization of neutrals in the plasma. (Over much of the range of parameters of interest in the present application, namely  $n \leq 10^{15}$  per cubic centimeter,  $B \geq 10^4$  gauss and  $\Theta \geq 1$  ev,  $\omega_c \tau_c \gg 1$ . As a result the first term in the preceding equation, the joule heating term, increases rather than decreases with increasing temperature.)

The second term contains no heating effect, but as we shall see in Section 5.4 determines the impedance of the secondary switch plasma. In principle this drift does affect the ionization rate, but the magnitude of the effect is not great unless the drift velocity of the electrons is much greater than the thermal velocities arising from the joule heating. Since this is not the case for the cases that we consider, we shall neglect the drift ionization. Moreover this effect would go away with vanishing voltage; whereas thermally heated electrons would continue to ionize while cooling after the voltage disappeared. We suspect that this may be the reason for the delayed buildup in density in certain cases referred to in Section 5.1.

The equations describing the evolution of electron density and temperature in the plasma are:

$$\frac{dn}{dt} = nS(\Theta)(N_0 - n) + f\sigma_p(N_0 - n) \quad (5.14)$$

and

$$\frac{d}{dt}(n(\frac{3}{2}\Theta + I)) = \vec{j} \cdot E + f\sigma_p(N_0 - n)(\varepsilon + I) , \quad (5.15)$$

where  $N_0$  is the initial density of neutrals,  $I$  their ionization potential and  $\varepsilon$  the mean energy of a photoelectron. Here we have neglected recombination processes, which occur at a negligible rate over the range of densities, temperatures and times of interest. In the absence of photoionization the solution of the density rate equation can be reduced to the calculation of a quadrature, viz.

$$\frac{n(t)}{N_0} = \frac{ge^{\tau}}{1 + ge^{\tau}} \quad (5.16)$$

where

$$g = \frac{n(0)}{N_0 - n(0)} \quad (5.17)$$

which is of little interest except to exhibit the saturation of the electron density to the initial neutral density at times  $\tau \gg 1$ , an effect observed in the Hawk experiments. Much greater interest attaches to the solution of these equations in the switch electrical environment and to determining the interplay between the solutions and the impedance presented by the evolving secondary plasma. Before coupling the preceding equations to circuit equations to determine the effects on voltage and current transfer to a load, we first consider the calculation of impedance presented by the secondary plasma.

#### 5.4 IMPEDANCE OF THE SECONDARY PLASMA.

In the crossed field configuration with  $\omega_c \tau_c \gg 1$  described in the previous section, the electron drift is primarily in the axial direction, parallel to the electrodes. The variation of magnetic field is in the radial direction. The integration of ampere's law over the anode-cathode gap leads to

an expression relating the voltage across the gap, the Hall voltage, to the currents flowing in the plasma, and on the electrode surfaces. Ampere's law is:

$$\frac{1}{r} \frac{\partial rB}{\partial r} = -4\pi ne \frac{E}{B} \quad (5.18)$$

Here we have assumed that  $\omega_c \tau_c \gg 1$  and that the component of current parallel to the radial electric field is small in comparison with the Hall component. We assume further that  $n$  and  $E$  are uniform in the gap. Integration across the gap from the cathode radius  $r_c$  to the anode radius  $r_a$  gives:

$$V_H / 300 = -E(r_a - r_c) = \frac{1}{8\pi e r_m^2} (r_a^2 B_a^2 - r_c^2 B_c^2) \quad (5.19)$$

where  $V_H$  is in volts,  $B_a$  and  $B_c$  are in gauss, lengths are in centimeters,  $e = 4.8 \cdot 10^{-10}$  esu and

$$r_m^2 = \frac{1}{3} (r_a^2 + r_a r_c + r_c^2) \quad (5.20)$$

Expressed in terms of anode and cathode currents  $I_a$  and  $I_c$  given in amperes the result is:

$$V_H = 9.95 \cdot 10^8 \frac{I_a^2 - I_c^2}{n r_m^2} \quad (5.21)$$

The current carried by the secondary plasma electrons is  $I_a - I_c$ . In analogy with the corresponding case of launched electron flow in magnetically insulated transmission lines (MITL) (Reference 18), it is assumed that this current is lost, that is, it does not appear in the load. For MITL's this appears to be a good approximation except for a load impedance smaller than the switch impedance (References 19 and 20). Thus we take the Hall or flow impedance of the secondary plasma to be:

$$Z_H = 9.95 \cdot 10^8 \frac{I_a + I_c}{n r_m^2} \text{ ohms} \quad (5.22)$$

For currents adding to one megampere, a mean radius of 6 cm and an electron density of  $10^{14}$  per cc, the impedance in parallel with the primary POS is  $0.28 \Omega$ . Provided that the assumed density is achieved before the opening of the primary POS, the switch impedance could be no greater than  $0.28 \Omega$ . It would be even smaller were larger electron densities to be achieved in the secondary plasma.

From a theoretical as well as a practical point of view the impedance model is not robust. The plasma density measured by interferometry shows strong spatial variations contrary to the uniform density assumption of the model. The effects of plasma inhomogeneities have been considered by Gordeev (Reference 2) arguing that the switch voltage is determined by the differences between maximum and minimum values of the inverse density in the switch. They further argue that ion acceleration by the Hall electric field through thin sheaths can lead to local densities which are very much less than the average density, and can increase the Hall voltage by a factor of the square root of the ion to electron mass ratio over that determined from Equation 5.22 using an average density. With these limitations in mind we now consider the effect that ionization of neutrals may have on the performance of a plasma opening switch.

## 5.5 EFFECT OF NEUTRALS ON SWITCH PERFORMANCE.

In the preceding paragraphs we have presented evidence indicating the presence of neutral atoms in the switch gap and that they become ionized as a result of electron heating during a voltage pulse. When ionized to form a plasma of sufficiently high density the switch presents a low impedance, Equation 5.22, determined by the Hall effect. Now we will incorporate these elements into a switch model to determine the effects on switch voltage and current transfer into a load. For this purpose we imagine the switch as composed of two parts, a primary switch plasma and a secondary or parasitic plasma, Figures 5-16 and 5-23. The primary switch plasma consists of the plasma which has been swept up during the conduction phase. We model this plasma as one which can open rapidly to a high impedance and affect nearly complete transfer of generator current into a load such as a PRS. The model we choose to represent the electrical characteristics of the primary plasma is:

$$V_p = Z_f(t)(I_a^2 - I_c^2)^{1/2} \quad (5.23)$$

where  $I_a$  and  $I_c$  are the anode and cathode currents at the switch and  $V_p$  the voltage at the switch. The flow impedance (Reference 20), Section 6, permits rapid opening to a high

impedance and efficient current transfer into a load, such as a PRS, in the absence of the deleterious effects associated with the secondary plasma.

The secondary, or parasitic, plasma is considered as providing a current path in parallel with the primary plasma (Figure 5-23). The electrical characteristics of this plasma are determined from Equation 5.22, wherein the electron density  $n(t)$  follows from the population rate equation and the energy equation.

We apply the model first to the ACE 4 extended anode configuration shown in Figure 5-1. Figure 5-5 shows electron line densities and current and voltage wave forms for shot 1305. The calculated currents and voltage are shown in Figure 5-24 for an initial density of  $1.8 \times 10^{15}$  neutral fluorine atoms per cc in the parasitic plasma. That the calculated and measured switch voltage and generator current compare favorably is not surprising considering the number of free parameters available to the calculation. The calculated load current rises from zero more rapidly than the measured current, but compares favorably beyond about  $1.5 \mu\text{s}$ . The effect of the neutrals on the current transfer into the inductive load is clear however from a comparison of the results of the corresponding calculation without the shorting effect of the parasitic plasma, Figure 5-25. Figure 5-26 shows the effect of varying amounts of neutral concentrations and the extremely poor current transfer associated with the highest densities considered. For completeness, we show in Figures 5-27 and 5-28 the electron number density and temperature in the parasitic plasma.

Observe that in the circuit calculation there is only one density in the parasitic plasma at any given time. The model cannot account for line electron density variations across the gap. The density used in the calculations is best associated with the minimum observed line densities, which include contributions from both the primary and parasitic plasmas. Even then the calculated density appears not to compare favorably with the measured density. A more favorable comparison could be achieved if it is assumed that Equation 5.22 underestimates the impedance of the parasitic plasma as discussed in the previous section.

Considering the uncertainties in the impedance model, the effects of density variations should be considered in relative terms. If the impedance of the secondary plasma is substantially diminished by ion acceleration effects, the neutral densities required to produce a load current similar to that shown in Figure 5-24 could be correspondingly higher. In this case the calculated densities would be greater and the saturation of densities may occur at times beyond the time range of the data. In view of all the uncertainties a more definitive conclusion is not justified.

It is important to notice that the foregoing description of the parasitic plasma is within the framework of quasineutral plasma theory. Thus all of the effects considered here could be incorporated within Mach2. In principle then the effects of plasma inhomogeneity and ion acceleration on POS performance, including parasitic plasmas, could be determined by this code. The question of the importance of charge separation would still remain, but the switch may well sustain high impedance without ever entering a regime dominated by charge separation.



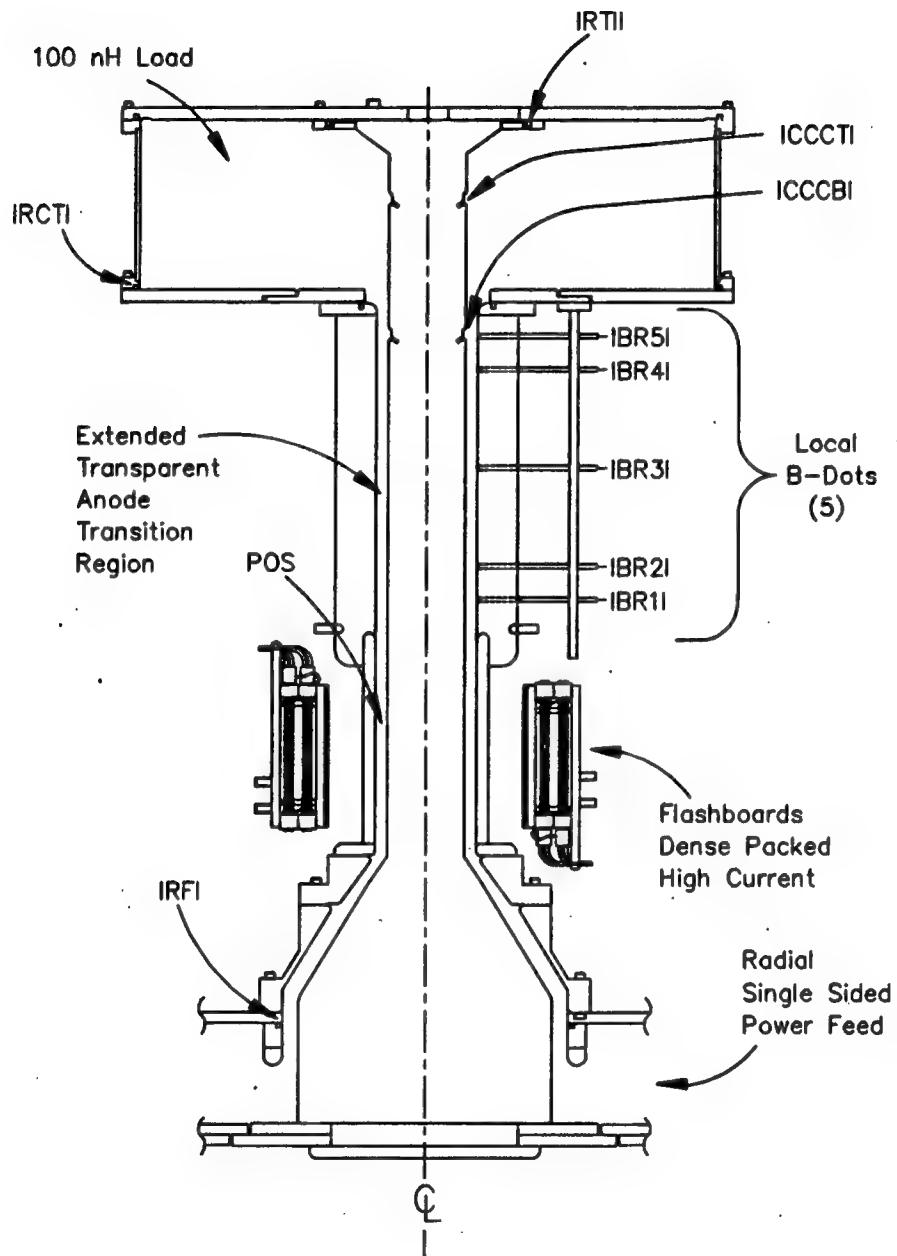


Figure 5-1. ACE 4 extended transport anode configuration.

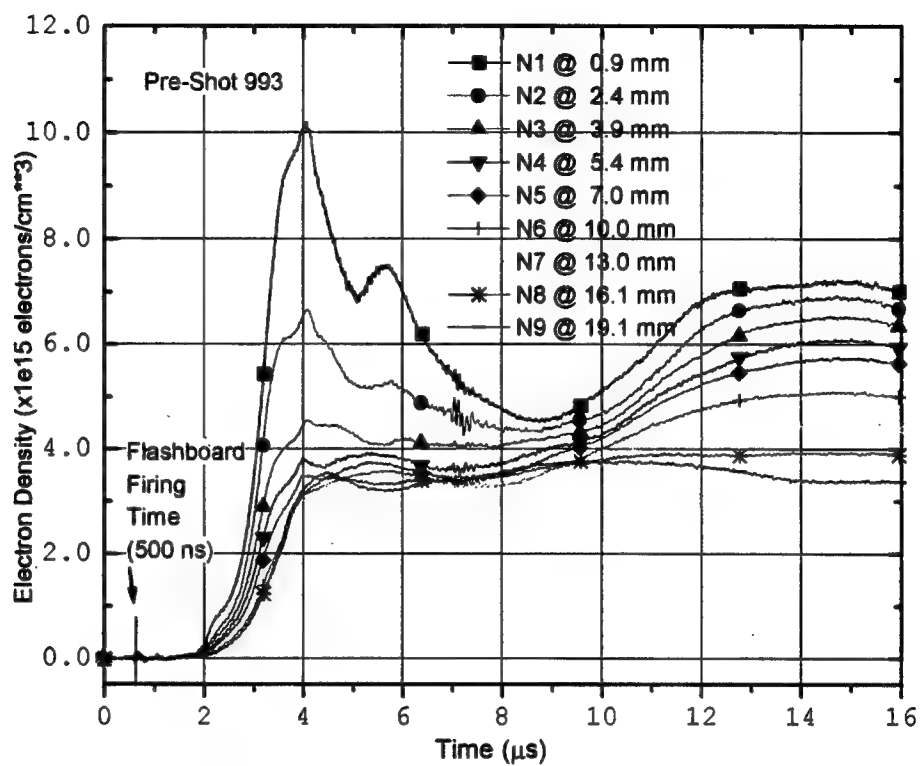


Figure 5-2. Typical density distribution in the POS. The signals come up sequentially as the interferometer positions move from near the cathode toward the anode.

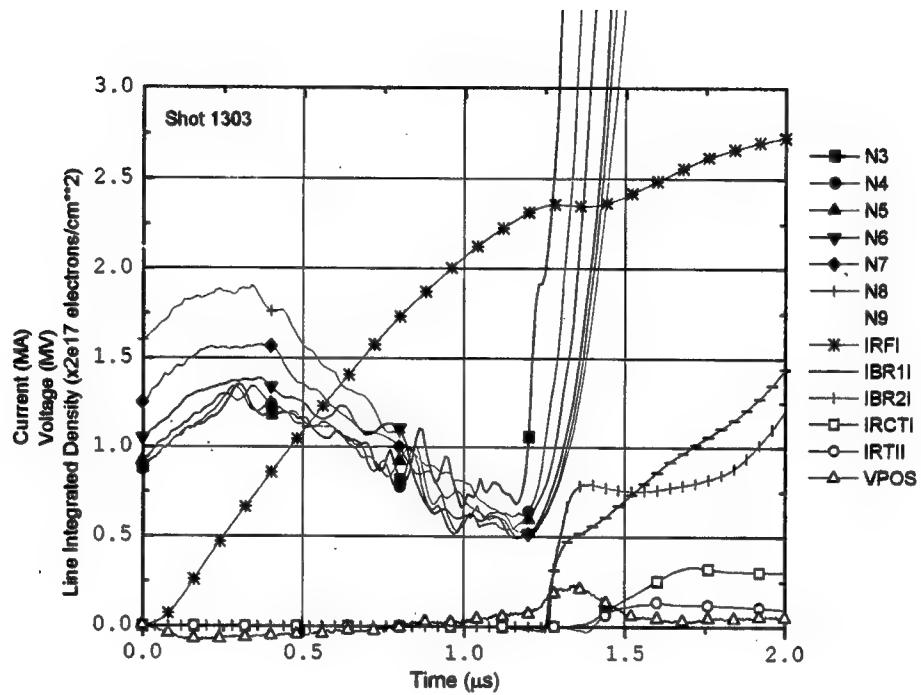


Figure 5-3. Densities, current and switch voltage for 3.0  $\mu$ s delay.

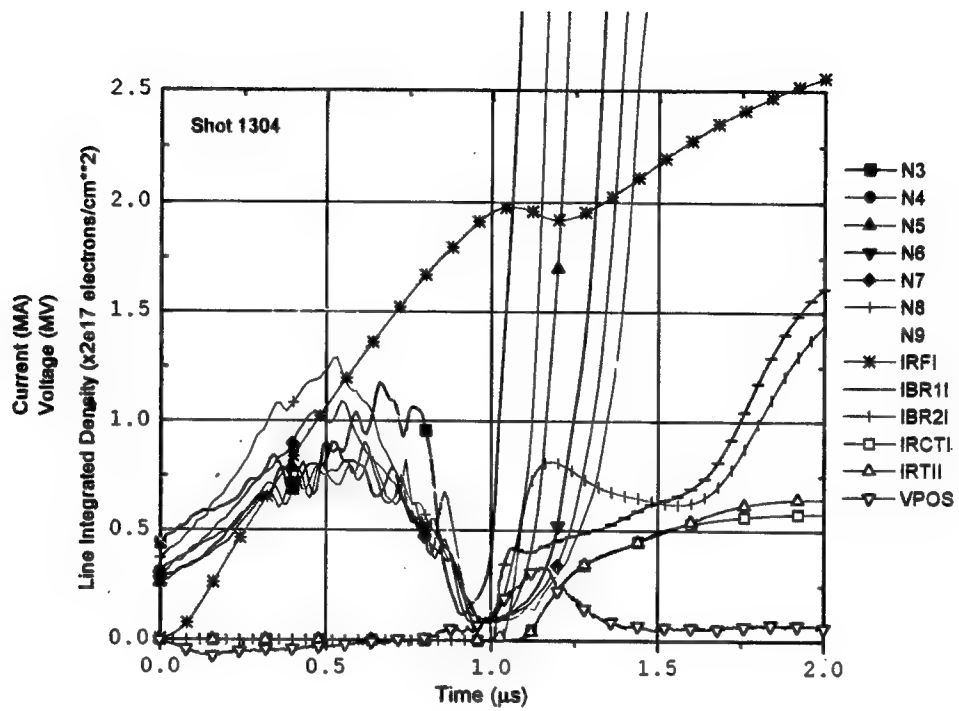


Figure 5-4. Densities, currents and switch voltage for 2.5  $\mu$ s delay.

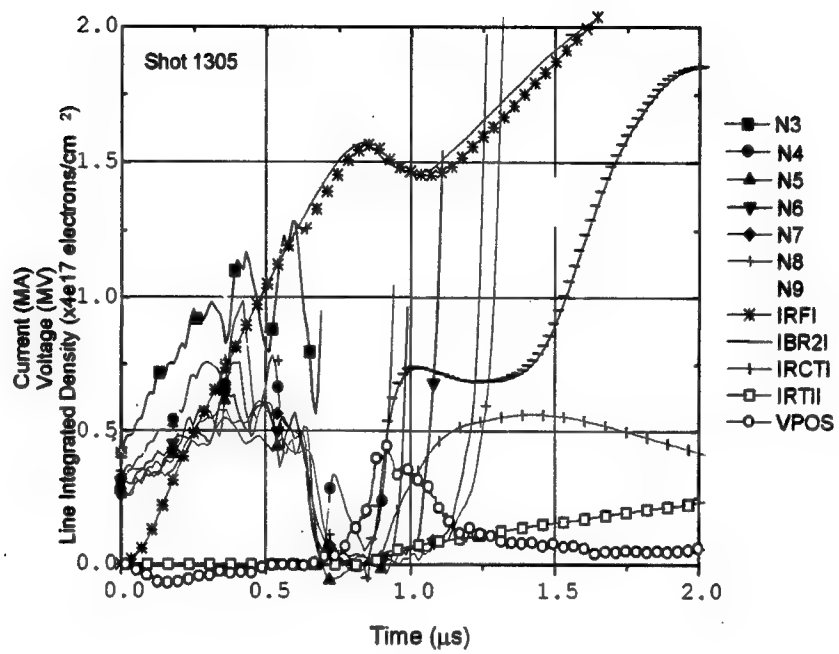


Figure 5-5. ACE 4 Shot 1305.

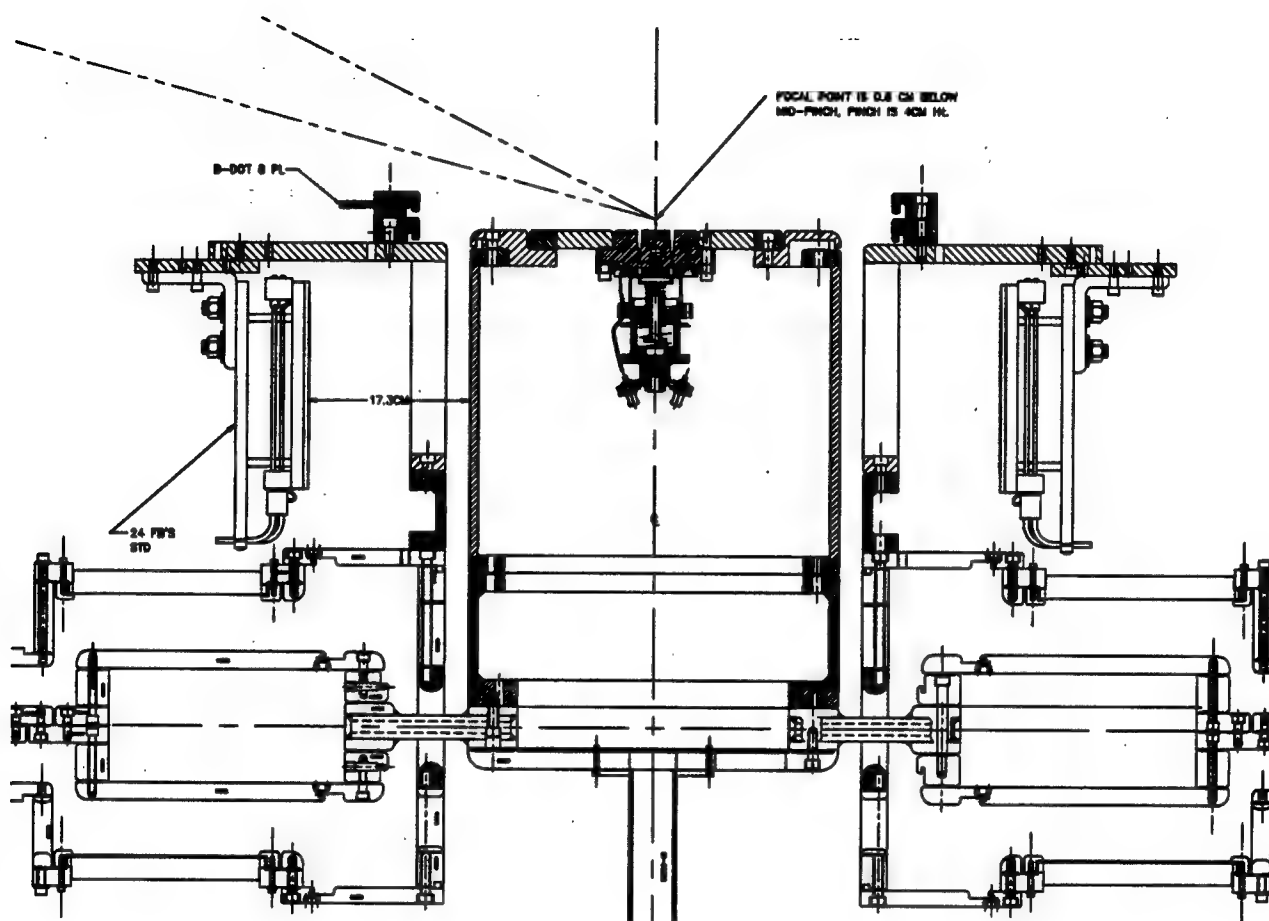


Figure 5-6. Experimental configuration used with interferometry.



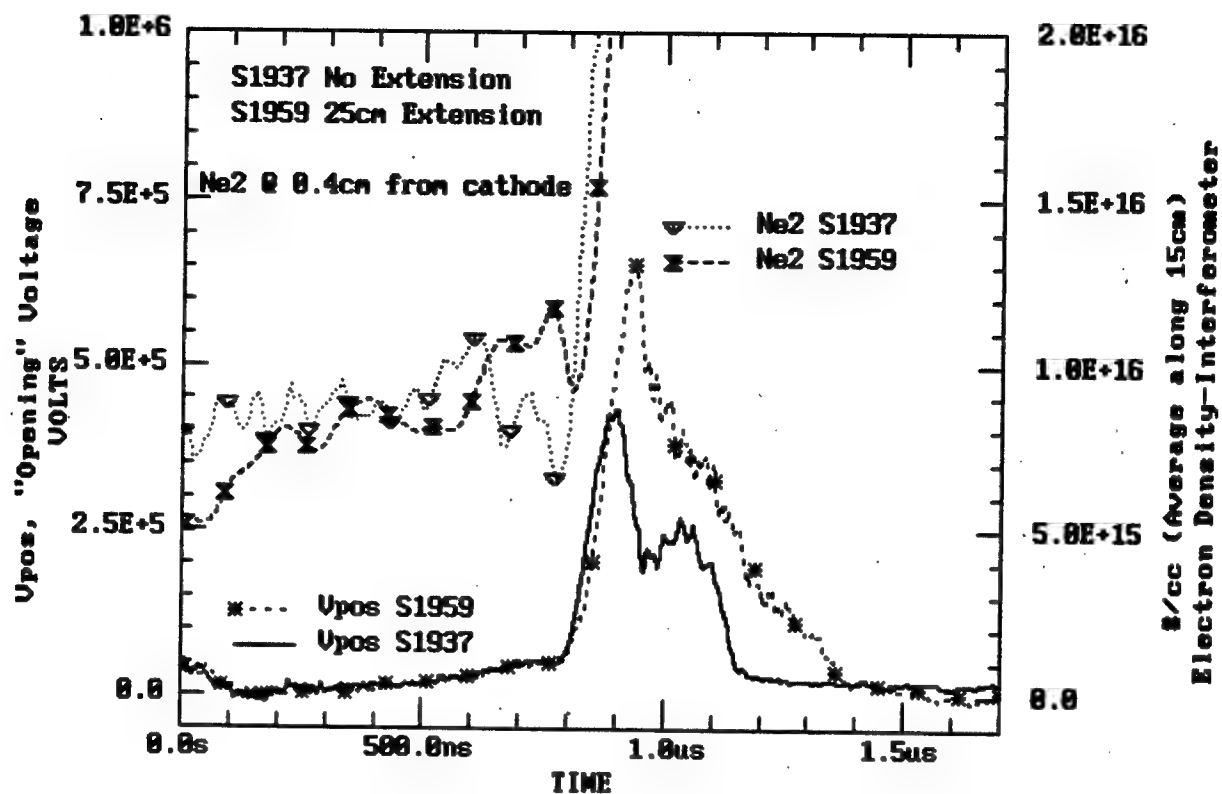


Figure 5-8. Switch voltage and electron densities observed in shots 1937 (no extension) and 1959 (2.5 cm extension). Density at 0.4 cm from cathode.



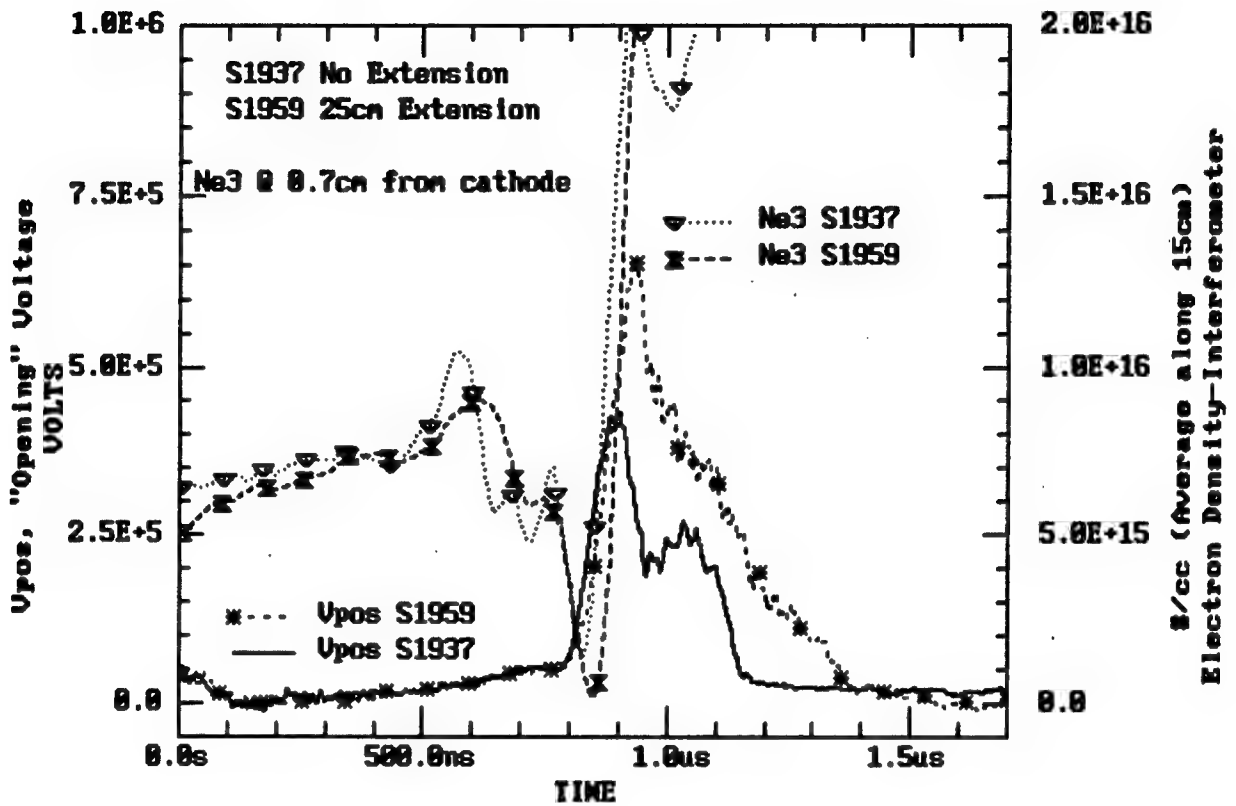


Figure 5-9. Switch voltage and electron densities observed in shots 1937 (no extension) and 1959 (2.5 cm extension). Density at 0.7 cm from cathode.

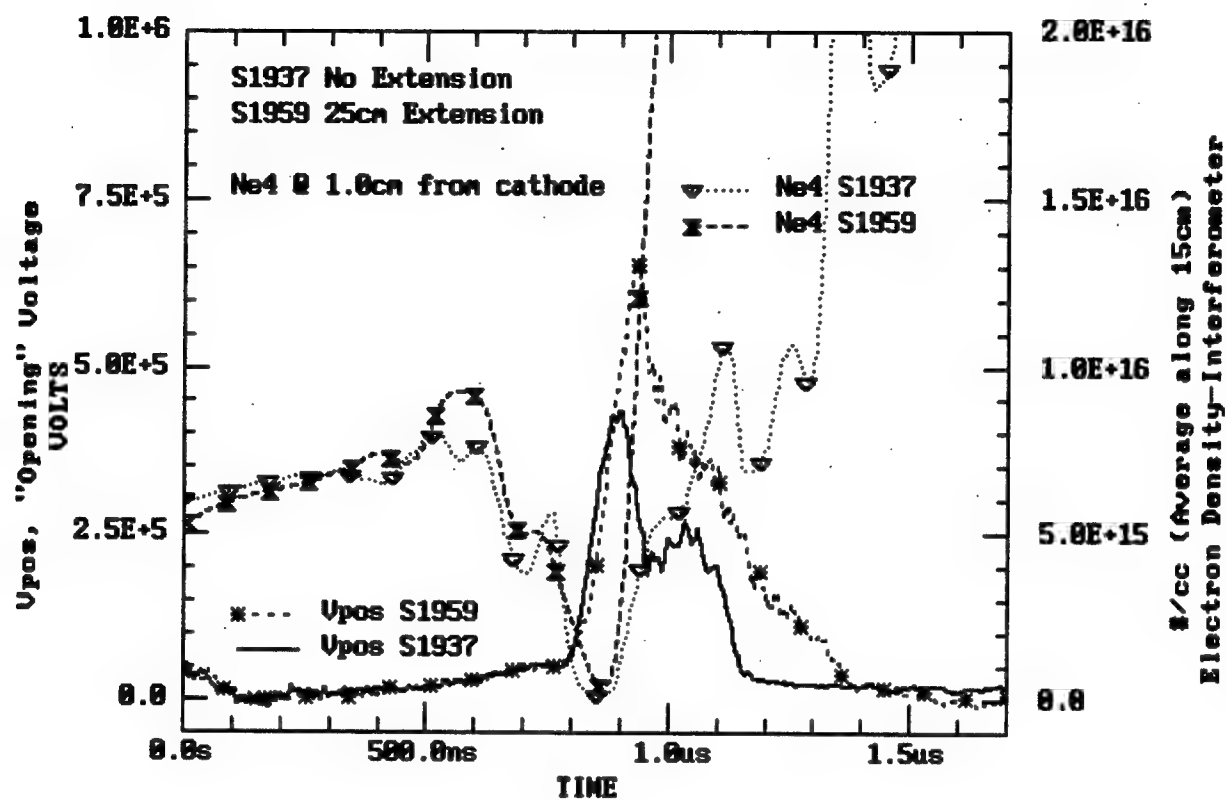


Figure 5-10. Switch voltage and electron densities observed in shots 1937 (no extension) and 1959 (2.5 cm extension). Density at 1.0 cm from cathode.

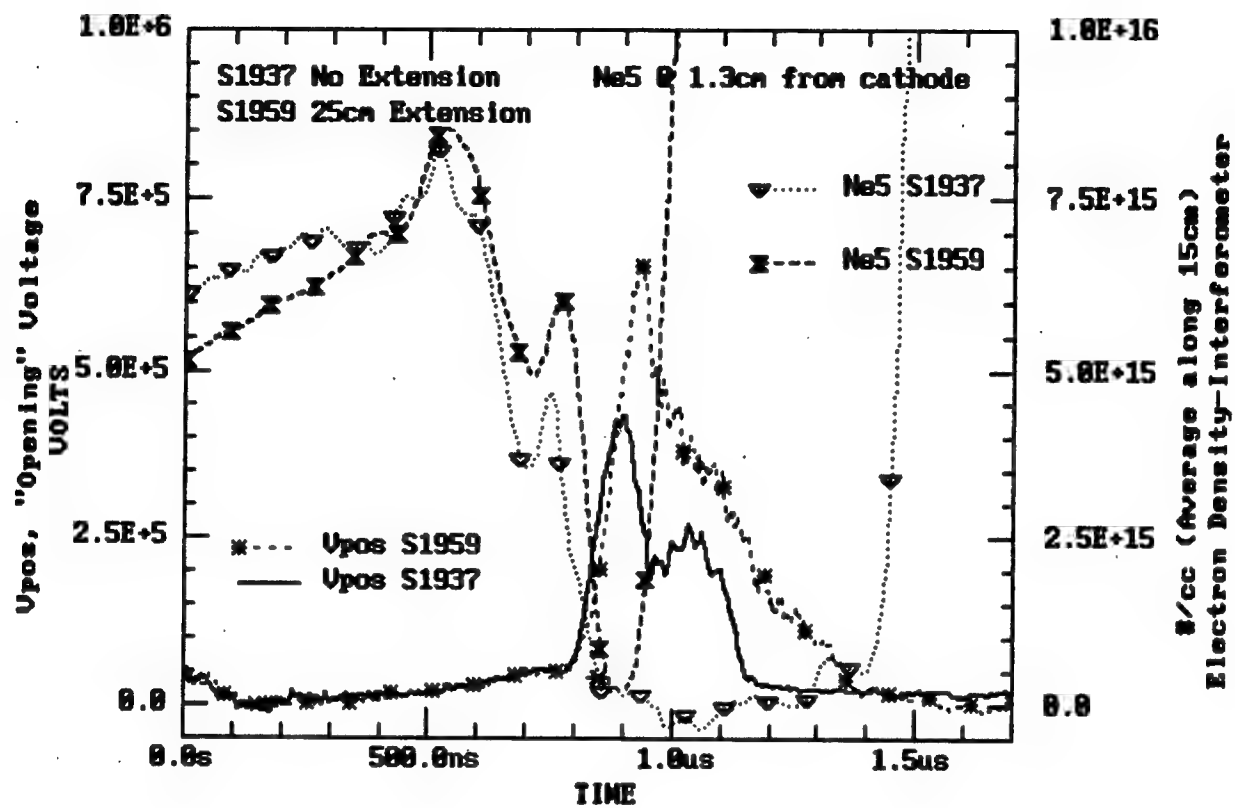


Figure 5-11. Switch voltage and electron densities observed in shots 1937 (no extension) and 1959 (2.5 cm extension). Density at 1.3 cm from cathode.

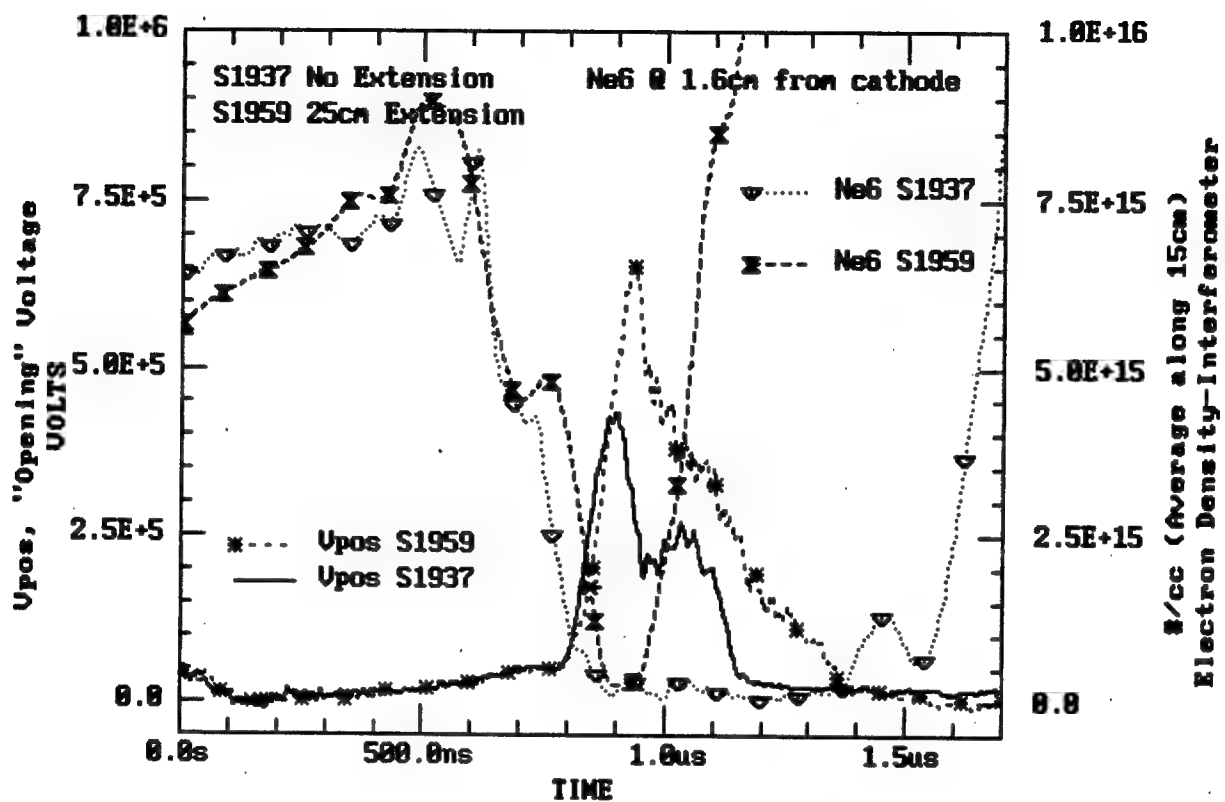


Figure 5-12. Switch voltage and electron densities observed in shots 1937 (no extension) and 1959 (2.5 cm extension). Density at 1.6 cm from cathode.

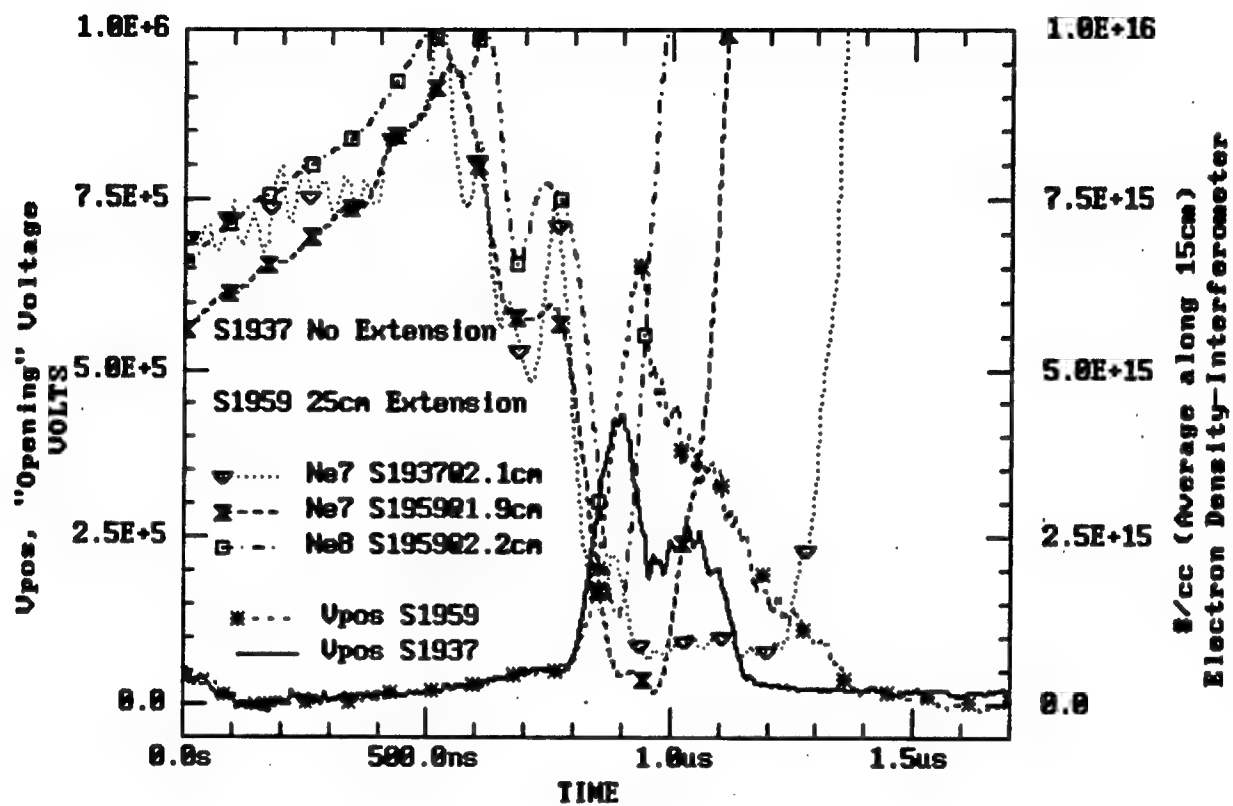


Figure 5-13. Switch voltage and electron densities observed in shots 1937 (no extension) and 1959 (2.5 cm extension). Density at about 2.0 cm from cathode.

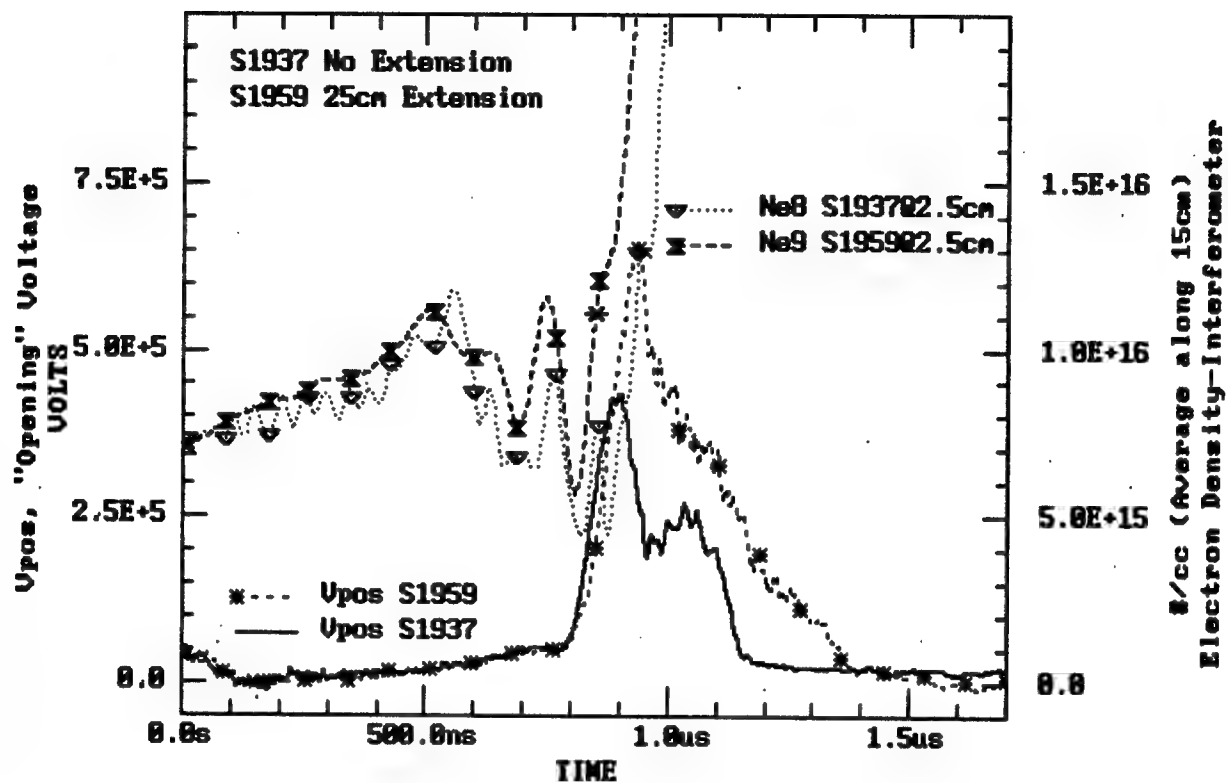


Figure 5-14. Switch voltage and electron densities observed in shots 1937 (no extension) and 1959 (2.5 cm extension). Density at 2.5 cm from cathode.

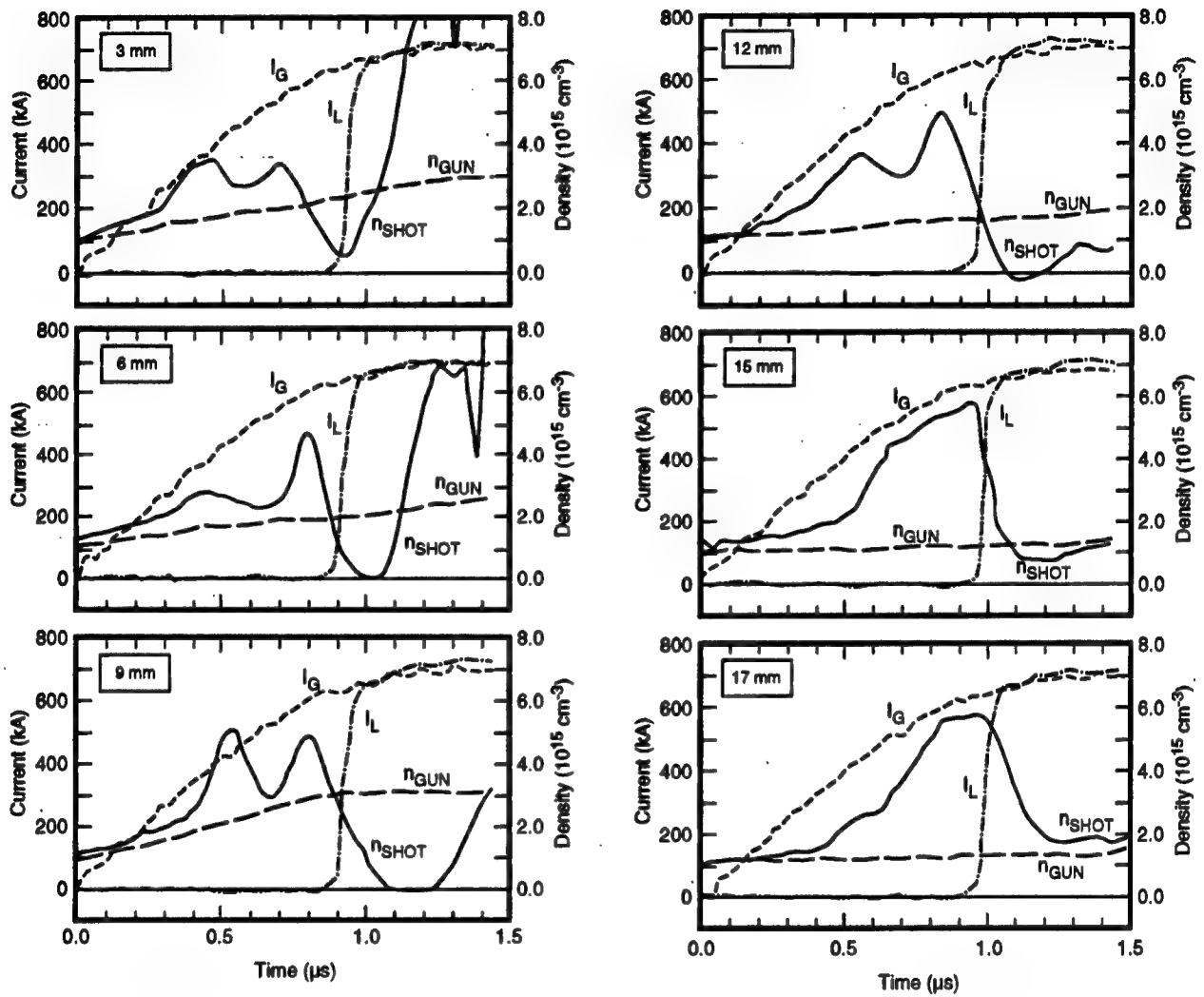


Figure 5-15. Density and current measurements on HAWK using guns.

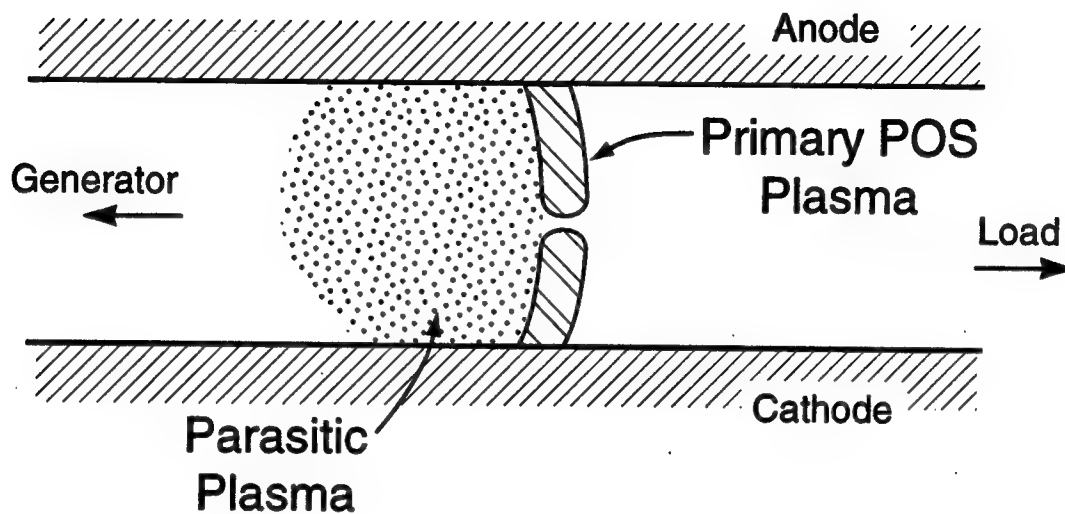


Figure 5-16. Ionizing neutrals form a magnetized parasitic plasma on the generator side of the primary snowplowed plasma.



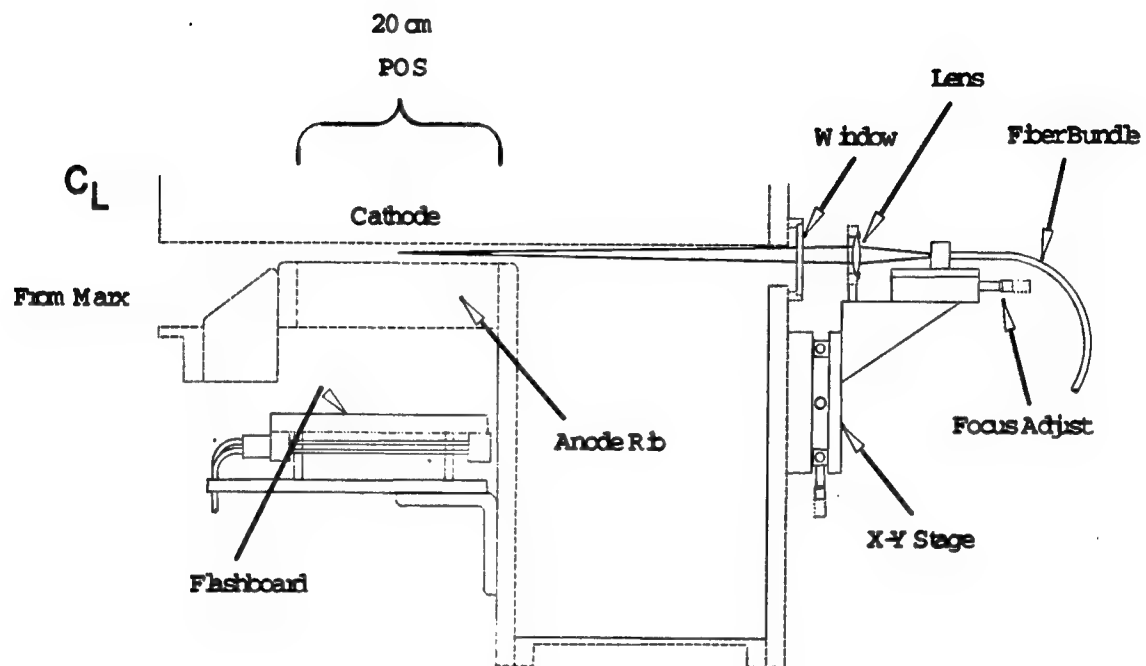


Figure 5-17. Experimental arrangement used for spectroscopic measurements on ACE 4.

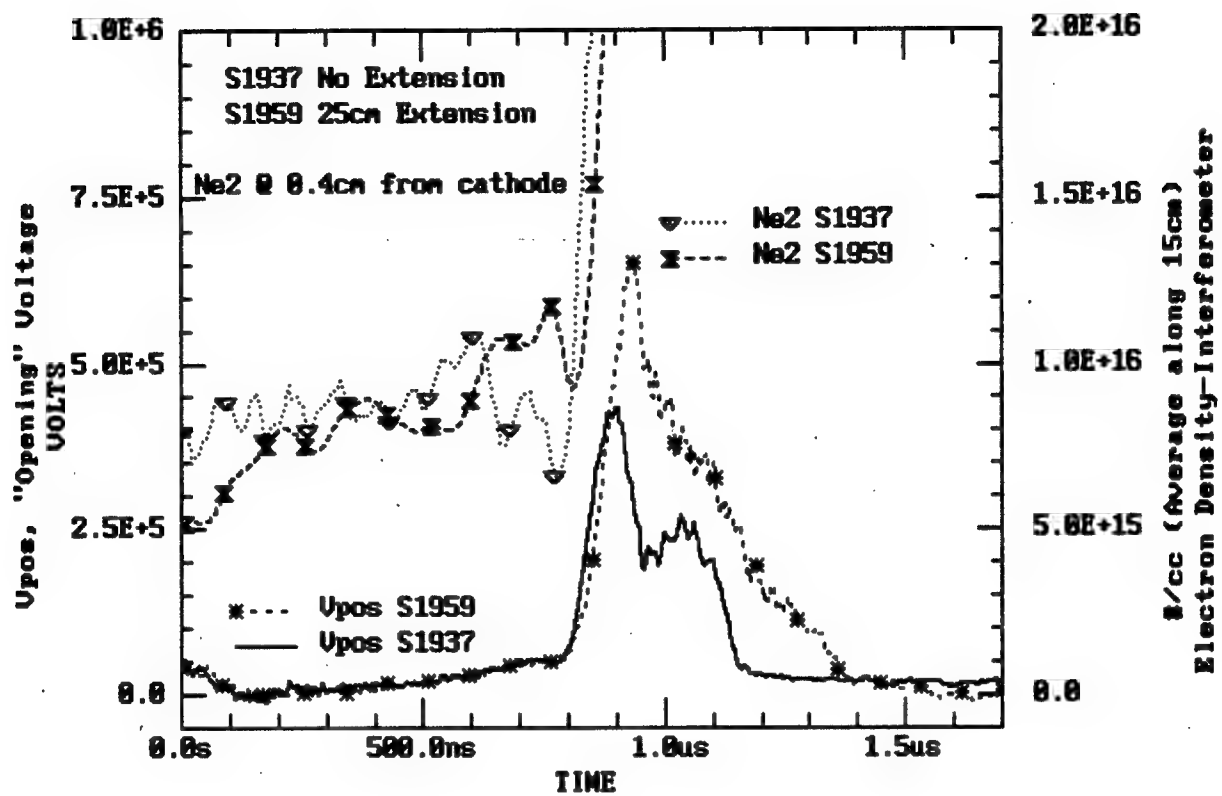


Figure 5-18. Switch voltage relative H $\alpha$  and >5 keV intensities observed for Shot 1937.

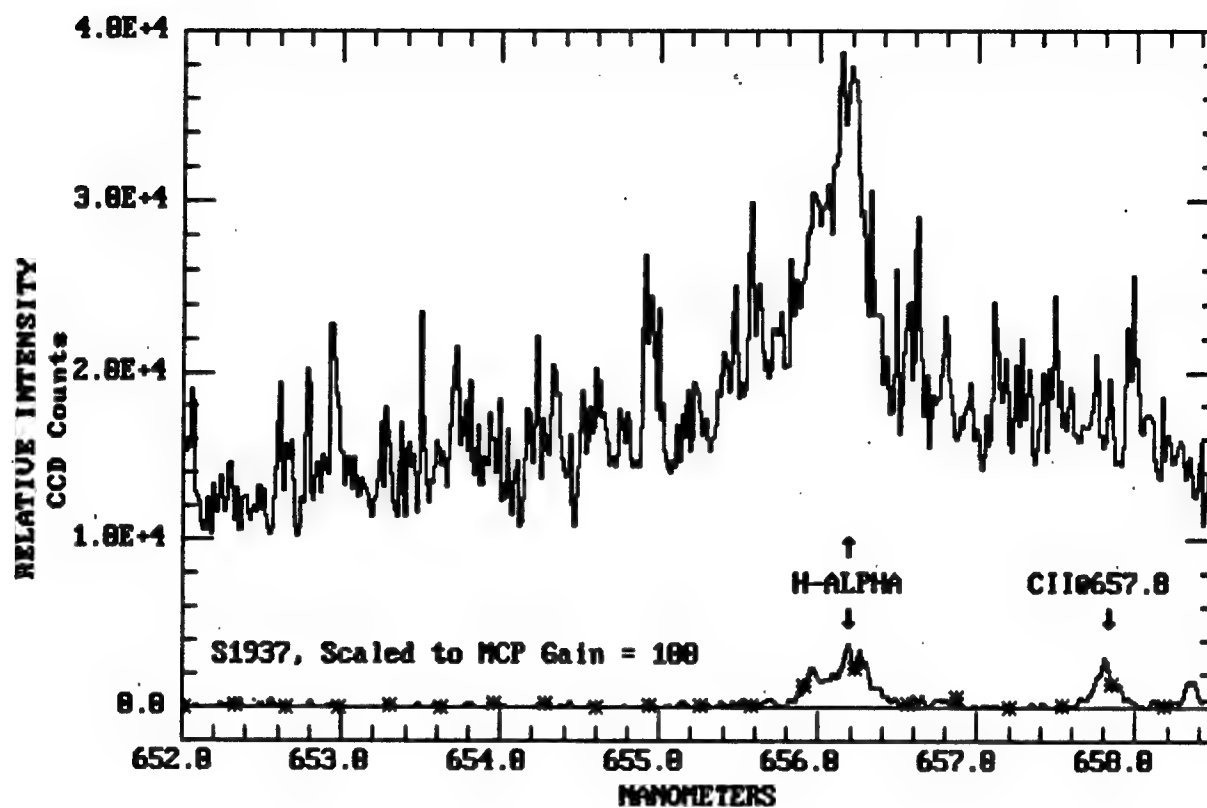
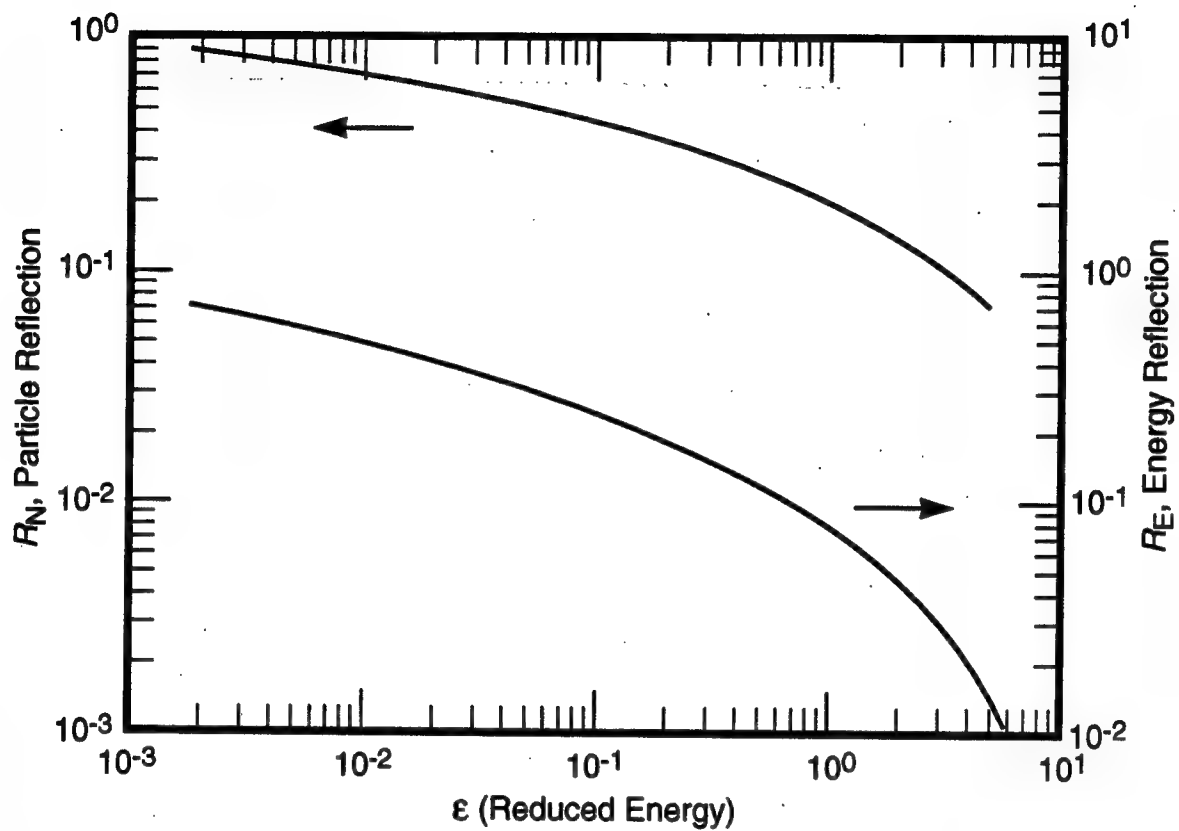


Figure 5-19. Line profiles versus wavelength for Shot 1937. The time of the measurement was the internal 0.6  $\mu$ s to 0.8  $\mu$ s following the onset of conduction current. Lower curves show pre-shot profiles for hydrogen and singly ionized carbon.



Particle and energy reflection coefficients based on Oen and Robinson, Nuclear Instruments and Methods, 132, pp 647-653 (1976).

Figure 5-20. Reflection coefficients.

# NORMAL INCIDENCE WITH HYDROCARBONS

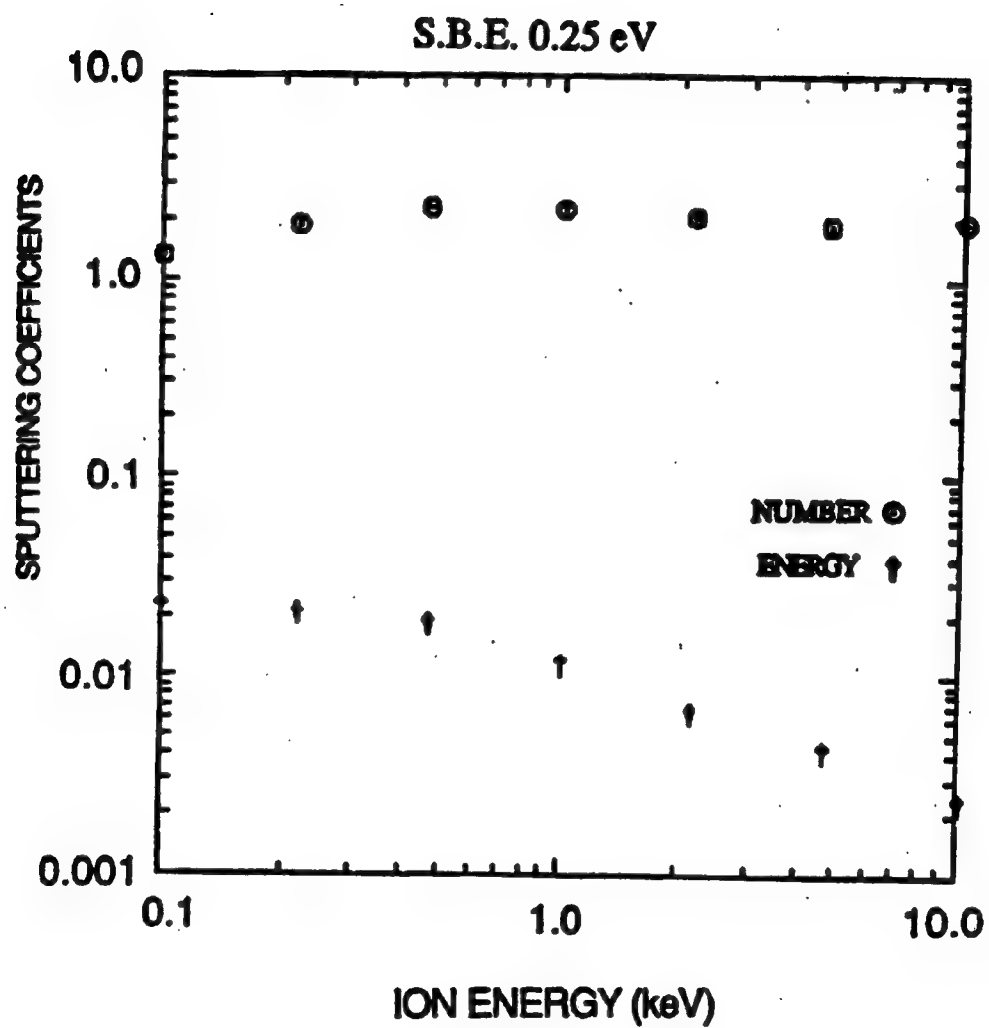


Figure 5-21. Particle and energy sputtering coefficients by hydrocarbons with normally incident particles. Surface binding energy - 0.25 eV.

# NORMAL INCIDENCE WITH HYDROCARBONS

S.B.E. 1.0 eV

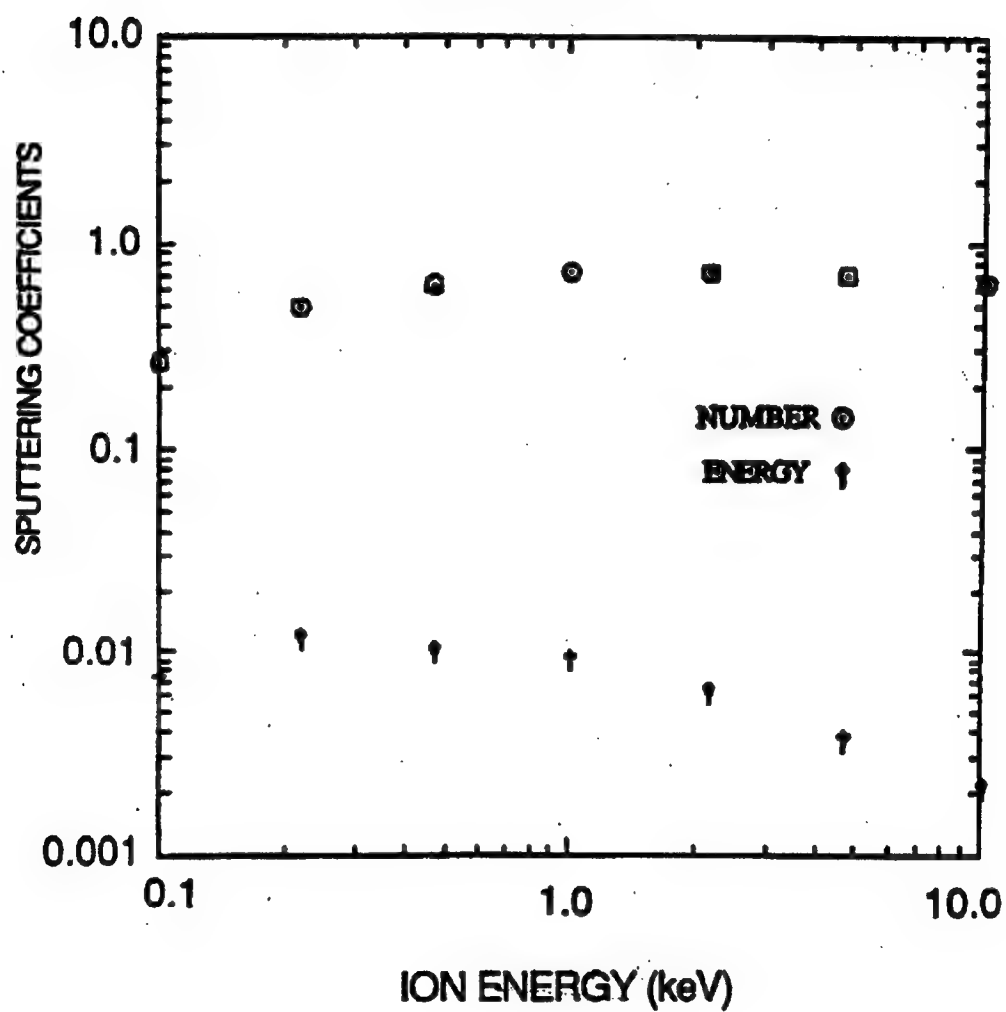


Figure 5-22. Particle and energy sputtering coefficients of hydrocarbons with normally incident particles. Surface binding energy = 1.0 eV.

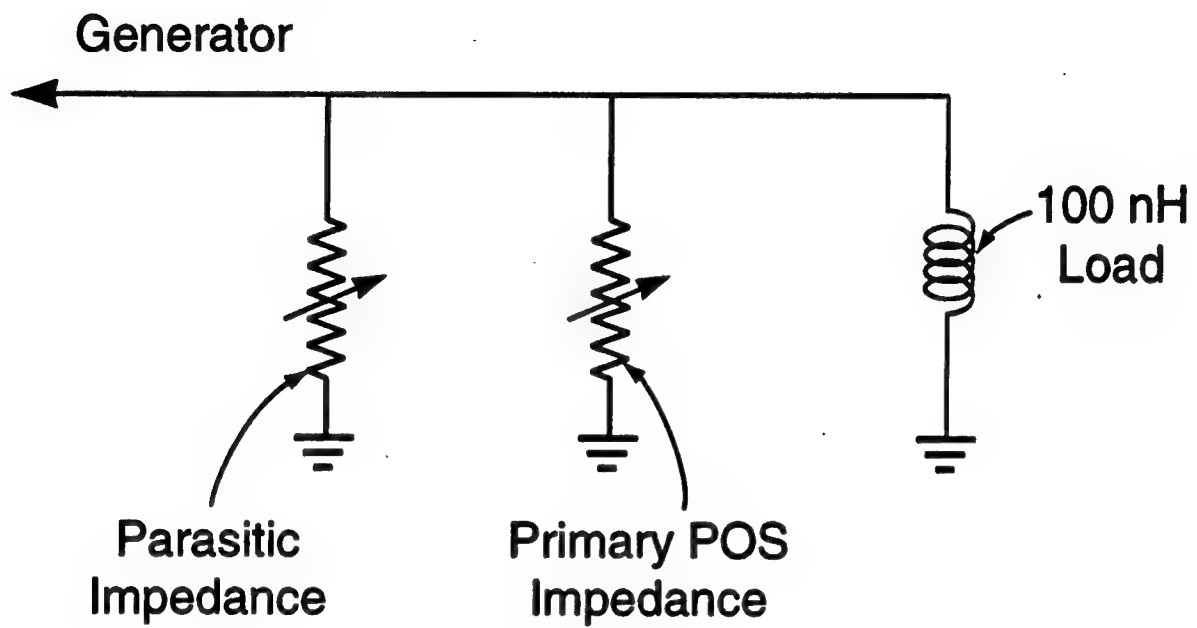


Figure 5-23. Circuit model used to analyze effects of parasitic plasma on switch voltage and load current.

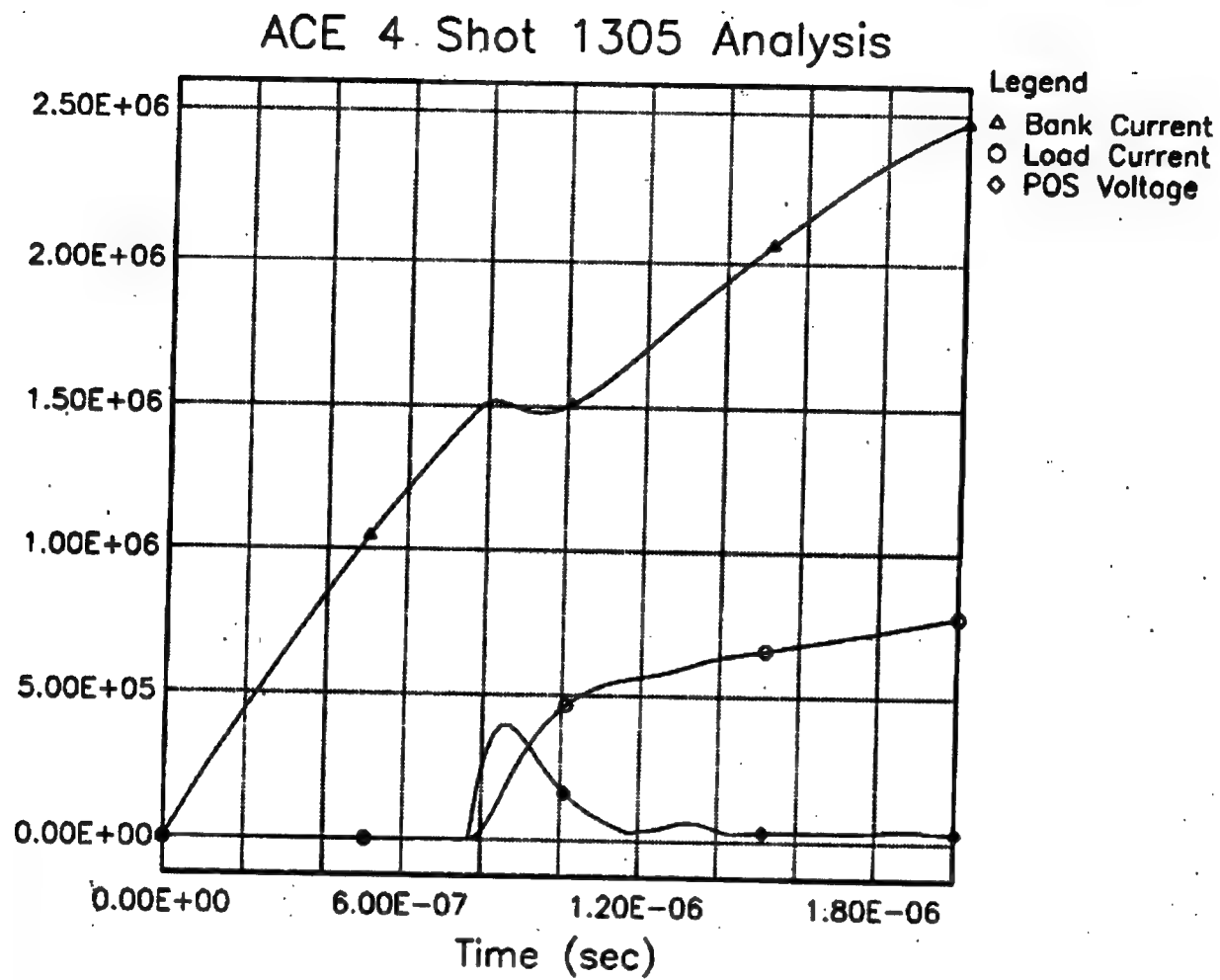


Figure 5-24. Circuit model applied to ACE 4 Shot 1305, including parasitic plasma.



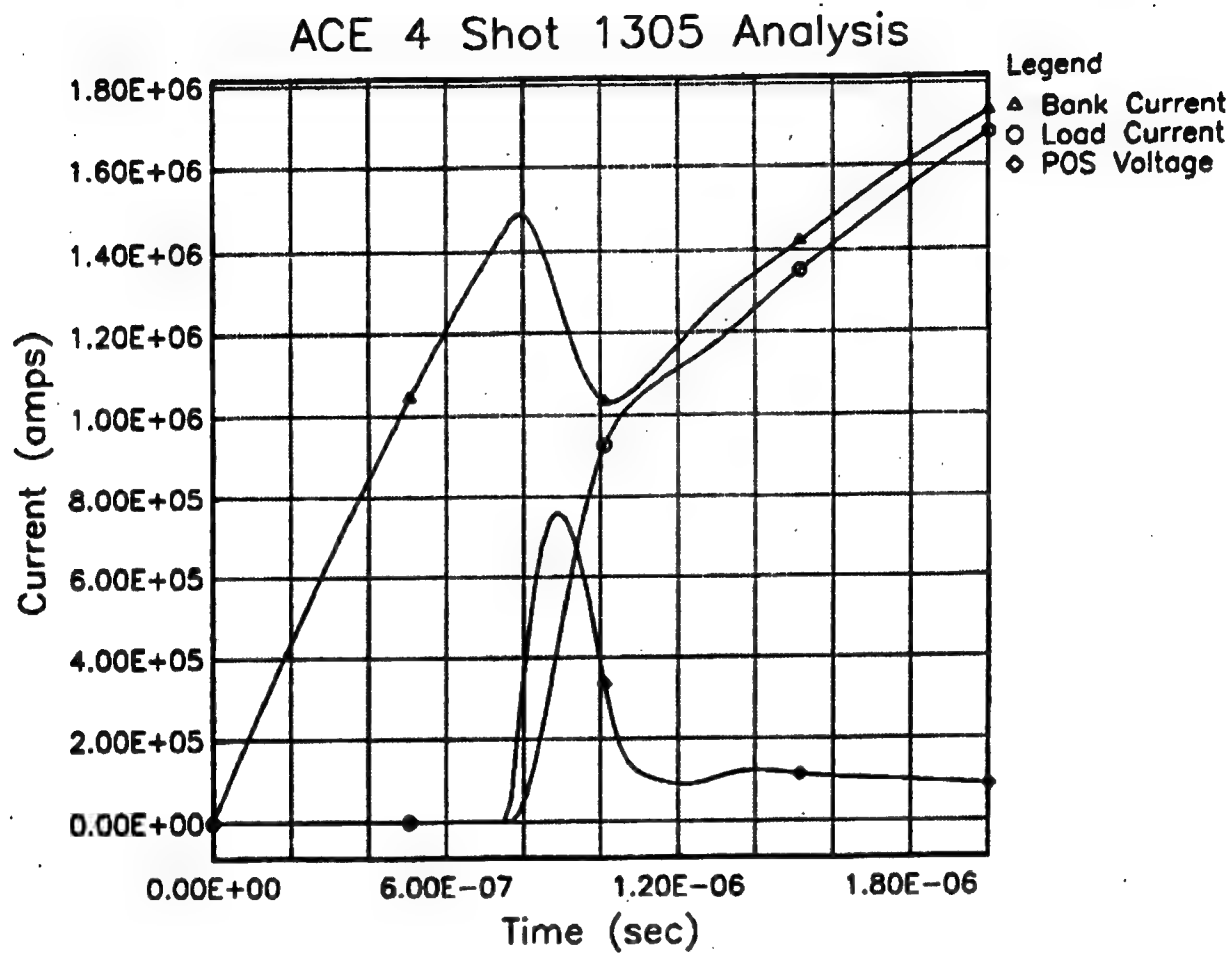


Figure 5-25. Circuit model applied to ACE 4 Shot 1305, but without parasitic plasma.

# ACE 4 Shot 1305, Parameter Study

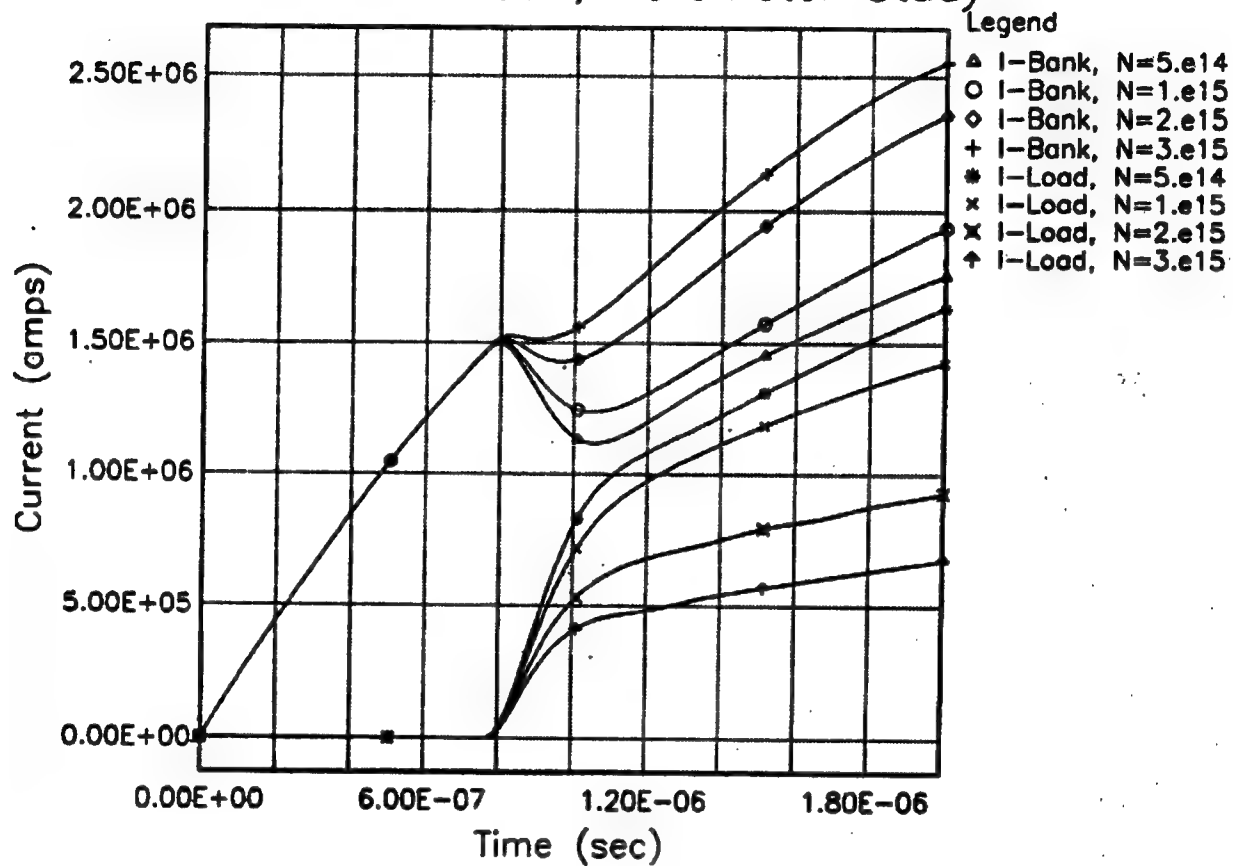


Figure 5-26. The effect of varying amounts of initial neutral concentration.

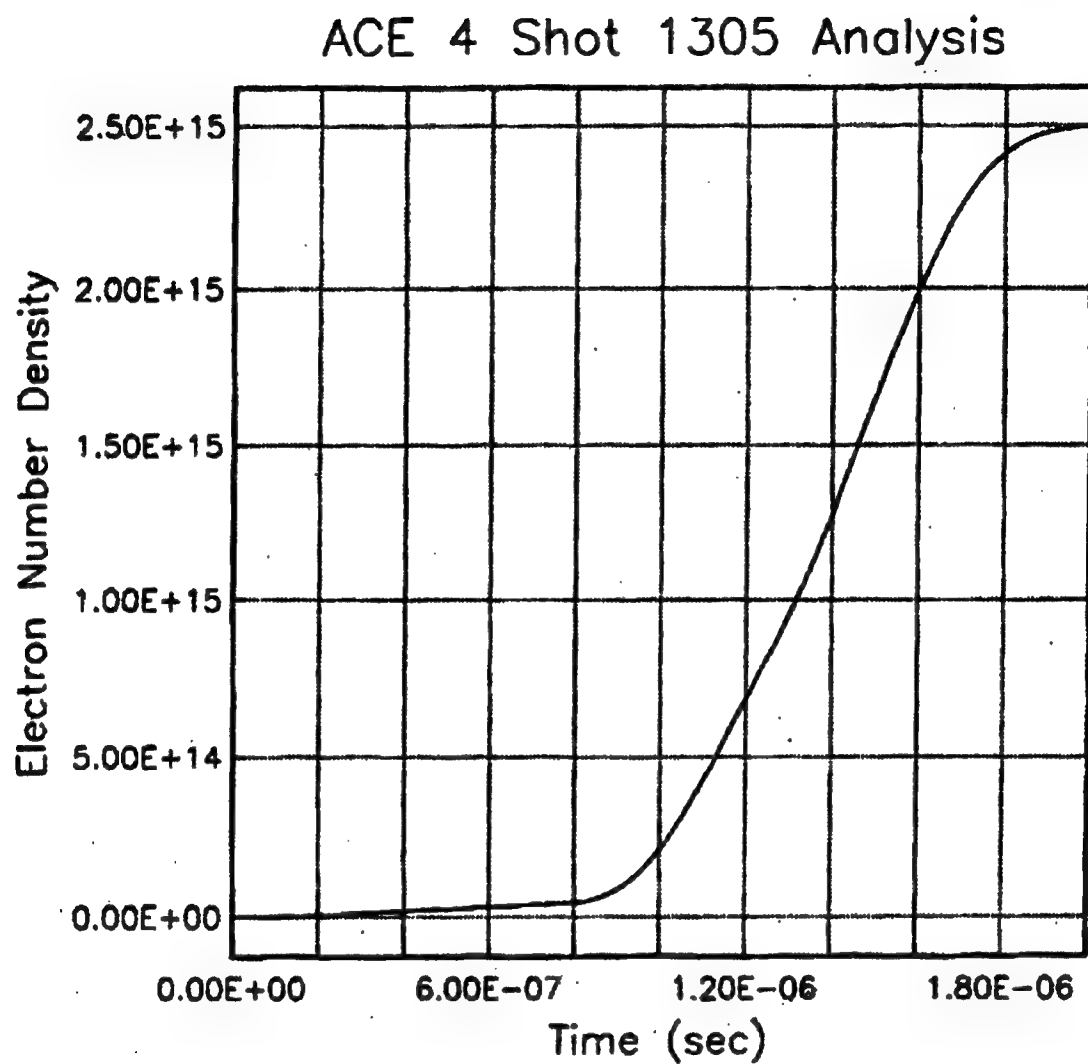


Figure 5-27. The electron number density in the neutral plasma corresponding to Figure 5-24.

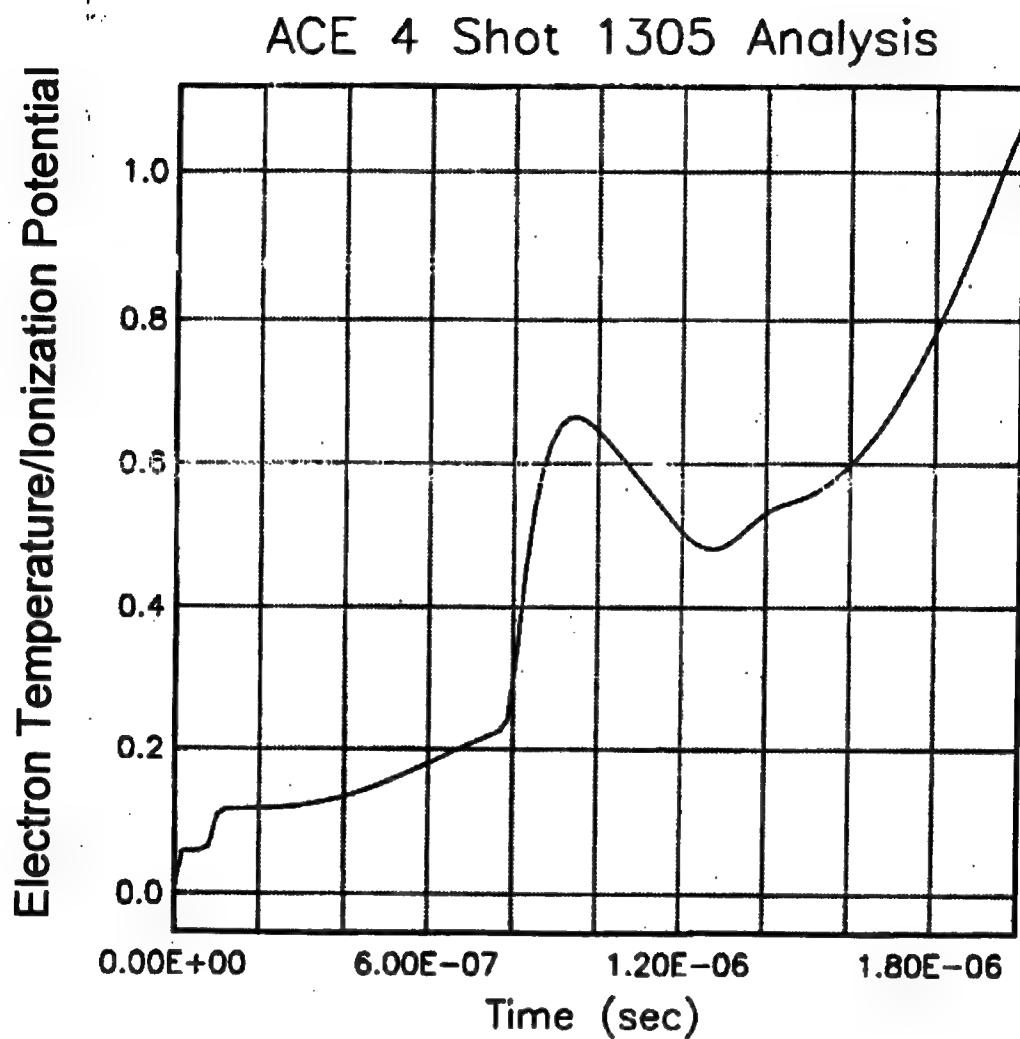


Figure 5-28. The electron temperature in the plasma corresponding to Figure 5-24.

## **SECTION 6**

### **SPOCK: SPICE-BASED POWERFLOW OPTIMIZING CIRCUIT KIT**

Work was completed on the circuit code SPOCK. SPOCK depends on three essential ingredients:

1. SPICE, an industry-standard electrical circuit code developed by the University of California at Berkeley over the last two Decades.
2. MIRIAD, a proprietary "software bus" code created by Maxwell Technologies, Inc.
3. A number of simple physical models of pulsed-power devices that have been developed by the plasma physics group at Maxwell over the last several years. The new code SPOCK uses SPICE as a framework on which to add our own pulsed-power devices. MIRIAD supplies the problem management and plotting features.

Below we summarize briefly those aspects of SPICE and MIRIAD which are most relevant to the development of our new circuit code, as well as the new device models required by this code.

#### **6.1 SPICE.**

SPICE allows the user to build complex circuits from simple components: resistors, capacitors, inductors, transmission lines, diodes, MOSFETS, etc. Many of these are of no interest to the pulsed-power community. Conversely, SPICE knows nothing of a number of devices unique to pulsed-power: plasma opening switches, plasma radiation sources, bremsstrahlung diodes, plasma filled diodes, convolutes, etc.

However, SPICE also allows the programmer to build new devices in the C programming language and integrate them into SPICE. The new devices are then available to the user exactly like any other SPICE device. The prescription for building new SPICE devices is contained in Reference 21. A great deal of useful information on how SPICE works can also be found in Reference 22.

#### **6.2 MIRIAD.**

MIRIAD was created by a team of programmers in the Space Sector of the Federal Division of Maxwell Technologies. MIRIAD provides a framework for linking one or more codes with a

graphical user interface, including menus, forms, and plotting capabilities. A unique feature of MIRIAD is its ability to connect the outputs and inputs of multiple codes together into one seamless whole. MIRIAD stores these outputs and inputs in a database, and keeps track of data dependencies between codes. This allows MIRIAD to determine at runtime which codes need to be run (or rerun) in order to produce up-to-date answers to particular questions.

In one sense, the use of MIRIAD for this project was overkill, since only one code was used, SPICE. However, there are several good reasons for using MIRIAD as an application framework:

1. MIRIAD comes with a good graphical user interface and plot package.
2. MIRIAD allows the programmer to easily create multiple versions of a code on a variety of Unix workstations, and also on IBM PC clones running Windows 95 or Windows NT.
3. One particular MIRIAD application, EWB-SPICE already had been developed with SPICE embedded into it. This allowed us to build on previous work, rather than writing code from scratch.
4. MIRIAD allows the integration of other codes at some later date, if this should become appropriate. For example, if a programmer decided to create a rail gun simulation circuit code, it would be easy to link in an analysis package to unfold rail gun B-dot probe data.

The best reference for MIRIAD is an internal document (Reference 23). Unfortunately, this document is a bit out of date, and some useful information lives only in the heads of the MIRIAD team.

### **6.3 PHYSICS MODELS.**

Over the last several years, Maxwell Technologies has developed a number of simple models for various pulsed-power devices. Examples are:

1. The 1-dimensional snowplow model of the POS conduction phase.
2. Several versions of a magnetically enhanced erosion model of the POS opening phase.
3. A neutral-atom model that may explain the short circuiting sometimes seen in the POS opening phase.

In addition, several models are widely known in the community, such as the Child-Langmuir/magnetically insulated model of the bremsstrahlung diode, and the slug model of the

Z-pinch plasma radiation source. Some of these models have analytic solutions. Most, however, must be solved numerically. Numerical solution of nonlinear differential equations is rather a dark art, which means that quite some effort must go into their solution. This effort should not be wasted. By putting this effort into developing a SPICE device, the numerical solution becomes reusable in a wide variety of contexts.

#### **6.4 WRITING A SPICE DEVICE.**

In a previous Annual Report (Reference 10), we discussed the details of writing a new SPICE device. We will not repeat that lengthy technical discussion here. However, we will summarize the essentials.

The state of any given circuit can be defined by the values of the voltages at all the nodes and the currents through all the branches. These must satisfy the Kirchhoff relations:

1. The sum of voltage drops around any loop must be zero.
2. The sum of currents entering any node must be zero.

In addition, there may be constraint equations between the current through a given branch and the voltage across it.

SPICE uses the "modified nodal" approach to solving this complicated set of equations. In this formulation, all nodal voltages are dynamical variables. Note that this automatically satisfies the Kirchhoff voltage equations, since the sum of voltage drops around a loop then reduces to pairwise cancellation of the form:

$$(V1 - V2) + (V2 - V3) + (V3 - V4) \dots = 0 \quad (6.1)$$

Using the constraint equations, the currents through each branch can then be calculated from the nodal voltages and substituted into the Kirchhoff current equations. This provides enough constraints to solve for the nodal voltages, and thus the currents.

In writing a SPICE device, it is sometimes a simplification to augment the nodal voltages with other dynamical variables. For example, in creating an inductor, it is useful to add the branch current through the inductor as a dynamical variable. This means that one must then add to the Kirchhoff current relations an extra equation in order to eliminate the new degree of freedom.

For the SPICE devices which we created for SPOCK, it was often necessary to add auxiliary dynamical variables which have nothing to do with electricity. For example, the PRS device has a time-dependent mass, momentum, kinetic energy, radius, and inductance. Equations for these can all be included in the SPICE formulation.

## **6.5 NEW SPICE DEVICES.**

In this section, we give a brief overview of the two dozen plus SPICE devices which we created for SPOCK. These fall into four categories:

1. POS devices
2. Load devices
3. Function devices
4. Miscellaneous devices.

We will also discuss very briefly a fifth category, the conventional devices defined by SPICE which we have found useful for pulsed-power simulations.

### **6.5.1 POS Devices.**

A plasma opening switch is characterized by an enormous parameter space. The geometry can be coaxial, radial, or rectangular. The dimensions can vary widely. The plasma source creates a plasma distribution function in two dimensions which may vary from shot to shot. The regime of the conduction phase may be Hall effect or MHD, or something else. The mechanism for the opening phase is not known exactly, but a number of different models have been used to describe it, with some degree of success. The switch performance may be degraded by a shorting mechanism which is not fully understood.

All this complexity is far too great to be described by a single device. We have chosen to break the POS down into several pieces, each described by a separate SPICE device. At a minimum, a POS requires a conduction phase device, a plasma source device, and an opening phase device. It may optionally have one or more devices to simulate short circuiting of the opening phase. These devices may be connected together like LEGO pieces to construct the full POS.

At present, two conduction phase devices have been written. One simulates a 1-D snowplow model. Another simulates a 1-D Hall Effect model. We have taken care to specify these devices



in such a way that new devices can be written in the future (such as a 2-D snowplow device). The new devices would be interchangeable with the existing ones. This is a principal feature of the programming technique we are using, object-oriented technology, which allows for plug-and-play swappable components.

The conduction phase devices allow the user to specify up to three other devices defining the plasma sources. One of these represents the plasma mass density; the other two represent the two components of the plasma velocity. These three plasma source devices can be individually chosen from the list of "2-D function devices" available in SPOCK. At present, there are only two of these, but they are a reasonably powerful subset of function space, and more devices can be added as needed. 2-D function devices are written to be interchangeable with each other.

And what is a 2-D function device? It is a device whose only purpose is to let the user define a mapping from  $(X,Y,T)$  onto the real line. Function devices can be assigned domains, overlaid on top of each other, and scaled or shifted. The mapping may be analytic or numerical, or a combination. A summary of function devices is given below.

We have written a number of opening phase devices, all interchangeable, which model the opening phase of the POS with varying levels of accuracy. So far, we have an R-dot model, a Z-flow model, and two variations of erosion models that include current conservation and dynamical Z-flow.

Finally, we have written two variations on a model for shorting a POS. This model assumes that neutrals behind the snowplow front begin to ionize during the opening phase, causing current to be shunted through a low impedance, and limiting the current transfer of the switch. These models are able to explain qualitatively, and semi-quantitatively, certain shots on ACE 4.

### **6.5.2 Load Devices.**

We have written three devices representing common load devices on pulsed-power machines:

1. The bremsstrahlung diode.
2. The plasma-filled diode.
3. The plasma radiation source using a slug or snowplow model of an imploding Z-pinch. The PRS model incorporates yield estimates, based on ideas from the NRL radiation group.

### 6.5.3 Function Devices.

Mathematically, a function is a mapping from one topological space (the domain) to another (the range). In SPOCK, we're going to limit this definition drastically. We'll require the range to cover N-dimensional space (and possibly also time), where N is 0, 1, or 2. And we'll require the range to be the real line. For our purposes, we'll need only the following conventions:

1. When we speak of 0-D functions, we mean real-valued functions of time only.
2. When we speak of 1-D functions, we mean real-valued functions of a 1-D space only.
3. When we speak of 2-D functions, we mean real-valued functions of the cross product of a 2-D space and time.

In keeping with our object-oriented philosophy, we also require that all 0-D function devices must be interchangeable, all 1-D functions must be interchangeable, and all 2-D function devices must be interchangeable. This means that a POS conduction device (which must specify a 2-D function device), can use any 2-D function device that has been written, or that ever will be written. All such devices can compute a value at (X,Y,T), and also partial derivatives of the function in X, Y, and T.

We also observe that functions often require shifting or scaling to be useful. Shifts are needed because there is no such thing as absolute space or time. Scaling is needed because people like to annoy each other by using different systems of physical units. We therefore require that all function devices allow us to easily shift and scale both the domain and the range.

Finally, we note that functions may be limited in domain. For example, a 0-D function may be defined over the range 0 to 1  $\mu$ s. What happens if a functional value is demanded outside this domain? The default result is that zero is returned. If this is unacceptable, then a "background value" can be supplied in the function definition. For points outside the domain, this background value would be returned. Sometimes, this is not enough either. Sometimes, it may be useful to supply a "background function" as a fallback. For points outside the domain of the first function, the background function would be called. Note that the background function can have its own domain, background value, and background function, and so on, ad infinitum.

At present, we have defined the following 0-D functions:

1. An analytic function of time. This can be a damped sine wave, a gaussian, or a fourth-order polynomial.
2. A numerical function of time, as specified in a file. This can be in the 1-column format used by Maxwell, the n-column format used by NRL, or the n-column format created by SPOCK's table output feature.

Similarly, we have defined the following 1-D functions:

1. An analytic function of 1-D space. This can be a sin wave, a gaussian, an exponential, a logarithm, or a fourth-order polynomial with poles of up to fourth order.
2. A numerical function of 1-D space, as specified in a file. This can be in the 1-column format used by Maxwell, the n-column format used by NRL, or the n-column format created by SPOCK's table output feature.

We have also defined the following 2-D functions:

1. A constant function of 2-D space and time.
2. A product function of 2-D space and time. This would take the form  $F(x,y,t) = F1(x)F2(y)F3(t)$ . Here, F1 and F2 are 1-D function devices and F3 is a 0-D function device.

Finally, we have defined an auxiliary "history" device that does nothing more than plot a time history of a 2-D function device at some chosen (X,Y) position. The history device could have been folded into the 2-D function devices, but this would have raised the complexity of that device, since an infinite number of (X,Y) points can be specified.

#### **6.5.4 Miscellaneous Devices.**

Here we summarize a number of other devices useful for completing this project.

The convolute device provides a simple 1-D Child-Langmuir model of a convolute. Convoluters are intrinsically 3-D objects, and are poorly understood. We make no claim that our 1-D device accurately represents the true physical device. However, it should be able to model a convolute qualitatively.

The explosively driven flux compressor is a component that amplifies current. It works by using high explosives to squeeze the volume of an inductance that has been charged with current. Flux conservation then produces a higher current.

SPICE provides the capability for voltage and current sources. However, they're a bit inconvenient to use. Therefore, we've written voltage and current source devices that are easier to use. They require the user to specify a 0-D function device. A 0-D function is a mapping from time to the real line. It can be either analytic or numerical. More details are provided above in the section on function devices.

SPICE also provides a couple of switch devices, triggered either by voltage or current. Neither of these is very convenient. We have written a switch device which rapidly changes from one resistance to another at a particular time. This is very useful in pulsed power applications, especially for circuits with closing switches in them. (Idealized opening switches can also be modeled, but these are less relevant.)

In pulsed power experiments, one often finds something that looks like a changing inductance (due to a spark moving along two parallel conductors). By time-integrating the measured voltage waveform, and dividing by the measured current waveform, one produces a time history of a quantity with dimensions of inductance. If there are resistive or nonlinear elements in the circuit, then the interpretation can be muddled somewhat, but it is useful to plot this "inductance" anyway. We have written a device which takes a voltage and a current waveform, and produces an "inductance" curve.

Since SPICE works with voltages explicitly, and calculates currents implicitly, it is sometimes useful to put an ammeter device directly into a circuit to measure the current. Our ammeter device does more; it numerically differentiates and integrates the current, which is very useful for those cases in which experimental data for  $I$ -dot or charge is available. In addition, (and at no extra expense), we have included the same "inductance" calculation discussed above. Here, the calculation is applied to the current and voltage computed in the circuit simulation. (The previously mentioned device computes the "inductance" only for experimental waveforms.)

## **6.6 CONVENTIONAL SPICE DEVICES.**

While the above types of exotic devices are extraordinarily useful, the majority of devices used to simulate pulsed-power circuits are already defined by SPICE. We simply list these here, without further comment:

1. Capacitor
2. Inductor
3. Resistor
4. Lossy transmission line
5. Mutual inductance between two inductors.

## **6.7 SPOCK SIMULATION OF DM1 WITH ELECTRON-BEAM LOAD.**

As an example of SPOCK's ability to simulate complex circuits, we set up the circuits shown in a recent technical note (Reference 24). In that technical note, DM1 was simulated using a combination of BERTHA, a circuit code, and CYLTRAN, a radiation code. Here, we reproduce some of the circuit simulations.

Figure 6-1 shows the results of simulation of DM1 shot 1143. The load was a bremsstrahlung diode with a 1-inch gap. We used a Z-flow POS opening model identical to that finally settled on in the NRL simulation. The flow impedance rose linearly to  $1.35 \Omega$  in 25 ns, and then decayed exponentially with a decay time of 55 ns.

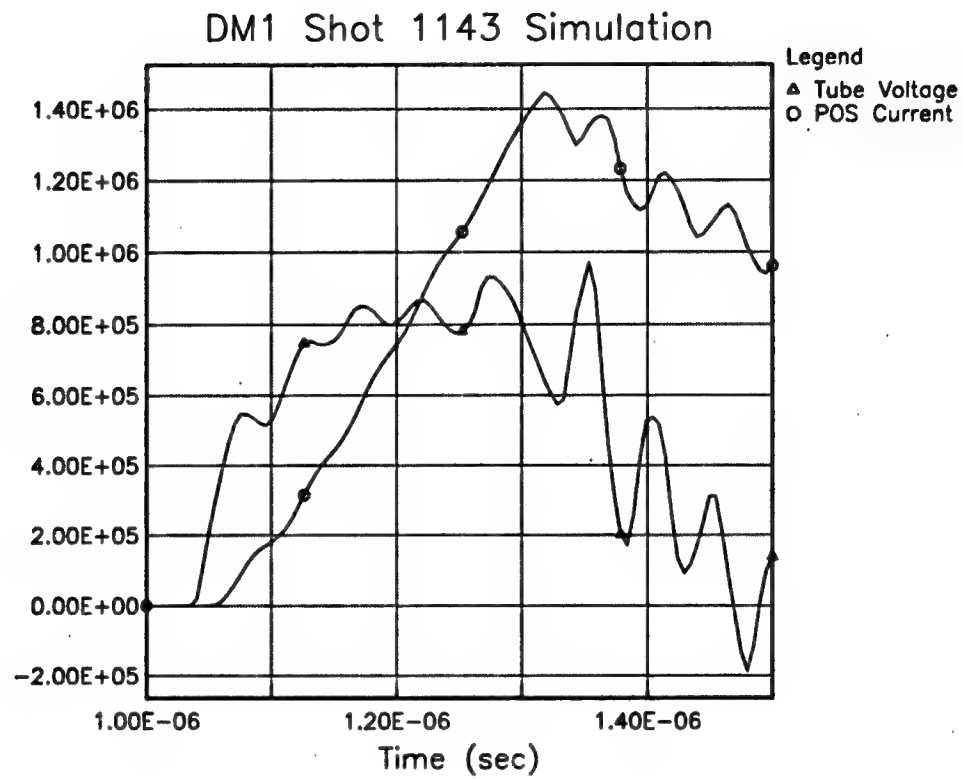
Figure 6-2 shows the results of simulation of DM1 shot 1322. The circuit is slightly changed from that studied in shot 1143, in accordance with the NRL technical note. Again, the load was a bremsstrahlung diode with a 1-inch gap, and we used the same opening model.

Figure 6-3 shows the results of simulation of DM1 shot 1353. The circuit is essentially that studied in shot 1322. Again, the load was a bremsstrahlung diode with a 1-inch gap, and we used the same opening model.

## **6.8 CONCLUSIONS.**

SPOCK provides a powerful tool for analyzing pulsed-power machines. It allows the user to easily build complicated circuits and study them interactively. It allows automatic parameter

studies, with good plotting capabilities in 1, 2, and 3 dimensions. It contains numerous specialized components of interest to the pulsed-power community, such as plasma opening switches, plasma radiation sources, bremsstrahlung diodes, plasma-filled diodes, and convolutes. New devices can be added to the code with minimal effort—typically a few hours to a few days, depending on the complexity of the equations of motion.



**Figure 6-1. Simulation of the POS Current and Tube Voltage for DM1 Shot 1143. This compares quite closely with Fig. 2 of the NRL technical note.**

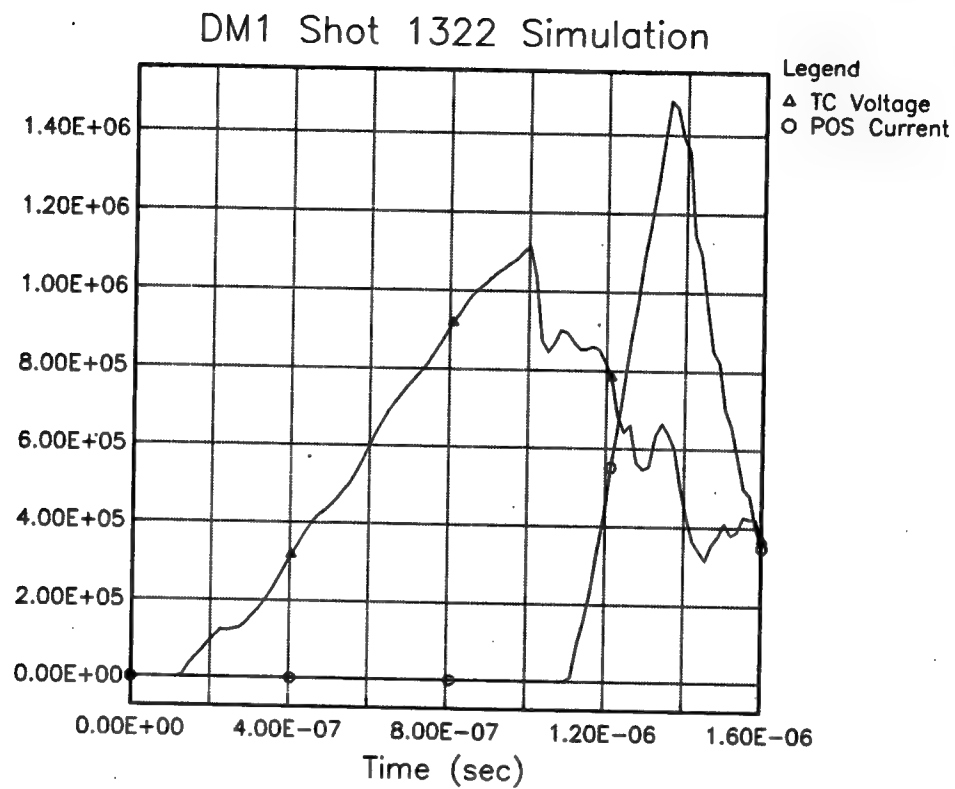


**Figure 6-2.** Simulation of the POS Current and Transfer Capacitor Voltage for DM1 Shot 1322. This compares quite closely with Fig. 4 of the NRL technical note.



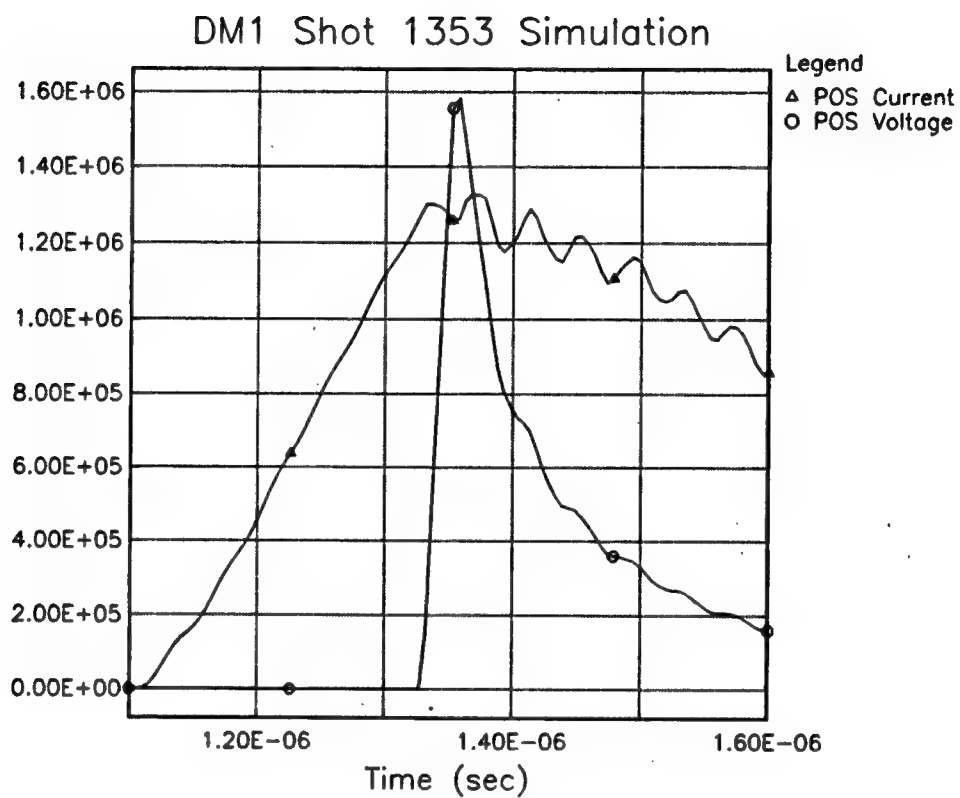


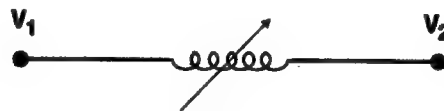
**Figure 6-3. Simulation of the POS Current and POS Voltage for DM1 Shot 1353. This compares quite closely with Fig. 6 of the NRL technical note.**

## SECTION 7 POS DEVICES

### 7.1 POS CONDUCTION MODELS.

#### 7.1.1 I-D Snowplow (SP1).

Model the I-D snowplow electrically as a time-varying inductance:



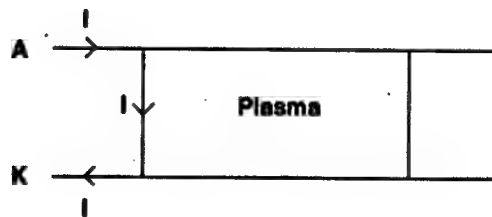
$$V_1 - V_2 = \frac{d\Phi}{dt}$$

(7.1)

$$\Phi = L I$$

where  $\Phi$  is the flux, and the inductance  $L$  is given by a formula that depends on the geometry (coaxial, radial, or rectangular). This formula will be given shortly.

We assume that the snowplow front is infinitely thin and scoops up plasma inelastically as it moves from one end of the switch to the other.



Let  $x$  = position of the snowplow front  
 $v$  = its velocity  
 $p$  = its momentum  
 $M$  = its mass

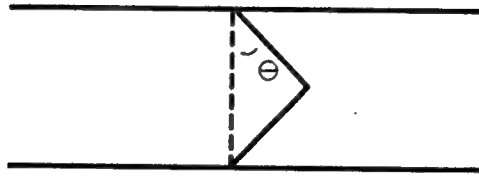
$A$  = its area

$B$  = magnetic field at the front

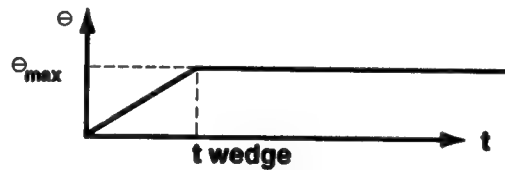
$\dot{M}_+$  = rate of mass accretion due to motion of snowplow into the plasma

$\dot{M}_-$  = rate of mass loss due to plasma being pushed to the electrodes.

We assume that the snowplow front evolves from a flat front into a wedge shape, with an angle  $\theta$  defined as shown:



We assume, in general, that  $\theta$  develops in time as:



but  $\theta_{\max}$  may be kept at zero to retain the conventional one-dimensional snowplow.

We also assume that the plasma has a mass density  $\rho(x,y,t)$  and a directed velocity  $\vec{U}(x,y,t)$ . Then the equations of motion are:

$$\frac{dx}{dt} = v \quad (7.2)$$

$$\frac{dM}{dt} = \dot{M}_+ - \dot{M}_- \quad (7.3)$$

$$V = \begin{cases} \frac{\rho}{M} & \text{if } M \neq 0 \\ \frac{\sigma B}{\sqrt{8\pi\rho(x,y,t)}} + U_x(x,y,t) & \text{if } M = 0 \end{cases} \quad (7.4)$$

$$\frac{dp}{dt} = \frac{\sigma B^2 A}{8\pi} + \dot{M}_+ U_+(x, y, t) - \dot{M}_- v \quad (7.5)$$

$$\dot{M}_+ = \sigma A \rho(x, y, t) [v - U_x(x, y, t)] \quad (7.6)$$

$$\dot{M}_- = \frac{2vM}{D} \tan(\theta(t)) \quad (7.7)$$

where  $D$  is the A-K gap and  $\sigma$  is the sign of the snowplow motion ( $\sigma = 1$  for coaxial and XYZ geometries,  $\sigma = -1$  for radial geometry).

The equations for the area  $A$ , magnetic field  $B$ , and inductance  $L$  are geometry dependent. We consider the three cases:

#### Coaxial geometry

$$A = \pi |r_A^2 - r_c^2| \quad (7.8)$$

$$B = \frac{I}{5\bar{r}} \quad (7.9)$$

$$L = 2 \times 10^{-9} (x - x_i) \log \left| \frac{r_A}{r_c} \right| \quad (7.10)$$

where  $r_A$  = anode radius

$r_c$  = cathode radius

$\bar{r}$  = mean snowplow radius

$x_i$  = initial position of snowplow

and  $x$  is axial position of snowplow.

#### Radial geometry

$$A = 2\pi X (\Delta Z) \quad (7.11)$$

$$B = \frac{I}{5X} \quad (7.12)$$

$$L = 2 \times 10^{-9} (\Delta Z) \log \left( \frac{X_i}{X} \right) \quad (7.13)$$

where  $\Delta Z$  = anode-cathode gap

$X$  = radial position of snowplow

$X_i$  = initial position.

XYZ geometry

$$A = (\Delta Y) (\Delta Z) \quad (7.14)$$

$$B = \frac{4 f I \left[ \tan^{-1} \left( \frac{\Delta Z}{\Delta Y} \right) \right]}{(\Delta Z)} \quad (7.15)$$

$$L = \frac{16 \times 10^{-9} f^2}{\pi} \left( \frac{\Delta Y}{\Delta Z} \right) \left[ \tan^{-1} \left( \frac{\Delta Y}{\Delta Z} \right) \right]^2 (X - X_i) \quad (7.16)$$

where  $\Delta Y$  = anode-cathode gap

$\Delta Z$  = width of switch

$f$  = fudge factor approximately equal to 1

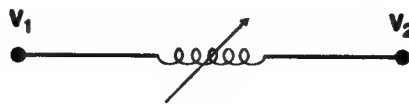
$X$  = position of snowplow front

$X_i$  = initial position.

The fudge factor  $f$  was introduced to account for possible non-uniformities of the magnetic field in the  $Y$  or  $Z$  directions.

### 7.1.2 1-D Hall Effect Device (EH1).

This device is very similar to the 1-D snowplow:



$$V_1 - V_2 = \frac{d\Phi}{dt} \quad (7.17)$$

$$\Phi = L I$$

$$\frac{dx}{dt} = V \quad (7.18)$$

$$V = \frac{\sigma c B}{2\pi e \ell n(x,y,t)} + U_x(x,y,t) \quad (7.19)$$

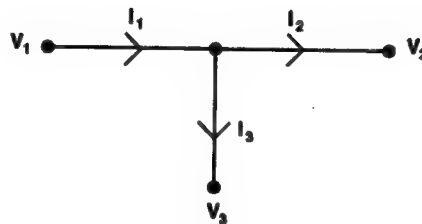
where  $\ell$  is a length scale for plasma non-uniformities

$n(x,y,t)$  is the number density of electrons in the plasma.

The magnetic field  $B$  and inductance  $L$  are given by the same geometry-dependent formulae as the 1-D snowplow model, so we will not repeat them here.

## 7.2 POS OPENING MODELS.

All POS opening models will be required to have the following topology:



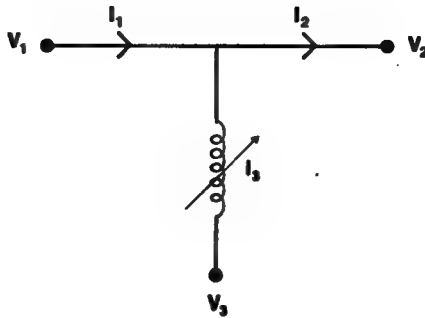
$V_1$  is the upstream anode voltage,

$V_2$  is the downstream anode voltage, and

$V_3$  is the cathode voltage.

An opening device has an associated conduction phase device. As long as the conduction phase continues,  $V_1$  and  $V_3$  are required to be essentially identical. Only when the conduction phase ends is the voltage difference  $V_1 - V_3$  allowed to rise.

### 7.2.1 R-dot Opening Model (ORD).



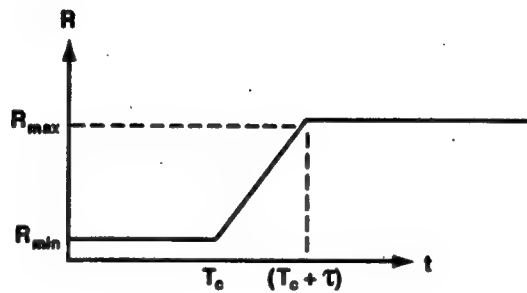
The equations of motion are:

$$V_1 = V_2$$

$$I_1 - I_2 - I_3 = 0$$

$$V_1 - V_3 = R(t) I_3 \quad (7.20)$$

where  $R(t)$  has the behavior:



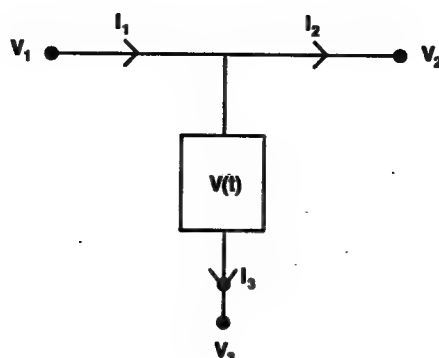
$T_c$  is the time when the conduction phase ends

$\tau$  is the rise time of the resistance

$R_{\min}$  is the initial switch resistance (may be 0)

$R_{\max}$  is the final switch resistance.

### 7.2.2 Z-flow Opening Model (OZF).



The equations of motion are:

$$V_1 = V_2$$

$$I_1 - I_2 - I_3 = 0$$

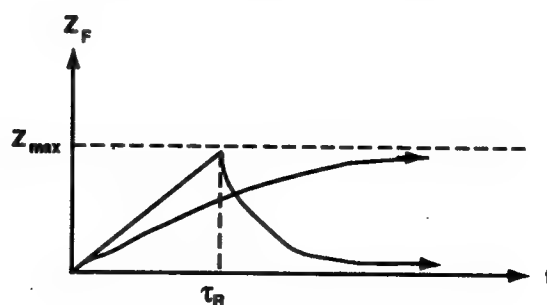
$$V_1 - V_3 = V$$

$$V = \sigma_- Z_F \bar{I}$$

$$\bar{I} = \sqrt{I_1^2 - I_2^2} \quad (7.21)$$

where  $\sigma_- = \text{sign}(I_1 - I_2)$ .

The flow-impedance  $Z_F$  is allowed to have two different behaviors.





In one variation,  $Z$  rises asymptotically to  $Z_{max}$ :

$$\frac{dZ_F}{dt} = \frac{Z_{max} - Z_F}{\tau_R} \quad (7.22)$$

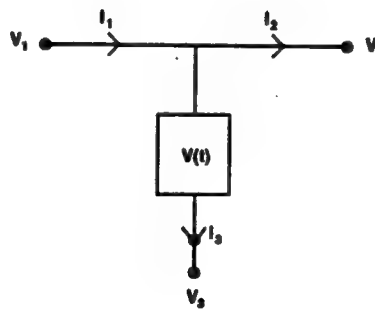
In the other variation, the "NRL model,"  $Z_F$  rises linearly to  $Z_{max}$ , then falls exponentially to 0:

$$\frac{dZ_F}{dt} = \begin{cases} \frac{Z_{max}}{\tau_R} & \text{if } t < \tau_R \\ -\frac{Z_F}{\tau_0} & \text{if } t > \tau_R \end{cases} \quad (7.23)$$

In both of these cases, we have shifted the origin of time to the end of the conduction phase for clarity.

### 7.2.3 Erosion Z-flow Opening Model (OEZ).

In this model,  $Z$ -flow is computed dynamically.



The equations of motion are:

$$V_1 = V_2$$

$$I_1 - I_2 - I_3 = 0 \quad (7.24)$$

$$V = V_1 - V_3$$

$$B_a = \left( \frac{\partial B}{\partial I} \right) I_1$$

$$B_c = \left( \frac{\partial B}{\partial I} \right) I_2$$

$$\dot{D} = j - V_T$$

$$j\sqrt{V} = \frac{1}{8\pi n_1} \sqrt{\frac{150}{eZM} (B_a^2 - B_c^2)}$$

$$Z_F = \frac{60 \alpha D}{\bar{r}}$$

$$V = \sigma_- Z_F \bar{I}$$

$$\bar{I} = \sqrt{I_1^2 - I_2^2}$$

where

$$\frac{\partial B}{\partial I} = \frac{1}{5\bar{r}} \quad (7.25)$$

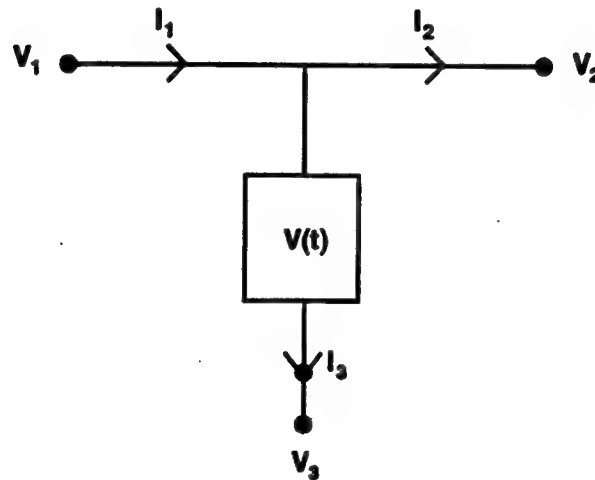
$\bar{r}$  is the mean radius at the position of opening  
 $j$  is an ion current scaled to have dimensions of velocity  
 $D$  is the gap, which opens from zero  
 $V_T$  is a thermal velocity, typically 1 cm/ $\mu$ s  
 $\alpha$  is a fudge factor, nominally about 1/2  
 $n_i$  is the ion number density  
 $Z$  is the ionization number

$M$  is the ion mass

$$\sigma = \text{sign} (I_1 - I_2).$$

#### 7.2.4 Limited Erosion Z-flow Opening Model (OEL).

This model is very similar to the erosion z-flow opening model, but it includes effects due to the transition from the load-limited regime to the switch-limited regime.



The equations of motion are:

$$V_1 = V_2$$

$$I_1 - I_2 - I_3 = 0$$

$$V = V_1 - V_3$$

$$B_a = \left( \frac{\partial B}{\partial I} \right) I_1 \quad (7.26)$$

$$B_c = \begin{cases} \left( \frac{\partial B}{\partial I} \right) I_2 & \text{if load - limited} \\ \frac{B_a}{\gamma_m} & \text{if switch - limited} \end{cases}$$

$$1 + \frac{V}{\tilde{V}} = \gamma_m + (\gamma_m^2 - 1)^{3/2} \log [\gamma_m + \sqrt{\gamma_m^2 - 1}]$$

$$\dot{D} = j - V_T$$

$$j \sqrt{V} = \frac{1}{8\pi m_i} \sqrt{\frac{150}{eZM}} (B_a^2 - B_c^2)$$

$$V = \sigma_- Z_F \bar{I}$$

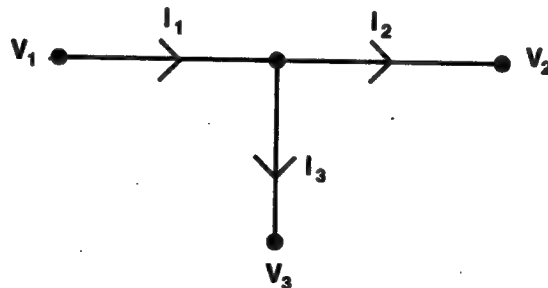
$$\bar{I} = \sqrt{|I_1^2 - I_2^2|}$$

$$Z_F = \frac{60 \alpha D}{\bar{r}}$$

Since most of these are identical to the OEZ device, we will not repeat the discussion given for that device.  $\tilde{V} = 511$  keV and  $\gamma_m$  is the  $\gamma$ -factor applicable to the switch-limited regime. We note that the initial conditions  $V = 0$ ,  $D = 0$  define an unstable fixed point. The solution is to tweak the value of  $V_T$  for very small values of  $D$ .

### 7.3 POS SHORTING MODELS.

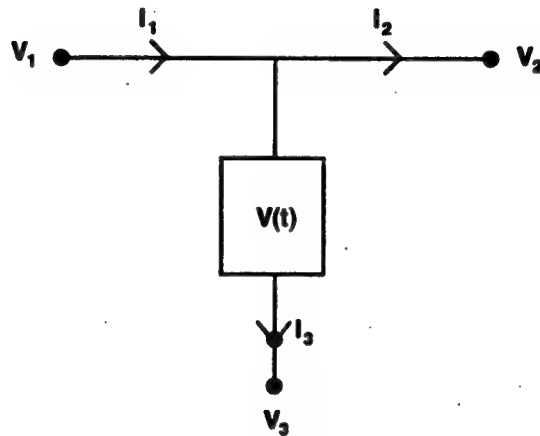
POS shorting models have the same topology as ordinary opening models:



The difference is that the short-circuit models represent the development of a low impedance anode-cathode current path in parallel with a high-impedance opening switch. The short-circuit is postulated to be an effect of neutrals left behind the current path in the anode-cathode gap.

When the opening phase begins, these neutrals ionize rapidly and conduct current, shorting the POS.

### 7.3.1 Simple Short-circuit Model (OSM).



The equations of motion are:

$$V_1 = V_2$$

$$I_1 - I_2 - I_3 = 0$$

$$V = V_1 - V_3$$

(7.27)

$$V = \frac{10^{-6}}{\nu(t)\bar{r}^2} (I_1^2 - I_2^2)$$

where  $\bar{r}^2 = r_A r_C$

$$\nu(t) = \frac{\nu_o X_o}{(1 - X_o) \exp(-t/\tau) + X_o}$$

$$\nu_o = \frac{N_o}{10^{15}}$$

$r_A$  = anode radius

$r_c$  = cathode radius

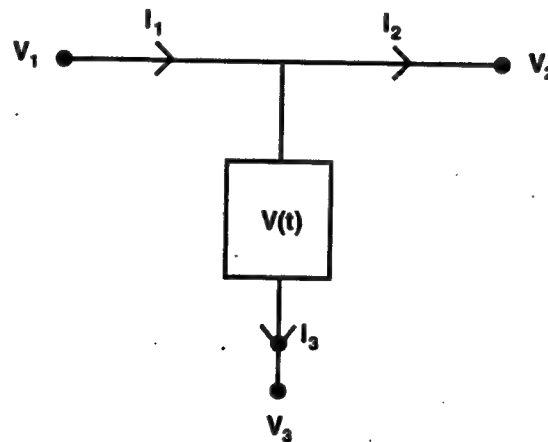
$X_o$  is an initial ionization fraction, nominally .001 to .1

$N_o$  is an initial neutral density, nominally  $10^{13}$  to  $10^{16}$  /cm<sup>3</sup>

$\tau$  is a relaxation time, nominally 100 ns.

This model is an experimental model to test the principle. We have largely supplanted it with the more detailed temperature-dependent short-circuit model.

### 7.3.2 Temperature-Dependent Shorting Model (OST).



The equations of motion are:

$$V_1 = V_2$$

$$I_1 - I_2 - I_3 = 0$$

$$V = V_1 - V_3 = \frac{9.95 \times 10^8}{\bar{r}^2} \frac{I_3 (I_1 + I_2)}{n} \quad (7.28)$$

$$\frac{dn}{dt} = n (N_o - n) <\sigma v> + f \sigma_p (N_o - n)$$

$$\langle \sigma v \rangle = \frac{10^{-5} \left( \frac{\theta}{I} \right)^{1/2} e^{-11\theta}}{I^{3/2} \left( 6 + \frac{\theta}{I} \right)}$$

$$\frac{d}{dt} \left[ n \left( \frac{3}{2} \theta + I \right) \right] = \frac{e^2 n}{m} \left( \frac{\tau_c}{w^2 \tau_c^2 + 1} \right) E^2$$

$$+ \frac{3}{2} \theta_r f \sigma_p (N_o - n)$$

$$w_c = \frac{e}{10\bar{r} mc} (I_1 + I_2)$$

$$E = \frac{300 \text{ V}}{d}$$

$$\tau_c = \frac{10^4 \theta^{3/2}}{n}$$

$$\bar{r}^2 = \frac{1}{3} (r_a^2 + r_a r_c + r_c^2)$$

$r_a$  = anode radius

$r_c$  = cathode radius

$n$  = electron density

$N_o$  = initial neutral density

$f = 4 \times 10^{22} \text{ cm}^{-2} \text{ sec}^{-1}$

where

$$\sigma_p = \begin{cases} 6 \times 10^{-18} \text{ cm}^2 & t > T_{\text{delay}} \\ 0 & t < T_{\text{delay}} \end{cases}$$

$T_{\text{delay}}$  = delay time before ionization begins

$d$  = anode – cathode gap size

$\theta_r$  = creation temperature of  $\sim 2 \text{ eV}$

$I$  = ionization energy, species – dependent

For hydrogen,  $I = 13.595 \text{ eV}$

For carbon,  $I = 11.256 \text{ eV}$

For oxygen,  $I = 13.614 \text{ eV}$

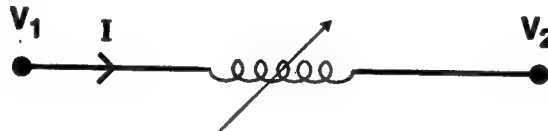
For nitrogen,  $I = 14.53 \text{ eV}$

For fluorine,  $I = 17.418 \text{ eV}$ .

## 7.4 LOAD DEVICES.

### 7.4.1 1-D PRS (PRS).

We consider both slug and puff models of the PRS in a 1-dimensional approximation. Electrically, the device is a variable inductance. Mechanically, it is a thin cylindrical shell which implodes radially on the z-axis. The slug variation of the model does not accrete mass. The puff variation does accrete mass. Schematically, the device looks like this:



The equations of motion are:

$$V_1 - V_2 = V$$

$$V = \frac{d\Phi}{dt} + IR$$

$$\Phi = LI \tag{7.29}$$

$$L = (2 \times 10^{-9}) \ell \log \left( \frac{r_c}{r} \right)$$

$$\frac{dr}{dt} = -v$$

$$\frac{dp}{dt} = \frac{\ell}{4} r B^2$$



$$\frac{dM}{dt} = \begin{cases} \Phi \pi \ell v r \rho(r) & (\text{puff model}) \\ 0 & (\text{slug model}) \end{cases}$$

$$v = \begin{cases} \rho / M & \text{if } M > 0 \\ \frac{B}{\sqrt{8\pi\rho(r)}} & \text{if } M = 0 \end{cases}$$

$$B = \frac{I}{5r}$$

$$K = \frac{1}{2} (10^{-7}) p v$$

$$\eta = \left( \frac{v}{v_{\min}} \right)^2$$

$$Y_{wg} = \begin{cases} M^2 A_{wg} & \text{if } M < M_{BP} \\ M B_{wg} & \text{if } M > M_{BP} \\ 0 & \text{if } \eta < 1 \end{cases}$$

where  $V$  is the voltage across the device

$R$  is the resistance of the plasma shell

$\Phi$  is the flux

$L$  is the inductance

$r$  is the radius of the shell

$p$  is the momentum of the shell

$M$  is the mass of the shell

$v$  is the velocity of the shell

$B$  is the magnetic field

$K$  is the kinetic energy in Joules

$\eta$  is the Whitney eta parameter

$V_{\min}$  is the minimum velocity required to excite K-shell radiation

$Y_{wg}$  is the Whitney-Giuliani yield estimate

and

$$A_{WG} = A_0 + \frac{A_1}{N} + \frac{A_2}{n^2}$$

$$B_{WG} = B_0 N$$

$$M_{BP} = \frac{B}{A}$$

$$A_0 = 33.7 \bar{A}$$

$$A_1 = 595 \bar{A}$$

$$A_2 = -70.7 \bar{A}$$

$$B_0 = (.3) (9.1 \times 10^4) Z^{2.41}$$

$$\bar{A} = \left( \frac{10^{15}}{6\ell Z^{3.55}} \right) \exp \left( \frac{-20.6}{Z^9} \right)$$

and  $Z$  is the atomic number of the imploding material.

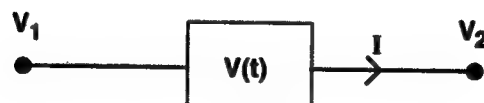
Also,  $\ell$  is the length of the shell

$r_c$  is the cage radius

$\rho(r)$  is the distribution function of the mass density.

#### 7.4.2 Bremsstrahlung Diode (BRD).

The model used here was developed at NRL. Schematically it looks like this:



The equations of motion are:

$$V_1 - V_2 \doteq V$$

$$I_c = PV^{3/2}$$

$$I_M = \frac{K_M}{d} (\gamma^2 - 1)^{1/2} \quad (7.30)$$

$$I = \begin{cases} 0 & \text{if } V < V_{\text{threshold}} = d_1 E_{\text{thresh}} \\ I_c & \text{if } I_c < I_M \text{ and } V > V_{\text{thresh}} \\ I_M & \text{if } I_c < I_M \text{ and } V > V_{\text{thresh}} \end{cases}$$

$$P = \left( \frac{p_1}{d^2} + \frac{p_2}{di\alpha^2} \right) g(t)$$

$$\alpha = \begin{cases} \beta - 0.4 \beta^2 + 0.097 \beta^3 - 0.0142 \beta^4 + 0.00168 \beta^5 - 0.00016 \beta^6 & \text{if } 0 < \beta < 2.3 \\ .99 & \text{if } \beta > 2.3 \end{cases}$$

$$\beta = \log \left( \frac{di + R_e}{R_e + v(t - t_o)} \right)$$

$$p_1 = 2.33 \times 10^{-6} \pi (R_{out}^2 - R_{in}^2)$$

$$p_2 = \left( \frac{14.66 \times 10^{-6}}{8} \right) 2\pi (R_{out} + R_{in})$$

$$K_M = 8500 F R_{out}$$

$$d = \begin{cases} d_i & t < t_o \\ d_i - v(t - t_o) & t_o < t < t_f \\ d_f & t > t_f \end{cases}$$

$$t_f = t_o + \frac{d_i - d_f}{v}$$

where:  $V$  is the voltage across the device

$I_c$  is the Child-Langmuir current that could flow through the device

$I_m$  is the magnetic-limited current that could flow through the device

$I$  is the actual device current

$P$  is the perveance

$\gamma$  is the relativistic factor of electrons

$K_M$  is the magnetic-limiting factor

$F$  is the geometry factor, nominally about 1.6

$\tilde{V}$  is the electron rest mass of 511 keV

$E_{thresh}$  is a threshold electric field for electron emission

$d_i$  is the initial diode gap

$d_f$  is the final (minimum) diode gap

$v$  is the gap closure velocity

$t_f$  is the time required for the gap to close

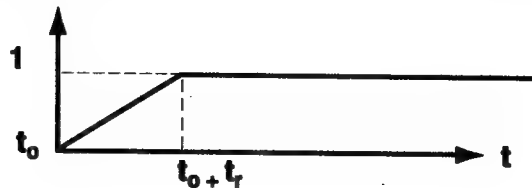
$R_{in}$  is the cathode inner radius

$R_{out}$  is the cathode outer radius

$R_e$  is the cathode edge radius of curvature

$t_o$  is the time at which the electric field first exceeds  $E_{thresh}$

$g(t)$  is a linear ramping function for the Child-Langmuir emission law:



$t_r$  is the time required for emission to ramp up fully. Finally, for convenience we include equations for power and energy:

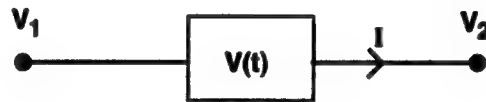
$$P = IV \quad (7.31)$$

$$\frac{dE}{dt} = P$$

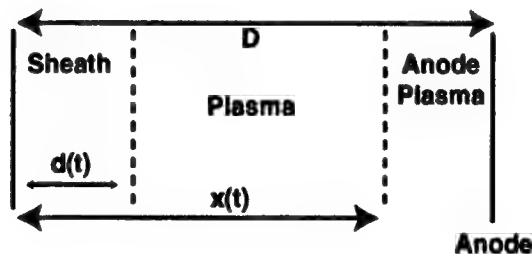
where  $P$  is the power dissipated and  
 $E$  is the accumulated energy.

### 7.4.3 Plasma-Filled Diode (PFD).

Schematically, the plasma-filled diode looks like this:



Physically, the device is quite complicated. We simplify it to a 1-dimensional model as shown below:



We assume that the sheath obeys a bipolar Child-Langmuir voltage-current relation, and that the sheath grows by erosion into the plasma. At early times, energy is deposited on the anode until a threshold is reached. Then, a dense anode gas is desorbed and ionized to form an anode plasma, which moves toward the cathode. Eventually, the sheath boundary reaches the edge of the anode plasma. The equations of motion are:

$$V_1 - V_2 = V$$

$$I = 4.33 \times 10^{-6} \frac{A V^{3-2}}{d^2}$$

(7.32)

$$\frac{d\varepsilon}{dt} = \frac{IV}{A}$$

$$j = \frac{\alpha I}{ZenA}$$

$$\frac{\partial d}{\partial t} = \begin{cases} j & \text{if } d < X \\ \frac{\partial X}{\partial t} & \text{if } d \geq X \end{cases}$$

$$\frac{\partial X}{\partial t} = \begin{cases} \frac{-V_a X}{D} & \text{if anode plasma has been emitted} \\ 0 & \text{otherwise} \end{cases}$$

where  $\varepsilon$  is the energy/area absorbed by the anode  
 $j$  is ion current, normalized to velocity units  
 $d$  is the sheath size  
 $X$  is the position of the anode plasma

and  $A$  is the area of the cathode

$\alpha = \sqrt{\frac{Z m_e}{M_i}}$  is the bipolar mass ratio

$D$  is the initial gap size

$Z$  is the ionization number of the plasma

$m_e$  is the electron mass

$M_i$  is the ion mass

$n$  is the plasma ion number density

$V_0$  is the initial velocity of the anode plasma  
 $\epsilon_T$  is the threshold for anode desorption.

The anode plasma is desorbed when  $\epsilon = \epsilon_T$ .

## 7.5 FUNCTION DEVICES.

### 7.5.1 O-D Analytic Function (FANØ).

A O-D analytic function in SPOCK is a function of time alone. At present there are three varieties:

#### Damped Sin

$$f(t) = A_{\text{exp}} [-\gamma (t - t_0)] \sin [\omega t + \phi]$$

#### Gaussian

$$f(t) = A \exp \left[ -\left( \frac{t - T_D}{\tau} \right)^2 \right]$$

#### Polynomial (4th order)

$$f(t) = C_0 - C_1 t + C_2 t^2 + C_3 t^3 + C_4 t^4$$

### 7.5.2 O-D Function on Grid (FGRØ).

A O-D function on a grid is a function of time alone, defined by a set of data points in a text file. At present, three file formats are allowed:

#### Maxwell 1-column Format

N, dt

Y<sub>1</sub>

Y<sub>2</sub>

.

.

.

$Y_N$

where  $N$  is the number of data points

$dt$  is the time-separation between data points

$Y_i$  is the  $i$ th data point

#### NRL N-column Format

$N$

$T_1, Y_{11}, Y_{12}, \dots Y_{1M}$

.

.

.

.

$T_N, Y_{N1}, Y_{N2}, \dots Y_{NM}$

where  $N$  is the number of data points

$M$  is the number of functions in the file

$T_i$  is the time of the  $i$ th point

$Y_{ij}$  is the  $i$ th data point in the  $j$ th function.

#### MIRIAD N-column Format

Label	Label	....	Label
Units	Units	....	Units
$T_1,$	$Y_{11},$	$Y_{12},$	$\dots Y_{1M}$
.			
.			
.			
$T_N,$	$Y_{N1},$	$Y_{N2},$	$\dots Y_{NM}$

This is nearly identical to the NRL format, except that  $N$  is not given explicitly, and the first two rows are ignorable text.



### 7.5.3 1-D Analytic Function (FAN1).

A 1-D function in SPOCK is a function of one spatial variable alone. We will call that variable  $S$  here. It can be  $x, y, z, r, \theta, \phi$ , etc. At present, there are five varieties:

#### Sin

$$f(s) = A \sin (ks + \phi)$$

#### Gaussian

$$f(s) = A \exp \left[ - \left( \frac{s}{\sigma} \right)^2 \right]$$

#### Exponential

$$f(s) = A \exp (ks)$$

#### Logarithm

$$f(s) = A \log (ks)$$

#### Polynomial

$$f(s) = C_0 + C_1 S + C_2 S^2 + C_3 S^3 + C_4 S^4 \\ + C_{-1} S^{-1} + C_{-2} S^{-2} + C_{-3} S^{-3} + C_{-4} S^{-4}$$

### 7.5.4 1-D Function on Grid (FGR1).

A 1-D function on a grid is a function of one spatial variable alone. This variable, we call  $s$ . The function is defined by a set of data points in a text file. At present, three file formats are allowed, and these are explained in detail in the discussion of the O-D function on grid.

### 7.5.5 2-D Constant Function (FCN2).

A 2-D constant function in SPOCK is a function that is constant over some domain in two spatial dimensions and in time.

### 7.5.6 2-D Product Function (FPR2).

A 2-D product function in SPOCK is a function over two spatial dimensions and over time, and which can be factored as a product of three functions:

$$F(x,y,t) = F_1(x) F_2(y) F_3(t)$$

Here,  $F_1$  and  $F_2$  are 1-D functions, and  $F_3$  is a 0-D function.

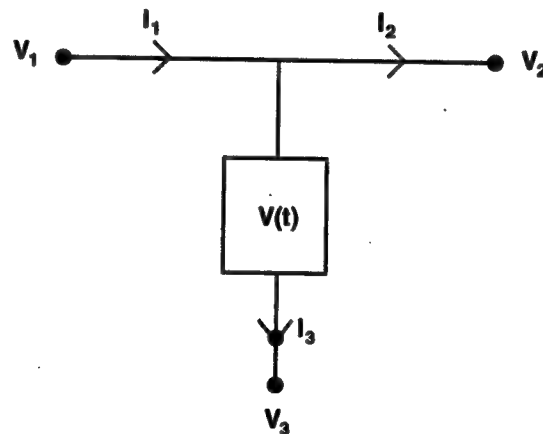
### 7.5.7 Function History (HIST).

It is sometimes useful to plot the time history of the value of a 2-D function at some particular point  $(X_o, Y_o)$ . The history device lets you specify  $X_o$  and  $Y_o$ , and it then makes available a plot of the function  $F(X_o, Y_o, t)$ .

## 7.6 MISCELLANEOUS DEVICES.

### 7.6.1 Convolute (CNV).

Convolutees are complicated 3-dimensional circuit elements. We present here a 1-D model which should provide a qualitatively correct simulation of a convolute. Schematically, the device looks like this:



Physically, we model the device as follows. Early on, there is some small leakage current defined by a large resistance  $R_o$ . When the mean electric field across the gap exceeds some threshold value  $E_{\text{thresh}}$ , the device begins emitting electrons according to a Child-Langmuir law. Also, a cathode plasma forms and begins moving toward the anode with a velocity  $v_c$ . As the anode continues to absorb energy from the current flow, it reaches the threshold for desorption of gases, which ionize to form an anode plasma with a velocity  $v_a$  toward the cathode. We

assume that the device can be characterized by an effective area  $A$  and gap  $D$ . The equations of motion are:

$$\begin{aligned} V_1 &= V_2 \\ I_1 - I_2 - I_3 &= 0 \\ V_1 - V_3 &= V \end{aligned}$$

(7.33)

$$I_3 = \begin{cases} \frac{V}{R_o} & \text{before cathode emission} \\ \frac{KA|V|^{3/2}}{D^2} & \text{after cathode emission} \end{cases}$$

$$\dot{\epsilon} = \begin{cases} 0 & \text{before cathode emission} \\ \frac{I_3 V}{A} & \text{after cathode emission} \end{cases}$$

$$\dot{D} = \begin{cases} 0 & \text{before cathode or anode emission} \\ -v_c D/D_i & \text{after cathode emits, before anode emits} \\ -(v_c + v_a) D/D_i & \text{after cathode and anode emit} \\ 0 & \text{when } D \leq D_{\min} \end{cases}$$

$R_o$  is the initial impedance, chosen to match the dynamic impedance at cathode breakdown:

$$R_o = \frac{2}{3} \frac{D_i^{3/2}}{K A E_{\text{thresh}}^{1/2}}$$

$$K = 2.33 \times 10^{-6}$$

$A$  is the effective area of emission

$D_i$  is the initial effective gap

$\epsilon$  is the energy absorbed per unit area on the anode

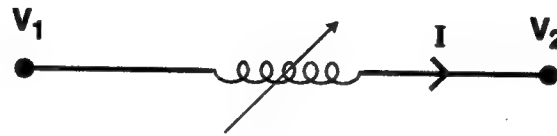
$D$  is the effective gap

$E_{\text{thresh}}$  is the threshold electric field for cathode emission,  $\sim 100$  kV/cm

$\epsilon_{\text{thresh}}$  is the threshold value of  $\epsilon$  for anode emission, ~few hundred J/gm  
 $D_{\text{min}}$  is the minimum gap size allowed.

### 7.6.2 Explosively Driven Flux Compressor (EDFC).

This device amplifies current by charging an inductive region with current, and then compressing the region with high explosives. At present, we assume an exponentially decreasing volume, for simplicity. Schematically the device looks like:



The equations of motion are:

$$V_1 - V_2 = \frac{d\Phi}{dt}$$

$$\Phi = LI \quad (7.34)$$

$$L = \begin{cases} L_0 & t < T_0 \\ L_0 \exp[-(t - T_0)/\tau] & t \geq T_0 \end{cases}$$

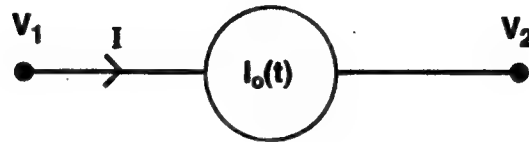
where  $L_0$  is the initial inductance

$T_0$  is the time of explosion

$\tau$  is the time constant of compression.

### 7.6.3 Current Source (ISC).

SPOCK allows you to create a current source, using many O-D function device to specify the current. Schematically, the device looks like:

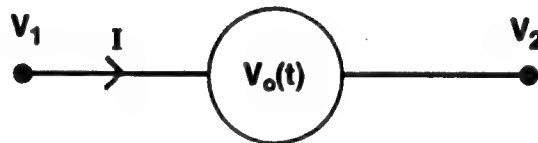


The equations of motion are:

$$\begin{aligned} I &= I_o(t) \\ V_1 - V_2 &= V \end{aligned} \quad (7.35)$$

### 7.6.4 Voltage Source (VSC).

SPOCK allows you to create a voltage source, using any O-D function device to specify the voltage. Schematically, the device looks like:



The equations of motion are:

$$\begin{aligned} V_2 - V_1 &= V \\ V &= V_o(t) \end{aligned} \quad (7.36)$$

### 7.6.5 Timed Switch (SWT).

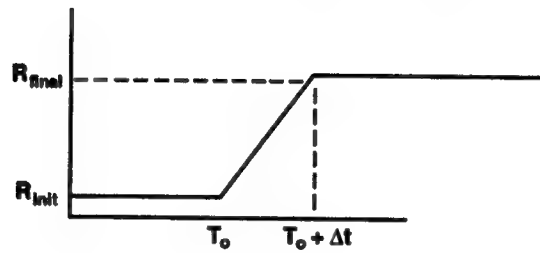
SPOCK allows you to create a nearly ideal switch. Schematically, the switch looks like this:



The equations of motion are:

$$\begin{aligned} V_1 - V_2 &= V \\ V &= I R(t) \end{aligned} \quad (7.37)$$

where  $R(t)$  is a resistance function with a time-history of this form:



where  $R_{init}$  is the initial impedance

$R_{final}$  is the final impedance

$t_0$  is the time the switch begins to open or close

$\Delta t$  is the time required for the switch to fully open or close.

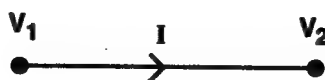
The switch can be either an opening or closing switch. That is,  $R_{init}$  can be less than or greater than  $R_{final}$ .

As a practical matter, we note that the device performs well even for  $\Delta t \sim 1$  ns, and

$\frac{R_{init}}{R_{final}} \sim 10^{12}$ . These are fairly extreme values.

#### 7.6.6 Ammeter (IMR).

This device is a multi-purpose passive measuring tool. It can probe the current,  $I$ -dot, integrated charge, and estimated inductance-to-ground. Schematically, the device looks like:



The equations of motion are:

$$V_1 - V_2 = 0$$

$$\dot{X}(t) = \frac{dI}{dt}$$

$$\frac{dQ}{dt} = I \quad (7.38)$$

$$\frac{d\Phi}{dt} = V_i$$

$$L = \frac{\Phi}{I}$$

It is understood that  $L$  is an estimate of the inductance to ground. Also, the numerical differentiation  $\frac{dI}{dt}$  may not be smooth.

#### 7.6.7 Inductance Estimator (LVI).

This device performs the same inductance-to-ground estimate that the ammeter does. Here, however, there is no schematic representation, because this device does not connect into a SPOCK circuit. Instead, it uses SPOCK O-D function devices to represent voltage and current waveforms  $V_o(t)$  and  $I_o(t)$ . The equations of motion are:

$$\frac{d\Phi}{dt} = V_o(t) \quad (7.39)$$

$$L = \begin{cases} \frac{\Phi}{I_o(t)} & \text{if } I_o(t) \neq 0 \\ 0 & \text{if } I_o(t) = 0 \end{cases}$$

$\Phi$  is the integrated flux, and  $L$  is an estimate of the inductance to ground. Because of resistive or non-linear effects, this estimate may well be incorrect.

## **SECTION 8**

### **TRIMAX UNSTRUCTURED GRID ELECTROMAGNETIC PIC CODE EXTENSIONS**

#### **8.1 MOTIVATION.**

Traditional finite difference time domain (FDTD) electromagnetic particle-in-cell (PIC) codes such as MAGIC, TWOQUICK and FRED are fundamentally based upon a structured grid methodology. While usually adequate for "textbook" problems, faced with real-world pulsed power applications, these codes frequently suffer from some serious limitations. Often fine-zoning requirements in one region of the mesh dictate that many additional zones be wasted in unrelated regions. Additional zones may also be squandered on the description of multiply-connected regions. Unnecessarily high aspect mesh size ratios may be required sometimes leading to loss of accuracy at best and incursion of non-physical instabilities at worst. Space-charge-limited emission from complex curved surfaces is generally problematic with stair-step approximation of boundaries often leading to non-physical local field enhancements. While these problems may sometimes be ameliorated by the use of boundary-fitted coordinates (Reference 39) (the ISIS code, for example) we believe the most satisfactory resolution of these problems is best facilitated within an unstructured grid formulation (Reference 29). With a modification to the S-Cubed TRIMAX electromagnetic field solver and incorporation of a finite element generalization of the FRED particle current algorithm we have successfully developed such a formulation. In this section we outline the details of this formulation, provide a summary of the resulting code capabilities, and present several examples of code applications including an analysis of an ACE 4 POS/load electron flow experiment.

#### **8.2 TRIMAX FINITE ELEMENT FIELD SOLVER.**

A number of techniques for the finite element solution of Maxwell's electromagnetic equations have been proposed in the literature over the past decade (References 26, 29, 30, 31, 34, 37, 38, and 39). The ECHL, MECHL, and ELnHC methods analyzed by Monk (References 25, 26, 27, and 28) are of particular interest because they are able to handle discontinuous media without modification to the finite-element spaces and all of the schemes have three-dimensional counterparts. We implemented an algorithm in TRIMAX which is identical to ECHL during our PBFA II electromagnetic modeling effort for Sandia National Laboratories in 1985. Evidently this algorithm was independently discovered by Madsen and Ziolkowski (Reference 31) who



appear to have coined the ECHL term. The method later came to be known as the method of Lee and Madsen (Reference 32) in the literature (see Reference 27, for example.) We have also considered the initially promising Petrov-Galerkin mass-lumped method (non-conforming elements) of Ambrosiano (Reference 35) but were obliged to dismiss it following Monk's demonstration of wave speed convergence failure in Reference 25. Based upon our previous success with the ECHL method in vacuum power flow applications we expected the addition of particle capability to the TRIMAX code to be straightforward. In practice we have encountered some difficulty obtaining stable and accurate solutions to space-charge-limited emission problems with the ECHL field solution method. This motivated us to seriously consider the more complex MECHL (Monk) and ELnHC (Nédélec) methods which have subsequently proved to be much more robust for 2-D PIC applications in TRIMAX.

### 8.2.1 Variational Principles for Maxwell's Equations.

Following Monk (Reference 27) we derive two general classes of methods for Maxwell's equations. For linear isotropic media we have:

$$\epsilon \frac{\partial \mathbf{E}}{\partial t} + \sigma \mathbf{E} = \nabla \times \mathbf{H} - \mathbf{J} , \quad (8.1)$$

$$\mu \frac{\partial \mathbf{H}}{\partial t} = -\nabla \times \mathbf{E} , \quad (8.2)$$

where the dielectric constant  $\epsilon$  permeability  $\mu$ , and conductivity  $\sigma$  are known spatial functions and  $\mathbf{J}$  is a function of space and time giving the current density. Equations 8.1 and 8.2 are to be solved in a plane polygonal region with boundary  $\Gamma$  and we assume the boundary condition:

$$\mathbf{n} \times \mathbf{E} = \gamma , \quad (8.3)$$

where  $\mathbf{n}$  is the unit outward normal to  $\Gamma$  and  $\gamma$  is a specified (surface) function (possibly dependent on time). If  $\gamma = 0$  this boundary condition models a perfectly conducting boundary. In addition, initial data must be specified so that we assume

$$\mathbf{E}(0) = \mathbf{E}_0 \quad \text{and} \quad \mathbf{H}(0) = \mathbf{H}_0 \quad (8.4)$$

where  $E_o$  and  $H_o$  are given functions. Equations 8.1, 8.2, 8.3 and 8.4 are a well-posed system of equations provided  $\epsilon$ ,  $\mu$ ,  $\gamma$ ,  $\sigma$ , and  $J$  are sufficiently smooth and satisfy standard positivity and boundedness assumptions. Define the inner product of (vector) functions  $u$ ,  $v$  by

$$\langle u, v \rangle = \int_{\Omega} u \cdot v \, dV .$$

A weak or variational formulation of Equations 8.1 through 8.4 is obtained formally by multiplying Equation 8.1 by a (vector) test function  $\phi$  and Equation 8.2 by another vector test function  $\psi$ . Using the inner product definition to integrate over  $\Omega$  we obtain the following equations:

$$\langle \epsilon \frac{\partial E}{\partial t} + \sigma E, \phi \rangle = \langle \nabla \times H, \phi \rangle - \langle J, \phi \rangle , \quad (8.5)$$

$$\langle \mu \frac{\partial H}{\partial t}, \psi \rangle = - \langle \nabla \times E, \psi \rangle . \quad (8.6)$$

This pair of equations is unsuitable for discretization since, in general, it would not result in an energy-conserving discrete problem. Instead one chooses to integrate one of the curl terms in Equations 8.5 or 8.6 by parts. One choice leads to the ECHL method, the other to ELnHC (method of Nédélec). Let the Hilbert (function) spaces be given by:

$$\mathcal{H}(\text{curl}; \Omega) = \left\{ u \in (L^2(\Omega))^3 \mid \nabla \times u \in (L^2(\Omega))^3 \right\} , \quad (8.7)$$

$$\mathcal{H}_o(\text{curl}; \Omega) = \left\{ u \in \mathcal{H}(\text{curl}; \Omega) \mid n \times u = 0 \text{ on } \Gamma \right\} \quad (8.8)$$

(see Reference 42 for a complete discussion of the curl spaces).

### 8.2.2 Nédélec's Method.

If Equation 8.5 is integrated by parts, then provided the test function  $\phi \in \mathcal{H}_o(\text{curl}; \Omega)$  we are led to the conclusion that  $E \in \mathcal{H}(\text{curl}; \Omega)$ ,  $H \in (L^2(\Omega))^3$  satisfies:

$$\langle \epsilon \frac{\partial E}{\partial t} + \sigma E, \phi \rangle = \langle H, \nabla \times \phi \rangle - \langle J, \phi \rangle \quad \forall \phi \in \mathcal{H}_o(\text{curl}; \Omega) , \quad (8.9)$$

$$\langle \mu \frac{\partial H}{\partial t}, \psi \rangle = - \langle \nabla \times E, \psi \rangle \quad \forall \psi \in (L^2(\Omega))^3, \quad (8.10)$$

$$\text{and} \quad \mathbf{n} \times \mathbf{E} = \gamma \quad \text{on } \Gamma \quad (8.11)$$

together with the initial condition in Equation 8.4. In this case the test function  $\phi$  must have a well-defined curl and must satisfy the boundary condition  $\mathbf{n} \times \phi = 0$ . In this formulation the boundary conditions are essential. To discretize Equations 8.9 through 8.11 we seek to find  $\mathbf{E}, \mathbf{H}$  from appropriate (finite-element) subspaces. We have that  $(\mathbf{E}, \mathbf{H}) \in U_h^N \times V_h^N$  where  $U_h^N \subset \mathcal{H}(\text{curl}; \Omega)$ ,  $V_h^N \subset (L^2(\Omega))^3$  are finite dimensional spaces indexed by  $h$ . We note that  $U_h^N$  need only be a subspace of  $\mathcal{H}(\text{curl}; \Omega)$  and need not be in  $\mathcal{H}^1(\Omega)$ . Standard linear finite elements are in  $\mathcal{H}^1(\square)$  and thus are too smooth. This distinction manifests itself in the complex way that standard elements must be adapted to handle interfaces where the dielectric constant  $\epsilon$  is discontinuous. Nédélec's construction gives elements in  $\mathcal{H}(\text{curl}; \Omega)$  but not in  $\mathcal{H}^1(\Omega)$  (see Reference 27).

**8.2.2.1 Nédélec Type 1 Basis Functions for ELnHC Method in 2-D.** We specialize to 2-D for the first mode set where we have  $\mathbf{E} = e_x \hat{i} + e_y \hat{j}$  with  $e_x \hat{i} = e_x(x, y)$ ,  $e_y \hat{j} = e_y(x, y)$  and  $\mathbf{H} = h_z(x, y) \hat{k}$ . The 2-D ELnHC (E linear, H constant) formulation employs Nédélec first type edge elements for the electric field and piecewise constant elements for the magnetic field. Thus on triangle  $K$ ,

$$\bar{\mathbf{E}}(\bar{r}) = \mathbf{E}^k|_k = \begin{pmatrix} a_k + b_k y \\ c_k - b_k x \end{pmatrix},$$

where  $a_k$ ,  $b_k$ , and  $c_k$  are constants on each triangle. The degrees of freedom can be taken to be the value of the tangential component of the electric field at the midpoint of each edge. Let these edge components (d.o.f.s) be given by  $\epsilon_i$ . Then we have:

$$\bar{\mathbf{E}}(\bar{r}) = \sum_{i=1}^3 \epsilon_i \bar{\phi}_i$$

where the edge basis functions are:

$$\vec{\phi}_i = \frac{\hat{k} \times (\vec{r} - \vec{r}_j)}{2A}$$

where  $A$  = area of element triangle,  $\vec{r}_j$  is the vertex opposite edge  $i$ , and  $\vec{r} = x\hat{i} + y\hat{j}$ . The elements have the property that the tangential electric field is continuous (and constant) on all edges (conforming elements). For the magnetic field we simply have:

$$H^n|_k = d_k \hat{k}$$

a constant which may be associated with the centroid of each triangle.

**8.2.2.2 Nédélec Type 2 Basis Functions for E<sub>LN</sub>HC Method in 2-D.** This formulation employs Nédélec second type edge elements for the electric field and piecewise constant elements for the magnetic field. The magnetic field basis functions are the same as in the type 1 (mode set 1) formulation. The electric field has the form:

$$E^n|_k = \begin{pmatrix} a_k + b_k x + c_k y \\ d_k + e_k x + f_k y \end{pmatrix},$$

where  $a_k$ ,  $b_k$ ,  $c_k$ ,  $d_k$ ,  $e_k$ , and  $f_k$  are constants on each triangle. This choice results in six degrees of freedom per triangle. In TRIMAX we elect to use the tangential component of the electric field along each edge of the triangle at the vertices. These elements again are conforming, having continuity of the tangential E-field across all element edges. Furthermore, the tangential component is linear along each element edge. We note there are twice as many electric field unknowns per unit area as compared to the first type edge element formulation. In terms of basis functions we can again express the field in the form:

$$\vec{E}(\vec{r}) = \sum_{i=1}^6 \varepsilon_i \vec{\phi}_i$$

The expression for the  $\vec{\phi}_i$  is rather complex and will not be given here.

### 8.2.3 ECHL and MECHL Methods.

Alternatively integrating Equation 8.6 by parts we obtain that  $E \in (L^2(\Omega))^3$  and  $H \in \mathcal{H}(\text{curl}; \Omega)$  satisfy:

$$\langle \epsilon \frac{\partial E}{\partial t} + \sigma E, \phi \rangle = \langle \nabla \times H, \phi \rangle - \langle J, \phi \rangle \quad \forall \phi \in (L^2(\Omega))^3 \quad (8.12)$$

$$\langle \mu \frac{\partial H}{\partial t}, \psi \rangle = -\langle E, \nabla \times \psi \rangle + \langle \gamma, \psi \rangle \quad \forall \psi \in \mathcal{H}(\text{curl}; \Omega) \quad (8.13)$$

together with the initial condition (Equation 8.4).

To discretize Equations 8.12 and 8.13 we take finite dimensional spaces  $U_h^L \subset (L^2(\Omega))^3$  and  $V_h^L \subset \mathcal{H}(\text{curl}; \Omega)$ . Then seek  $(E^h, H^h) \in U_h^L \times V_h^L$ . In this case the boundary condition need not be imposed on the finite element functions. Note that  $V_h^L \subset \mathcal{H}(\text{curl}; \Omega)$  and so, in a 2-D setting one needs  $V_h^L \subset \mathcal{H}^1(\Omega)$ . Thus in this case, standard (linear) finite elements can be used to construct  $V_h^L$ . The space  $U_h^L \subset (L^2(\Omega))^2$ , and thus a candidate space, is the space of piecewise constant vectors (ECHL). An augmented space is used for the MECHL method.

**8.2.3.1 Element Basis Functions for ECHL Method in 2-D (Mode Set 1).** For triangle element  $k$ :

$$E_k(x, y) = (e_x \ i + e_y \ j) H_k$$

where  $H_k = 1$  over triangle  $k$ , zero otherwise.

$$B_k(x, y) = \sum_{i=1}^3 (N_i(x, y) \ b_i)_k \ \hat{k}$$

where

$$(N_i(x, y))_k = (a_{0,i} + a_{1,i} x + a_{2,i} y)_k$$

are the usual nodal linear finite element basis functions having the property of being 1 at node  $i$  and 0 at the remaining two nodes of triangle  $k$ . The coefficients  $b_i$  are the nodal d.o.f.s. The

form for cylindrical coordinates is obtained by replacement of basis function  $\hat{i}$  by  $\hat{r}$ ,  $\hat{j}$  by  $\hat{k}$ ,  $\hat{k}$  by  $\hat{\phi}$ , and by replacement of coordinates  $x$  by  $r$ , and  $y$  by  $z$ .

**8.2.3.2 Basis Functions for MECHL in 2-D.** If we know  $\epsilon$  is continuous we can decrease the dimension of  $U_h^M$  by enforcing continuity of normal components across elements. In that case,  $U_L^M$  becomes the lowest order Raviart-Thomas divergence-conforming space and MECHL simplifies. The function space for the magnetic field is still the same as that for ECHL. The electric field space is very similar to the Nédélec type 1 edge elements but in this case the normal component is constant along and continuous across an edge. The form for a (type 1) element is now:

$$\vec{E}(\vec{r}) = \vec{E}^*|_k = \begin{pmatrix} a_k + b_k x \\ c_k + b_k y \end{pmatrix},$$

where  $a_k$ ,  $b_k$ , and  $c_k$  are constants on each triangle. The degrees of freedom are taken to be the value of the normal component of the electric field at the midpoint of each edge. Let these components (d.o.f.s) be given by  $\epsilon_i$ . Then we have:

$$\vec{E}(\vec{r}) = \sum_{i=1}^3 \epsilon_i \vec{\phi}_i \quad \text{where the edge basis functions are}$$

$$\vec{\psi}_i = \frac{\vec{r} - \vec{r}_i}{2A}$$

where  $A$  = area of element triangle,  $\vec{r}_i$  is the vertex opposite edge  $i$ , and  $\vec{r} = x\hat{i} + y\hat{j}$ .

Note that an interesting alternative to the constant  $\epsilon$  assumption might be to work with the electric displacement field  $\vec{D}$  instead of  $\vec{E}$ .

#### 8.2.4 Energy Conservation.

One can easily demonstrate that (at least prior to time discretization) either of the methods embodied in Equations 8.9, 8.10, 8.11, 8.12 and 8.13 conserve energy. For the details, see Reference 27.

### 8.2.5 Timestepping.

Each of the methods we have outlined gives rise to a (sparse) matrix problem of the following form. Let  $(\vec{E}(t), \vec{H}(t))$  be the vectors of free degrees of freedom for the electric and magnetic fields, respectively. Then these vectors satisfy matrix problems of the form (Reference 27):

$$[M_{uu}^\epsilon] \frac{d\vec{E}}{dt} + [M_{uu}^\sigma] \vec{E} - [C_{uv}] \vec{H} = \vec{G}$$

$$[M_{vv}^\mu] \frac{d\vec{H}}{dt} + [C_{uv}]^T \vec{E} = \vec{F}$$

where  $\vec{G}$  and  $\vec{F}$  account for boundary conditions and applied currents. For example, in the ECHL (MECHL) methods:

$$\begin{aligned} [M_{uu}^\epsilon]_j &= \int_{\Omega} \epsilon \vec{\phi}_i \cdot \vec{\phi}_j dV \\ [M_{uu}^\sigma]_j &= \int_{\Omega} \sigma \vec{\phi}_i \cdot \vec{\phi}_j dV \end{aligned} \quad \left\{ \begin{array}{l} 1 \leq i, j \leq N_E \end{array} \right.$$

$$[C_{uv}]_j = \int_{\Omega} (\nabla_x \vec{\psi}_j) \cdot \vec{\phi}_i dV \quad \left\{ \begin{array}{l} 1 \leq j \leq N_H \\ 1 \leq i \leq N_E \end{array} \right.$$

$$[\vec{G}]_i = \int_{\Omega} \vec{J} \cdot \vec{\phi}_i dV \quad i = 1 \leq i \leq N_E$$

where, in general for PIC, we have  $\vec{J} = \sum_i q_i \vec{v}_i \delta(\vec{x}_i)$

$$[M_{vv}^\mu]_j = \int_{\Omega} \mu \vec{\psi}_i \cdot \vec{\psi}_j dV \quad 1 \leq i, j \leq N_H$$

$$[\vec{F}]_j = \int_{\Omega} \gamma \vec{\psi}_j dV \quad 1 \leq j \leq N_H$$

where  $\{\vec{\varphi}_i\}_{i=1}^{N_E}$  is a basis for the electric field space  $U_h^L$  ( $U_h^M$ ) and  $\{\vec{\psi}_i\}_{i=1}^{N_H}$  is a basis for the magnetic field space  $V_h^L$  ( $V_h^M$ ). Similar equations hold for the Nédélec methods after allowing for the fact that boundary degrees of freedom for  $U_h^N$  are specified via the boundary data. The semi-discrete scheme is completed by choosing a time integration method. The choice of leap frog, for example, leads to the following. Given  $(\vec{E}^n, \vec{H}^{n+1/2})$ , we compute  $(\vec{E}^{n+1}, \vec{H}^{n+3/2})$  by solving the system:

$$\begin{aligned} [M_{uu}^\varepsilon] \left( \frac{\vec{E}^{n+1} - \vec{E}^n}{\Delta t} \right) + [M_{uu}^\sigma] \left( \frac{\vec{E}^{n+1} + \vec{E}^n}{2} \right) - [C_{uv}] \vec{H}^{n+1/2} \\ = \vec{G}^{n+1/2} \end{aligned}$$

where  $\vec{G}^{n+1/2} \equiv \vec{G}(t^{n+1/2})$  then solving

$$[M_{vv}^\mu] \left( \frac{\vec{H}^{n+3/2} - \vec{H}^{n+1/2}}{\Delta t} \right) + [C_{uv}] \vec{E}^{n+1} = \vec{F}^{n+1}$$

For ECHL,  $[M_{uu}^\varepsilon]$  and  $[M_{uu}^\sigma]$  are diagonal, but for MECHL they are only sparse.  $[M_{vv}^\mu]$  is sparse and identical for ECHL and MECHL (continuous  $\varepsilon$ ) and may be solved using a preconditioned conjugate gradient method. One attractive choice is to use the mass lumped matrix as a diagonal preconditioner. In general, one always iterates to completion at each timestep so that successive iterates differ by less than machine precision in the  $L^2$  norm. A coarser tolerance may be possible although there could be a penalty in overall long-time integration stability (more work is needed in this area).

In the case of the ELnHC (Nédélec method)  $[M_{vv}^\mu]$  is diagonal and easily inverted.  $[M_{uu}^\varepsilon]$  and  $[M_{uu}^\sigma]$  are not, however, and must be solved by the conjugate gradient method (again possibly with a lumped pre-conditioner).

The number of PCG iterations required per timestep for ELnHC is typically less than for ECHL or MECHL. However, for ELnHC the size of  $[M_{uu}^\varepsilon]$  is approximately five times the number of edges (type 1) and ten times for type 2, while for ECHL/MECHL the dimension of  $[M_{vv}^\mu]$  is the number of nodes in the mesh times the average number of node neighbors (Reference 30). (The



number of edges is ~1.5 times the number of elements which in turn is about twice the number of nodes in the mesh). Thus the system for ELnHC is significantly larger than that for ECHL.

### 8.2.6 Mass Matrix Solution.

One of the significant advantages enjoyed by the ECHL method (2-D TM Mode) is that the "mass matrix" is diagonal, eliminating the need for a linear system solve at each timestep. According to Monk (Reference 25) lumping is not possible on a general unstructured triangular grid for the MECHL and ELnHC (Nédélec) methods. The resulting sparse (symmetric) system of equations is, however, easily inverted by a preconditioned conjugate gradient algorithm. We observe the number of non-zero entries per row in this matrix only depends on the span of the edge basis functions and for all interior element d.o.f.s (faces) this is five for type 1 Nédélec edge elements and ten for type 2 elements. The d.o.f equations associated with boundary edges (or interior edges of elements which have other boundary edges will have a reduced width. One must note that in the case of highly graded meshes and/or large inter-element dielectric constant jumps, the convergence rate may be expected to deteriorate, as observed by Monk (Reference 27). In many pulsed power applications we have found this is not a significant limitation, however.

### 8.2.7 Time Integration Methods.

We have successfully employed both of the following time integration techniques with both the ECHL and Nédélec methods.

#### Explicit LF

$$E^{n+1} = E^n + c \Delta t \text{Curl}(B)^{n+1/2} - 4 \pi J^{n+1/2}$$

$$B^{n+3/2} = B^{n+1/2} - c \Delta t \text{Curl}(E)^{n+1}$$

#### Implicit forward biased

$$E^{n+1} = E^n + c \Delta t [a_1 \text{Curl}(B)^{n+1/2} + a_2 \text{Curl}(B)^{n+3/2}] - 4 \pi J^{n+1/2}$$

$$B^{n+3/2} = B^{n+1/2} - c \Delta t \text{Curl}(E)^{n+1}$$

where  $a_1 + a_2 = 1$ .

We have implemented this algorithm with an iterative solver similar to that employed in the MAGIC and FRED codes. We have used the method mainly to provide high-frequency field smoothing. We have not attempted to integrate at timesteps  $>$  Courant limit. The simple iterative relaxation technique is not practical much beyond an implicit factor of  $a_2 = 0.75$ . To practically exceed this would perhaps require implementation of a direct Krylov space method. It would also require generalization of the particle push algorithm to permit multiple-cell crossings per timestep, a modification which we believe is probably not cost-effective in most cases. In such cases one should generalize the Direct Implicit PIC method of B. Langdon [?] to unstructured meshes. An alternative to the leap frog methods would be to use a Runge Kutta scheme. One possible implementation of this is discussed in Monk (Reference 27).

### **8.3 SOME FIELD ALGORITHM CONSIDERATIONS.**

#### **8.3.1 Difficulties with the ECHL Method.**

Monk (Reference 27) encounters difficulties when attempting to prove convergence of the ECHL method on a general domain. He notes that ECHL suffers a big theoretical drawback in that the spaces  $(U_H^L, V_H^L)$  do not satisfy an appropriate inf-sup condition hence excluding ECHL from the general theory of Brezzi (Reference 34). Nevertheless he notes that "...for smooth data it is possible for the method to converge and work well in practice." While his comments in this context are directed at a quadrilateral implementation, we and other authors (Reference 31) have come to similar conclusions based on numerical experiments with the vacuum equations on a triangular grid. We have, however, noted some long term instability problems that appear to be dependent on the precision with which the computations are performed. In 32-bit precision these problems usually do not manifest themselves for simulations up to the order of  $10^5$  cycles. Nevertheless, with real time and length scales, we have observed this can sometimes be a significant limitation.

#### **8.3.2 Some Comments on Criticism of the Nédélec Method.**

According to F. Assous, et al. (Reference 29) a Maxwell solver in the context of numerical modeling in plasmas physics must fulfill, if possible, the following requirements:

1. The electromagnetic fields have to be continuous. (Stability condition for classical Vlasov solvers).
2. The electric field must satisfy Gauss law and the magnetic field must be divergence free.
3. The space and time discretizations have to lead to an explicit scheme in order to avoid the solution of a linear system at each step.

He notes that while the Nédélec method implicitly satisfies condition (2) it fails (1) and (3). We must take some issue with his criteria (at least in 2-D PIC). In light of the fact that the "mass matrix" can be efficiently evaluated with a PCG algorithm and that the particle push step tends to dominate the overall computation time, we believe the importance of (3) is significantly overstated. (We also note that Assous' alternative "explicit" method also relies on an Uzawa algorithm for inversion of a system of equations. It is unclear how the computational effort in this method compares with PCG in the methods we have adopted. We are dubious.) While true continuously, we must also question requirement (1). We note that even typical electrostatic finite difference (or linear finite element) PIC field solvers do not meet this requirement directly. The condition is "met" by grid cell field averaging in momentum-conserving electrostatic codes, a technique which may be easily employed on an unstructured grid as well.

Some authors (notably Reference 35) have complained that the method of Nédélec uses a complicated variational formalism which is awkward to interpret (in terms of shape and test functions) and implement. We believe that with due reflection one can easily understand the method in these terms. The role of shape and test functions is clearly displayed in the formulation presented in this report and there is no reason a competent programmer can't create appropriate data structures to support them. (Indeed we have done so!)

#### **8.4 PARTICLE PUSH AND CURRENT ALGORITHMS.**

Economical implementation of PIC capability in the TRIMAX code was made possible by reuse of a significant amount of software borrowed from the FRED (structured grid) PIC code. The relativistic Boris' particle push subroutines and associated machinery for managing the particle lists, RISC caching, etc. was straightforward to import. The implementation of the field lookup and particle/mesh current allocation was new, however. Location of a particle on an unstructured grid is a significantly more involved process than that for structured grids. Our technique for maintaining vectorization/parallelization has similarities to that described by Lohner (Reference 33). In addition to determining a particles cell index, however, our PIC method requires the additional feature of being able to determine which cell faces a particle

enters and exits during a timestep. More specifically, during an explicit timestep, a particle is permitted to cross more than one triangular cell so long as those cells share a common vertex. In our ECHL PIC algorithm, current apportionment to each of these cells is proportional to the fraction of the total particle (linear) trajectory timestep spent in a cell. In the MECHL and ELnHC implementations the connection is not quite as obvious. The required inner product integrations depend on knowing the triangle face intersection times very accurately. We mention that our "generalization" of Lohner's method also avoids the problem of a particle chasing itself between adjacent cells due to rounding errors. (As published, we believe Lohner's technique may suffer from this malady.) We also note that in 2.5-D we make the (usual) simplifying assumption that a particle trajectory is linear in the X-Y or R-Z (projection) plane over a timestep. This is exact in X-Y coordinates but only approximate in cylindrical coordinates if there is a non-zero azimuthal velocity component. A more careful treatment has been described in the literature (G.A. Bird, Reference 41) and could be implemented if the accuracy loss was deemed of significance.

#### 8.4.1 Weak Form of Continuity Equation.

The rigorous per-particle evaluation of the inner product integrals in the source term in Maxwell's equations implies the following weak form of the continuity equation is (exactly) satisfied at each timestep for the ECHL method. (A less transparent statement can be made for our PIC implementation of the Nédélec method as well.)

$$\int_{\Gamma} N_i \vec{J} \cdot d\vec{A} - \int_{\Omega} (\vec{J} \cdot \nabla N_i) dV + \int_{\Omega} \frac{\partial \rho}{\partial t} N_i dV = 0 .$$

Where  $N_i$  is the usual nodal (generalized pyramid) basis function which is non-zero only over those elements which share node  $i$  in common. (This equation is obtained by multiplication of the continuity equation  $\dot{\rho} + \nabla \cdot \vec{J} = 0$  by a basis function  $N_i$  and integrating (over  $\Omega$ ) by parts followed by a final application of Stokes' theorem.) One can show that this equation holds particle-by-particle over a finite timestep  $\Delta t$  if we assume point particles, i.e.,  $\vec{J} = q_j \vec{v}_j \delta(\vec{x}_j)$ ,  $\rho = q_j \delta(\vec{x}_j)$  where  $q_j$  = particle  $j$  charge,  $\vec{v}_j$  = particle velocity, and  $\vec{x}_j(t)$  is the particles position. The surface term (first term of the equation) accounts for charges which enter/exit the domain boundary of  $\Omega$ .

#### 8.4.2 Weak Form Determination of Charge for Space-Charge Limited Surface Emission.

There is also an associated weak form of the  $\vec{E}$  - field divergence relation. It is derived similarly:

$$\nabla \cdot \vec{D} = \rho, \quad \vec{D} = \epsilon \vec{E}$$

$$\int_{\Omega} N_i \nabla \cdot \vec{D} \, dV = \int_{\Omega} N_i \rho \, dV$$

$$\int_{\Omega} (\nabla \cdot N_i \vec{D} - \vec{D} \cdot \nabla N_i) \, dV = \int_{\Omega} N_i \rho \, dV$$

$$\int_{\Gamma} N_i \vec{D} \cdot d\vec{A} - \int_{\Omega} \vec{D} \cdot \nabla N_i \, dV = \int_{\Omega} N_i \rho \, dV$$

This equation forms the basis for space-charge-limited emission. Demanding that the surface electric field vanish eliminates the left-hand integral leaving:

$$-\int_{\Omega} \epsilon \vec{E} \cdot \nabla N_i \, dV = \int_{\Omega} (\rho + \rho_e) N_i \, dV,$$

where  $\rho_e$  is the amount of charge (density) required at node  $i$  to maintain the space-charge-limited condition. (In the event the required sign of  $\rho_e$  differs from that of the species being emitted we suppress particle creation at the node.)

#### 8.4.3 Evaluation of Particle Current Basis Function Inner Products.

Let the particle distribution consist of a set of point particles. Let the charge on the  $i$ th particle be  $q_i$ , its constant velocity during a given timestep be  $\vec{v}_i$  and its position be  $\vec{x}_i(t)$ . Then the current density is given by:

$$\vec{J}(t) = \sum_i q_i \vec{v}_i \delta(\vec{x}_i(t))$$

The inner product with basis function  $\ell$  gives:

$$\begin{aligned} (1/\Delta t) \int_t^{t+\Delta t} \langle \tilde{J}, \tilde{\psi}_\ell \rangle dt &\equiv \langle \tilde{J}^{n+1/2}, \tilde{\psi}_\ell \rangle \\ &= (1/\Delta t) \sum_i \int_t^{t+\Delta t} \int_\Omega q_i \tilde{v}_i^{n+1/2} \delta(\tilde{x}_i(t)) \cdot \tilde{\psi}_\ell dV dt \end{aligned}$$

Since  $q_i$  and  $\tilde{v}_i$  are constant over the time interval  $(t, t+\Delta t)$ , the basis function  $\tilde{\psi}_\ell$  is a linear function of  $x, y, z$  and the particle position  $\tilde{x}_i(t) = x_o + \tilde{v}_i \Delta t$  is a linear (vector) function of  $t$ , we conclude the integrand is a linear function of  $t$  and may therefore be integrated exactly using the trapezoidal rule. Thus,

$$\langle \tilde{J}^{n+1/2}, \tilde{\psi}_\ell \rangle = \sum_i (q_i \tilde{v}_i) \cdot \sum_j^{N_c(i)} \tau_{ji} \tilde{\psi}_\ell(\tilde{x}_{ji})$$

where  $j$  indexes the set of  $N_c(i)$  triangles intersected by particle  $i$  during the timestep  $\Delta t$ ,  $\tau_{ji}$  is the normalized timestep fraction spent by particle  $i$  in each intersected cell and  $\tilde{x}_{ji}$  is the midpoint of the trajectory segment overlap with the  $j$ th intersected cell. Note that  $(0 \leq \tau_{ji} \leq 1)$  and

$$\sum_j^{N_c(i)} \tau_{ji} = 1 \text{ for all } i.$$

For the ECHL method there is only a single basis function which is non-zero over any given element. Thus there is a total of  $N_c(i)$  contributions to the inner products of d.o.f.s. from a given particle  $i$ . In the case of Nédélec type 1 elements there are three (edge) basis functions which are non-zero over each element so there are 3  $N_c(i)$  contributions to be summed for each particle  $i$ . For Nédélec type 2 elements there are 6  $N_c(i)$  contributions. It should be noted that the Nédélec inner products are smoother than those for ECHL, the contribution to a given edge d.o.f. changing linearly with particle motion. On the other hand, the ECHL inner products result in NGP-like behavior with cell current contributions making abrupt step jumps as particles cross adjacent cell boundaries. The step jump may be smoothed somewhat by the  $\tau_{ji}$  factors, however, so that ECHL should be somewhat smoother than a pure NGP weighting. One should note that the simple form for the inner products is a consequence of the leap-frog field solver and (Boris)

particle pusher. Use of a Runge-Kutta time integration scheme (as suggested by Monk (Reference 27) would, in general, invalidate use of the trapezoidal rule, and would lead to a considerably more complex algorithm. The linear movement of particles along a trajectory segment would be destroyed making the cell intersection problem considerably more formidable.

## 8.5 TRIMAX PIC CODE CAPABILITIES.

The PIC algorithms based on Sections 8.2 through 8.4 have been successfully implemented in the TRIMAX PIC code. Taken together with the S3Mesh triangular grid generator (Reference 43) this code now provides the pulsed power flow analyst with an exceptionally flexible engineering tool. The current options available in the code allow the user to select from either rectilinear (XY) or cylindrical (axisymmetric RZ) geometries. Particle kinematics is fully relativistic and may be either 2 or 2.5-D (two spatial coordinates, three velocity components). Multiple particle species (electrons and ions) and multiple material dielectrics and conductivities are supported. Both TE and TM electromagnetic modes are provided. Five field solution algorithms are available, one electrostatic (Reference 43), based upon linear potential basis functions, and four electromagnetic: ECHL, MECHL, and ELnHC (Nédélec type 1 and 2 linear elements). The linear system solution in the electrostatic case and the 'mass matrix' system (MECHL/ELnHC) may be inverted using either the Incomplete Cholesky Conjugate Gradient or the Scaled (diagonal) Conjugate Gradient methods. In the time-dependent cases one may select among three temporal integration techniques: LF (Leap Frog), centered LF, or forward biased LF. For the electrostatic field solver, boundary conditions on any surface may be of type Dirichlet, Neumann, floating, mixed, or periodic. These conditions may be specified on both exterior and interior (multiply-connected surface) boundaries. For the time-dependent electromagnetic field solvers the boundary conditions may be selected from one of the following:

1. Perfectly conducting.
2. 1-D TEM voltage boundary condition:  $V(t)$
3. 1-D TEM current boundary condition:  $I(t)$
4. 1-D TEM wave boundary condition:  $V(t) = 2V_{oc}(t) - IZ$
5. 1-D TEM inductive load boundary condition:  $V = -L(t)dl/dt$
6. 1-D TEM resistive load boundary condition:  $V = IZ$  where  $V = -\text{Integral } E \cdot dl$  with  $dl$  taken along a coordinate direction and  $E(r)$  assumed proportional to  $1/r$ .

$$\text{and } I(t) = \frac{5}{(r_2 - r_1)} \int_{r_1}^{r_2} r b_{\phi}(r) dr .$$

Currently space charge limited emission or (mono-energetic) beam injection is permitted from any conducting surface boundary (both exterior and interior). An interface to the AVS visualization system is available for high-quality interactive postprocessing of results. Among other things, this provides the capability to generate animations of contour plots and particle trajectories in either QuickTime or MPEG formats.

## 8.6 PARALLEL PROCESSING.

The coding paradigms and data structures employed in the TRIMAX PIC code are easily amenable to task-oriented parallelization on MIMD architectures having a modest number of processors connected to a large shared memory. Specifically, the coding has been structured to take advantage of the UNICOS CRAY CF77 Autotasking compiling system. (On the CRAY Y/MP, C90 the code both vectorizes and parallelizes well.) It appears that a port to a multi cpu DEC Alpha workstation using KAP parallelization software or to HP's HPUX 10.1 f77 parallelizing compiler would be fairly straightforward. Porting to current f77/ f90 HPF implementations would be somewhat more involved due to the rather limited "data parallel" model employed by such systems.

## 8.7 APPLICATIONS.

In this section we document some simple benchmark problems which were employed to verify acceptable TRIMAX PIC code performance and accuracy levels. Also included is an example application of the code to the study of electron flow in an ACE 4 POS problem.

### 8.7.1 Space-Charge Limited Emission Tests.

The solution for (steady-state) 1-D planar (and cylindrical) surface emission within a gap across which a given voltage is applied is well-known. We formulated a 2-D test problem which approximates this 1-D idealization as follows. Consider a coaxial segment of inner radius (cathode)  $R_c=10$  cm, outer radius  $R_a=11$  cm and axial length  $\Delta Z=5$  cm. At both axial ends ( $Z=0, 5$  cm) of this coax a forward-going wave condition of the form  $V = 2V_m - IZ$  is applied. We permit space charge limited (electron) emission from the cathode over the interval  $(1 \leq Z \leq$



4 cm). The incoming wave  $V_{in}$  is assumed to be a voltage which ramps linearly from 0 to 60 kV in 0.5 ns, remaining constant thereafter. The equivalent generator impedances are assumed to be matched to the coax giving  $Z = 5.72 \Omega$ . Using the S3Mesh triangular grid generator the coaxial segment was zoned up with an essentially uniform resolution of about 0.5 mm. The resulting grid consisted of approximately 4,000 triangular elements. The problem was then integrated for several tens of ns using the TRIMAX PIC code running in the edge-based (ELnHC) RZ field solver mode. Several calculations were performed using electrons and/or  $H^+$  ions. The results are summarized as follows: a) The effective impedance of the emission region is seen to be low compared with the internal impedance of the generators ( $5.72 \Omega$ ) at the coax ends. Thus the current drain due to emission is insufficient to pull down the generator voltages, i.e., essentially the full  $2 V_{in} = 120$  kV is achieved across the 1 cm gap at steady state. b) The correct current density consistent with the analytic Child-Langmuir law was achieved at steady state for either electron or ion emission. (We also verified that the code performs correctly with an interchange of cathode and anode surfaces and a generator voltage sign change). c) An approximate ten percent  $1/r$  variation in the radial current density (at the gap center,  $Z=2.5$  cm) is observed in the TRIMAX (RZ) calculations. This is consistent with the radial extent of the approximately planar problem chosen for simulation. d) The radial gap electric field is seen to have the correct  $E(r) \sim r^{1/3}$  behavior (we neglect the cylindrical correction). e)  $H^+$  ion emission in lieu of electron emission was observed to produce a current ratio  $J_i / J_e$  which correctly corresponds to the square root of the electron/ion mass ratio. f) Edge effects near the particle boundaries ( $Z=1$  cm, 4 cm) are clearly visible in the 2-D PIC simulations. g) A case was run with electron emission from the cathode and ion emission from the anode to try to reproduce the canonical 1.86 current enhancement factor. Unfortunately, the results of this calculation were somewhat noisy and 2-D effects were much more evident. (An axial standing wave is seen developing within the plasma on the ion timescale. Two-stream effects?) Plasma oscillation levels are also significant relative to the DC levels we are seeking. We may attempt a repeat of this calculation in the future using a larger number of particles, and possibly with the forward biased implicit field integration method which should be significantly quieter.

### 8.7.2 Gyro Orbit Test.

Some simple consistency tests were performed to verify that the correct electron and ion gyro orbit radii are produced by the TRIMAX particle pusher. The coding for this pusher is not new, having been directly borrowed from the FRED PIC code. The purpose of these (successful) tests was to verify that the FRED coding had been correctly integrated into TRIMAX.

### 8.7.3 MITL Test.

The canonical problem outlined in Section 8.7.1 was repeated (electron emission) with the modification that one of the voltage generators (at  $Z=0$  cm) was replaced with a TEM resistive load boundary condition ( $V = IZ$ ). The forward wave  $V_m(t)$  was rescaled to achieve megavolt levels. Magnetic insulated flow (load dominated regime) was observed for load  $Z < \sim 2.5 \Omega$ . At impedances higher than this the electrons were observed to cross the gap resulting in Child-Langmuir like (switch dominated) flow.

### 8.7.4 TEM Lumped Inductive Boundary Condition Test (ELnHC).

A test problem involving a (TEM) lumped inductive termination originally failed to integrate properly. The source of the difficulty was traced to the fact that we had implemented the inductive boundary condition in the ELnHC method by using the same approximate technique that we had employed within the ECHL method. While leading to satisfactory results with the ECHL method, the technique was not rigorously consistent with the ELnHC variational formulation and this led to the instability. A more consistent form for this type of boundary condition was then developed by numerically integrating the tangential electric field (using the edge basis function expansion of  $E$  evaluated along the boundary surface) to obtain the voltage  $V^n$  across the lumped inductive termination. The current in the inductance is then stepped according to  $I^{(n+1/2)} = I^{(n-1/2)} + V^n \Delta t/L$ . Finally the TEM assumption gives  $B\phi^{(n+1/2)} = I^{(n+1/2)}/(5r)$ . This magnetic field is inserted into the surface term which arises from integration by parts of the  $\text{Curl}(H)$  Maxwell equation which one encounters in the edge-based (ELnHC) field solver formulation. This technique was found to eliminate all of the previously observed numerical difficulties with this boundary condition. We have also successfully generalized it to handle the case in which the lumped inductance is time-dependent, i.e., a PRS load, for example.

### 8.7.5 Space-Charge Limited Emission from Complex Floating Conductors.

As a non-trivial test of the complex geometrical space charge limited emission capabilities of the TRIMAX 2-D PIC code, a multiply connected region was created within the canonical coaxial segment (Section 8.7.1). One sub-region was defined by a circular polygon of revolution (torus), the second was defined by an ellipse of revolution (see Figure 8-1.) Rather than emitting from the flat coax anode and/or cathode surfaces we instead permit electron emission from the (floating) circular conductor and  $H^+$  ion emission from the (floating) elliptical conductor. After arrival of the generator pulses the circular conductor was observed to charge positively over a

period of a few ns. Electron flow from the half of the circular surface nearest the anode is initially observed but the highest electron density tends quickly to concentrate nearest the anode as steady-state conditions are approached. As the steady-state condition is approached the electron emission current is seen to correctly fall to zero. Particle movies clearly show the slowdown and eventual suppression of surface emission as the conductor charges positively. Similar behavior is exhibited by the  $H^+$  ions emitted from the adjacent elliptical conductor. The timescale for the elliptical conductor to charge negatively (ions flowing to the cathode) is seen to be much longer, being the order of several tens of ns, as one expects from the mass ratio difference. We remark that, while somewhat artificial, this test problem demonstrates code capabilities necessary for treatment of more realistic problems such as electron emission from floating grading rings of an insulator stack, for example.

#### **8.7.6 Dielectric Test.**

To verify the new edge-based (ELnHC) field solver algorithm correctly treats dielectrics the circular sub-region (Section 8.7.5) was filled with material having a dielectric constant of 10. The elliptic sub-region was filled with material having a dielectric constant of 81 (water). The floating conductor boundary conditions on both of these surfaces was eliminated. The remaining volume within the coax was assigned a dielectric constant of 1 (vacuum). All space charge limited emission conditions on surfaces were eliminated. After running this problem to steady-state (same  $V_{in}$  pulse as in Section 8.7.1) the continuity conditions on the normal component of the displacement  $\vec{D}$  and the tangential component of the electric field  $\vec{E}$  were verified to hold accurately across the interior dielectric surfaces. Previous attempts at integrating similar problems using the old element-based electric field solver (ECHL) have been met with violent instabilities after 50-100 K code cycles (in 32-bit IEEE single precision floating point). We successfully integrated this problem for over 400 K code cycles with no hint of instability. This bodes well for our new edge-based (ELnHC) field solver.

#### **8.7.7 TRIMAX Test Problem Result Summary.**

In summary, the new edge-based field solution algorithm has proven highly robust in treating all problems attempted thus far. In particular, the new method has eliminated a potential for numerical instabilities which is evidently inherent in the previous element-centered field solver (a formulation which we have long favored in this application due to its simplicity, efficiency, and ease of boundary condition implementation). It appears that the additional computational overhead of the edge-based field solver is low in PIC applications where the cpu time tends to be

highly dominated by the particle push code phase. For purely vacuum field calculations (which only involve a modest dielectric constant spread and slowly varying field gradients) the original element-centered field algorithm may be useful and certainly can be faster. We therefore still retain this capability as an option in the TRIMAX code.

#### **8.7.8 TRIMAX 2-D PIC Simulations of ACE 4.**

An S3Mesh unstructured triangular grid model of the POS + dummy load currently attached to ACE 4 in its present convolute configuration was constructed. This model was provided as input to the TRIMAX 2-D PIC code and several calculations were performed in an attempt to obtain some correlation of electron flow patterns with the X-ray output which has been recently observed experimentally in the downstream load region (can). In order to make best contact with the experimental data it was decided that the most appropriate way to drive the PIC calculations was to simply assume that the upstream POS current is that which is observed in the actual experiments. In order to do this it was necessary to make some additions to the boundary condition formulation in the TRIMAX code. These were obtained as straightforward extensions of the technique previously used to develop a TEM lumped inductive boundary condition capability (Section 8.7.4). For all of the simulations described here the axial length of the POS was taken to be 20 cm. To avoid unacceptable resolution and timestep limitations the POS plasma was simulated as a conducting region which forms a specified (possibly moving) vacuum gap with the cathode.

**8.7.8.1 25 mm POS Constant Gap Simulation.** This was a preliminary run which was completed prior to the implementation of the TRIMAX current boundary condition capability. The upstream POS was driven with a 1 MV voltage source (ramped up over a few ns). An MPEG particle movie was generated by post-processing the run output. Representative electron density snapshots from this movie are shown in Figures 8-2 and 8-3. The movie reveals the primary electron flow features observed in all of the subsequent runs. In particular, magnetically insulated electron flow develops within the POS gap within a few ns. Downstream of the POS the electron flow tends to form a narrow sheath which closely follows the conducting boundary of the load. A large region of re-circulating electron flow develops downstream (in the load can) and a large electric field gradient forms along the innermost radius of the load can (see Figure 8-4). Magnetic vortices are clearly seen developing within the downstream POS gap region. These vortices are subsequently launched into the downstream sheath region and their "center of mass" tends to follow the sheath flow. As they become entrained in the complex downstream rotating flow they appear to develop turbulent interactions.

**8.7.8.2 5.0 mm and 2.5 mm POS Constant Gap Simulations.** Parameters for this run were similar to the 25 mm gap case. The main difference was the inclusion of the current boundary condition instead of the voltage one. The current was ramped up to the 5 MA level over a few ns. It appears that some of the current loss seen at the anode edge of the downstream plasma in the 5 mm case is eliminated in the 2.5 mm case. More current gets downstream but it ultimately runs into the 'glitch' on the opposite side of the can. The current sheath along the downstream load boundaries appears somewhat thicker than it is in the 2.5 mm case. Apparently its characteristic length scale is set by the length scale of the POS gap itself (see Figures 8-5 through 8-7.)

**8.7.8.3 Time-dependent POS Gap Simulation.** This simulation is similar to the previous ones except for the added feature that an attempt is made to simulate a time-dependent POS gap which linearly opens from 0 to 5 mm (from the cathode) over a 100 ns duration. This is achieved by zeroing the electric field in (plasma) regions where the gap has not yet opened. (Note that this approach would not be suitable for modeling space-charge-limited ions within the gap!) In this simulation it appears that electron flow does not develop downstream. The electron flow shorts across the gap at the downstream POS edge. These features develop over a 68 ns run duration. A peak of 200 K (electron) macroparticles is attained. The gap voltage is of 100 kV level and eventually damps out to much lower values. No current gets to the load. One possible problem with this simulation is the inability to suppress the B-field inside the "fake gap" region where particles find themselves. Perhaps we need to actually kill particles in this region. The coding changes to accomplish this are not trivial, however, and could not be implemented within the current scope of work.

**8.7.8.4 Inclusion of Space-Charge-Limited Ions.** This run was made with an assumed 5.0 mm POS constant gap. In addition to electron emission from the cathode surfaces (within the POS gap and along the downstream POS cathode surfaces) space-charge-limited ion emission from the anode surface of the gap was allowed. The simulation was carried out for a duration spanning nearly 50 ns (200,000 cycles with an approximate average of 0.2 M macroparticle electrons and 0.3 M macroparticle ions). During the first 10-20 ns of this simulation an ion 'beam' is seen to form perpendicular to the downstream surface of the POS. This beam diverges moderately, striking the downstream load surface (along a line of constant Z.) As time progresses beyond this the beam tends to spread out more and eventually most of the downstream load is seen to be filled with ions. The electron sheath which forms downstream of the POS gap is initially split into two pieces. One piece carries current in a sheath which closely follows the electrode surfaces. The other splits off, tending to follow the ion beam.

Eventually as the beam spreads out this distinct secondary current path tends to disappear. A significant amount of current is lost within the POS gap during the bulk of this run. The downstream current in the load is seen to have only achieved about 2/3 of the 5 MA upstream POS current after 50 ns. At the point at which the run was terminated it is clear that the downstream current was continuing to increase and if the simulation could be continued for another 50 ns the load current would probably achieve most of the upstream value.

**8.7.8.5 Possible Future Simulations.** In all of the calculations performed so far the majority of the current downstream of the POS flows in sheaths along the load surfaces. The grid zoning in the downstream load region was relatively uniform for all of the runs reported on here. It would be interesting to employ the highly flexible zoning capability of the S3Mesh/TRIMAX codes to better resolve this sheath and assess the effects on the accuracy of the numerical simulation.

**8.7.8.6 Correlation with ACE 4 Experiments.** The PIC calculations indicate some electron losses to the surfaces of the downstream ACE 4 load can. Quantification of the effects await better diagnosed experiments and possibly implementation of more detailed electron surface flux diagnostics within the code.

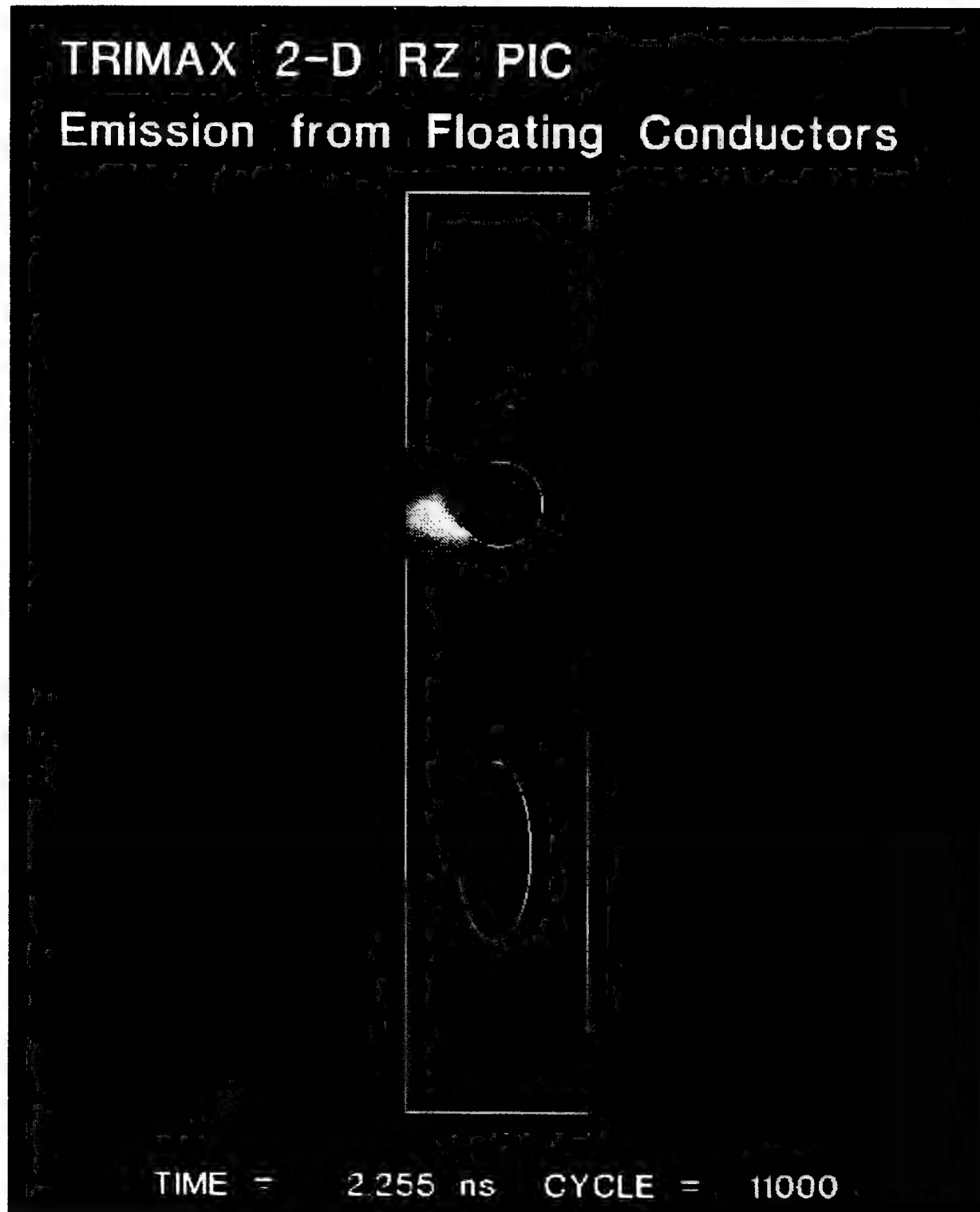


Figure 8-1. Steady-state electric field magnitude contours for 2-D TRIMAX PIC complex floating conductor emission test problem.

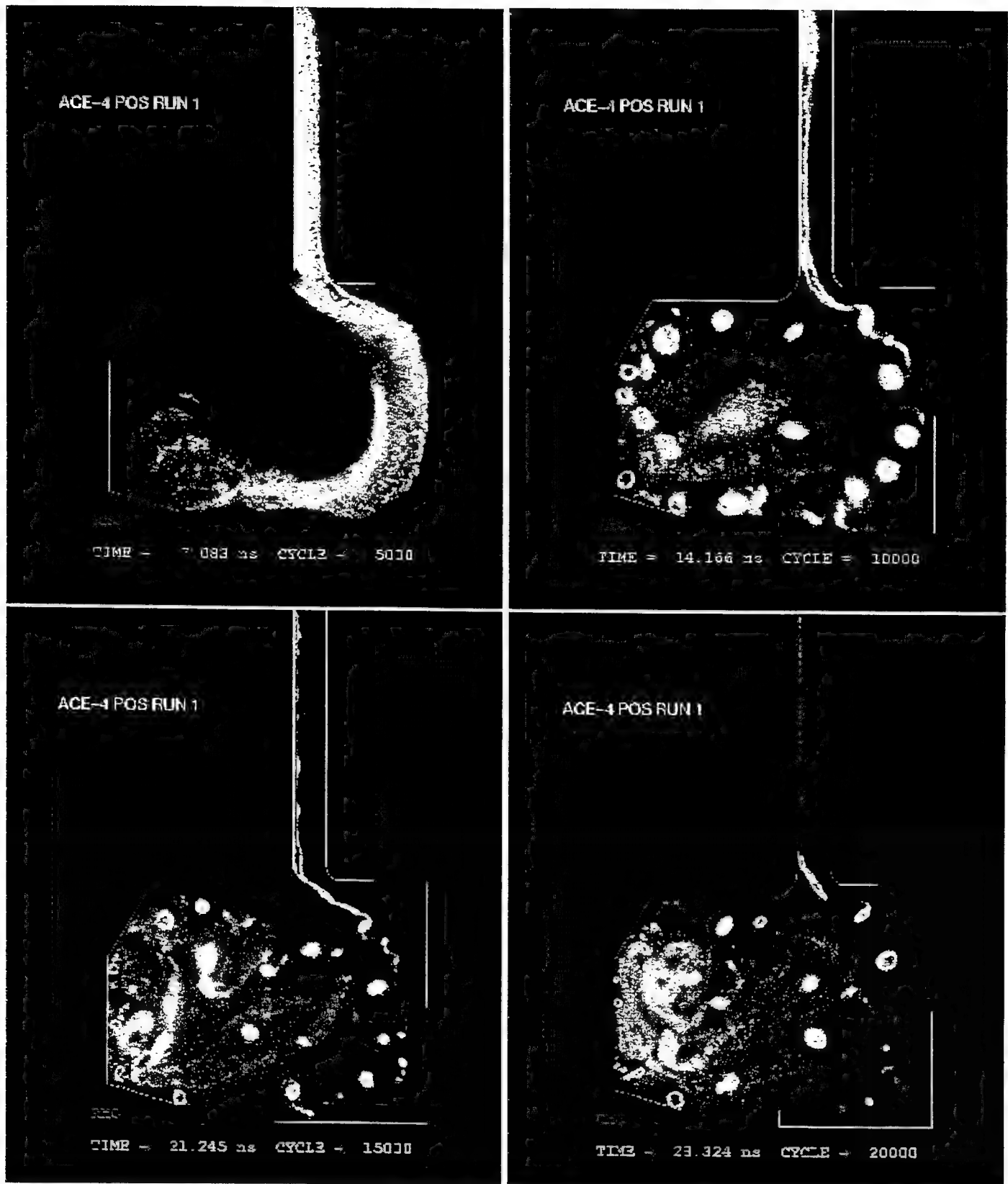


Figure 8-2. Electron charge density contours at  $t = 7, 14, 21,$  and  $23$  ns for 2-D TRIMAX PIC simulation of ACE 4 with POS gap = 25 mm.



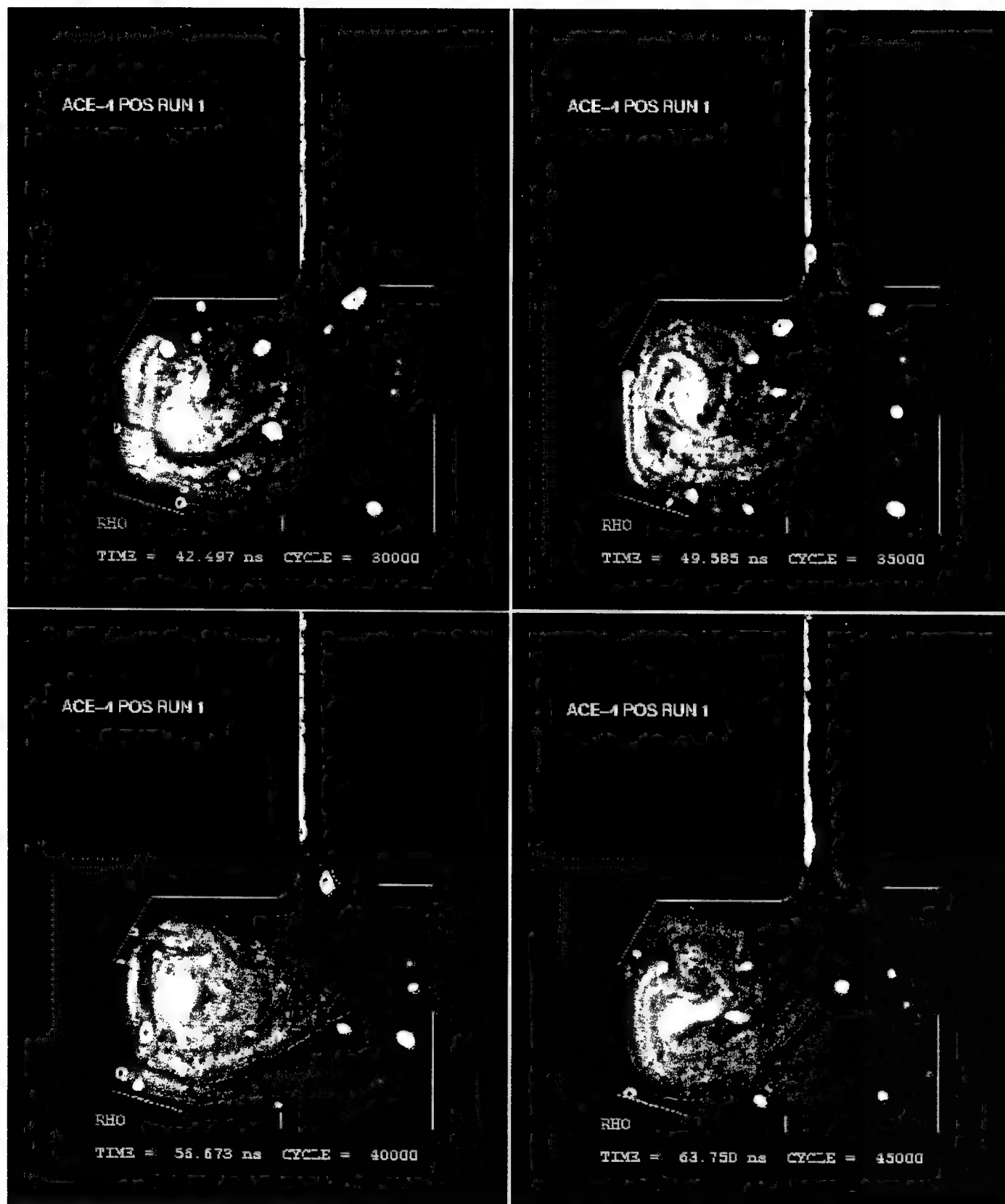


Figure 8-3. Electron charge density contours at  $t = 42.5$ ,  $49.6$ ,  $56.6$ , and  $63.8$  ns for 2-D TRIMAX PIC simulation of ACE 4 with POS gap = 25 mm.

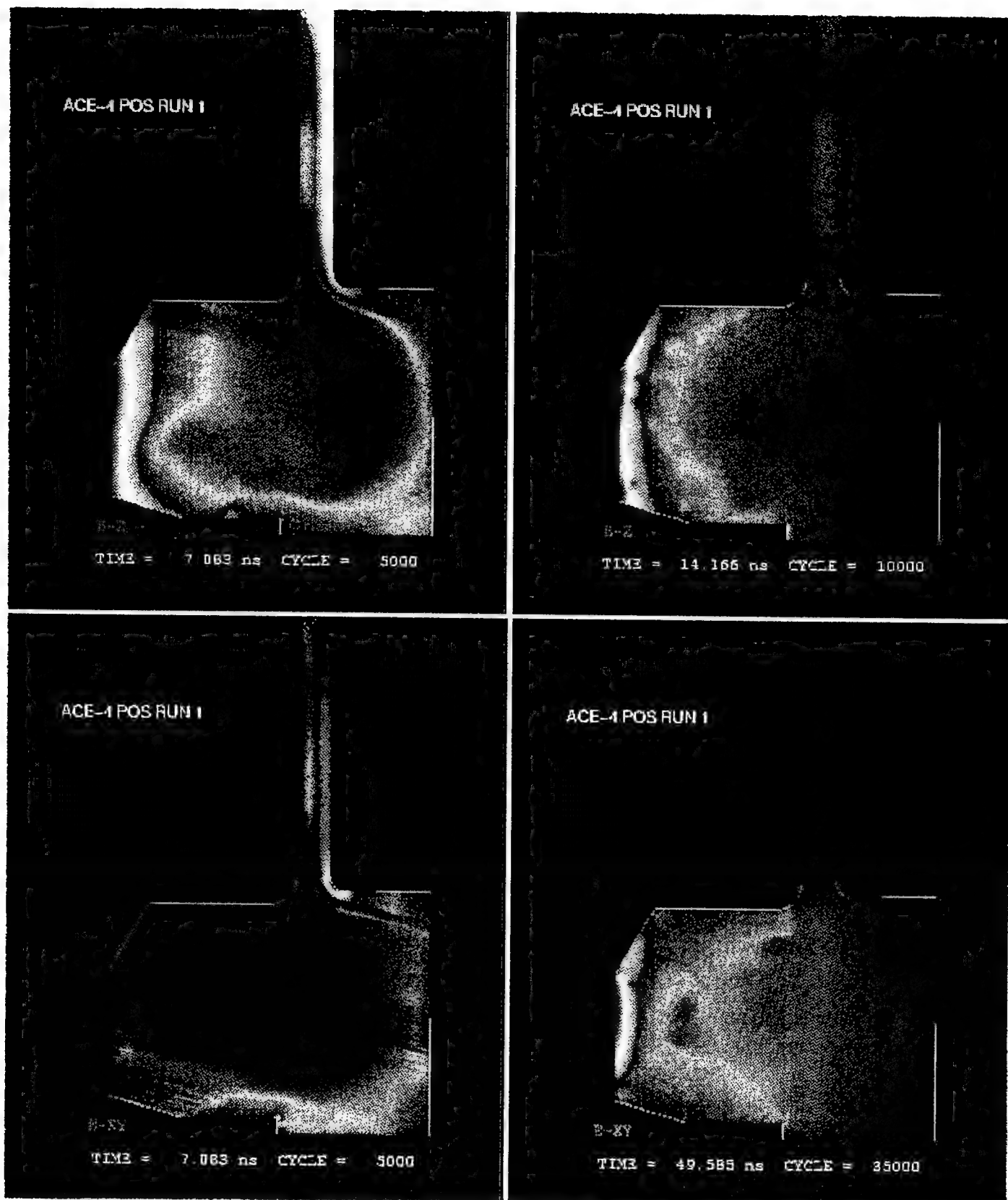


Figure 8-4. Magnetic (top) and electric field (bottom) magnitudes for 2-D TRIMAX simulation of ACE 4 with POS gap = 25 mm.

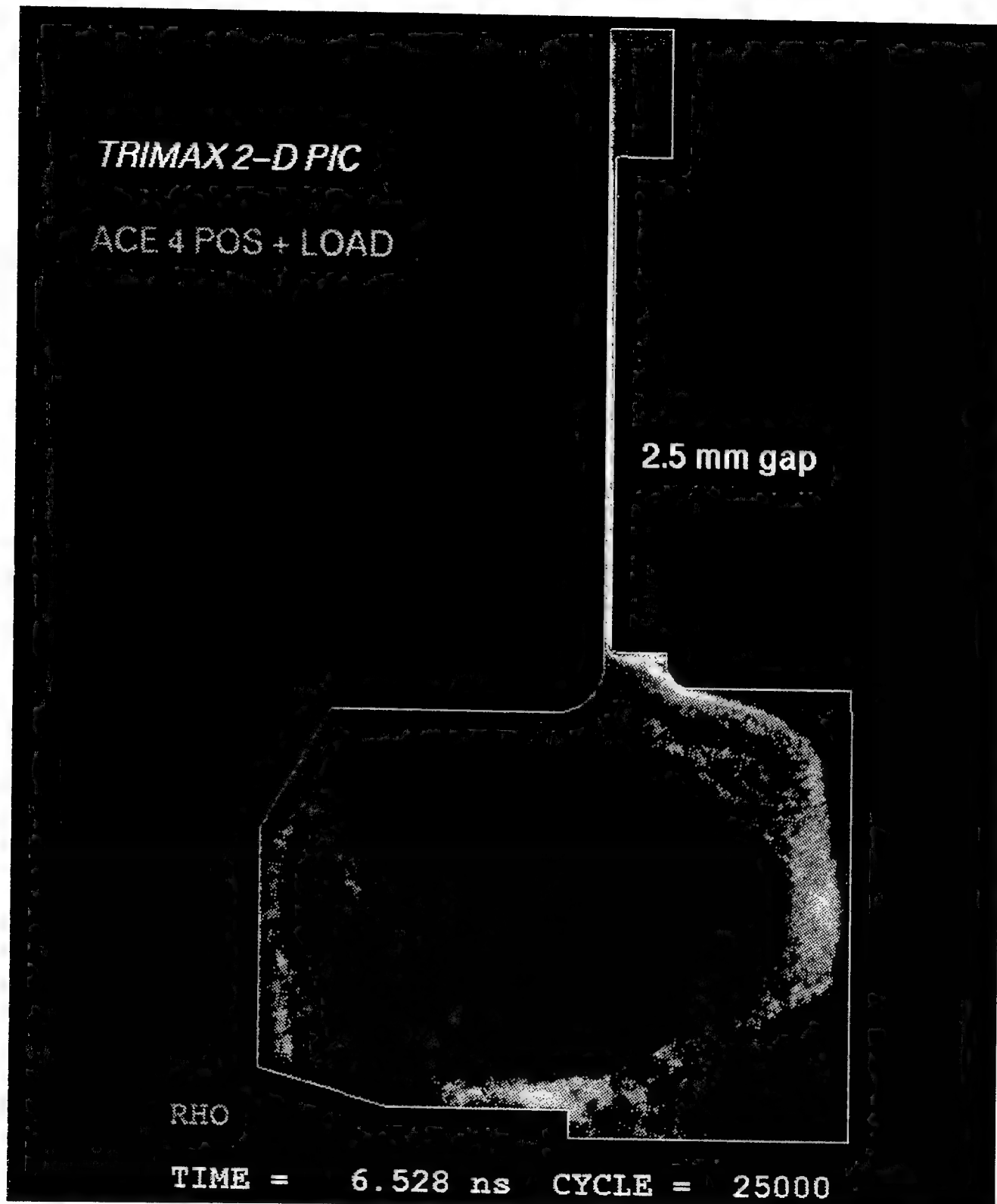


Figure 8-5. Electron charge density contours at  $t = 6.5$  ns for 2-D TRIMAX PIC simulation of ACE 4 with POS gap = 2.5 mm.

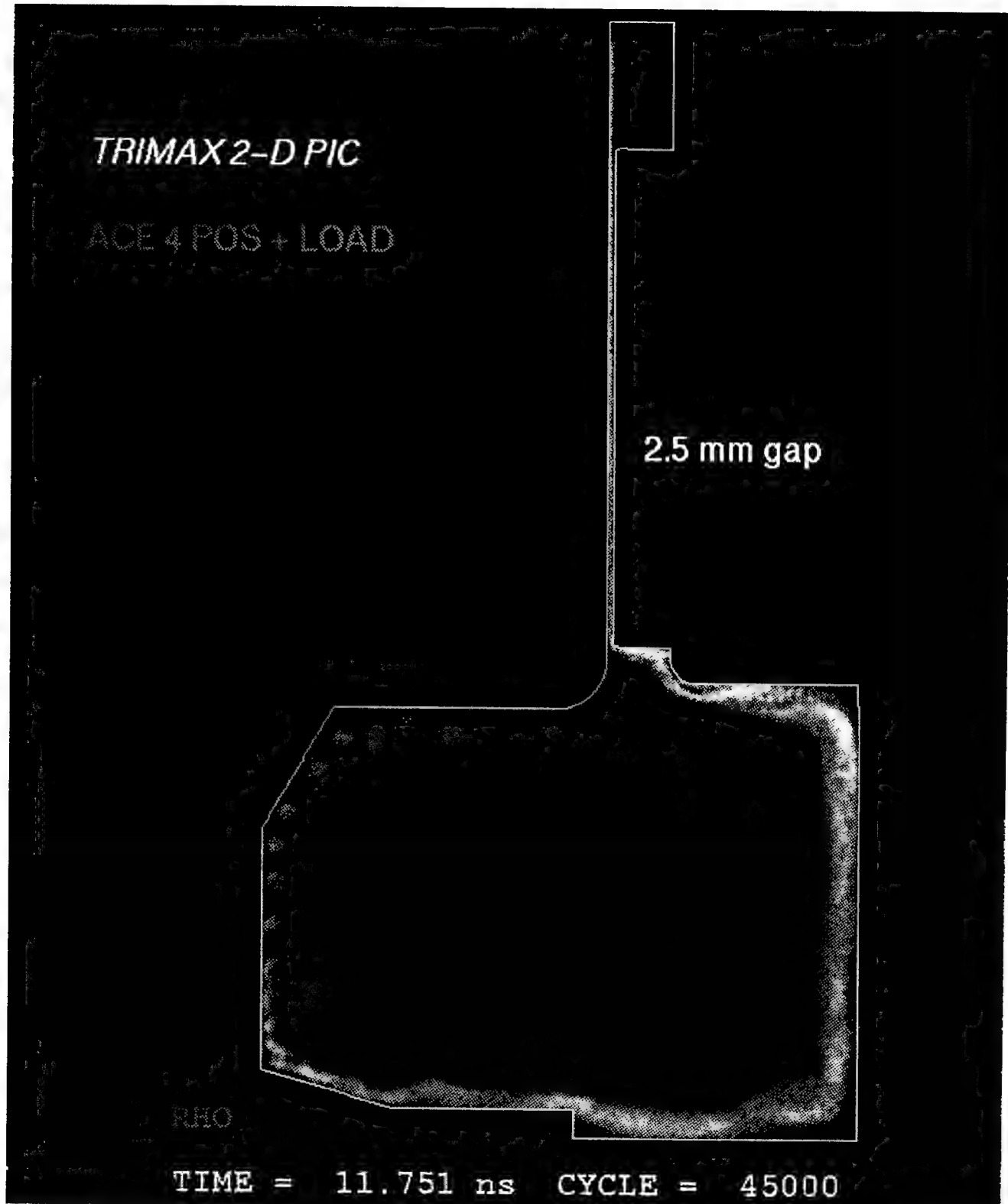


Figure 8-6. Electron charge density contours at  $t = 11.75$  ns for 2-D TRIMAX PIC simulation of ACE 4 with POS gap = 2.5 mm.

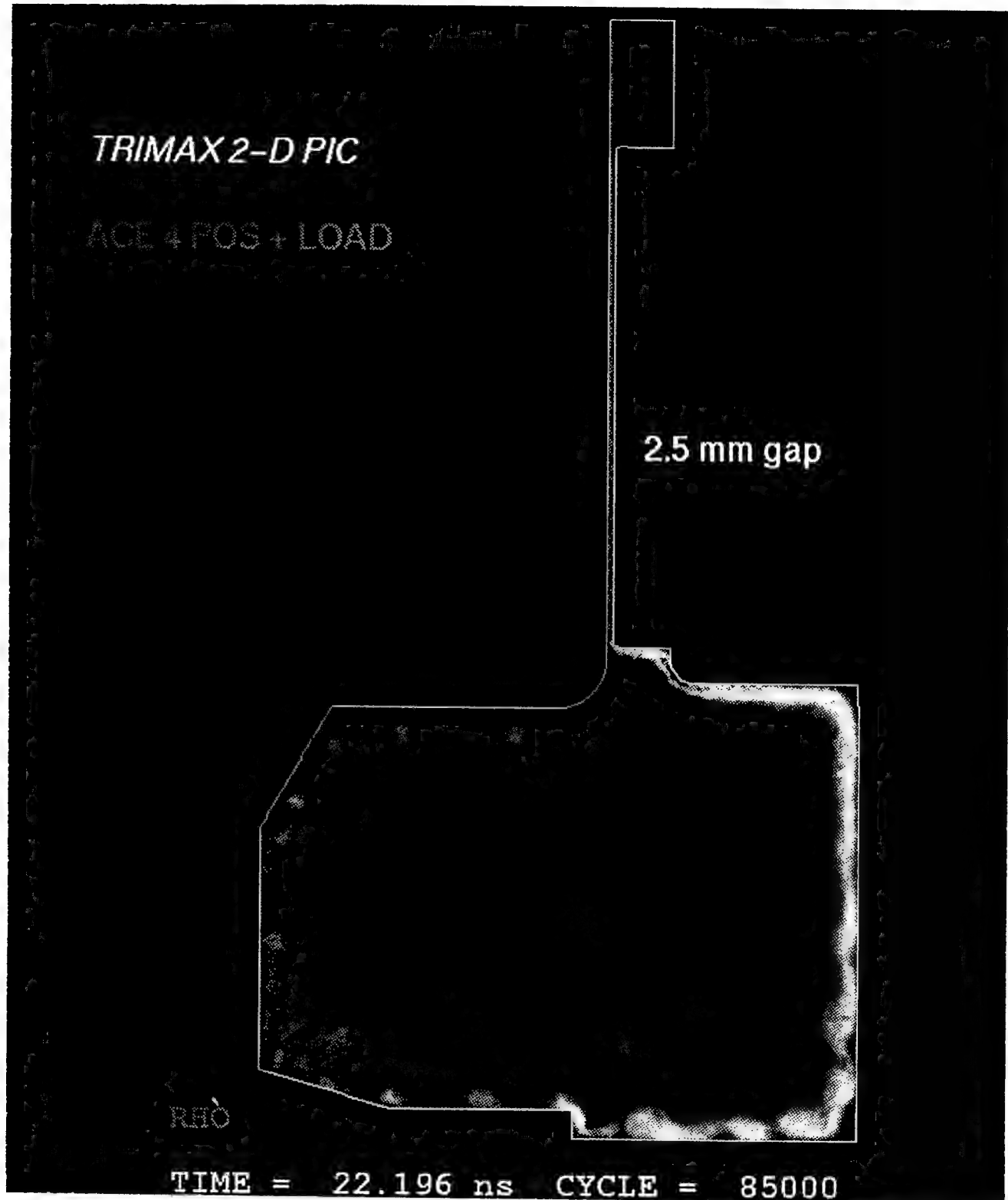


Figure 8-7. Electron charge density contours at  $t = 22$  ns for 2-D TRIMAX PIC simulation of ACE 4 with POS gap = 2.5 mm.

## SECTION 9

### REFERENCES

1. A.S. Kingsep, K.V. Chukbar and V.V. Yan'kov, Reviews of Plasma Physics, Ed. B. Kadomtsev, Vol. 16, p 243, Consultants Bureau, New York, 1990 (U).
2. A.V. Gordeev, A.S. Kingsep, L.I. Rudakov, Electron Magnetohydrodynamics Physics Reports, 243, pp 215-315 (1994) (U).
3. G.B. Whitham, Linear and Nonlinear Waves, John Wiley and Sons, New York, 1974 (U).
4. R.A. Riley, B.V. Weber, R.J. Commisso, S.M. Grossman, "Hall Effects Observed in 700 kA/600 ns Conduction POS," Pulsed Power Physics Technote, No. 95-32, Naval Research Laboratory, Washington, D.C., November 21, 1995 (U).
5. R.A. Riley, B. Weber, R. Commisso, D. Hinshelwood, and J. Grossman, "Parallel Plate POS Performance on HAWK," DNA/RAST POS Workshop, NSWC, White Oak, Maryland, March 28-30, 1995 (U).
6. D. Parks, P. Coleman, R. Ingermanson, P. Steen, J. Thompson, and J. Watrous, "Advanced Simulator Power Flow Technology/Advanced Radiation Simulation," Maxwell Technologies 1995 Annual Report, SSS-DTR-96-15347, July 1996 (U).
7. D. Parks, R. Ingermanson, E. Salberta, P. Steen, and J. Thompson, "Advanced Simulator Power Flow Technology/Advanced Radiation Simulation," Technical Report No. DNA-TR-95-59, Defense Nuclear Agency, Alexandria, Virginia 22310-3398, March 1996 (U).
8. B.V. Weber, J.R. Boller, R.J. Commisso, J.R. Goyer, D.D. Hinshelwood, and J.C. Kellogg, "Interaction of Flowing Plasma with a Metal Plate Paper," 9T26, *American Phy. Soc.*, Div. Plasma Phys., Tampa, Florida, 1991 (U).
9. D. Parks, R. Ingermanson, E. Salberta, P. Steen and J. Thompson, Advanced Simulator Power Flow Technology/Advanced Radiation Simulation, Maxwell Laboratories Annual Technical Report 1994, DNA-TR-95-59, March 1996 (U).
10. D. Parks, R. Ingermanson, E. Salberta, P. Steen and J. Thompson, Advanced Simulator Power Flow Technology/Advanced Radiation Simulation, Maxwell Laboratories/S-Cubed Division, Annual Technical Report 1995, SSS-DTR-96-15347 (U).
11. B. Weber, D. Hinshelwood and R. Commisso, "Initial Cable Gun POS Experiments on HAWK," Pulsed Power Physics Technote No. 93-06, Naval Research Laboratory, Washington, D.C., 29 March 1993 (U).

12. N.F. Mott and H.S.W. Massey, "The Theory of Atomic Collisions," Oxford, 1965, Third Edition, p. 643 (U).
13. CRC Handbook of Chemistry and Physics, Ed. David R. Lide, Ph.D., CRC Press 73rd Edition, 1992-1993 (U).
14. N.H. Tolk, J.C. Tully, W. Heiland, and C.W. White, Inelastic Ion-Surface Collisions, Academic Press, Ind. New York, 1977 (U).
15. Oen and Robinson, *Nucl. Inst. and Methods*, **132**, p 647-653, 1976 (U).
16. Robert Terry, private communication, 1992 (U).
17. Geoffrey V. Marr, Photoionization Processes in Gases, Academic Press, New York, 1967, p108 (U).
18. C.W. Mendel, D.B. Seidel, and S.E. Rosenthal, *Laser Particle Beams* **1**, 3713 (1979) (U).
19. S.B. Swanekamp, J.M. Grossman, P.F. Ottinger, and R.J. Commisso, Power Flow Between a Plasma-opening Switch and a Load Separated by a High-inductance Magnetically Insulated Transmission Line, *J. Appl. Phys.* **76**, p. 2648, Sept. 1994 (U).
20. D.E. Parks and P. Steen, "Circuit Characterization of Magnetically Insulated Electron Flow," *10<sup>th</sup> International Conference on High Power Particle Beams*, San Diego, CA, June 20-24, 1994, p 291 (U).
21. Memorandum No. UCB/ERL M89/45, "Adding Devices to SPICE3," dated April 24, 1989, written by Thomas L. Quarles, and published by the Electronics Research Laboratory of the College of Engineering at the University of California at Berkeley (U).
22. Memorandum No. UCB/ERL M520, "SPICE2: A Computer Program to Simulate Semiconductor Circuits," dated May 9, 1975, written by Laurence W. Nagel, also published by the Electronics Research Laboratory (U).
23. "MIRIAD Programmer's Reference Manual," by Thomas V. Rankin, dated April 8, 1992 (U).
24. Commisso, Boller, Rose and Swanekamp, "Circuit Simulations of DM1 with an Electron-Beam Load," NRL/MR/6770-96-7750, March 22, 1996 (U).
25. P.B. Monk and A.K. Parrott, "A Dispersion Analysis of Finite Element Methods for Maxwell's Equations," *SIAM J. Sci. Comput.*, Vol. 15, No. 4, pp 916-937, July 1994 (U).

26. P. Monk, "Analysis of a Finite Element Method for Maxwell's Equations," *SIAM J. Numer. Anal.*, Vol. 29, No. 3, pp. 714-729, June 1992 (U).
27. P. Monk, "A Comparison of Three Mixed Methods for the Time- Dependent Maxwell's Equations," *SIAM J. Sci. Stat. Comput.*, Vol. 13, No. 5, pp. 1097-1122, September 1992 (U).
28. P. Monk, "An Analysis of Nedelec's Method for the Spatial Discretization of Maxwell's Equations," *SIAM J. Numer. Anal.*, 28 (1991), pp. 1610-1634 (U).
29. F. Assous, P. Degond, E. Heintze, P.A. Raviart, and J. Segre, "On a Finite-Element Method for Solving the Three-Dimensional Maxwell Equations," *J. Comput. Phys.* 109, pp. 222-237 (1993) (U).
30. N.K. Madsen, "Divergence Preserving Discrete Surface Integral Methods for Maxwell's Curl Equations Using Non-orthogonal Unstructured Grids," *J. Comput. Phys.* 119, pp. 34-35 (1995) (U).
31. N.K. Madsen and R.W. Ziolkowski, "Numerical Solution of Maxwell's Equations in the Time Domain Using Irregular Nonorthogonal Grids," *Wave Motion* 10 (1988) pp 583-596 (U).
32. R.L. Lee and N.K. Madsen, "A Mixed Finite Element Formulation for Maxwell's Equations in the time domain," *J. Comput. Phys.*, 88 (1990) pp 284-304 (U).
33. Rainald Lohner, "A Vectorized Particle Tracer for Unstructured Grids," *J. Comput. Phys.*, 91 pp. 22-31 (1990) (U).
34. J.J. Ambrosiano, S.T. Brandon, R. Lohner, C.R. DeVore, "Electromagnetics Via the Taylor-Galerkin Finite Element Method on Unstructured Grids," UCRL-JC-107079 Preprint May 1991 (U).
35. J.J. Ambrosiano and S.T. Brandon, R. Lohner, "A New Weighted Residual Finite Element Method for Computational Electromagnetics in the Time Domain," UCRL-JC-106408 Preprint February 4, 1991 (U).
36. Brezzi, "On the Existence and Uniqueness of Saddle-point Problems Arising from Lagrange Multipliers," *RAIRO Anal. Numer.*, 8-R2 (1974), pp. 129-1513 (U).
37. J. Nedelec, "Mixed Finite Elements in R, *Numer. Math.*," 35 (1980), pp. 315-341 (U).
38. James Eastwood, "Virtual Particle Electromagnetic Particle-Mesh Algorithms," Culham Laboratory Report CLM-P870, 1990 (U).



39. M.E. Jones, "Electromagnetic PIC Codes with Body-Fitted Coordinates," Proceedings of the 12th Conference on the Numerical Simulation of Plasmas, San Francisco, California, September, 1987 (U).
40. R. Hollan, "The Case Against Staircasing," in Proceedings, 6th Annual Review of Progress in Applied Computational Electromagnetics, March 1990, p. 89 (unpublished) (U).
41. G.A. Bird, "Application of the DSMC Method," AIAA Professional Studies Series Seminar Notes, San Diego, CA, June 23-24, 1995 (U).
42. V. Girault and P. Raviart, "Finite Element Methods for Navier-Stokes Equations," Springer-Verlag, New York, 1986 (U).

**DISTRIBUTION LIST**

**DNA-TR-95-59-V3**

**DEPARTMENT OF DEFENSE**

**DEFENSE SPECIAL WEAPONS AGENCY**

ATTN: ESA, W SUMMA

ATTN: EST, K WARE

2 CY ATTN: TRC

**DEFENSE TECHNICAL INFORMATION CENTER**

2 CY ATTN: DTIC/OCF

**FC DEFENSE SPECIAL WEAPONS AGENCY**

ATTN: FCT - S, G BALADI

**DEPARTMENT OF THE NAVY**

**NAVAL POSTGRADUATE SCHOOL**

ATTN: F SCHWIRZKE, CODE 61SW

**NAVAL RESEARCH LABORATORY**

ATTN: S OSSAKOW, CODE 6700

ATTN: R MEGER, CODE 6750

ATTN: G COOPERSTEIN, CODE 6770

ATTN: R COMMISSO, CODE 6770

**NAVAL SURFACE WARFARE CENTER**

ATTN: CODE B-20

**DEPARTMENT OF THE AIR FORCE**

**AIR FORCE OFFICE OF SCIENTIFIC RSCH**

ATTN: DR. R. BARKER

**AIR WEATHER SERVICE, MAC**

ATTN: AWS TECH LIBRARY

**ARNOLD ENGINEERING DEVELOPMENT CENTER**

ATTN: DOT, MAJ J ROWLEY

**DEPARTMENT OF ENERGY**

**SANDIA NATIONAL LABORATORIES**

ATTN: J HARRIS

ATTN: J MARTIN

ATTN: M BUTTRAM

ATTN: W BEEZHOLD

**OTHER GOVERNMENT**

**CENTRAL INTELLIGENCE AGENCY**

ATTN: OSWR, J PINA

**NASA**

ATTN: J LEE, MS - 493

**NATIONAL INSTITUTE OF STANDARDS AND TECHNOLOGY**

ATTN: R HEBNER

**DEPARTMENT OF DEFENSE CONTRACTORS**

**BERKELEY RSCH ASSOCIATES, INC.**

ATTN: R KARES

ATTN: S BRECHT

**ENERGY COMPRESSION RESEARCH CORP**

ATTN: D S WEIN

**FORD MOTOR COMPANY CORPORATION**

ATTN: M MOSBROOKER

**FORD MOTOR COMPANY CORPORATION**

ATTN: C NAKAYAMA

**GA TECHNOLOGIES, INC.**

ATTN: DOCUMENT CONTROL

**ITT INDUSTRIES**

ATTN: DASIAC

ATTN: DASIAC/DARE

**ITT SYSTEMS & SCIENCES**

ATTN: D MOFFETT

**JAYCOR**

ATTN: DR CYRUS P KNOWLES

**LOCKHEED MARTIN VUGHT SYSTEMS**

ATTN: LIBRARY EM - 08

**MAXWELL TECHNOLOGIES**

2 CY ATTN: D PARKS

2 CY ATTN: J THOMPSON

2 CY ATTN: J WATROUS

2 CY ATTN: P STEEN

2 CY ATTN: R INGERMANSON

2 CY ATTN: WILLIAM H RIX

**MINNESOTA MINING &**

**MANUFACTURING COMPANY**

ATTN: D REDMOND

ATTN: E HAMPL

MISSION RESEARCH CORP.  
ATTN: B GOPLEN

PRIMEX PHYSICS INTERNTIONAL  
ATTN: C STALLINGS  
ATTN: P SINCERNY

PULSE SCIENCES, INC.  
ATTN: P W SPENCE

TETRA CORP  
ATTN: W MOENY

TEXAS TECH UNIVERSITY  
ATTN: DR M KRISTIANSEN

UNIVERSAL VOLTRONICS CORP  
ATTN: W CREWSON

UNIVERSITY OF MISSOUR - COLUMBIA  
ATTN: DR W NUNNALLY

W J SCHAFER ASSOCIATES, INC.  
ATTN: E ALCARAZ

WESTINGHOUSE STC  
ATTN: DR A H COOKSON

**DIRECTORY OF OTHER**

AUBURN UNIVERSITY  
ATTN: M ROSE

CALIFORNIA - DAVIS, UNIVERSITY OF  
ATTN: J S DEGROOT

NEW YORK - BUFFALO,  
STATE UNIVERSITY OF  
ATTN: R DOLLINGER

## **REPRODUCTION QUALITY NOTICE**

**This document is the best quality available. The copy furnished to DTIC contained pages that may have the following quality problems:**

- **Pages smaller or larger than normal.**
- **Pages with background color or light colored printing.**
- **Pages with small type or poor printing; and or**
- **Pages with continuous tone material or color photographs.**

**Due to various output media available these conditions may or may not cause poor legibility in the microfiche or hardcopy output you receive.**



**If this block is checked, the copy furnished to DTIC contained pages with color printing, that when reproduced in Black and White, may change detail of the original copy.**